UNIVERSITY OF OKLAHOMA

GRADUATE COLLEGE

OPTIMAL SPATIOTEMPORAL REDUCED ORDER MODELING FOR NONLINEAR DYNAMICAL SYSTEMS

A DISSERTATION

SUBMITTED TO THE GRADUATE FACULTY

in partial fulfillment of the requirements for the

Degree of

DOCTOR OF PHILOSOPHY

By

ALLEN LABRYER
Norman, Oklahoma
2012

OPTIMAL SPATIOTEMPORAL REDUCED ORDER MODELING FOR NONLINEAR DYNAMICAL SYSTEMS

A DISSERTATION APPROVED FOR THE
SCHOOL OF AEROSPACE AND MECHANICAL ENGINEERING

BY

Dr. Peter Attar, Chair

Dr. Prakash Vedula, Co-Chair

Dr. Ramkumar Parthasarathy

Dr. Cengiz Altan

Dr. Dimitrios Papavassiliou

To the women for whom I am eternally grateful:

Rita (Grandmother)
Yvonne (Mother)
Lauren (Wife)
Lily (Baby)

Acknowledgements

There are numerous people I would like to thank for their contributions during my dissertation research. First and foremost, I owe an enormous debt of gratitude to my advisors, Dr. Peter Attar and Dr. Prakash Vedula. This research is in fact their brainchild come to fruition. While I was in the early stages of learning how to conduct scientific research, both Dr. Attar and Dr. Vedula remained patient, upbeat, helpful and committed to my professional development. None of this would have been possible without their ingenuity and support.

I would also like to thank the rest of my committee members both past and present: Dr. Ramkumar Parthasarathy, Dr. Cengiz Altan, Dr. Dimitrios Papavassiliou and Dr. Kanthasamy Muraleetharan. Their selfless contributions to this research and my development are much appreciated.

I am most thankful for my beloved wife and soulmate, Lauren, who carries with her our first child. Together, we eagerly await the arrival of our daughter, Lily. I hope she opens her eyes to a world of wonder and love. Thank you, Lauren, for teaching me that the time to be happy is now, the place to be happy is here, and the way to be happy is to make others so.

I am also grateful to have been blessed by God with supportive family members. My mother, Yvonne, is the living embodiment of love and sacrifice. As a single parent, she worked long hours in the automotive industry to provide me with an opportunity to succeed. My mother-in-law, Jody, has taken me in as her own. My Uncle Richard is responsible for stirring my curiosity with flight by building dozens of rockets with me as a young child. My grandparents, Frank and Rita, truly are two of the best people I have ever known. Grandpa has based his life upon principles of hard work,

good character, unshakable courage and integrity. Parkinson's disease has never met a greater foe. Grandma has always been a second mother to me, and I miss her hugs more than anything. May we all aspire to live our lives as they have, and perhaps we would be so loved.

I would also like to thank several influential teachers who instilled in me at an early age a love for science and mathematics, as well as the drive to succeed. In the sixth grade, at John Ball Zoo School, Dennis Kretschman taught me how to appreciate nature, think critically, and take nothing for granted. During my first year of high school, I learned from Kelly Conrad how to find beauty in the field of mathematics. As I matured, Sergeant Major Bruce Brissette taught me how to overcome obstacles through hard work and dedication. It was David Lyons who encouraged me to use my talents wisely and emphasized the importance of remaining humble. Jim White took me under his wing and gave me the confidence to make a difference in this world.

This dissertation is based on research sponsored by the Ohio Aerospace Institute and the Air Force Research Laboratory under agreement number FA 8650-11-2-3112. I would also like to acknowledge the financial support provided though subcontract with Advanced Dynamics, Inc. (flow-through funding from NASA).

Contents

List of Tables **ix**

List of Figures **xii**

Abstract **xiii**

1 Introduction **1**
- 1.1 Fully resolved simulations . . . 3
- 1.2 Reduced order modeling . . . 3
- 1.3 Multiscale modeling . . . 7
- 1.4 Reduced order modeling with optimal prediction . . . 10
- 1.5 Optimal spatiotemporal reduced order modeling . . . 12
- 1.6 Overview . . . 14

2 Proposed theoretical framework **15**
- 2.1 Subgrid-scale dynamics . . . 16
- 2.2 Subgrid-scale models . . . 19
- 2.3 Discretization . . . 21
- 2.4 Discrete subgrid-scale dynamics . . . 22
- 2.5 Discrete subgrid-scale models . . . 26
- 2.6 Optimal reduced order modeling variants . . . 28
- 2.7 Simplifying assumptions . . . 29
- 2.8 Model construction . . . 31
- 2.9 Model appraisal . . . 33
- 2.10 Error measures . . . 35
- 2.11 Implementation . . . 36
  - 2.11.1 Time-marching formulation . . . 37
  - 2.11.2 Time-spectral formulation . . . 38
- 2.12 Summary of proposed theoretical framework . . . 42

3 Selected nonlinear dynamical systems **43**
- 3.1 Van der Pol oscillator description . . . 43
- 3.2 Duffing oscillator description . . . 45
- 3.3 Viscous Burgers flow description . . . 47
- 3.4 Nonlinear beam description . . . 50
- 3.5 Summary of selected systems . . . 53

4 Characterization of subgrid-scale dynamics **55**
4.1 Van der Pol oscillator characterization 57
4.2 Duffing oscillator characterization 61
4.3 Viscous Burgers flow characterization 66
4.4 Nonlinear beam characterization 75
4.5 Summary of characterization of subgrid-scale dynamics 90

5 Performance of optimal reduced order models **92**
5.1 Van der Pol oscillator results 93
5.1.1 Time-marching solutions 93
5.1.2 Time-spectral solutions 98
5.1.3 Summary of results for the van der Pol oscillator 100
5.2 Duffing oscillator results 101
5.2.1 Time-marching solutions 102
5.2.2 Lyapunov exponents 105
5.2.3 Time-spectral solutions 109
5.2.4 Summary of results for the Duffing oscillator 115
5.3 Viscous Burgers flow results 116
5.3.1 Performance of direct models 117
5.3.2 Performance of models based upon estimated moments 119
5.3.3 Summary of results for the viscous Burgers flow 121
5.4 Nonlinear beam results 122
5.4.1 Performance of direct models 122
5.4.2 Computational efficiency 133
5.4.3 Performance of models based upon estimated moments 137
5.4.4 Tracing bifurcations 139
5.4.5 Temporal complexity 142
5.4.6 Lyapunov exponents 144
5.4.7 Summary of results for the nonlinear beam 147

6 Conclusion **150**
6.1 Summary of proposed theoretical framework 150
6.2 Summary of results for selected systems 152
6.3 Areas for future research 156

Bibliography **162**

Appendices **175**
Appendix A – Conditional average 175
Appendix B – Stochastic estimate 176
Appendix C – An exact subgrid-scale model 177
Appendix D – Grid convergence for the nonlinear beam 180

Appendix E – Subgrid-scale models for the nonlinear beam 186
Appendix F – Potential application to fluid-structure interaction problems 190

Nomenclature **202**

List of Tables

2.1 General procedure for constructing an optimal subgrid-scale model . . 32
2.2 Direct calculation of subgrid-scale dynamics 33
2.3 Estimation of subgrid-scale dynamics 33

4.1 Qualitative FRS solution behavior for the Duffing oscillator 62
4.2 Subgrid-scale moments for the Duffing oscillator with an arbitrarily chosen set of external forcing parameters 65
4.3 Subgrid-scale moments for the Burgers flow with an arbitrarily chosen set of flow parameters 74
4.4 Qualitative FRS solution behavior for the SS beam 83
4.5 Subgrid-scale models for the nonlinear beam 90

5.1 Computation times required to produce the Lyapunov exponents for the Duffing oscillator 109
5.2 Percentage of the forcing parameter space for which the Lyapunov exponents are positive for the Duffing oscillator 109
5.3 *A posteriori* moment comparison for the Burgers flow 121
5.4 Computation times required to produce temporal complexity maps for the SS beam 144
5.5 Computation times required to produce Lyapunov exponent maps for the SS beam 147

D.1 Resolutions achievable for the SS beam 181
E.1 Appraisal metrics for various subgrid-scale models for the SS beam . 187

List of Figures

1.1 Forms of error in the numerical analysis of nonlinear dynamical systems 2
1.2 Resolutions achievable in a limiting sense by varying the computational grid in space and time with an appropriate scheme. 5
1.3 Case study into the effects of under-resolution for an elastic-plastic beam 6

2.1 Decomposition of a solution into filtered and residual components. . . 17
2.2 Spatial grids for a FRS and a ROM. 22
2.3 Temporal grids for a FRS and a ROM. 22
2.4 Filtered representations of a FRS signal. 24

4.1 Steady state FRS solutions for the van der Pol oscillator 58
4.2 LCO frequency errors for the van der Pol oscillator 59
4.3 Estimated moments for the van der Pol oscillator 60
4.4 Time history of FRS solutions for the Duffing oscillator 63
4.5 Estimated moments for the Duffing oscillator 64
4.6 Spatial variation in select moments amongst the filtered velocity field for the Burgers flow 67
4.7 Spatial variation in select moments amongst the filtered velocity field and subgrid-scale acceleration for the Burgers flow 68
4.8 Spatial variation in select moments amongst the filtered velocity field and subgrid-scale force for the Burgers flow 68
4.9 Snapshots of FRS solutions for the Burgers flow 70
4.10 Estimated moments amongst the filtered velocity for the Burgers flow 71
4.11 Estimated moments amongst the filtered velocity and subgrid-scale acceleration for the Burgers flow 72
4.12 Estimated moments amongst the filtered velocity and subgrid-scale force for the Burgers flow 73
4.13 Time history of FRS solutions for the SS beam 77
4.14 Spatial variation in select moments on a three-point backward temporal stencil for the SS beam with $F = 10$ and $\omega = 3.76$ 78
4.15 Spatial variation in select moments on a three-point central spatial stencil for the SS beam with $F = 10$ and $\omega = 3.76$ 79
4.16 Temporal variation in select moments on a three-point backward temporal stencil for the SS beam with $F = 10$ and $\omega = 3.76$ 80
4.17 Temporal variation in select moments on a two-state stencil for the SS beam with $F = 10$ and $\omega = 3.76$ 80

4.18 Temporal variation in select moments on a three-point backward temporal stencil for the SS beam with $F = 8.5$ and $\omega = 3.76$ 81
4.19 Temporal variation in select moments on a two-state stencil for the SS beam with $F = 8.5$ and $\omega = 3.76$ 81
4.20 Estimated moments for the SS beam on a two-state stencil 84
4.21 Estimated moments for the SS beam on a three-point backward temporal stencil 85
4.22 Estimated moments for the SS beam with various computational grids 86
4.23 Temporal variation in select moments for the SS, CC and CF beams with $F = 10$ and $\omega = 3.76$ 88
4.24 Temporal variation in select moments for the SS, CC and CF beams with $F = 8.5$ and $\omega = 3.76$ 88

5.1 Time-marching solutions for displacement of the van der Pol oscillator 94
5.2 Time-marching solutions for the fundamental frequency of the van der Pol oscillator 95
5.3 Frequency and displacement errors for the van der Pol oscillator with the IE time-marching scheme 96
5.4 Frequency error contours for the van der Pol oscillator with the IE time-marching scheme 97
5.5 Displacement error contours for the van der Pol oscillator with the IE time-marching scheme 97
5.6 Time-spectral solutions for displacement of the van der Pol oscillator 99
5.7 Time-spectral solutions for the fundamental frequency of the van der Pol oscillator 100
5.8 Errors for the van der Pol oscillator with the HB time-spectral scheme 101
5.9 FRS, standard IE and OPTROM solutions for the Duffing oscillator with $F = 125$ and $\omega = 1.25$ 103
5.10 FRS, standard IE and OPTROM solutions for the Duffing oscillator with $F = 125$ and $\omega = 2.25$ 104
5.11 Highly resolved Lyapunov exponent map for the Duffing oscillator . . 107
5.12 Coarse Lyapunov exponent maps for the Duffing oscillator 108
5.13 HB1 solutions for the Duffing oscillator 110
5.14 HB3 solutions for the Duffing oscillator 111
5.15 HB5 solutions for the Duffing oscillator 112
5.16 Errors for the HB solutions for the Duffing oscillator 113
5.17 Surfaces for the first harmonic amplitude of the Duffing oscillator . . 115
5.18 Velocity profile of the Burgers flow with $Re = 100$ and $St = 3$ 118
5.19 Velocity profile of the Burgers flow with $Re = 50$ and $St = 2.25$ . . . 120
5.20 USUT solutions for the SS beam with an external forcing of $F = 10$ and $\omega = 3.76$ with a moderate spatial grid and a very coarse timestep 125

5.21 USUT solutions for the SS beam with an external forcing of $F = 10$ and $\omega = 3.76$ with a moderate spatial grid and a moderate timestep . 126
5.22 USUT solutions for the SS beam with an external forcing of $F = 10$ and $\omega = 3.76$ with a very coarse spatial grid and a very fine timestep 127
5.23 USUT solutions for the SS beam with an external forcing of $F = 10$ and $\omega = 15$ with a moderate spatial grid and a very coarse timestep . 128
5.24 USUT solutions for the SS beam with an external forcing of $F = 1$ and $\omega = 3.76$ with a moderate spatial grid and a very coarse timestep . . 129
5.25 USUT solutions for the CC beam with an external forcing of $F = 10$ and $\omega = 3.76$ with a moderate spatial grid and a very coarse timestep 130
5.26 USUT solutions for the CF beam with an external forcing of $F = 2$ and $\omega = 3.76$ with a moderate spatial grid and a very coarse timestep 131
5.27 Computational efficiency of the standard USUT scheme with various grids for the SS beam 135
5.28 Computational efficiency of the USUT scheme with OPSROM and various grids for the SS beam 135
5.29 Computational efficiency of the USUT scheme with OPTROM and various grids for the SS beam 136
5.30 Computational efficiency of the USUT scheme with OPSTROM and various grids for the SS beam 136
5.31 Maximum computational efficiency curves for the USUT schemes for the SS beam 137
5.32 USUT solutions for the SS beam with an external forcing of $F = 11.5$ and $\omega = 9.5$ with a moderate spatial grid and a very coarse timestep . 138
5.33 Forcing amplitude bifurcations for the SS beam 140
5.34 Temporal complexity maps for the SS beam 143
5.35 Convergence of Lyapunov exponents for the SS beam 145
5.36 Lyapunov exponent maps for the SS beam 146

D.1 Spectral breakdown of USFT solutions for the SS beam 182
D.2 Spectral breakdown of FSUT solutions for the SS beam 183
D.3 Spectral breakdown of USUT solutions for the SS beam 184
F.1 Aeroelasticity explained through the Collar diagram 191
F.2 Physical specimen of a dragonfly wing 199
F.3 Finite element mesh of a dragonfly wing 199

Abstract

Proposed in this dissertation is a novel reduced order modeling (ROM) framework called optimal spatiotemporal reduced order modeling (OPSTROM) for nonlinear dynamical systems. The OPSTROM approach is a data-driven methodology for the synthesis of multiscale reduced order models (ROMs) which can be used to enhance the efficiency and reliability of under-resolved simulations for nonlinear dynamical systems. In the context of nonlinear continuum dynamics, the OPSTROM approach relies on the concept of embedding subgrid-scale models into the governing equations in order to account for the effects due to unresolved spatial and temporal scales. Traditional ROMs neglect these effects, whereas most other multiscale ROMs account for these effects in ways that are inconsistent with the underlying spatiotemporal statistical structure of the nonlinear dynamical system.

The OPSTROM framework presented in this dissertation begins with a general system of partial differential equations, which are modified for an under-resolved simulation in space and time with an arbitrary discretization scheme. Basic filtering concepts are used to demonstrate the manner in which residual terms, representing subgrid-scale dynamics, arise with a coarse computational grid. Models for these residual terms are then developed by accounting for the underlying spatiotemporal statistical structure in a consistent manner. These subgrid-scale models are designed to provide closure by accounting for the dynamic interactions between spatiotemporal macroscales and microscales which are otherwise neglected in a ROM. For a given resolution, the predictions obtained with the modified system of equations are optimal (in a mean-square sense) as the subgrid-scale models are based upon principles of mean-square error minimization, conditional expectations and stochastic estimation.

Methods are suggested for efficient model construction, appraisal, error measure, and implementation with a couple of well-known time-discretization schemes.

Four nonlinear dynamical systems serve as testbeds to demonstrate the technique. First we consider an autonomous van der Pol oscillator for which all trajectories evolve to self-sustained limit cycle oscillations. Next we investigate a forced Duffing oscillator for which the response may be regular or chaotic. In order to demonstrate application for a problem in nonlinear wave propagation, we consider the viscous Burgers equation with large-amplitude inflow disturbances. For the fourth and final system, we analyze the nonlinear structural dynamics of a geometrically nonlinear beam under the influence of time-dependent external forcing.

The practical utility of the proposed subgrid-scale models is enhanced if it can be shown that certain statistical moments amongst the subgrid-scale dynamics display to some extent the following properties: spatiotemporal homogeneity, ergodicity, smooth scaling with respect to the system parameters, and universality. To this end, we characterize the subgrid-scale dynamics for each of the four problems. The results in this dissertation indicate that temporal homogeneity and ergodicity are excellent assumptions for both regular and chaotic response types. Spatial homogeneity is found to be a very good assumption for the nonlinear beam problem with models based upon single-point but not multi-point spatial stencils. The viscous Burgers flow, however, requires spatially heterogeneous models regardless of the stencil. For each of the four problems, the required statistical moments display a functional dependence which can easily be characterized with respect to the physical parameters and the computational grid. This observed property, in particular, greatly simplifies model construction by way of moment estimation.

We investigate the performance of the subgrid-scale models with under-resolved simulations (in space and time) and various discretization schemes. For the canonical Duffing and van der Pol oscillators, the subgrid-scale models are found to improve

the accuracy of under-resolved time-marching and time-spectral simulations by one to two orders of magnitude. The models are also found to improve the reliability of predictions for both regular and chaotic response types by eliminating the onset of artificial regularity due to strong numerical damping with a coarse temporal grid. For the viscous Burgers flow and nonlinear beam problems, both subgrid spatial and temporal scales prove to be important as finite-difference-based simulations are expedited by coarsening the computational grid in space and time. For the viscous Burgers flow, the subgrid spatial and temporal models alone appear to be insufficient for error reduction, but when used in conjunction, the models are shown to improve statistical descriptions of the flow by five-fold. For the nonlinear beam, we perform a set of numerical experiments designed to capture the complex bifurcation behavior of the beam response. Maps for the Lyapunov exponents are also obtained with greater accuracy by including the subgrid-scale models. We find that a specified level of accuracy can be obtained one to two orders of magnitude faster by including the models instead of refining the computational grid.

CHAPTER 1

Introduction

Multiscale structures are prevalent in many nonlinear dynamical systems. Interactions between large-scale and small-scale structures are often responsible for many features, including bifurcations, chaos, intermittency, turbulence, and other phenomena [1, 2]. For many scientific and engineering applications, however, not all of the multiscale structures in a system may be important. Occam's razor (also known as the principle of parsimony) suggests that at some point, it may be appropriate to neglect the scales below a certain threshold. Mathematical models based upon principles of continuum mechanics, for example, neglect atomistic and molecular processes which typically occur on nanometer (10^{-9}m) length scales and femtosecond (10^{-15}s) time scales [3]. As a general rule for a practical study, the analyst should consider only those physical processes deemed important and measurable when deriving a set of partial differential equations (PDEs) to model a system and define a problem.

A complete problem definition consists of a set of PDEs along with the necessary boundary conditions (BCs) and initial conditions (ICs). Once a problem is defined, the next step in an analysis is to solve the equations for the quantities of interest. If an exact analytical solution to the PDEs can be found (often this is not the case), the fidelity of any model is limited by the difference between the exact solution and the true physical process, also referred to as the *epistemic error* [4–6].

Additional forms of error may occur when analytical solutions are not possible and numerical solutions with computers must be sought [7, 8], as illustrated in Figure 1.1. *Discretization errors* occur as a result of representing the set of continuous PDEs as

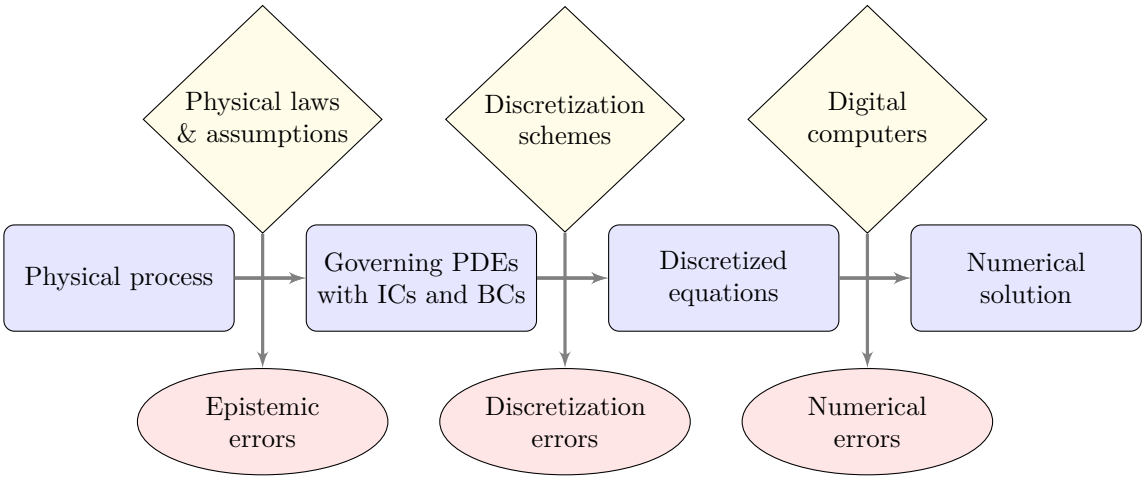

Figure 1.1: Forms of error in the numerical analysis of nonlinear dynamical systems. The blue boxes indicate the various stages of numerical analysis, the yellow diamonds indicate the tools with which each step is made, and the red ovals indicate the various forms of error which occur as a result of the analysis.

algebraic expressions in a discrete domain space, which is typically referred to as the computational mesh or grid [9]. Discretization errors are intrinsic to any numerical analysis based upon finite-difference (FD), finite-element (FE), finite-volume (FV) or spectral schemes with a coarse grid [10]. *Numerical errors*, which are also referred to as round-off errors, occur during simulation due to finite machine precision and are unavoidable with modern digital computers [11, 12].

In this dissertation, we propose a novel theoretical framework that can be used to reduce discretization errors in under-resolved numerical simulations for nonlinear dynamical systems. As the technique will be developed for a general set of PDEs, we acknowledge that epistemic errors may exist and numerical errors will also be present. The remainder of this introduction is organized as follows. To provide context for the proposed theoretical framework, in Section 1.1, we discuss the notion of fully resolved simulations. Then we review the vast amount of literature on reduced order modeling in Section 1.2 and multiscale modeling in Section 1.3. The need for a new approach will be established in Section 1.4, and in Section 1.5, we outline the key features of the proposed theoretical framework. Section 1.6 provides an overview of the dissertation.

1.1 Fully resolved simulations

The range of scales to be represented in a numerical simulation is determined by the computational grid (both spatial and temporal) and the accuracy of the discretization scheme. Often the analyst aims to predict only large-scale quantities of interest and practical relevance [13]. For some systems, however, it may be necessary to resolve small-scale quantities below the threshold of interest due to widespread coupling between multiscale spatiotemporal structures [14]. Hence, with a standard discretization scheme, a highly refined computational grid may be required for reliable predictions. A so-called fully resolved simulation (FRS) contains negligible discretization errors and renders the most accurate solution with respect to the scales considered relevant.

Here we draw a distinction between the scales deemed important in a physical process (*macroscale*) and those considered negligible (*microscale*). We further distinguish the scales resolved in a numerical simulation (*coarse*) from those left unresolved (*subgrid*). These are subtle differences which become moot if the PDEs are considered to be an exact description of the physical process and a FRS solution can be found. For under-resolved simulations, however, distinction of these scales can be important.

1.2 Reduced order modeling

For many systems, the computational expense required to obtain a FRS can be prohibitive. When a large number of degrees of freedom (DOFs) are used in a simulation, the required memory can exceed available resources and the computation time can become unwieldy. These challenges can, in principle, be overcome by developing a reduced order model (ROM) [15, 16]. The primary objective of a ROM is to predict macroscale behavior as accurately as possible with a reduced computational burden such that

$$\frac{\text{cost of ROM}}{\text{cost of FRS}} \ll 1.$$

Standard ROMs are able to provide affordable simulations by resolving fewer scales than a FRS.

The development of ROMs (in space and time) has become an interdisciplinary endeavor [15, 16]. From a mathematical perspective, the construction of a ROM typically involves to the expansion of a problem field into a set of known basis vectors whose unknown coefficients are found using either a Ritz or weighted residual method [17]. Normal mode analysis (NMA) for solid mechanics [17, 18] is perhaps the most well-known example in which the basis vectors are functions of space. The harmonic balance (HB) approach [19, 20] is a classic example of constructing a ROM with basis vectors that are functions of time. In electrical engineering, ROMs are commonly developed for nonlinear circuit analysis by means of Krylov subspace techniques, Hankel norm model reduction, and Schur interpolation [15]. Many of the ROMs fundamental to the fields of aerodynamics and aeroelasticity are based upon Volterra series [16] and proper orthogonal decomposition (POD) [21]. For many of these "standard" ROMs, the construction process is based upon prior knowledge about the system obtained from highly resolved simulation. Information from a select number of resolved modes is typically retained, whereas information about effects due to unresolved scales is typically discarded. By no means should this be considered an exhaustive list, but the common theme with standard ROMs is that they produce coarse approximations of the true solution.

We suggest that any simulation method should be considered a ROM if it fails to provide the resolution of a FRS. This includes standard discretization schemes based upon FD, FE, FV and spectral methods. Consider, for example, a FD-based time-marching simulation for an initial value problem: in order to completely resolve all relevant time scales, the analyst should choose a sufficiently small timestep. Equivalently, for a time-spectral simulation [22], the choice becomes one of retaining enough temporal modes. But for many problems, the timestep or number of temporal modes

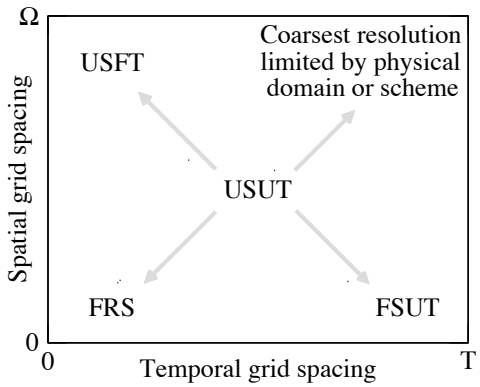

Figure 1.2: Resolutions achievable (in a limiting sense) by varying the computational grid (in space and time) with an appropriate scheme (one that is stable, consistent and convergent): under-resolved in space and under-resolved in time (USUT), fully-resolved in space and under-resolved in time (FSUT), under-resolved in space and fully-resolved in time (USFT), and a fully resolved simulation (FRS). Ω denotes the spatial domain in which the system resides and T denotes the largest time scale. Any simulation other than a FRS should be considered a ROM.

required for a FRS may be just as prohibitive as the required spatial grid. In practice, the analyst may achieve a more affordable simulation (i.e. a ROM) by coarsening the computational grid or reducing the number of DOFs. Such an approach, however, often comes with a compromise in accuracy. As illustrated in Figure 1.2, a ROM may be under-resolved in space and under-resolved in time (USUT), fully-resolved in space and under-resolved in time (FSUT), or under-resolved in space and fully-resolved in time (USFT). Not all resolutions in Figure 1.2 may be feasible, or even possible, depending on the numerical method and available resources.

When ROM simulations are used to help make decisions in engineering design and analysis, discretization errors due to coarse computational grids can potentially lead to unexpected outcomes and result in unexpected failure of the system. As an example, we discuss a well-known case study conducted by Symonds and Yu [23]. This particular case study has been identified by Cook and his colleagues [24] as a cautionary tale of computer misuse in engineering. Symonds and Yu considered a simply supported beam with elastic-plastic constitutive properties subjected to a uniformly distributed pressure pulse. The problem was sent out to ten analysts regarded as experts with

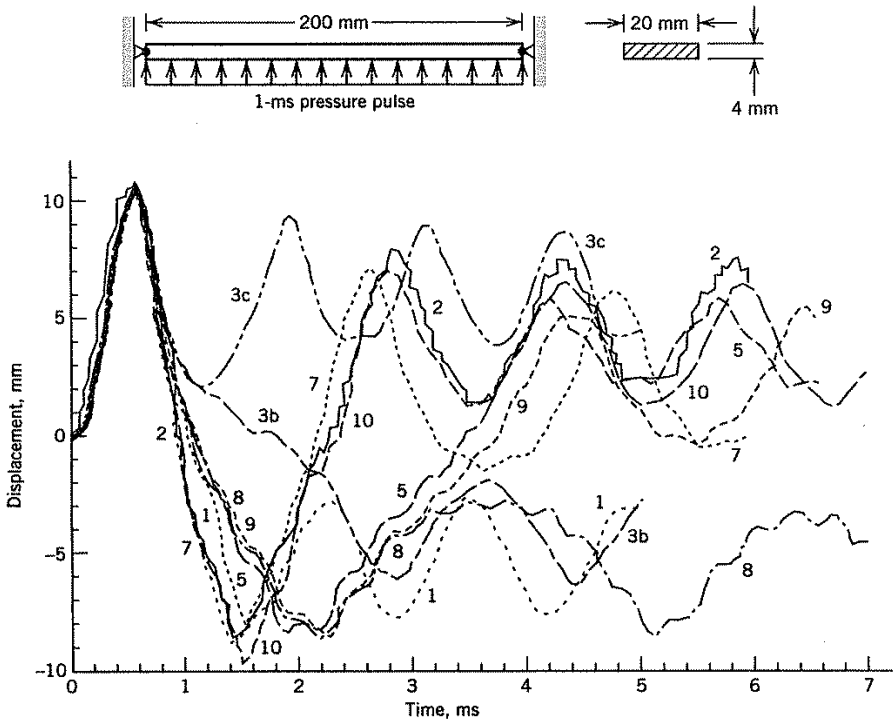

Figure 1.3: Case study into the effects of under-resolution for an elastic-plastic beam, conducted by Symonds and Yu [23] and reproduced courtesy of ASME. The beam is simply supported on both ends and is subjected to a uniformly distributed pressure pulse. Shown in the figure are solutions for the transverse displacement obtained by ten expert analysts with various structural dynamics codes and computational grids.

the objective to predict the time-history for transverse displacement. The simulation results, shown in Figure 1.3, were obtained with ten reputable structural dynamics codes, including ABAQUS, ANSYS, MARC and others. Two of the curves, labeled 3b and 3c, were obtained from the same code with two different timesteps, and yet they suggest that the beam will reach two different equilibrium points as a result of plastic deformation. So long as all of the codes are consistent, the differences in the curves are the result of coarse spatial and temporal grids chosen by the analysts. Without further analysis, it is impossible to tell which of the curves, if any, are correct.

The origin of errors intrinsic to any ROM can be traced back to the subgrid-scale dynamics and their interactions with the resolved dynamics. Macroscale quantities in a nonlinear system are, in fact, coupled with the microscale quantities [3]. Therefore, without proper knowledge about the subgrid-scale dynamics, the discretized equations

describing the evolution of the resolved quantities cannot be solved accurately [13]. This sort of issue is known throughout the physics literature as the closure problem [2]. In a standard ROM, closure is implicitly neglected as the subgrid-scale dynamics, and their statistical moments, are effectively set to zero. For many applications, though, neglecting closure can lead to intolerable discretization errors. To be useful for design and analysis, a reliable ROM should not violate the constraint

$$\text{ROM errors in quantities of interest} < \text{tolerance (problem-specific)}.$$

From an engineering perspective, the analyst is faced with a predicament when all affordable ROMs are unreliable, or equivalently, when all reliable ROMs are unaffordable. The search for remedies to this dilemma has become one of many focal points in the field of multiscale modeling.

1.3 Multiscale modeling

The body of literature on multiscale modeling is both multidisciplinary and extensive. A review article by Horstemeyer [14] provides historical perspective while focusing on scientific and engineering applications. Another review article by Fish [3] compares technical aspects of various types of methods that have emerged throughout the years. Broadly speaking, multiscale modeling can refer to any simulation technique capable of extracting certain quantities of interest from problems in which important features exist on multiple scales [14]. The term *enrichment* is often used to signify various forms of improvement in a simulation [3]. Throughout the literature, multiscale methods are typically classified as either *information-passing* or *concurrent* [3]. Information-passing (also referred to as serial or parameter-passing) methods involve one-way coupling and are formulated to enrich the simulation of one set of scales using information obtained previously from another set of scales. Concurrent (also referred

to as hand-shaking) methods generally involve two-way coupling as microscale and macroscale quantities are computed simultaneously "on-the-fly" [3].

Much of the work in recent years has concentrated on bridging scale methods, most of which attempt to improve the description of a physical process by solving one set of PDEs for macroscale dynamics while solving another set of equations for microscale dynamics. An extensive overview of various bridging scale methods can be found in a review article by Liu and Park [25] and in a book by Liu and his colleagues [26]. Belytschko and Xiao [27], for example, developed a framework for coupling molecular dynamics (MD) simulations with continuum mechanics simulations based upon the FE method. Wagner and Liu et al [28, 29] also presented a framework for projecting MD simulations onto a global set of coarse scale shape functions. Kadowaki and Liu [30] proposed a bridging scale method in which two continuum-based FE meshes (one coarse, the other fine) are coupled for a class of localized failure problems. In the field of fluid mechanics, bridging scale methods have been developed for problems in non-Newtonian flows and microfluidics [31]. For instance, numerical simulations based upon the Lattice Boltzmann method have been used as microscale models to enrich solutions for flows governed by the continuum-based Euler equations [32] and Navier-Stokes equations [33]. In this sense, the common objective of most atomistic-to-continuum and continuum-to-continuum bridging scale methods is to reduce epistemic errors by accounting for information otherwise neglected by a set of PDEs based upon continuum mechanics.

Multiscale modeling can also refer to methods geared to address closure, or reduce discretization errors, by accounting for information unresolved by standard ROMs. In the fluids literature, for example, a simulation that completely resolves all relevant spatial and temporal scales in the Navier-Stokes equations is said to be a direct numerical simulation (DNS) [34]. Conceptually equivalent to a FRS, the computational expense required for a DNS is often prohibitive. As an alternative, the numerical

method known as large-eddy simulation (LES) [35, 36] is formulated to resolve only the large-scale motions in a turbulent flow whereas the smallest scales [37], which are most expensive to resolve, are modeled in various ways [35, 36]. With the LES approach, these subgrid-scale models are embedded into the governing equations and are designed to provide closure (to some degree) by accounting for the effects due to unresolved spatial scales. Out of all the subgrid-scale models for LES, the one proposed by Smagorinsky [38, 39] is perhaps the most widely known.

The framework to be presented in this dissertation shares several features with the LES approach in addition to a number of other multiscale methods. For example, Hughes and his colleagues [40] presented a class of variational multiscale (VMS) methods to enrich coarse scale FE solutions by assuming the fine scale structures to be residual-free bubbles that vanish on the coarse scale element boundaries. As such, with the VMS method, the fine scales structures can be "condensed out" of the coarse scale FE solution. Hughes first developed the VMS method for problems with spatial dependence [41] and later extended the technique for problems with time dependence [42]. Liu et al [43] also developed a reproducing kernel particle method (RKPM) for under-sampled spatial and temporal discretization schemes. More recently, Fish and his colleagues [44] proposed a general framework for improving the accuracy of spatial ROMs by adding to the governing equations information based upon a nonlocal quadrature scheme.

Our proposed framework also shares some features with a class of heterogeneous multiscale methods (HMMs) described by E and his colleagues [13]. In the spatial domain, Abdulle [45] proposed a HMM for elliptical and parabolic PDEs. In the time domain, Engquist [46] and Sharp [47] developed HMMs to improve the numerical properties of stiff ODEs with multiple time scales. HMMs have also been developed by E [48] and Vanden-Eijnden [49] for stochastic ODEs governing advection and diffusion processes with multiple time scales.

Other temporal multiscale models have been developed to provide enrichment in the form of numerical stability, convergence or solvability [3]. To this end, a variety of time-integration strategies have been deployed, including multi-time-step methods [50, 51], time-homogenization [52], variational techniques [53] and domain decomposition into orthogonal [54] and proper generalized [55] components. Unlike the more popular spatial multiscale methods, however, enrichment in the form of temporal accuracy is seldom addressed, let alone in an optimal sense.

1.4 Reduced order modeling with optimal prediction

A wide variety of mathematical formalisms have been proposed [56] to address the issue of closure in multiscale ROMs. In this dissertation, we employ the first-order optimal prediction formalism, which originates from concepts first put forth in the statistical physics literature by Mori [57] and Zwanzig [58], and was further developed by Chorin and his colleagues [59–62]. The optimal prediction formalism is based upon principles of mean-square error minimization [63], conditional expectations [64] and stochastic estimation [65, 66]. Chorin first presented what is known as the first-order optimal prediction formalism within the context of nonlinear dynamical systems [59]. He later proposed a higher-order version [60], specialized the technique for use with Hamiltonian systems [61], and modified the system of equations to include the effects due to non-Markovian memory [62].

In the analysis of turbulent flows, for example, a special (data-driven) variant of LES known as optimal LES (OLES) [67–71] is based upon the optimal prediction formalism such that the mean-square error is minimized between the subgrid-scale models and the quantities for which they are designed to replace. The OLES approach can be used to expedite numerical simulations for turbulent flows (by coarsening the computational grid in the spatial domain) while maintaining reliable predictions for the quantities of interest (by preserving the underlying spatial statistical structure).

Previous OLES models have been appraised for their ability to account for the effects of subgrid-scale convection and diffusion terms, which arise due to the use of coarse spatial grids [67–71]. It should be emphasized, however, that in OLES and all other known LES models to date, only the effects due to subgrid spatial scales are addressed. Valid or not, all time scales are assumed to be fully resolved. As such, OLES models are able to improve the accuracy of predictions for multi-point in space, but only single-point in time statistics of turbulent flows. This limitation may perhaps be the reason why some state of the art LES models are unable to accurately predict the evolution of certain flow structures [72, 73]. Nevertheless, the basic principles behind OLES can be applied to any nonlinear dynamical system in addition to turbulent flows. As such, we consider OLES to be a specialized form of optimal ***spatial*** reduced order modeling (OP**S**ROM).

Beyond what is done in OLES and OPSROM, there exists an opportunity to improve the efficiency of numerical simulations for nonlinear dynamical systems (by coarsening the computational grid in time) while maintaining reliable predictions for the quantities of interest (by preserving the underlying temporal statistical structure). To this end, LaBryer, Attar and Vedula proposed the optimal ***temporal*** reduced order modeling (OP**T**ROM) framework for nonlinear dynamical systems [74, 75]. With OPTROM, subgrid-scale models based upon the optimal prediction formalism are embedded into the governing equations (like OLES and OPSROM) in order to account for the effects due to unresolved time scales (unlike OLES and OPSROM). As a proof of concept, LaBryer, Attar and Vedula used the OPTROM approach to improve the accuracy of under-resolved simulations for the canonical van der Pol [74] and Duffing [75] oscillators with coarse time-marching and time-spectral schemes. Since the van der Pol and Duffing oscillators contain no spatial dependence, there was no need to address subgrid spatial scales. Both of these problems will be studied extensively in this dissertation.

1.5 Optimal spatiotemporal reduced order modeling

For nonlinear dynamical systems with spatiotemporal dependence, we hypothesize that it may be possible to improve the reliability and efficiency of under-resolved simulations by accounting for the combined effects due to subgrid spatial and temporal scales. In this context, we aim to fill a knowledge gap by addressing several research questions, including: What kind of information is required in order to model the effects due to subgrid spatial and temporal scales? Out of all possible choices for the subgrid-scale models, which functional forms will provide optimal predictions for the quantities of interest? What are the ways in which these models can be constructed? When can one expect these models to successfully improve the reliability and efficiency of under-resolved simulations?

In this dissertation, we propose the new optimal ***spatiotemporal*** reduced order modeling (OP**ST**ROM) framework [76–78], which can be used to expedite numerical simulations for nonlinear dynamical systems (by coarsening the computational grid in space and time) while maintaining reliable predictions for the quantities of interest (by preserving the underlying spatiotemporal statistical structure). The proposed framework is essentially the combination of any spatiotemporal ROM with a special type of two-way interactive subgrid-scale model, and therefore, can be classified as a form of concurrent multiscale modeling [3]. The OPSTROM framework is based upon the following key features:

- Effects due to unresolved spatial and temporal scales are accounted for
- Subgrid-scale dynamics are derived using filters tailored to the ROM
- Subgrid-scale models are designed to interact with the resolved scales
- Model construction is data-driven, and is based upon principles of mean-square error minimization, conditional expectations and stochastic estimation

- By construction, the subgrid-scale models are consistent with the underlying spatiotemporal statistical structure

Whereas some of the features listed above can also be found in several other multiscale models, when taken as a whole, they make the OPSTROM framework unique. The final feature, in particular, distinguishes OPSTROM from most other HMM, VMS, LES and bridging scale methods. Unlike the OLES approach for turbulent flows, OPSTROM accounts for subgrid temporal scales (in addition to subgrid spatial scales) and is formulated for any nonlinear dynamical system (in addition to turbulent flows). To the author's knowledge, OPSTROM marks the first application of the optimal prediction formalism to a spatiotemporal multiscale ROM.

The OPSTROM approach has practical application for a wide range of multiscale problems in engineering and physics, particularly if the inputs required for model construction (multi-point statistical moments amongst the subgrid-scale dynamics) display (at least to some extent) the following statistical properties: spatiotemporal homogeneity, ergodicity, smooth scaling with respect to the system parameters, and universality [79]. Each of these properties have been observed to a large degree in turbulent flows [2]. Smagorinsky-type LES models, for example, are based on the assumption of universal dissipation on the microscale level [80]. In this dissertation, we expect to find (as others have suggested [79, 81]) a similar type of behavior in other nonlinear dynamical systems. While this proposed work will concentrate on continuum-based ROMs, the technique should also be applicable to multiscale ROMs in which the subgrid-scale dynamics are derived from molecular dynamics or statistical physics based simulations.

1.6 Overview

This dissertation is organized as follows. In Chapter 2, we present the OPSTROM framework for nonlinear dynamical systems. Our presentation of the technique will begin with a derivation of subgrid-scale dynamics and subgrid-scale models followed by suggestions for practical application, including simplifying assumptions for model construction, appraisal, error measures and implementation. Then, in Chapter 3, we describe four nonlinear dynamical systems with unique features that will serve as testbeds to demonstrate the technique. We will investigate the canonical van der Pol and Duffing oscillators, a viscous Burgers flow subject to large amplitude inflow disturbances, and a geometrically nonlinear beam under the influence of time-dependent external forcing. In Chapter 4, we characterize the subgrid-scale dynamics for each of the four problems. The results of this characterization will greatly influence the construction of subgrid-scale models. In Chapter 5, we study the performance of standard ROM, OPTROM, OPSROM and OPSTROM simulations with various subgrid-scale models. We aim to determine which ROM(s) provide the best trade-off between computational expense and accuracy for each problem. Various tools and measures will be used in order to investigate the numerical solutions, including time history plots, Fourier transformations, contour plots, surface plots, Poincaré maps, phase portraits, bifurcation diagrams and Lyapunov exponents. Concluding remarks and recommendations for future work are offered in Chapter 6.

CHAPTER 2

Proposed theoretical framework

As discussed in the previous chapter, the objective of the optimal spatiotemporal reduced order modeling (OPSTROM) framework is to expedite numerical simulations for nonlinear dynamical systems (by coarsening the computational grid in both space and time) while maintaining reliable predictions for the quantities of interest (by preserving the underlying spatiotemporal statistical structure). The technique to be presented here is valid for any nonlinear dynamical system governed by PDEs in space and time. The number of states and spatial dimensions may be arbitrarily large, and the trajectories may be regular or chaotic. Such a system can be written as

$$A\mathbf{u} = \mathbf{R}\left(\mathbf{u}, \mathbf{x}, t\right) \text{ in } \mathbf{\Omega}, \tag{2.1}$$

along with an appropriate set of BCs and ICs. The system contains N_S states in $\mathbf{u}\left(\mathbf{x}, t\right)$ with components u_i, which evolve in physical space and time, where $\mathbf{x}$ is a vector of N_D spatial coordinates with components x_k and t is the time. A is a linear time-derivative operator (typically first-order or second-order) and $\mathbf{R}$ is a generally nonlinear function of the states, their spatial derivatives, position and time. $\mathbf{\Omega}$ denotes the spatial domain in which the system resides.

We presume the analyst has chosen to discretize the governing equations with a coarse computational grid out of necessity or convenience. The chosen scheme does not properly resolve all spatiotemporal scales of interest, and therefore, discretization errors will occur (at times substantial). If certain statistical information is known *a priori* about the interactions between unresolved spatiotemporal scales and resolved

spatiotemporal scales, it can be used to improve the accuracy of numerical solutions. Such a method will now be outlined.

2.1 Subgrid-scale dynamics

In this section, we demonstrate the manner in which subgrid-scale dynamics arise in the governing PDEs using basic filtering concepts. For the sake of pedagogy, we assume the analyst has *a priori* knowledge of the true solution $\mathbf{u}$ for any set of parameters. Where this knowledge comes from is not of immediate importance. To be discussed in Section 2.8, complete knowledge of $\mathbf{u}$ should not be considered a requirement, but rather, knowledge of some invariant statistical measures should be sufficient for model construction.

Under-resolved solutions can be considered filtered representations of the true solution, as depicted in Figure 2.1. Similar to what is done for LES of turbulent flows [2,35] and other multiscale methods [25,40], the true signal $\mathbf{u}$ can be decomposed into filtered $\tilde{\mathbf{u}}$ and residual $\hat{\mathbf{u}}$ components

$$\mathbf{u}(\mathbf{x},t) = \tilde{\mathbf{u}}(\mathbf{x},t) + \hat{\mathbf{u}}(\mathbf{x},t). \tag{2.2}$$

The filtering operation [2, 35] used to obtain $\tilde{\mathbf{u}}$ can be represented as an integral transform in space and time

$$\tilde{\mathbf{u}}(\mathbf{x},t) = \int\int G(\mathbf{x}',t')\,\mathbf{u}(\mathbf{x}-\mathbf{x}',t-t')\,d\mathbf{x}'dt'. \tag{2.3}$$

The amount of information contained in $\tilde{\mathbf{u}}$ is generally less than that contained in $\mathbf{u}$. Such irreversible loss of information introduces an intrinsic error, which serves as a lower bound for any ROM. The kernel G can take on any form. For certain schemes, G can be split into spatial and temporal kernels, $G_{\mathbf{x}}$ and G_t, such that the filtering

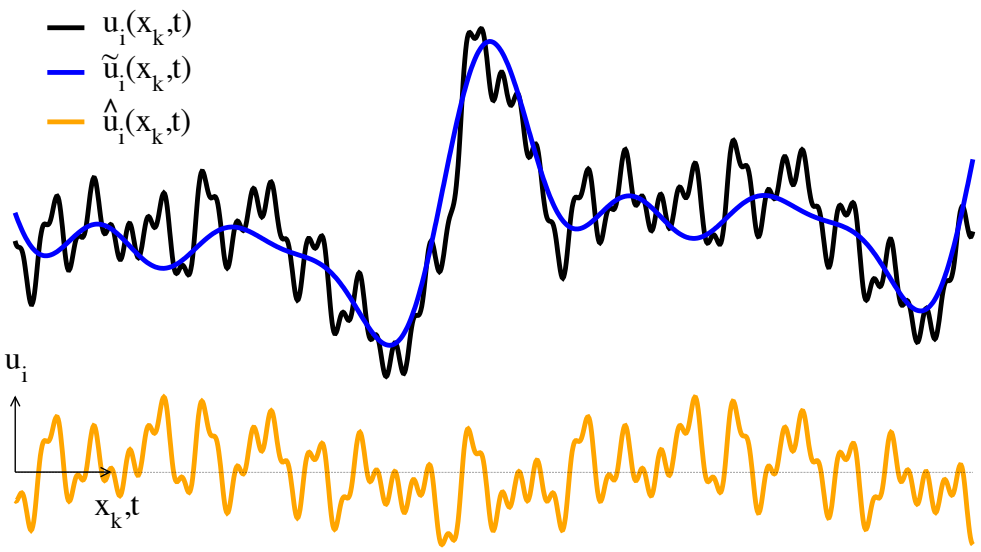

Figure 2.1: Decomposition of the true solution $u_i(x_k, t)$ into filtered $\tilde{u}_i(x_k, t)$ and residual $\hat{u}_i(x_k, t)$ components.

operation in (2.3) is a two-step process. Equivalently, in the Fourier domain, the filtering operation can be written as a Fourier smoothing or spectral cutoff filter

$$\tilde{\bar{\mathbf{u}}}_l^k = \mathcal{G}\left(l,k\right)\bar{\mathbf{u}}_l^k, \tag{2.4}$$

where l and k denote the spatial and temporal wavenumbers, $\bar{\mathbf{u}}$ are the true Fourier modes, $\tilde{\bar{\mathbf{u}}}$ are the filtered Fourier modes, and $\mathcal{G}\left(l,k\right)$ is the Fourier filter.

To produce $\tilde{\mathbf{u}}$ with any ROM, each term in the governing PDEs and BCs in (2.1) must be filtered with the chosen $G\left(\mathbf{x}',t'\right)$ or $\mathcal{G}\left(l,k\right)$. Doing so effectively separates the coarse quantities from the subgrid-scale quantities. This filtering operation can also be viewed as a non-invertible mapping from an infinite-dimensional solution space to a finite-dimensional space [22]. The modified governing PDEs become

$$\widetilde{A\mathbf{u}} = \widetilde{\mathbf{R}\left(\mathbf{u},\mathbf{x},t\right)}. \tag{2.5}$$

We can rewrite (2.5) in terms of $\tilde{\mathbf{u}}$ by introducing the residual field $\boldsymbol{\tau}$, which accounts

for all forms of commutation error associated with the filtering operator:

$$
\begin{aligned}
A\tilde{\mathbf{u}} &= \mathbf{R}\left(\tilde{\mathbf{u}}, \mathbf{x}, t\right) + \boldsymbol{\tau}\left(\mathbf{u}, \tilde{\mathbf{u}}, \mathbf{x}, t\right) \qquad (2.6)\\
\boldsymbol{\tau}\left(\mathbf{u}, \tilde{\mathbf{u}}, \mathbf{x}, t\right) &= \boldsymbol{\alpha}\left(\mathbf{u}, \tilde{\mathbf{u}}, \mathbf{x}, t\right) + \boldsymbol{\gamma}\left(\mathbf{u}, \tilde{\mathbf{u}}, \mathbf{x}, t\right)\\
\boldsymbol{\alpha}\left(\mathbf{u}, \tilde{\mathbf{u}}, \mathbf{x}, t\right) &= A\tilde{\mathbf{u}} - \widetilde{A\mathbf{u}}\\
\boldsymbol{\gamma}\left(\mathbf{u}, \tilde{\mathbf{u}}, \mathbf{x}, t\right) &= \widetilde{\mathbf{R}\left(\mathbf{u}, \mathbf{x}, t\right)} - \mathbf{R}\left(\tilde{\mathbf{u}}, \mathbf{x}, t\right).
\end{aligned}
$$

The system in (2.6) represents the set of PDEs modified for a ROM. We refer to the total residual field $\boldsymbol{\tau}$ as the *subgrid-scale dynamics*. For problems in continuum mechanics, it may be insightful to refer to $\boldsymbol{\alpha}$ as the *subgrid-scale acceleration* and $\boldsymbol{\gamma}$ as the (mass normalized) *subgrid-scale force*. This terminology aligns with the fluids literature [36] in which unresolved components of the Navier-Stokes equations are commonly referred to as the subgrid-scale viscosity and subgrid-scale convection. Additional residual terms, referred to as *subgrid-scale boundary conditions* (not shown), will arise if the BCs contain nonlinear terms or derivative operators.

It should be noted at this point that standard ROMs ignore the residual fields in (2.6). Closure is neglected as the following equations are solved for instead:

$$
A\tilde{\mathbf{u}} \;\cong\; \mathbf{R}\left(\tilde{\mathbf{u}}, \mathbf{x}, t\right). \qquad (2.7)
$$

While for some applications the solution to (2.7) may be acceptable, for others the solution to (2.7) may contain intolerable errors, especially if there are many interacting scales. When the residual terms in (2.6) are neglected, the filtering operation used to construct the ROM is no longer consistent with the filter relating $\mathbf{u}$ to $\tilde{\mathbf{u}}$.

2.2 Subgrid-scale models

If the exact expression for $\boldsymbol{\tau}$ is known, the filtered solution $\tilde{\mathbf{u}}$ can be obtained by solving the modified PDEs in (2.6). For most systems, however, it is not feasible [60] to derive an exact expression for $\boldsymbol{\tau}$ due to its functional dependence on the true solution $\mathbf{u}$. Our approach is to evolve a simpler form of the governing equations instead of the true form in (2.6) by removing the functional dependence of $\boldsymbol{\tau}$ on $\mathbf{u}$. This can be done by modeling $\boldsymbol{\tau}$ as a function of the filtered solution $\tilde{\mathbf{u}}$. If we let $\boldsymbol{\mathcal{M}}$ represent the model for $\boldsymbol{\tau}$, we can rewrite (2.6) as

$$A\tilde{\mathbf{u}} \;\cong\; \mathbf{R}\left(\tilde{\mathbf{u}}, \mathbf{x}, t\right) + \boldsymbol{\mathcal{M}}\left(\tilde{\mathbf{u}}, \mathbf{x}, t\right). \tag{2.8}$$

The next task is to find a model which best approximates the projection of $\boldsymbol{\tau}$ onto $\tilde{\mathbf{u}}$. Out of all possible representations for $\boldsymbol{\mathcal{M}}$, it can be shown (see Appendix A) that the mean-square error between $\boldsymbol{\mathcal{M}}$ and $\boldsymbol{\tau}$ is minimized when the model takes on the form of a conditional average:

$$\boldsymbol{\mathcal{M}}\left(\tilde{\mathbf{u}}, \mathbf{x}, t\right) = \left\langle \boldsymbol{\tau}\left(\mathbf{u}, \tilde{\mathbf{u}}, \mathbf{x}, t\right) | \boldsymbol{\phi} \right\rangle, \tag{2.9}$$

where $\boldsymbol{\phi}$ is the subset of $\tilde{\mathbf{u}}$ onto which $\boldsymbol{\tau}$ is projected

$$\boldsymbol{\phi} = \{\tilde{\mathbf{u}}\left(\mathbf{x}', t'\right) : \mathbf{x}' \in \boldsymbol{\Omega}, 0 \leq t' \leq t\}. \tag{2.10}$$

Note that $\boldsymbol{\mathcal{M}}$ depends not on $\mathbf{u}$ but $\tilde{\mathbf{u}}$. Choosing a model of the form in (2.9) is the premise of first-order optimal prediction [60]. No other model can be more accurate (in a mean square sense). Our selection of $\boldsymbol{\phi}$ in (2.10) may include any subset of $\tilde{\mathbf{u}}$ in the spatial domain, $\boldsymbol{\Omega}$, and any portion of the time history from zero to present time. Besides introducing a model and following the mean-square error minimization

approach in Appendix A, derivation of the result in (2.9) can also be motivated [61] by choosing to remove the functional dependence of $\boldsymbol{\tau}$ on $\mathbf{u}$ by simply taking the mean of (2.6) conditional on $\boldsymbol{\phi}$.

An exact model for $\langle \boldsymbol{\tau} | \boldsymbol{\phi} \rangle$ (or any quantity in the system for that matter) can be found if $\boldsymbol{\mathcal{M}}$ takes on the form of the generalized Langevin equation [58, 60]:

$$\boldsymbol{\mathcal{M}}(\tilde{\mathbf{u}}, \mathbf{x}, t) = \boldsymbol{\mathcal{P}}(\tilde{\mathbf{u}}, \mathbf{x}, t) + \int_0^t \boldsymbol{\kappa}(t') \, \langle \boldsymbol{\tau}(\mathbf{u}, \tilde{\mathbf{u}}, \mathbf{x}, t - t') | \boldsymbol{\phi} \rangle \, dt' + \boldsymbol{\mathcal{N}}(\mathbf{x}, t), \tag{2.11}$$

or simply, $\boldsymbol{\mathcal{M}} = \boldsymbol{\mathcal{P}} + \boldsymbol{\mathcal{K}} + \boldsymbol{\mathcal{N}}$. The Markovian contribution $\boldsymbol{\mathcal{P}}$ is the projection of $\langle \boldsymbol{\tau} | \boldsymbol{\phi} \rangle$ onto the known data $\tilde{\mathbf{u}}$ at present time. $\boldsymbol{\mathcal{K}}$ is a manifestation of non-Markovian memory (referred to as the friction [58]), which depends on the history of the data from zero to present time, and the kernel $\boldsymbol{\kappa}$ represents the memory function. The noise $\boldsymbol{\mathcal{N}}$ is uncorrelated with the known data (the portion of $\boldsymbol{\tau}$ orthogonal to $\tilde{\mathbf{u}}$), and hence, is unpredictable without some additional knowledge other than $\tilde{\mathbf{u}}$. Similar types of Langevin descriptions have been used by Liu and his colleagues for a number of bridging scale methods [25].

Developing an exact model for $\langle \boldsymbol{\tau} | \boldsymbol{\phi} \rangle$ as in (2.11) is often impractical [61], in which case the closure problem now becomes one of estimating $\langle \boldsymbol{\tau} | \boldsymbol{\phi} \rangle$ as accurately as possible. Such models have been developed in previous works [65, 66] using principles of stochastic estimation. The premise behind the technique is to assume $\langle \boldsymbol{\tau} | \boldsymbol{\phi} \rangle$ and $\tilde{\mathbf{u}}$ are correlated in space and time. It is then possible to predict $\langle \boldsymbol{\tau} | \boldsymbol{\phi} \rangle$ if $\boldsymbol{\mathcal{M}}$ is chosen to be some function of $\tilde{\mathbf{u}}$. The stronger the correlation (positive or negative), the more accurately we should be able to estimate $\langle \boldsymbol{\tau} | \boldsymbol{\phi} \rangle$. The most general form of such a model can be written in the form of a Volterra series expansion [66] with respect to $\tilde{\mathbf{u}}$. As shown in (2.10), the support for such a model may span the entire spatial domain in $\boldsymbol{\Omega}$ and may include any portion of the time history from zero to present time. Simpler (and perhaps more useful) approximations can be made with a local

estimate such that the model has limited extent in space and time. Such methods will be explored in Section 2.5 where $\boldsymbol{\mathcal{M}}$ will be projected onto a multivariate power series in terms of discrete values of $\tilde{\mathbf{u}}$. To write such an expansion, the field variables must first be discretized.

2.3 Discretization

The subgrid-scale dynamics in Section 2.1 and subgrid-scale models in Section 2.2 were derived in terms of the *continuous* field variables in the physical domain. In the following sections, we demonstrate how these general concepts translate to the *discrete* field variables in the computational domain. To this end, we consider an arbitrary numerical method which requires full discretization of the governing PDEs in space and time. Spatial discretization of (2.6) into N_N spatial DOFs results in a system of nonlinear ordinary differential equations (ODEs) in time. The semi-discretized (in space) components of $\tilde{\mathbf{u}}$ can be written as $(\tilde{u}_i)_j(t)$, where the outer subscript denotes the spatial node with coordinates $(x_k)_j$. Temporal discretization results in a system of nonlinear algebraic equations to be solved for at N_T temporal DOFs. The fully-discretized components of $\tilde{\mathbf{u}}$ become $(\tilde{u}_i)_j^n$, where the outer superscript denotes the timestep with time t^n. Similarly, the remaining field variables in (2.6) can be written as $(R_i)_j^n$, $(\tau_i)_j^n$, $(\alpha_i)_j^n$ and $(\gamma_i)_j^n$. The total number of DOFs to be solved for in a simulation is $N_S \times N_N \times N_T$.

Computational grids for the discrete field variables (in physical space and time) are illustrated in Figures 2.2 and 2.3 for a FRS and a ROM. Observe that the spacing between neighboring spatial nodes and timesteps for the fully resolved signal (Δx_k^{FRS} and Δt_{FRS}) is smaller than the spacing for the coarse signal (Δx_k^{ROM} and Δt_{ROM}). This comes from the notion that ROMs provide less resolution in space and time. Uniform grid parameters Δx_k and Δt could also be written as $(\Delta x_k)_j^n$ and $(\Delta t)_j^n$ to allow for spatial nonuniformity and temporal grid adaptation.

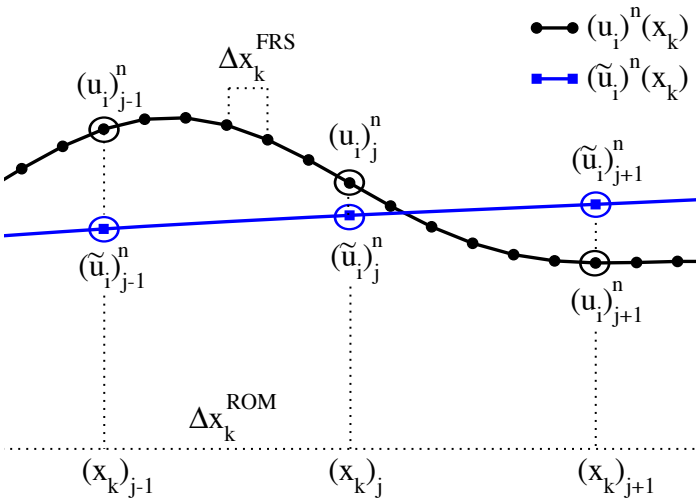

Figure 2.2: Spatial grids for a FRS and a ROM.

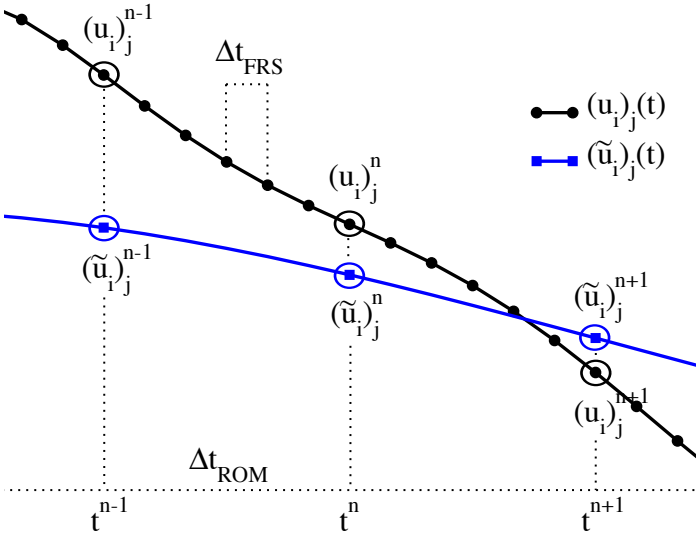

Figure 2.3: Temporal grids for a FRS and a ROM.

2.4 Discrete subgrid-scale dynamics

The discrete subgrid-scale dynamics depend largely on the chosen filtering operation. Previous works in LES for turbulent flows [67, 82] have recognized the importance of filter selection. In this work, we suggest that the filtering operation used to derive the subgrid-scale dynamics should be tailored to the chosen ROM. To demonstrate, we

consider a scenario in which the analyst has *a priori* knowledge of the true solution, $\mathbf{u}$, which we assume to be equivalent to the FRS solution. Any filter may be selected arbitrarily by the analyst in order to produce $\tilde{\mathbf{u}}$. One filter in particular, however, would result in $\tilde{\mathbf{u}}$ being equivalent to the *a posteriori* result of the chosen ROM if the discretization errors could (hypothetically) be removed. We consider such a filter to be ***consistent*** with the ROM, as shown in Figure 2.4. The choice of any other filter is said to be inconsistent with the ROM.

Taylor-series-based FD schemes, for example, produce space-time-limited signals, which require finite support in physical space and infinite support in the Fourier domain [22]. A consistent filter for a ROM based on a FD scheme should produce a signal which coincides with the FRS result at every spatial node and timestep. A comb-type sampling filter [22] should then be applied, in which case the filtered states $(\tilde{u}_i)_j^n$ and fully resolved states $(u_i)_j^n$ are equivalent at coincidental grid points, as depicted in Figure 2.4. The subgrid-scale dynamics, $(\alpha_i)_j^n$ and $(\gamma_i)_j^n$, can then be calculated by applying the FD expressions for $A(u_i)_j^n$ and $(R_i)_j^n$ in (2.6) to the filtered signals. Note that the actual kernel G in (2.3) need not be known when a comb-type sampling filter is chosen to produce $(\tilde{u}_i)_j^n$.

To illustrate application of a comb-type sampling filter, we consider a system in which $A\mathbf{u} = \partial\mathbf{u}/\partial t$. A temporal ROM can be constructed using a first-order accurate backward FD scheme. The subgrid-scale acceleration in (2.6) then becomes

$$(\alpha_i)_j^n = \frac{(u_i)_j(t^n) - (u_i)_j(t^n - \Delta t_{\mathrm{ROM}})}{\Delta t_{\mathrm{ROM}}} - \frac{(u_i)_j(t^n) - (u_i)_j(t^n - \Delta t_{\mathrm{FRS}})}{\Delta t_{\mathrm{FRS}}}. \tag{2.12}$$

Since we have chosen a comb-type sampling filter, the first term on the right hand side of (2.12) is equivalent to $\partial(u_i)_j^n/\partial t + \epsilon_t$, where ϵ_t represents the $\mathcal{O}(\Delta t_{\mathrm{ROM}})$ discretization errors for the FD scheme. From the definition of a FRS, the second term

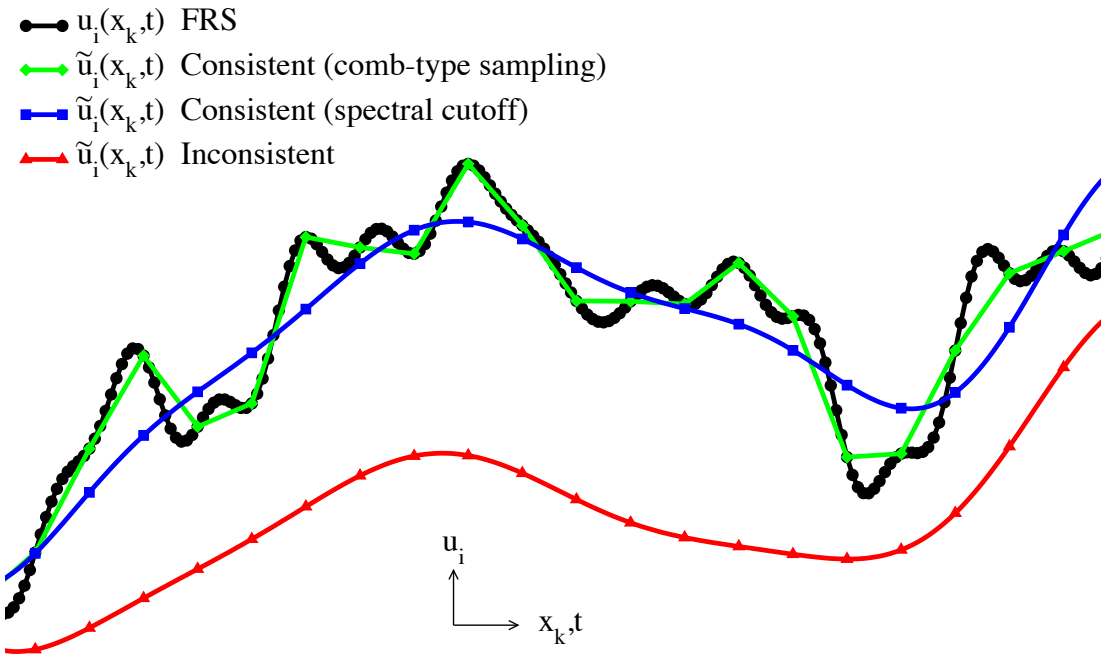

Figure 2.4: Filtered representations of a FRS signal, $u_i(x_k, t)$. Possible choices for $\tilde{u}_i(x_k, t)$ can be obtained with consistent filters, which of course depend on the ROM, or inconsistent filters, which can be chosen arbitrarily. Comb-type sampling filters are typically consistent with FD, FE and FV schemes, whereas cutoff filters are typically consistent with spectral schemes.

on the right hand side of (2.12) is an error-free representation of $\partial(u_i)_j^n/\partial t$. The expression for $(\alpha_i)_j^n$ in (2.12) then becomes $(\alpha_i)_j^n = \epsilon_t$. When added to the modified PDEs in (2.6), $(\alpha_i)_j^n$ eliminates all discretization errors associated with the temporal FD scheme. The choice of any other filter for a temporal FD scheme would introduce additional forms of error.

Similarly, for a system in which $\mathbf{R} = -\mathbf{u} \cdot \nabla \mathbf{u}$, a spatial ROM can be constructed using a second-order accurate central FD scheme. With the selection of a comb-type sampling filter, the subgrid-scale force in (2.6) then becomes

$$\begin{aligned}(\gamma_i)_j^n =& (u_k)_j^n \frac{(u_i)^n((x_k)_j + \Delta x_k^{\mathrm{ROM}}) - (u_i)^n((x_k)_j - \Delta x_k^{\mathrm{ROM}})}{2\Delta x_k^{\mathrm{ROM}}} \\ &- (u_k)_j^n \frac{(u_i)^n((x_k)_j + \Delta x_k^{\mathrm{FRS}}) - (u_i)^n((x_k)_j - \Delta x_k^{\mathrm{FRS}})}{2\Delta x_k^{\mathrm{FRS}}}.\end{aligned} \tag{2.13}$$

Again, since we have chosen a consistent filter, we have $(\gamma_i)_j^n = -\epsilon_x$, where ϵ_x represents the $\mathcal{O}((\Delta x_k^{\mathrm{ROM}})^2)$ discretization errors in (2.13). When added to the modified PDEs in (2.6), $(\gamma_i)_j^n$ eliminates the discretization errors associated with the spatial FD scheme. The choice of any other filter for a spatial FD scheme would introduce additional forms of error.

Spectral schemes, such as the HB method [19, 20], produce band-limited signals, which require finite support in Fourier space and infinite support in physical space [22]. A consistent filter for a spectral-based ROM should recover (exactly) the same number of FRS Fourier modes to be resolved by the ROM (N_N and N_T). If the FRS data is represented in physical space, it should be transformed to the Fourier domain where the filtering operation takes place. The Fourier modes should then be truncated using a spectral cutoff filter [22] to match the desired resolution. The cutoff filter in (2.4) is given by

$$\mathcal{G}(l,k) = \begin{cases} 1 & \text{if} \quad l \leq N_N \quad \text{and} \quad k \leq N_T \\ 0 & \text{if} \quad l > N_N \quad \text{or} \quad k > N_T. \end{cases} \tag{2.14}$$

Once the filtering operation is complete, the filtered Fourier modes $(\tilde{\tilde{u}}_i)_l^k$ can then be transformed back to physical space to obtain $(\tilde{u}_i)_j^n$ and the subgrid-scale dynamics can readily be calculated. Note that the subgrid-scale dynamics have a convenient property when a cutoff filter is chosen: the filtering operator commutes through the time-derivative operator, $\widetilde{A\mathbf{u}} = A\tilde{\mathbf{u}}$, in which case the subgrid-scale acceleration is zero and only the subgrid-scale force remains. When added to the modified PDEs in (2.6), $(\gamma_i)_j^n$ eliminates the truncation errors associated with the spectral scheme.

Other filtering operations for FD and spectral schemes are conceivable. FE and FV schemes can be treated in a similar manner. Depending on the application, the analyst may consider an inconsistent filter to be appropriate. Regardless of the ROM, the chosen filter should represent the desired *a posteriori* result when applied to the FRS solution.

2.5 Discrete subgrid-scale models

Discrete subgrid-scale models can be derived using a stochastic estimate [65, 66] with local support in space and time. Analogous to a Volterra series, we proceed by expanding $(\mathcal{M}_i)_j^n$, the model for the i^{th} state at spatial node j and timestep n, in the form of a multi-point (in space and time) power series about the filtered states $(\tilde{u}_i)_j^n$:

$$\begin{aligned}(\mathcal{M}_i)_j^n \;\cong\; & (\mathcal{A}_i)_j^n \\ & + \sum_{\alpha}^{M_S} \sum_{\xi}^{M_N} \sum_{\mu}^{M_T} (\mathcal{B}_{i\alpha})_{j\xi}^{n\mu} \, (\tilde{u}_\alpha)_\xi^\mu \\ & + \sum_{\alpha,\beta}^{M_S} \sum_{\xi,\eta}^{M_N} \sum_{\mu,\nu}^{M_T} (\mathcal{C}_{i\alpha\beta})_{j\xi\eta}^{n\mu\nu} \, (\tilde{u}_\alpha)_\xi^\mu \, (\tilde{u}_\beta)_\eta^\nu \\ & + \ldots\end{aligned} \tag{2.15}$$

The subgrid-scale model in (2.15) involves a constant term $(\mathcal{A}_i)_j^n$, a linear kernel $(\mathcal{B}_{i\alpha})_{j\xi}^{n\mu}$ and a quadratic kernel $(\mathcal{C}_{i\alpha\beta})_{j\xi\eta}^{n\mu\nu}$. Higher-order expansions are indeed possible. Information considered useful in the estimate are M_S states at M_N spatial nodes and M_T timesteps. The multi-point spatiotemporal stencil implied by the summation in (2.15) may be taken to be as large or small as desired, as long as the required information is available (recall Figures 2.2 and 2.3). With regards to implementation, this choice may be influenced by the amount of information the analyst is willing to process and store during a simulation.

The fidelity of the subgrid-scale model in (2.15) depends not only on the functional form and chosen stencil size, but also on the accuracy of the estimation coefficients. Out of all possible choices, it can be shown (see Appendix B) that the mean-square error between the conditional average in (2.9) and the multi-point power series approximation in (2.15) is minimized when the following system of stochastic equations

are satisfied:

$$
\begin{aligned}
\left\langle (\tau_i)_j^n \right\rangle &= (\mathcal{A}_i)_j^n \\
&\quad + \sum_{\alpha}^{M_S} \sum_{\xi}^{M_N} \sum_{\mu}^{M_T} (\mathcal{B}_{i\alpha})_{j\xi}^{n\mu} \left\langle (\tilde{u}_\alpha)_\xi^\mu \right\rangle \\
&\quad + \sum_{\alpha,\beta}^{M_S} \sum_{\xi,\eta}^{M_N} \sum_{\mu,\nu}^{M_T} (\mathcal{C}_{i\alpha\beta})_{j\xi\eta}^{n\mu\nu} \left\langle (\tilde{u}_\alpha)_\xi^\mu \, (\tilde{u}_\beta)_\eta^\nu \right\rangle \\
\left\langle (\tau_i)_j^n \, (\tilde{u}_\gamma)_\phi^\lambda \right\rangle &= (\mathcal{A}_i)_\xi^\eta \left\langle (\tilde{u}_\gamma)_\phi^\lambda \right\rangle \\
&\quad + \sum_{\alpha}^{M_S} \sum_{\xi}^{M_N} \sum_{\mu}^{M_T} (\mathcal{B}_{i\alpha})_{j\xi}^{n\mu} \left\langle (\tilde{u}_\alpha)_\xi^\mu \, (\tilde{u}_\gamma)_\phi^\lambda \right\rangle \\
&\quad + \sum_{\alpha,\beta}^{M_S} \sum_{\xi,\eta}^{M_N} \sum_{\mu,\nu}^{M_T} (\mathcal{C}_{i\alpha\beta})_{j\xi\eta}^{n\mu\nu} \left\langle (\tilde{u}_\alpha)_\xi^\mu \, (\tilde{u}_\beta)_\eta^\nu \, (\tilde{u}_\gamma)_\phi^\lambda \right\rangle \\
\left\langle (\tau_i)_j^n \, (\tilde{u}_\gamma)_\phi^\lambda \, (\tilde{u}_\delta)_\psi^\rho \right\rangle &= (\mathcal{A}_i)_\xi^\eta \left\langle (\tilde{u}_\gamma)_\phi^\lambda \, (\tilde{u}_\delta)_\psi^\rho \right\rangle \\
&\quad + \sum_{\alpha}^{M_S} \sum_{\xi}^{M_N} \sum_{\mu}^{M_T} (\mathcal{B}_{i\alpha})_{j\xi}^{n\mu} \left\langle (\tilde{u}_\alpha)_\xi^\mu \, (\tilde{u}_\gamma)_\phi^\lambda \, (\tilde{u}_\delta)_\psi^\rho \right\rangle \\
&\quad + \sum_{\alpha,\beta}^{M_S} \sum_{\xi,\eta}^{M_N} \sum_{\mu,\nu}^{M_T} (\mathcal{C}_{i\alpha\beta})_{j\xi\eta}^{n\mu\nu} \left\langle (\tilde{u}_\alpha)_\xi^\mu \, (\tilde{u}_\beta)_\eta^\nu \, (\tilde{u}_\gamma)_\phi^\lambda \, (\tilde{u}_\delta)_\psi^\rho \right\rangle .
\end{aligned}
\tag{2.16}
$$

The key feature of the stochastic estimate used here is that $\boldsymbol{\mathcal{M}}$ in (2.15) can be used to predict any quantity in a system, assuming the desired quantity is correlated with $\tilde{\mathbf{u}}$. To obtain the estimation coefficients for any model, the desired quantity should be substituted for $\boldsymbol{\mathcal{M}}$ in Appendix B. For OPSTROM, $\boldsymbol{\mathcal{M}}$ is used to approximate $\langle \boldsymbol{\tau} | \boldsymbol{\phi} \rangle$. Each of the moments amongst $\tilde{\mathbf{u}}$ and $\boldsymbol{\tau}$ in (2.16) are interpreted as inputs required for model construction. These inputs can be evaluated numerically once the true solution is obtained and a filter is chosen for the ROM. The mean operator $\langle \cdot \rangle$ is to be calculated over the spatiotemporal domain of interest. Once the moments are evaluated, the estimation coefficients in (2.15) can be found by solving the linear algebraic system of equations in (2.16).

The size of the linear algebraic system in (2.16) depends on the number of states to be included in the model M_S, the spatial stencil M_N, temporal stencil M_T, and

the order of the approximation. While it is reasonable to expect that increasing the number of these parameters will lead to a better prediction for $\boldsymbol{\tau}$, the presence of distant and poorly correlated data can sometimes worsen the estimate [68]. Moreover, no guarantees can be made regarding whether or not the equations we obtain in (2.16) can be solved [61]. Certain models may not be realizable. In addition to our choice of $\tilde{\mathbf{u}}$, other quantities in $\mathbf{R}$ could be used to improve the estimate.

2.6 Optimal reduced order modeling variants

The analyst may choose to implement one of several optimal reduced order modeling variants depending on which terms (if any) in the subgrid-scale dynamics are deemed important. We refer to these variants as follows: (i) standard ROM, which completely neglects the subgrid spatiotemporal structure,

$$\boldsymbol{\mathcal{M}} \cong 0, \tag{2.17}$$

(ii) OPTROM, which accounts for the subgrid temporal structure due to a coarse Δt and takes on the following form with a consistent filter in the time domain

$$\boldsymbol{\mathcal{M}} \cong \langle \boldsymbol{\alpha} | \boldsymbol{\phi} \rangle , \tag{2.18}$$

(iii) OPSROM, which accounts for the subgrid spatial structure due to a coarse Δx_k and takes on the following form with a consistent filter in the spatial domain

$$\boldsymbol{\mathcal{M}} \cong \langle \boldsymbol{\gamma} | \boldsymbol{\phi} \rangle , \tag{2.19}$$

and (iv) OPSTROM, which accounts for the total subgrid spatiotemporal structure,

$$\boldsymbol{\mathcal{M}} = \langle \boldsymbol{\tau} | \boldsymbol{\phi} \rangle = \langle \boldsymbol{\alpha} | \boldsymbol{\phi} \rangle + \langle \boldsymbol{\gamma} | \boldsymbol{\phi} \rangle . \tag{2.20}$$

The OPSROM approach is analogous to OLES for turbulent flows [67–71], whereas the OPTROM and OPSTROM variants were originally proposed by LaBryer, Attar and Vedula [74–77]. All four variants will be investigated for the problems with spatiotemporal dependence in Chapter 5.

2.7 Simplifying assumptions

The optimal subgrid-scale model $(\mathcal{M}_i)_j^n$ and its coefficients in (2.15) may vary as a function of the ICs, BCs, location x_k, time t, spatial grid $(\Delta x_k)_j$, temporal grid Δt and each of the physical parameters in the governing PDEs. This complex functional dependence carries over from the multi-point moments amongst $(\tau_i)_j^n$ and $(\tilde{u}_i)_j^n$ in (2.16). In theory, a unique subgrid-scale model could be derived for every conceivable set of parameters in a simulation. However, to be useful for large-scale systems with spatiotemporal dependency, we must explore methods to reduce the amount of inputs required for model construction. In this context, the utility of a subgrid-scale model can be enhanced when the multi-point moments in (2.16) display to some extent the following statistical properties: (i) spatial homogeneity, (ii) temporal homogeneity, (iii) ergodicity, (iv) a functional dependence which can easily be characterized with respect to the system parameters (referred to hereafter as "smooth scaling" [79]), and (v) universality.

To efficiently construct a subgrid-scale model for any nonlinear dynamical system, the analyst should determine which parameters affect the multi-point moments in (2.16). An observed lack of sensitivity to space or time would justify the assumption of spatiotemporal homogeneity, in which case the functional dependence on grid location can be removed from the multi-point moments in (2.16) and stochastic estimation coefficients in (2.15). For example, the coefficients $(\mathcal{A}_i)_j^n$, $(\mathcal{B}_{i\alpha})_{j\xi}^{n\mu}$ and $(\mathcal{C}_{i\alpha\beta})_{j\xi\eta}^{n\mu\nu}$ in (2.15) then become $(\mathcal{A}_i)$, $(\mathcal{B}_{i\alpha})_{\xi}^{\mu}$ and $(\mathcal{C}_{i\alpha\beta})_{\xi\eta}^{\mu\nu}$. The model $(\mathcal{M}_i)_j^n$ reduces to $(\mathcal{M}_i)$ and can be used at every spatial node and timestep in a simulation. Somewhat related is

the concept of ergodicity, which in a physical sense implies that the long-term behavior of a system "forgets" about the initial state from which it evolves. In a mathematical sense, it is necessary to show that the time average for any one trajectory should be equivalent to the ensemble average for the entire system [83, 84]. For our purposes, a system is considered ergodic if the sensitivity to ICs can be removed from the subgrid-scale model. Further simplifications can be made if smooth scaling is observed when characterizing the functional dependence of the multi-point moments with respect to the physical parameters and/or grid parameters. Smooth scaling would enable efficient construction of empirical functions (or interpolants) with which the analyst may estimate the multi-point moments. To be discussed in Section 2.8, models based upon these estimated moments would allow for rapid computation of the estimation coefficients once the system parameters are specified. Statistical universality [79], if observed, would further reduce the sensitivity of the subgrid-scale models to BCs, constitutive parameters, geometries, load configurations, or other system parameters. Many of these simplifications will be made for the models constructed in Chapter 4.

As an example to support what may seem like an ambitious task, a great deal of research has already been conducted in order to characterize microscale dynamics for turbulent flows governed by the Navier-Stokes equations [2]. Macroscale turbulent flow structures may be highly irregular, anisotropic and sensitive to many system parameters. It is somewhat remarkable, then, that microscale flow structures (also referred to as the Kolmogorov microscales [37]) typically obey to a large degree many of the statistical properties listed above. We expect (as others have suggested [79,81]) that a similar type of microscale behavior can be found in other nonlinear dynamical systems besides turbulent flows, even though the macroscale dynamics may be quite complicated. Many of these properties do in fact hold true for the nonlinear dynamical systems in Chapter 4.

2.8 Model construction

A general procedure for constructing optimal subgrid-scale models prior to simulation is outlined in Table 2.1. Observe in Step 3 that several options are currently available for acquiring statistical knowledge about the subgrid-scale dynamics. The approach described in Sections 2.1–2.5 will be referred to hereafter as ***direct calculation***, an algorithm for which is provided in Table 2.2. Some questions naturally arise regarding the utility of models based upon direct calculation: How are such models useful if FRS data is required *a priori* for every simulation? Why would the analyst be interested in OPSTROM (or any ROM for that matter) if the fully resolved solution is already available? In response, direct calculation by itself is often not practical for use. Nevertheless, it serves as the theoretical foundation upon which more practical models can be based. To address the issue of practicality, we suggest models based upon ***estimation*** of the subgrid-scale moments as described in Table 2.3.

To construct a model based upon estimated moments, the analyst should first identify the range of system parameters that may be explored in future analysis. Consider, for example, a two-parameter system with $p \in [p_1, p_n]$ and $q \in [q_1, q_m]$. The next step is to obtain FRS data for a *small set* of these parameters, such as $p_i \times q_j$ where $p_i = \{p_1, p_2, ..., p_n\}$ and $q_j = \{q_1, q_2, ..., q_m\}$. From the small set of FRS data, the analyst can acquire statistical knowledge about the subgrid-scale dynamics via direct calculation in Table 2.2. Empirical functions can then be developed to characterize (or interpolate) the multi-point moments with respect to the system parameters. Certain interpolation schemes may be particularly appealing as they allow for future refinement with additional nodes. The number of interpolation nodes to be used is left to the analyst. However, the observed type of scaling behavior with respect to the parameters should influence this choice. As with any interpolation scheme, precautionary measures should be taken to avoid peculiarities such as Runge's

1. Identify and discretize the nonlinear dynamical system in (2.1)
2. Specify system parameters that may affect the subgrid-scale dynamics:
   (a) Physical parameters in (2.1)
   (b) Computational grid (Δx_k and Δt) and/or number of modes
   (c) Boundary conditions (BCs) and initial conditions (ICs)
3. Acquire statistical knowledge about the subgrid-scale dynamics:
   Option I: Direct calculation (Table 2.2)
   Option II: Estimation (Table 2.3)
   Option III: Theoretical reconstruction
   Option IV: Experimental reconstruction
   End result $\rightarrow$ Required moments amongst $\boldsymbol{\tau}$ and $\tilde{\mathbf{u}}$ in (2.16)
   Determine which subgrid-scale terms are important:
   OPTROM: Model only the subgrid-scale acceleration ($\boldsymbol{\alpha}$)
   OPSROM: Model only the (mass normalized) subgrid-scale force ($\boldsymbol{\gamma}$)
   OPSTROM: Model the complete subgrid-scale dynamics ($\boldsymbol{\tau} = \boldsymbol{\alpha} + \boldsymbol{\gamma}$)
4. Choose a form for the subgrid-scale model $\boldsymbol{\mathcal{M}}$ in (2.15):
   (a) Order for the stochastic estimate
   (b) Spatial stencil (M_N)
   (c) Temporal stencil (M_T)
   (d) Number of states (M_S)
5. Assemble the linear system of stochastic equations (2.16)
6. Solve (2.16) for the estimation coefficients $\boldsymbol{\mathcal{A}}$, $\boldsymbol{\mathcal{B}}$ and $\boldsymbol{\mathcal{C}}$
7. *Optional*: Repeat Steps 4–6 if the following occur:
   (a) Large *a priori* errors (the model provides a poor estimate)
   (b) Ill-conditioned system in (2.16) (the model is unrealizable)

Table 2.1: General procedure for constructing an optimal subgrid-scale model

phenomenon [11]. From a conceptual standpoint, constructing models based upon estimated moments is somewhat analogous to building a Smagorinsky model for the subgrid stress in LES for turbulent flows; in particular, Smagorinsky models that take into account dynamic similarity and scale separation [80].

The estimation approach in Table 2.3 is one way to reduce or eliminate dependence on FRS data. Empirical functions for the subgrid-scale moments can easily be added to any nonlinear dynamics solver for a given set of governing equations. The required inputs (moments amongst $\boldsymbol{\tau}$ and $\tilde{\mathbf{u}}$) in (2.16) can then be calculated (estimated) from the empirical functions once the desired model and system parameters are specified. The estimation coefficients for $\boldsymbol{\mathcal{M}}$ can readily be found by solving (2.16) prior to

1.	Establish criteria for a FRS solution
2.	Obtain FRS data $\mathbf{u}$, which is independent of the solution method
3.	Define the filtered solution $\tilde{\mathbf{u}}$ for the chosen ROM
4.	Compute the subgrid-scale dynamics $\boldsymbol{\tau}$ in (2.6)
5.	Compute the raw moments amongst $\tilde{\mathbf{u}}$ and $\boldsymbol{\tau}$ in (2.16)

Table 2.2: Direct calculation of subgrid-scale dynamics

1.	Identify the range of system parameters under consideration
2.	Choose a small set of discrete values for each parameter
3.	For all possible combinations of system parameters, compute the raw moments amongst $\boldsymbol{\tau}$ and $\tilde{\mathbf{u}}$ via direct calculation in Table 2.2
4.	Develop empirical functions with which to model (or interpolate) the moments with respect to the system parameters

Table 2.3: Estimation of subgrid-scale dynamics

simulation. This approach also provides the analyst with a certain amount of freedom when constructing a model: unused moments in (2.16) need not be determined.

Other approaches are conceivable for model construction besides direct calculation and estimation. As an alternative to using FRS data, information about the subgrid-scale dynamics can (at least in principle) be obtained from theory, experiments, or reconstructions from multiple sources. Such ideas may be explored in future research.

2.9 Model appraisal

To appraise a subgrid-scale model, we wish to know the conditions under which the *a posteriori* ROM solution, denoted here as $\mathbf{v}(\mathbf{x}, t)$, will be exact with respect to the filtered FRS solution, $\tilde{\mathbf{u}}(\mathbf{x}, t)$. It seems rather obvious that choosing $\boldsymbol{\mathcal{M}} = \boldsymbol{\tau} \ \forall \ \mathbf{x}, t$ would accomplish this task, but herein we shall find this requirement unnecessarily strict. We consider a system in which $A\mathbf{u} = \partial\mathbf{u}/\partial t$. The desired scenario is to evolve the system using an under-resolved discretization scheme with spatial grid $\Delta\mathbf{x}$ and timestep Δt such that

$$\mathbf{v}\left(\mathbf{x}, t\right) = \tilde{\mathbf{u}}\left(\mathbf{x}, t\right) \ \forall \ \mathbf{x}, t. \tag{2.21}$$

We assume that the ROM and filtered FRS solutions are given the same BCs and ICs, $\mathbf{v}(\mathbf{x}, t^0) = \tilde{\mathbf{u}}(\mathbf{x}, t^0)$. For the first timestep of integration, $t^1 = t^0 + \Delta t$, the solutions to (2.6) and (2.8) in terms of the generalized Langevin quantities in (2.11) become

$$\tilde{\mathbf{u}}(\mathbf{x}, t^1) = \tilde{\mathbf{u}}(\mathbf{x}, t^0) + \int_{t^0}^{t^1} \int_{\mathbf{\Omega}} \mathbf{R} \; d\mathbf{x}dt + \int_{t^0}^{t^1} \int_{\mathbf{\Omega}} \boldsymbol{\tau} \; d\mathbf{x}dt, \tag{2.22}$$

$$\mathbf{v}(\mathbf{x}, t^1) = \mathbf{v}(\mathbf{x}, t^0) + \int_{t^0}^{t^1} \int_{\mathbf{\Omega}} \mathbf{R} \; d\mathbf{x}dt + \int_{t^0}^{t^1} \int_{\mathbf{\Omega}} (\boldsymbol{\mathcal{P}} + \boldsymbol{\mathcal{K}} + \boldsymbol{\mathcal{N}}) d\mathbf{x}dt. \tag{2.23}$$

In order for $\mathbf{v}(\mathbf{x}, t^1) = \tilde{\mathbf{u}}(\mathbf{x}, t^1)$ to be true, we require the last integrals in (2.22) and (2.23) to be equivalent. Since ultimately we desire $\mathbf{v} = \tilde{\mathbf{u}} \; \forall \; \mathbf{x}, t$, the integration should also hold for all spatial nodes, $(x_k)_j$ and timesteps, t^n. Integration of each quantity can be restated in terms of the spatiotemporal average over $\Delta\mathbf{x}$ and Δt, denoted by $\langle \cdot \rangle_{\Delta\mathbf{x}}^{\Delta t}$. Our appraisal criterion then becomes

$$\langle \boldsymbol{\mathcal{M}} \rangle_{\Delta\mathbf{x}}^{\Delta t} = \langle \boldsymbol{\tau} \rangle_{\Delta\mathbf{x}}^{\Delta t} = \langle \boldsymbol{\mathcal{P}} \rangle_{\Delta\mathbf{x}}^{\Delta t} + \langle \boldsymbol{\mathcal{K}} \rangle_{\Delta\mathbf{x}}^{\Delta t} + \langle \boldsymbol{\mathcal{N}} \rangle_{\Delta\mathbf{x}}^{\Delta t} \; \forall \; \mathbf{x}, t. \tag{2.24}$$

A subgrid-scale model satisfying (2.24) will produce exact solutions for $\mathbf{v}(\mathbf{x}, t)$ with respect to $\tilde{\mathbf{u}}(\mathbf{x}, t)$. In other words, the spatiotemporal average of a model over the coarse computational grid should be equivalent to that of the actual subgrid-scale dynamics. $\boldsymbol{\mathcal{M}}$ and $\boldsymbol{\tau}$ need not be identical $\forall \; \mathbf{x}, t$.

The generalized Langevin quantities in (2.24) can have profound implications on the choice of data to include in the model. Great simplifications can be made if it can be shown *a priori* that $\langle \boldsymbol{\mathcal{P}} \rangle_{\Delta\mathbf{x}}^{\Delta t} = \langle \boldsymbol{\tau} \rangle_{\Delta\mathbf{x}}^{\Delta t}$: either the non-Markovian memory cancels with the noise (unlikely), or $\langle \boldsymbol{\mathcal{K}} \rangle_{\Delta\mathbf{x}}^{\Delta t}$ and $\langle \boldsymbol{\mathcal{N}} \rangle_{\Delta\mathbf{x}}^{\Delta t}$ are both zero, in which case the subgrid-scale dynamics depend only on the chosen states at present time. If such an observation is true, the desired condition in (2.21) can be achieved with a one-point temporal stencil ($M_T = 1$ with t^n). If instead it can be shown for a given model that $\langle \boldsymbol{\mathcal{P}} \rangle_{\Delta\mathbf{x}}^{\Delta t} \neq \langle \boldsymbol{\tau} \rangle_{\Delta\mathbf{x}}^{\Delta t}$, then the subgrid-scale dynamics either depend on past information from the chosen states ($\boldsymbol{\mathcal{K}}$), information from states excluded in the model ($\boldsymbol{\mathcal{N}}$), or

some combination of both. To increase the accuracy of such a model, additional states can be included and a multi-point temporal stencil can be used. While it has been shown [58, 60] that the expected value of the noise $\boldsymbol{\mathcal{N}}$ should vanish for $t \in [0, \infty)$, this property does not necessarily hold for a time average in a finite domain.

2.10 Error measures

Prior to simulation, it is good practice to check how accurately $\boldsymbol{\mathcal{M}}$ approximates $\boldsymbol{\tau}$, if known. This can be done after the estimation coefficients are found and before OPSTROM solutions are computed. Based upon the appraisal criterion in (2.24), we define the global *a priori* error for the i^{th} state to be

$$e_i = \frac{\left\langle \left(\langle \tau_i \rangle_{\Delta\mathbf{x}}^{\Delta t} - \langle \mathcal{M}_i \rangle_{\Delta\mathbf{x}}^{\Delta t} \right)^2 \right\rangle^{1/2}}{\left\langle \tau_i^2 \right\rangle^{1/2}}, \tag{2.25}$$

where the mean operator $\langle \cdot \rangle$ is calculated over the spatiotemporal domain of interest. Limiting values for the *a priori* error have the following interpretations: As $\mathbf{e} \to 0$, the appraisal criterion (2.24) is satisfied, i.e., the ROM solution will be exact with respect to $\tilde{\mathbf{u}}$. As $\mathbf{e} \to 1$, the subgrid-scale model is zero, i.e., a standard ROM is used. A small (nonzero) *a priori* error should only serve as an indication of the model's ability to approximate $\boldsymbol{\tau}$ for a given FRS field; it does not necessarily guarantee improvement in the solution.

Perhaps of greater interest is how the *a posteriori* solutions (standard ROM and OPSTROM) compare to the FRS solution if available. Analogous to the error measure in (2.25), we define the global *a posteriori* error for each state in physical space as

$$E_{u_i} = \frac{\left\langle \left(u_i^{\text{FRS}} - u_i^{\text{ROM}} \right)^2 \right\rangle^{1/2}}{\left\langle \left(u_i^{\text{FRS}} \right)^2 \right\rangle^{1/2}}. \tag{2.26}$$

For spectral methods, however, it may be convenient to conduct the error analysis in the Fourier domain. We define the *a posteriori* errors for $(\bar{u}_i)_l^k$, the harmonic amplitudes of the i^{th} state, as

$$(\bar{E}_i)_l^k = \left\| \frac{(\bar{u}_i^{\text{FRS}})_l^k - (\bar{u}_i^{\text{ROM}})_l^k}{(\bar{u}_i^{\text{FRS}})_l^k} \right\|. \tag{2.27}$$

For time-periodic systems in which the fundamental frequency is unknown, i.e. for autonomous systems, the frequencies ω^{FRS} and ω^{ROM} are typically incommensurate. For such systems, the time interval of interest in (2.26) can be taken over one FRS period and the signals can be translated to be in phase at the beginning of the time averaging window. We may also measure the frequency error

$$E_\omega = \frac{\left\| \omega^{\text{FRS}} - \omega^{\text{ROM}} \right\|}{\omega^{\text{FRS}}}. \tag{2.28}$$

Other forms of error are conceivable. Note that the *a posteriori* errors may be small while the *a priori* errors may be large, and vice versa. This phenomenon is somewhat common in turbulence modeling [2].

2.11 Implementation

The OPSTROM approach is applicable to any spatiotemporal discretization scheme, including FD, FE, FV and spectral methods. Following a spatial discretization of the modified PDEs (with an arbitrary method of choice), the next step is to discretize the resulting system of ODEs in the time domain. In this section we demonstrate implementation with two well-known time-discretization schemes: the implicit Euler (IE) time-marching and harmonic balance (HB) time-spectral methods.

2.11.1 Time-marching formulation

Implicit time-marching schemes [8] are particularly appealing for OPSTROM as they allow the analyst to evolve solutions with very coarse timesteps (in contrast to explicit schemes in which stability limitations are common). Perhaps the most basic yet robust example is the first-order accurate implicit Euler (IE) time-marching scheme [8]. Once the initial conditions are specified, standard ROM solutions to (2.7) with the IE scheme can be evolved by

$$(u_i)_j^{n+1} = (u_i)_j^n + \Delta t \left[(R_i)_j^{n+1} \right], \tag{2.29}$$

whereas OPSTROM solutions to (2.8) with the IE scheme can be evolved by

$$(u_i)_j^{n+1} = (u_i)_j^n + \Delta t \left[(R_i)_j^{n+1} + (\mathcal{M}_i)_j^{n+1} \right]. \tag{2.30}$$

Our choice of the IE scheme is based on several appealing features, most importantly its unconditional stability for stiff systems [8], provided the iterative root finding scheme used to solve the equations is able to converge at each timestep. In this dissertation, we employ a Newton-Raphson (NR) scheme with a numerical Jacobian and a banded matrix solver [10, 11].

The standard IE scheme is a single-point method as it uses information from one timestep, t^{n+1}. However, the subgrid-scale model may require information from additional timesteps if a multi-point temporal stencil is used. For instance, if we use a linear estimate for $\boldsymbol{\mathcal{M}}^{n+1}$ with a three-point backward temporal stencil ($M_T = 3$), the IE scheme in (2.30) then becomes

$$\begin{aligned}(u_i)_j^{n+1} = (u_i)_j^n &+ \Delta t \left[(R_i)_j^{n+1} \right] \\ &+ \Delta t \left[(\mathcal{A}_i)_j^{n+1} + (\mathcal{B}_i)_j^{n+1} (u_i)_j^{n+1} + (\mathcal{B}_i)_j^n (u_i)_j^n + (\mathcal{B}_i)_j^{n-1} (u_i)_j^{n-1} \right].\end{aligned} \tag{2.31}$$

The equations in (2.31) now contain information from $(u_i)_j^{n+1}$, $(u_i)_j^n$ and $(u_i)_j^{n-1}$. In this sense, when the subgrid-scale model is included, the scheme is no longer a true first-order implicit Euler, but rather, it becomes a higher-order multi-point implicit time-marching scheme in which the estimation coefficients determine the order of accuracy. Comparisons can be made to other multi-point methods, such as the implicit Adams-Bashforth-Moulton family [8]. One major difference is that multi-point OPSTROM simply requires knowledge of $\mathbf{u}$ at several timesteps. Most multi-point methods, however, require evaluation of $\mathbf{R}$ at several timesteps, which is typically more difficult and expensive. When adding an optimal subgrid-scale model to any discretization scheme, the effects on stability and/or convergence are unknown and should be taken into consideration. Such effects could be favorable or adverse.

2.11.2 Time-spectral formulation

Time-spectral methods allow for rapid computation of steady state solutions for time-periodic systems. Any computational expense associated with a transient response is completely avoided. Here we provide an OPSTROM formulation for the harmonic balance (HB) methodology [19], which is perhaps the most widely used time-spectral method in nonlinear dynamics. The common approach with all HB schemes is to find a Fourier series approximation for the true (FRS) response of a system. We begin with the semi-discretized (in space) governing equations and assume that the field variables are smooth and periodic in time with period $T = 2\pi/\omega$, where ω is the fundamental frequency. The field variables can then be written as

$$\mathbf{u}(t) = \hat{\mathbf{u}}^0 + \sum_{k=1}^{N_H} \left[\hat{\mathbf{u}}^{2k-1} \cos(k\omega t) + \hat{\mathbf{u}}^{2k} \sin(k\omega t)\right], \tag{2.32}$$

where k is the wavenumber and N_H is the total number of temporal Fourier modes (harmonics) retained in the expansion. The total number of terms in each Fourier

series is $N_T = 2N_H + 1$. Expansions for the forces $\mathbf{R}(t)$ and subgrid-scale model $\boldsymbol{\mathcal{M}}(t)$ are of the same form as the states $\mathbf{u}(t)$ in (2.32).

With the classical HB approach, the Fourier series expansions for the field variables are substituted into the governing equations (2.8) and a Galerkin projection is performed with respect to the Fourier modes, resulting in

$$\omega \mathbf{A} \hat{\mathbf{U}} - \hat{\mathbf{R}} - \hat{\mathbf{M}} = \mathbf{0}, \tag{2.33}$$

where

$$\hat{\mathbf{U}} = \begin{bmatrix} (\hat{u}_1)_1^0 & \dots & (\hat{u}_{N_S})_{N_N}^0 \\ \vdots & (\hat{u}_i)_j^n & \vdots \\ (\hat{u}_1)_1^{2N_H} & \dots & (\hat{u}_{N_S})_{N_N}^{2N_H} \end{bmatrix}. \tag{2.34}$$

The HB solution array $\hat{\mathbf{U}}$ in (2.33) contains $N_S \times N_N \times N_T$ components. Arrays for the forces $\hat{\mathbf{R}}$ and subgrid-scale model $\hat{\mathbf{M}}$ are of the same form. An expression for the $N_T \times N_T$ wavenumber matrix $\mathbf{A}$ can be found in [85]. If the system is linear, solutions for the Fourier coefficients can be found analytically. For the nonlinear case, solutions must be obtained numerically using an iterative root finding scheme.

Implementing the classical HB approach for large-scale nonlinear dynamical systems can be cumbersome, especially when many harmonics are retained. Nonlinear terms (and the subgrid-scale model) must be expressed as a function of the Fourier coefficients, which are often complicated to derive, and do not exist in most standard computational fluid (CFD) or structural dynamic (CSD) codes.

Many variants of HB technology have emerged throughout the years [20]. In this dissertation, we will use a novel time domain formulation of the HB methodology called the high dimensional harmonic balance (HDHB) approach as it allows for straightforward implementation into large-scale CFD [86, 87] and CSD [88] codes. The Fourier coefficients can be directly related to the time domain variables using

the $N_T \times N_T$ discrete Fourier transform operator $\boldsymbol{\mathcal{F}}$, the analytical expression [85] for which depends only on the selection of N_H. The relationships are given by

$$\hat{\mathbf{U}} = \boldsymbol{\mathcal{F}}\tilde{\mathbf{U}}, \quad \hat{\mathbf{R}} = \boldsymbol{\mathcal{F}}\tilde{\mathbf{R}}, \quad \hat{\mathbf{M}} = \boldsymbol{\mathcal{F}}\tilde{\mathbf{M}}. \tag{2.35}$$

Thus, if the field variables are known in one domain (time or Fourier), they can be transformed to the other using $\boldsymbol{\mathcal{F}}$ or $\boldsymbol{\mathcal{F}}^{-1}$. This allows for the HB system (2.33) to be recast into the time domain, where expressions for the subgrid-scale models (and estimation coefficients) are known. The field variables are represented at N_T evenly spaced time intervals for one period of oscillation, and the solution array becomes

$$\tilde{\mathbf{U}} = \begin{bmatrix} (\tilde{u}_1)_1^0 & \dots & (\tilde{u}_{N_S})_{N_N}^0 \\ \vdots & (\tilde{u}_i)_j^n & \vdots \\ (\tilde{u}_1)_1^{2N_H} & \dots & (\tilde{u}_{N_S})_{N_N}^{2N_H} \end{bmatrix}, \tag{2.36}$$

where the uniform spacing between each point in time is given by

$$t^n = \frac{2\pi n}{\omega N_T} \quad \text{where} \quad N_T = 2N_H + 1. \tag{2.37}$$

It is now possible to transform the classical HB system of equations into the time domain. The resulting HDHB system of nonlinear algebraic equations becomes

$$\omega \mathbf{D}\tilde{\mathbf{U}} - \tilde{\mathbf{R}} - \tilde{\mathbf{M}} = \mathbf{0}, \tag{2.38}$$

where the time-derivative operator $\mathbf{D}$ is given by

$$\mathbf{D} = \boldsymbol{\mathcal{F}}^{-1}\mathbf{A}\boldsymbol{\mathcal{F}}. \tag{2.39}$$

Hence, solution of the HDHB equations is similar in concept to the solution of implicit

time-marching schemes with one subtle difference: the time-derivative operator for HDHB is fully populated, whereas most implicit time-marching schemes are sparse and banded [88]. No modifications need to be made if the fundamental frequency is known. For systems in which the fundamental frequency is unknown, the governing equations must be modified to accommodate one additional variable in ω. This can be done by imposing a phase condition on the first harmonic of motion [89].

In order to solve the HDHB system of equations, in this dissertation we employ a NR scheme with a numerical Jacobian and a banded matrix solver [88]. For each simulation, the physical parameters must be specified, an initial guess is required, and the number of Fourier modes must be chosen. If the nonlinear terms are polynomial-type [90], and the Fourier series expansions are treated properly [88, 91], the classical HB and HDHB formulations are identical in their respective domains. As such, we hereby refer to the HDHB approach as the HB for brevity. Once the HB solution is found, the N_T Fourier coefficients for each state can be obtained from (2.35), and the $N_H + 1$ harmonic amplitudes can be calculated by

$$(\bar{u}_i)_j^0 = (\hat{u}_i)_j^0 \quad \text{and} \quad (\bar{u}_i)_j^k = \left[\left((\hat{u}_i)_j^{2k-1} \right)^2 + \left((\hat{u}_i)_j^{2k} \right)^2 \right]^{1/2}. \tag{2.40}$$

If the smallest relevant time scale for the true solution is given by Δt_{FRS}, and N_H is chosen such that $2\pi / N_T \omega \leq \Delta t_{\text{FRS}}$, then the selection of N_H in (2.37) provides FRS resolution. Otherwise, the HB scheme should be considered a ROM, in which case OPSTROM can be used to decrease the errors.

A special case was discovered by LaBryer, Attar and Vedula [74] when developing an OPTROM model for the HB approach. Under certain conditions (see Appendix C), an exact subgrid-scale model (one with zero *a priori* error) can be constructed when one harmonic ($N_H = 1$) is retained in the analysis and certain conditions are satisfied. No other schemes with this property have been found by the authors to date.

2.12 Summary of proposed theoretical framework

In this chapter, we outlined the new OPSTROM framework for nonlinear dynamical systems. The approach can be used to construct data-driven spatiotemporal ROMs with minimum errors with respect to the chosen resolution. We began by modifying a general system of PDEs for an under-resolved simulation (in space and time) with an arbitrary discretization scheme. Basic filtering concepts were used to demonstrate the manner in which subgrid-scale dynamics arise with a coarse computational grid. Subgrid-scale models were then developed to account for the underlying spatiotemporal structure by embedding statistical information into the governing equations on a multi-point spatiotemporal stencil. Unlike most other multiscale ROMs, this information is formulated to be consistent with the underlying spatiotemporal statistical structure. Predictions with the modified system of equations are based upon principles of mean-square error minimization, conditional expectations and stochastic estimation, thus rendering the optimal solution with respect to the chosen resolution. Four variants of the OPSTROM technique were described: (i) standard ROM, (ii) OPTROM, (iii) OPSROM, and (iv) OPSTROM, depending on which terms in the subgrid-scale dynamics are deemed important. Practical methods were suggested for model construction, appraisal, and error measure. Implementation was demonstrated for the IE time-marching and HB time-spectral schemes.

CHAPTER 3

Selected nonlinear dynamical systems

This chapter describes four nonlinear dynamical systems to serve as testbeds for the OPSTROM framework. The governing equations for each system will be written in the form $A\mathbf{u} = \mathbf{R}(\mathbf{u}, \mathbf{x}, t)$ to match the general PDEs in (2.1) then modified for the OPSTROM approach and discretized. First we consider an autonomous van der Pol oscillator, which contains no spatial dependence and allows us to focus exclusively on subgrid time scales for time-periodic solutions. Next, we describe a Duffing oscillator under the influence of time-dependent external forcing. Unlike the unforced van der Pol oscillator, the Duffing oscillator is capable of undergoing a variety of response types. For the third system, we consider the viscous Burgers equation, which is a parabolic PDE describing nonlinear wave propagation. Time-periodic inflow BCs will be applied to excite the Burgers flow. For the final system, we investigate the response of a geometrically nonlinear beam under the influence of time-dependent external forcing, which is perhaps the most interesting example in the sense that it contains spatiotemporal dependence, and like the Duffing oscillator, is also capable of undergoing a variety of response types including time-periodicity, asymmetry, period N-tupling, intermittency and chaos.

3.1 Van der Pol oscillator description

The van der Pol oscillator [92] is one of the most extensively studied systems in the field of nonlinear dynamics by virtue of its ability to produce self-sustained limit cycle oscillations (LCOs) as a single DOF system [1]. The governing equation models

a mechanical oscillator with nonlinear damping, which plays the role of an energy source and sink as the system evolves. In this dissertation, we choose to study the unforced van der Pol oscillator, for which all nonzero initial trajectories evolve to self-sustained LCOs [1]. When external forces are applied, the response may exhibit frequency entrainment or chaos [93]. In the absence of external forces, the evolution is described by

$$\frac{\partial^2 u}{\partial t^2} - \alpha\left(1 - u^2\right)\frac{\partial u}{\partial t} + u = 0, \tag{3.1}$$

where u is the displacement. The first term on the left-hand side of (3.1) represents the (mass normalized) acceleration, the second term nonlinear damping, and the third term a linear (Hookean) restoring force. The physical parameter α controls the strength of the nonlinearity. If we let the displacement be $u_1 = u$ and velocity be $u_2 = \partial u/\partial t$, the second-order governing equation in (3.1) can be rewritten as a first-order system to match the general PDEs in (2.1) accordingly

$$\frac{\partial}{\partial t}\left\{\begin{array}{c} u_1 \\ u_2 \end{array}\right\} = \left\{\begin{array}{c} u_2 \\ -\alpha u_1^2 u_2 + \alpha u_2 - u_1 \end{array}\right\}. \tag{3.2}$$

The system now contains two states as opposed to one in displacement and velocity.

Solutions for the displacement and velocity in (3.2) can be evolved with a time-marching or time-spectral scheme. We presume that the method of choice does not completely resolve all time scales. Following the framework in Chapter 2, we modify the governing equations in (3.2) to include the subgrid-scale dynamics as in (2.6). The subgrid-scale acceleration for the van der Pol oscillator is given by

$$\boldsymbol{\alpha} = \left\{\begin{array}{c} \dfrac{\partial \tilde{u}_1}{\partial t} - \widetilde{\dfrac{\partial u_1}{\partial t}} \\ \dfrac{\partial \tilde{u}_2}{\partial t} - \widetilde{\dfrac{\partial u_2}{\partial t}} \end{array}\right\}, \tag{3.3}$$

and the subgrid-scale force becomes

$$\boldsymbol{\gamma} = \left\{ \begin{array}{c} 0 \\ \alpha\tilde{u}_1^2\tilde{u}_2 - \widetilde{\alpha u_1^2 u_2} \end{array} \right\}. \tag{3.4}$$

The subgrid-scale force in (3.4) vanishes for time-marching schemes with a consistent comb-type sampling filter, whereas the subgrid-scale acceleration in (3.3) vanishes for time-spectral schemes with a consistent spectral cutoff filter.

In this work, the modified governing equations for the van der Pol oscillator will be discretized for standard ROM and OPTROM simulations with the IE time-marching scheme described in Section 2.11.1 and the HB time-spectral scheme described in Section 2.11.2. We will also use the well-known fourth-order accurate Runge-Kutta (RK4) time-marching scheme [10, 11] to obtain FRS solutions. For the IE and HB schemes, we model the subgrid-scale dynamics with the stochastic estimate in (2.15). Once the subgrid-scale dynamics are characterized in Chapter 4, standard ROM and OPTROM solutions will be compared to FRS results in Chapter 5.

3.2 Duffing oscillator description

The Duffing oscillator [94–97] is a single DOF nonlinear dynamical system capable of undergoing a time-periodic or chaotic response. Physically, the system models a damped mechanical oscillator with a nonlinear spring (hardening or softening) under the influence of time-dependent external forcing, or "pumping". While several variants of the Duffing equation have been studied throughout the literature, we investigate the following nondimensional form

$$\frac{\partial^2 u}{\partial t^2} + 2\zeta\frac{\partial u}{\partial t} + u + u^3 = F\sin(\omega t), \tag{3.5}$$

where u is the displacement. The first term on the left-hand side of (3.5) represents the (mass normalized) acceleration, the second term linear (viscous) damping, the third term a linear (Hookean) restoring force, and the fourth term a nonlinear (hardening) restoring force. The right-hand side of (3.5) models time-periodic external forcing. The physical parameter ζ is the viscous damping ratio, F is the external forcing amplitude and ω is the forcing frequency. Each of these nondimensional parameters can be related to dimensional quantities [85]. By letting the displacement be $u_1 = u$ and velocity be $u_2 = \partial u/\partial t$, we can rewrite (3.5) as

$$\frac{\partial}{\partial t}\left\{\begin{array}{c} u_1 \\ u_2 \end{array}\right\} = \left\{\begin{array}{c} u_2 \\ -2\zeta u_2 - u_1 - u_1^3 + F\sin(\omega t) \end{array}\right\}, \tag{3.6}$$

which matches the general PDEs in (2.1) and hence can be modified for OPTROM. The subgrid-scale acceleration for the Duffing oscillator is given by

$$\boldsymbol{\alpha} = \left\{\begin{array}{c} \dfrac{\partial \tilde{u}_1}{\partial t} - \widetilde{\dfrac{\partial u_1}{\partial t}} \\ \dfrac{\partial \tilde{u}_2}{\partial t} - \widetilde{\dfrac{\partial u_2}{\partial t}} \end{array}\right\}, \tag{3.7}$$

and subgrid-scale force takes on the following form

$$\boldsymbol{\gamma} = \left\{\begin{array}{c} 0 \\ \tilde{u}_1^3 - \widetilde{u_1^3} \end{array}\right\}. \tag{3.8}$$

As with the van der Pol oscillator, the modified governing equations for the Duffing oscillator will be discretized for standard ROM and OPTROM simulations with the IE time-marching scheme and the HB time-spectral scheme. We will also employ the RK4 time-marching scheme to compute FRS solutions.

3.3 Viscous Burgers flow description

Much of our knowledge about the nature of convection and diffusion in fluids has been learned through various studies of the viscous Burgers equation [98–102]. Throughout the years, Burgers' equation has also become a popular testbed for CFD algorithms due to its relative simplicity and close resemblance to the Navier-Stokes equations [10]. For example, in order to test the numerical properties of a time-spectral method, Maple and his colleagues [103] explored time-periodic solutions to Burgers' equation for a set of oscillating BCs. Perhaps most relevant to this dissertation, Das and Moser [104] developed OLES models for the forced Burgers equation with an initial velocity distribution similar to that of a turbulent flow. Bernstein [105] later tested the performance of OLES models with memory for the Burgers equation with slowly dissipating shocks. When added to the simulations, their subgrid-scale models were found to improve predictions for the velocity and energy spectra. We emphasize, however, that Das and Moser [104] and Bernstein [105] considered only the effects of subgrid-scale convection and viscosity due to the use of a coarse spatial grid. In both studies, Das and Moser [104] and Bernstein [105] neglected the existence subgrid-scale accelerations due to the use of a coarse temporal grid, unlike the OPTROM and OPSTROM formulations in this dissertation.

The one-dimensional Burgers equation is a parabolic PDE for modeling nonlinear wave propagation with diffusion. The evolution of velocity field $u(x,t)$ is governed by

$$\frac{\partial u}{\partial t} + u\frac{\partial u}{\partial x} = \nu\frac{\partial^2 u}{\partial x^2}, \tag{3.9}$$

where the first term represents the local acceleration, the second term nonlinear convection, and the third term diffusion due to viscosity, ν. Independent variables in (3.9) are the time, t, and spatial location, x, in the domain $[0, L]$. When the viscous term in (3.9) is neglected, the result is a hyperbolic PDE capable of producing shock

discontinuities. Retaining the viscous term results in parabolic behavior.

Large-amplitude flow disturbances are implemented via a Dirichlet-type BC at the $x = 0$ inflow location. At the $x = L$ outflow location, we specify a transparent (or non-reflective [106]) Neumann-type BC. We impose

$$u(0,t) = \mathcal{U}\left(1 + \sin\left(2\pi f t\right)\right), \quad \frac{\partial u(L,t)}{\partial x} = 0, \tag{3.10}$$

where $\mathcal{U}$ represents the disturbance amplitude and $f = 2\pi/\omega$ is the disturbance frequency. For a sufficiently small spatial grid with spacing Δx, the transparent BC at $x = L$ is not felt upstream and has negligible effect on the flow [106]. Moreover, the transparent BC at $x = L$ is difficult to see in highly resolved simulations due to the fine spacing between the end grid points at $x = L$ and $x = L - \Delta x$.

Nondimensionalizing the system in (3.9) and (3.10) will enable us to investigate the flow in a generic manner. We proceed by letting $\mathcal{U}$ represent the characteristic velocity and L represent the characteristic length. By nondimensionalizing the variables

$$\hat{u} = \frac{u}{\mathcal{U}}, \quad \hat{x} = \frac{x}{L}, \quad \hat{t} = \frac{\mathcal{U}t}{L}, \tag{3.11}$$

and introducing the Reynolds number, Re, and Strouhal number, St, as

$$Re = \frac{\mathcal{U}L}{\nu}, \quad St = \frac{fL}{\mathcal{U}}, \tag{3.12}$$

we can rewrite the Burgers equation in the following nondimensional form (dropping the $\hat{u}$, $\hat{x}$ and $\hat{t}$ notation in favor of u, x and t for convenience):

$$\frac{\partial u}{\partial t} + u\frac{\partial u}{\partial x} = \frac{1}{Re}\frac{\partial^2 u}{\partial x^2}. \tag{3.13}$$

The nondimensional BCs at $x = 0$ and $x = 1$ become

$$u(0,t) = 1 + \sin\left(2\pi\ St\ t\right), \quad \frac{\partial u(1,t)}{\partial x} = 0. \tag{3.14}$$

Although the Burgers equation contains one state (as opposed to two with the Duffing and van der Pol oscillators), the velocity field is more difficult to solve for because the system must be discretized in both space and time.

Following the theoretical framework in Chapter 2, the subgrid-scale acceleration due to a coarse temporal grid is given by

$$\alpha = \frac{\partial \tilde{u}}{\partial t} - \widetilde{\frac{\partial u}{\partial t}}, \tag{3.15}$$

and the subgrid-scale force due to a coarse spatial grid becomes

$$\gamma = \left(\tilde{u}\frac{\partial \tilde{u}}{\partial x} - \widetilde{u\frac{\partial u}{\partial x}}\right) + \frac{1}{Re}\left(\widetilde{\frac{\partial^2 u}{\partial x^2}} - \frac{\partial^2 \tilde{u}}{\partial x^2}\right). \tag{3.16}$$

To align with the fluids literature [36], we refer to the individual components of γ in (3.16) as the (mass normalized) *subgrid-scale convection* (first term) and *subgrid-scale diffusion* (second term). The subgrid-scale acceleration in (3.15) has historically been neglected in previous works on OLES [104,105]. In this work, we consider the standard ROM, OPTROM, OPSROM and OPSTROM variants.

The modified governing PDEs for the Burgers equation will be discretized in space and time with two conventional finite difference schemes. The first will be used for FRS, whereas the second will be used for ROM simulations with a coarse space-time computational grid. Spatial derivatives are approximated using second-order accurate central differencing for $x \in (0,1)$ with ghost nodes at the boundaries [10]. The fourth-order accurate explicit Runge-Kutta method is used to semi-discretize in time for the first scheme. The fully discretized equations of motion are denoted as Runge-Kutta

centered-space (RKCS). As we shall see in the results, the RKCS scheme is able to fully resolve all time scales with a fine grid, but suffers from numerical instability with coarse timesteps. To allow for a coarse temporal grid for ROM simulations, we also employ the IE time-marching scheme described in Section 2.11.1. The fully discretized equations of motion are denoted as backward-time centered-space (BTCS) [10].

3.4 Nonlinear beam description

As a fourth and final example, we will study the nonlinear structural dynamics of a slender beam under the influence of a time-dependent, distributed transverse load. The nonlinear governing equations were originally derived by Crespo da Silva [107,108] for a flexural-flexural-torsional-extensional beam, then simplified to the problem of interest by Hall and Hanagud [109]. Linear elastic behavior is assumed and moments of inertia are neglected. Moderate axial and transverse displacements are allowed, and as a result, many of the geometric nonlinearities which are typically neglected in classical linear Euler-Bernoulli beam theory become important. We restrict our consideration to third-order nonlinearities in the transverse displacement and second-order nonlinearities in the axial displacement. The nondimensionalized system contains a total of eight parameters. Independent variables are time t and axial distance along the length of the beam x, while the dependent variables are axial displacement u and transverse displacement v. Physical parameters, which presumably will affect the subgrid-scale dynamics, are the damping ratio ζ, square of the slenderness ratio Λ, forcing amplitude F and forcing frequency ω. Note that each of the nondimensional parameters can be related to dimensional quantities given by Hall and Hanagud [109]. The governing PDEs can be written in the same form as the general system in (2.1) along with an appropriate set of BCs and ICs. The system contains $N_S = 6$ states in

$\mathbf{u}(x,t)$ with components u_i, which are given by

$$\begin{aligned} u_1 &= \frac{\partial u}{\partial t} \qquad & u_4 &= \frac{\partial v}{\partial t} \\ u_2 &= u & u_5 &= v \\ u_3 &= u'' & u_6 &= v'', \end{aligned} \tag{3.17}$$

where the primes denote derivatives with respect to x. The six components of the nonlinear force vector in (2.1) are

$$\begin{aligned} R_1 &= \Lambda\left[u_3 + u_5' u_6\right] & R_4 &= \mathcal{F}(x,t) - \zeta u_4 - u_6'' \\ &+ u_6 u_6' + u_5' u_6'' & &+ \Lambda\left[u_3 u_5' + u_2' u_6 + \tfrac{3}{2} u_6 \left(u_5'\right)^2\right] \\ & & &+ \left[2u_2' u_6'' + 4u_3 u_6' + 3u_3' u_6 + u_3'' u_5'\right] \\ & & &+ \left[2u_6'' \left(u_5'\right)^2 + 2\left(u_6\right)^3 + 8u_5' u_6 u_6'\right] \\ R_2 &= u_1 & R_5 &= u_4 \\ R_3 &= u_1'' & R_6 &= u_4''. \end{aligned} \tag{3.18}$$

The transverse loading function $\mathcal{F}(x,t)$ in R_4 can take on any form. To align with the work of Hall and Hanagud [109], we consider a time-dependent, distributed sinusoidal load of the form

$$\mathcal{F}(x,t) = F \sin(\pi x) \sin(\omega t) \qquad \forall\ x \in [0,1],\ t \in [0,\infty). \tag{3.19}$$

We will investigate the response of the beam with three different types of essential BCs. Our primary focus will be on a set of simply supported (SS) BCs at $x = 0$ and $x = 1$, which can be written as

$$u_2|_{x=0,1} = 0, \qquad u_5|_{x=0,1} = 0, \qquad u_3|_{x=0,1} = 0, \qquad u_6|_{x=0,1} = 0. \tag{3.20}$$

In our search for universality in Chapter 4, we also wish to know if the subgrid-scale

models developed for the SS beam will be valid for other BCs as well. As such, we will also consider briefly the following set of clamped-clamped (CC) BCs:

$$u_2|_{x=0,1} = 0, \qquad u_5|_{x=0,1} = 0, \qquad u_2'|_{x=0,1} = 0, \qquad u_5'|_{x=0,1} = 0, \tag{3.21}$$

and a set of clamped-free (CF) BCs for an inextensional cantilevered beam:

$$u_5|_{x=0} = 0, \qquad u_5'|_{x=0} = 0, \qquad u_6|_{x=1} = 0, \qquad u_6'|_{x=1} = 0. \tag{3.22}$$

When deriving the governing PDEs for the extensional beam, Crespo da Silva [107] assumed the deformations would be "restricted in magnitude" such that trigonometric nonlinearities in the strain components could be expanded in a third-order Taylor series about the equilibrium solution, $u = v = 0$. This is a very good assumption for the SS and CC problems. For the CF problem, however, the beam will undergo large transverse displacements in response to the loads considered in this study as a result of having a free end. As such, we will solve an inextensional form of the governing PDEs given by Crespo da Silva [110,111] for the CF problem instead of the extensional form [107,108] from which the forces in (3.18) were derived. Moments of inertia are again neglected. The inextensional assumption has been shown in other references [112] to be an excellent assumption for cantilevered beams undergoing large deflections due to distributed transverse loads.

Following the theoretical framework in Chapter 2, we derive the subgrid-scale dynamics for the beam. Subgrid-scale boundary conditions also exist for the CC and CF beams due to the presence of spatial derivatives, but are neglected in this study.

The six components of the subgrid-scale acceleration are given by

$$\begin{aligned}
\alpha_1 &= \frac{\partial \tilde{u}_1}{\partial t} - \widetilde{\frac{\partial u_1}{\partial t}} \qquad & \alpha_4 &= \frac{\partial \tilde{u}_4}{\partial t} - \widetilde{\frac{\partial u_4}{\partial t}} \\
\alpha_2 &= \frac{\partial \tilde{u}_2}{\partial t} - \widetilde{\frac{\partial u_2}{\partial t}} \qquad & \alpha_5 &= \frac{\partial \tilde{u}_5}{\partial t} - \widetilde{\frac{\partial u_5}{\partial t}} \\
\alpha_3 &= \frac{\partial \tilde{u}_3}{\partial t} - \widetilde{\frac{\partial u_3}{\partial t}} \qquad & \alpha_6 &= \frac{\partial \tilde{u}_6}{\partial t} - \widetilde{\frac{\partial u_6}{\partial t}},
\end{aligned} \tag{3.23}$$

and the six components of the subgrid-scale force take on the following form:

$$\begin{aligned}
\gamma_1 &= \Lambda\widetilde{u_5' u_6} - \Lambda \tilde{u}_5' \tilde{u}_6 \qquad & \gamma_4 &= -\widetilde{u_6''} + \tilde{u}_6'' \\
&+\widetilde{u_6 u_6'} - \tilde{u}_6 \tilde{u}_6' & &+\Lambda\left[\widetilde{u_3 u_5'} + \widetilde{u_2' u_6} + \tfrac{3}{2}\widetilde{u_6 \left(u_5'\right)^2}\right] \\
&+\widetilde{u_5' u_6''} - \tilde{u}_5' \tilde{u}_6'' & &-\Lambda\left[\tilde{u}_3 \tilde{u}_5' + \tilde{u}_2' \tilde{u}_6 + \tfrac{3}{2}\tilde{u}_6 \left(\tilde{u}_5'\right)^2\right] \\
& & &+\left[2\widetilde{u_2' u_6''} + 4\widetilde{u_3 u_6'} + 3\widetilde{u_3' u_6} + \widetilde{u_3'' u_5'}\right] \\
& & &-\left[2\tilde{u}_2' \tilde{u}_6'' + 4\tilde{u}_3 \tilde{u}_6' + 3\tilde{u}_3' \tilde{u}_6 + \tilde{u}_3'' \tilde{u}_5'\right] \\
& & &+\left[2\widetilde{u_6'' \left(u_5'\right)^2} + 2\widetilde{\left(u_6\right)^3} + 8\widetilde{u_5' u_6 u_6'}\right] \\
& & &-\left[2\tilde{u}_6'' \left(\tilde{u}_5'\right)^2 + 2\left(\tilde{u}_6\right)^3 + 8\tilde{u}_5' \tilde{u}_6 \tilde{u}_6'\right] \\
\gamma_2 &= 0 \qquad & \gamma_5 &= 0 \\
\gamma_3 &= \widetilde{u_1''} - \tilde{u}_1'' \qquad & \gamma_6 &= \widetilde{u_4''} - \tilde{u}_4''.
\end{aligned} \tag{3.24}$$

The modified PDEs for the beam will be discretized in space and time with the same FD schemes as the Burgers equation. The RKCS scheme will be used to compute FRS solutions with a highly refined computational grid, and the BTCS scheme will be used for ROM simulations with a coarse computational grid.

3.5 Summary of selected systems

Four nonlinear dynamical systems were described in this chapter, and will be used to investigate various aspects of the OPSTROM framework. The canonical van der Pol and Duffing oscillators contain no spatial dependence, which will allow us to focus

exclusively of subgrid time scales and the OPTROM approach. The van der Pol oscillator features a nonlinear damping mechanism, which plays the role of an energy source and sink as the system evolves to a steady state LCO. The Duffing oscillator features a nonlinear stiffness term, which allows for both regular and chaotic response types when subjected to time-periodic external forcing. The viscous Burgers equation with time-periodic BCs will enable us to demonstrate application of all four reduced order modeling variants (standard ROM, OPTROM, OPSROM and OPSTROM) to a fluid dynamics problem with spatiotemporal dependence. The nonlinear beam problem also contains spatiotemporal dependence, but is capable of undergoing a variety of structural response types ranging from time-periodic to chaotic. For each of these systems, we derived the subgrid-scale accelerations and forces. Discretization schemes were then described for both FRS and ROM simulations.

CHAPTER 4

Characterization of subgrid-scale dynamics

In this chapter, we characterize the subgrid-scale dynamics for each of the nonlinear dynamical systems and corresponding discretization schemes described in Chapter 3. The findings will then be used to guide the construction of subgrid-scale models for OPTROM, OPSROM and OPSTROM simulations.

Recall that the discrete subgrid-scale models in (2.15) require *a priori* knowledge of multi-point statistical moments (or correlations [113]) amongst $\boldsymbol{\tau}$ and $\tilde{\mathbf{u}}$ as shown in (2.16). In order to acquire such knowledge, FRS solutions will be computed for a select number of physical parameters. Each FRS solution will be filtered to match the desired ROM. For the IE and BTCS schemes, we apply a consistent comb-type sampling filter in space and time. For the HB scheme, we apply a consistent spectral cutoff filter. The subgrid-scale dynamics $\boldsymbol{\tau}$ for each problem will then be computed using the expressions for $\boldsymbol{\alpha}$ and $\boldsymbol{\gamma}$ derived in Chapter 3. The required multi-point moments amongst $\boldsymbol{\tau}$ and $\tilde{\mathbf{u}}$, several of which are given by

$$\left\langle (\tau_i)_j^n \right\rangle, \quad \left\langle (\tilde{u}_i)_j^n \right\rangle, \quad \left\langle (\tau_i)_j^n (\tilde{u}_k)_p^m \right\rangle, \quad \left\langle (\tilde{u}_i)_j^n (\tilde{u}_k)_p^m \right\rangle, \tag{4.1}$$

will then be obtained by direct calculation as shown in Table 2.2. The mean operator $\langle \cdot \rangle$ for each moment is to be computed over the spatiotemporal domain of interest. The purpose of the model $\boldsymbol{\mathcal{M}}$ is to approximate $\boldsymbol{\tau}$ over whatever domain is chosen.

In addition to the raw moments required for the models (see (2.16) and (4.1)), normalized moments (or correlation coefficients [113]) will also be useful in studying the statistical properties. To this end, the second-order moments amongst $\boldsymbol{\tau}$ and $\tilde{\mathbf{u}}$

will sometimes be normalized by the following quantity

$$\mathrm{Q}_{ik} = \left\langle (\tau_i)^2 \right\rangle^{1/2} \left\langle (\tilde{u}_k)^2 \right\rangle^{1/2}, \tag{4.2}$$

such that they vary in the domain $[-1, 1]$. A value of 1 indicates that $\boldsymbol{\tau}$ and $\tilde{\mathbf{u}}$ are (perfectly) positively correlated, 0 indicates that they uncorrelated, and -1 indicates that they are (perfectly) negatively correlated. The stronger the correlations, positive or negative, the more accurately we should be able to estimate $\boldsymbol{\tau}$ [65, 66].

While all of the moments in (4.1) are important, some are worth studying more than others. In particular, we shall find that the $\left\langle (\tau_i)_j^n (\tilde{u}_k)_p^m \right\rangle$ moments are most sensitive to the system parameters, and therefore, will be the focus of this analysis. In general, the observations to be made for the $\left\langle (\tau_i)_j^n (\tilde{u}_k)_p^m \right\rangle$ moments also hold (often to a greater extent) for the other moments in (4.1).

As discussed in Section 2.7, it may be possible to increase the practical utility of the subgrid-scale models by making some simplifying assumptions. For each of the problems, we explore the extent to which the following properties are valid:

- Spatial homogeneity
- Temporal homogeneity
- Ergodicity
- A functional dependence which can easily be characterized with respect to the system parameters (referred to as "smooth scaling" for brevity)
- Universality

If observed, smooth scaling would enable efficient construction of models based upon estimated moments as shown in Table 2.3. Once the "best" models are established for each problem, performance of the standard ROM, OPTROM, OPSROM and OPSTROM schemes will be investigated in Chapter 5.

4.1 Van der Pol oscillator characterization

The subgrid-scale dynamics for the van der Pol oscillator in (3.3) and (3.4) depend only on the strength of the nonlinear damping coefficient (α) and the temporal grid (Δt or N_H). In this work, we consider nonlinear damping coefficients within the range

$$\alpha \in (0, 20]. \tag{4.3}$$

To eliminate any potential ambiguity, we focus exclusively on steady state LCOs. For the time-marching solutions, transients are allowed to decay due to the presence of physical and numerical damping.

In order to characterize the subgrid-scale dynamics for the van der Pol oscillator, FRS solutions are obtained for a select number of α values. To achieve a true FRS solution with a time-marching scheme, an infinitesimally small timestep must be used to evolve the solution. Similarly, an infinite number of modes must be retained with a time-spectral scheme. To be practical, however, we consider a simulation to be a FRS when all variables (u_1, u_2 and ω) are resolved to within machine precision ($\mathcal{O}(10^{-16})$). For this problem, FRS solutions are computed with the RK4 time-marching scheme with a very fine timestep of $\Delta t = 10^{-6}$, which completely resolves all variables to within machine precision for $\alpha \in (0, 20]$.

Steady state FRS solutions are shown in Figure 4.1 for $\alpha = \{0^+, 5, 10, 15, 20\}$, where 0^+ denotes the upper limit as $\alpha \to 0$. Observe in Figure 4.1a that the system undergoes self-sustained relaxation oscillations with frequency ω and period $T = 2\pi/\omega$. Energy is rapidly introduced to the system near the origin in the form of negative damping. An abrupt transition to positive damping occurs away from the origin, whereupon energy is slowly extracted from the system. When the system is almost linear ($\alpha \to 0$), the response becomes sinusoidal with $\omega = 1$ and $T = 2\pi$. When the nonlinearity is large ($\alpha \to \infty$), the response approaches a square wave with

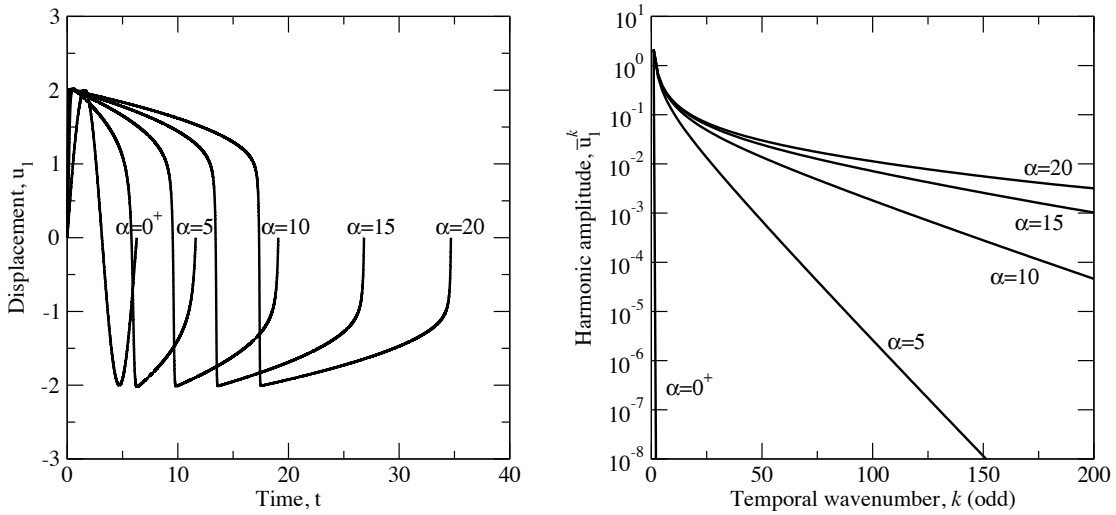

(a) Displacement time history

(b) Temporal spectra

Figure 4.1: Steady state FRS solutions for the van der Pol oscillator with five different nonlinearities: $\alpha = \{0^+, 5, 10, 15, 20\}$. The FRS solutions are computed with the RK4 time-marching scheme with a very fine timestep of $\Delta t = 10^{-6}$.

infinite period. Only the odd harmonic amplitudes are shown in Figure 4.1b, as the even (and zero$^{\text{th}}$) harmonic amplitudes are effectively zero.

As an alternative to the RK4 scheme, we could have chosen to produce FRS solutions with the IE or HB schemes, but the timestep (IE) or number of harmonics (HB) needed to satisfy our criteria for a FRS would require excessive computational resources. This can be seen in Figure 4.2, where the LCO frequency errors (2.28) are compared for a fixed nonlinearity of $\alpha = 20$. The largest Δt represents the coarsest grid for which each scheme is stable or able to converge. Decreasing Δt improves the resolution until machine precision is reached. For $\alpha = 20$, it is not feasible to obtain FRS solutions with the IE or HB schemes. Similarly, as an alternative to the IE and HB schemes, we could choose to produce ROM simulations with the explicit RK4 time-marching scheme. Due to its conditional stability, however, RK4 scheme is not a good choice for ROM simulations with coarse timesteps.

From each of the FRS solutions in Figure 4.1, the subgrid-scale moments are obtained by direct calculation, as described in Table 2.2. For now, it is sufficient to state

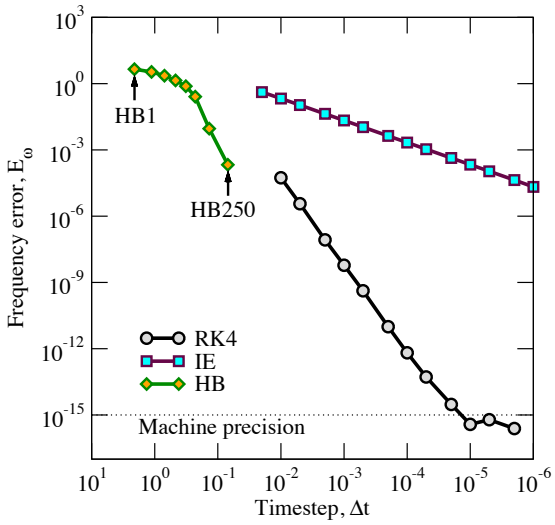

Figure 4.2: LCO frequency errors for the van der Pol oscillator with $\alpha = 20$ computed with the RK4, IE and HB schemes with various timesteps.

that the required moments are homogeneous in time when the system has reached a steady state response and the mean operator $\langle\cdot\rangle$ is evaluated over one period of oscillation. This is due to the fact that the mean of a time-periodic function is invariant when the domain of integration is taken over one period [113]. Moreover, since there exists only one stable LCO to which all nonzero trajectories evolve, the required moments are also ergodic. The concepts of temporal homogeneity and ergodicity will be explored in greater detail in Section 4.4 for the nonlinear beam. Spatial homogeneity is meaningless for this problem as it contains no spatial dependence.

In order to characterize the functional dependence of the moments with respect to the system parameters, we employ a fourth-order bivariate Lagrange interpolation scheme. For the IE scheme, we consider parameters within the range of $\alpha \in (0, 20]$ and $\Delta t \in [10^{-3}, 10^{-1}]$. The interpolation nodes are chosen to be $\alpha = \{0^+, 5, 10, 15, 20\}$ and five logarithmically spaced values of Δt. Two of the estimated moments required for model construction models are shown in Figure 4.3. Observe that the moments scale smoothly with respect to α and Δt, which implies that the functional dependence can easily be characterized with a small amount of FRS data (five solutions).

Various choices can be made for the van der Pol oscillator with regards to the

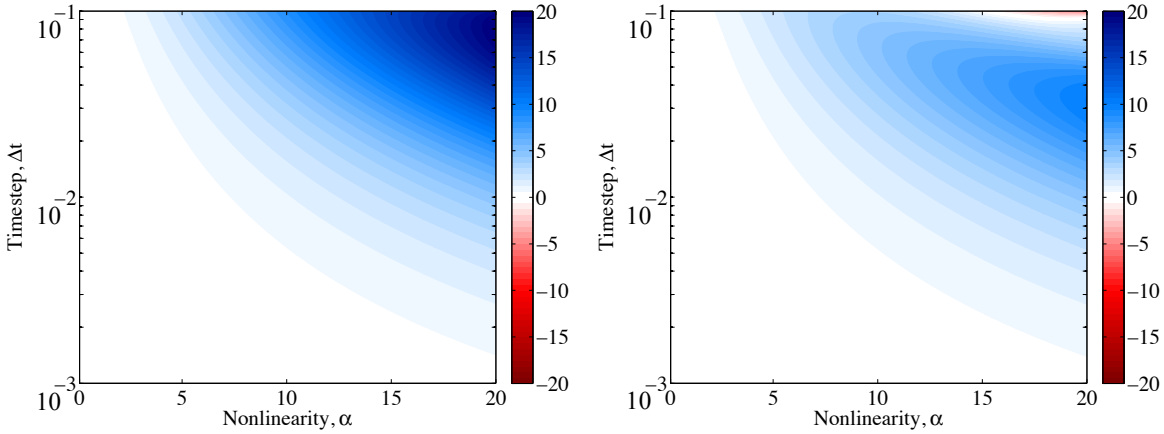

(a) $\langle \tau_2^n \tilde{u}_2^n \rangle$ (b) $\langle \tau_2^n \tilde{u}_2^{n-1} \rangle$

Figure 4.3: Estimated moments amongst τ_i^n and $\tilde{u}_k^m$ for the van der Pol oscillator as a function of the nonlinearity $\alpha \in (0, 20]$ and timestep $\Delta t \in [10^{-3}, 10^{-1}]$ for the IE scheme. A fourth-order bivariate Lagrange interpolation scheme is used to estimate the moments with nodes at $\alpha = \{0^+, 5, 10, 15, 20\}$ and five logarithmically spaced Δt values. For each of the five α-nodes, the moments are calculated directly from the FRS solutions in Figure 4.1.

functional form of the subgrid-scale model, including the order of approximation, the number of states (M_S) and the extent of support in time (M_T). For the IE scheme, we select a linear stochastic estimate with two states and a two-point temporal stencil, which uses $(\mathcal{A}_i)^n$ and $(\mathcal{B}_{i\alpha})^{n\mu}$ with $M_S = 2$ and $M_T = 2$ in (2.15). A total of 34 moments (inputs) are required in (2.16) for this particular model, 16 of which are redundant, and two of which are shown in Figure 4.3. Within the specified range of α and Δt, the chosen subgrid-scale model is found to provide the best combination of simplicity (low number of coefficients and correlations) and performance (low errors) for the IE scheme. Including quadratic and cubic terms in the estimate does not improve predictions. Further increasing the temporal stencil size improves the *a priori* errors, but not the *a posteriori* errors.

Moments required for the HB scheme are also interpolated as a function of the nonlinearity $\alpha \in (0, 20]$ using fourth-order Lagrange polynomials. A consistent spectral cutoff filter is used to compute the filtered solution. Each of the FRS solutions in Figure 4.1 are transformed to the Fourier domain where all modes greater than N_H

are truncated. The filtered spectra are then transformed back to the time domain where the moments amongst $\boldsymbol{\tau}$ and $\tilde{\mathbf{u}}$ are calculated. Due to the application of a consistent spectral cutoff filter, the subgrid-scale acceleration vanishes, leaving only the subgrid-scale force to be modeled.

For the HB scheme, we select a linear subgrid-scale model with two states and a one-point temporal stencil, which uses $(\mathcal{A}_i)^n$ and $(\mathcal{B}_{i\alpha})^{n\mu}$ with $M_S = 2$ and $M_T = 1$ in (2.15). When one harmonic is retained in the HB scheme (referred to throughout the literature as the *describing function method*), the direct subgrid-scale model is exact (zero *a priori* error). An explanation for this result is provided in Appendix A. The model appraisal criterion described in Section 2.9 suggests that ROM solutions with this particular model will also be exact. This actually occurs in Section 5.1 when direct models are used. When multiple harmonics are retained with the HB scheme, however, the *a priori* errors are nonzero but small nevertheless.

We emphasize that a total of five FRS solutions are used to construct subgrid-scale models for the van der Pol oscillator with the IE and HB schemes. In Section 5.1, however, we also compute FRS solutions for each α in order to determine the accuracy of ROM solutions. For the canonical van der Pol oscillator, it is feasible to do so.

4.2 Duffing oscillator characterization

The subgrid-scale dynamics for the Duffing oscillator in (3.7) and (3.8) depend on each of the physical parameters (F, ω and ζ) and the temporal grid (Δt or N_H). In this dissertation, we analyze the complex response of the Duffing oscillator as a function of the external forcing amplitude F and frequency ω. Analogous to focusing on one physical specimen, we fix the damping ratio ζ to 0.1 for the remainder of this study. We consider the following parametric values:

$$\zeta = 0.1, \qquad F \in (0, 150], \qquad \omega \in [0.5, 5]. \tag{4.4}$$

The frequency range is chosen to surpass the natural frequency of oscillation for the linearized system, $\omega_0 = 1$, while the large range of forcing amplitudes renders an assortment of highly nonlinear solutions.

In order to characterize the functional dependence of the required multi-point moments with respect to the forcing parameters, FRS solutions are obtained for sixteen combinations of F and ω, as shown in Table 4.1. Each solution is evolved beyond 100 forcing cycles. A variety of trajectories are encountered when transients are allowed to decay due to damping, including symmetric time-periodicity, asymmetry, period N-tupling and chaos. Four of these solutions, for example, are shown in Figure 4.4.

From each of the sixteen FRS solutions in Table 4.1, the required moments are obtained via direct calculation. Temporal homogeneity and ergodicity are excellent assumptions when the response is time-periodic and symmetric. When the response is asymmetric or chaotic, however, the moments display at least some sensitivity to the initial conditions and the time domain over which the mean operator is evaluated. Nevertheless, these variations are subtle, and we still consider temporal homogeneity and ergodicity to be reasonable assumptions for all response types. Moments for the chaotic solutions are evaluated over 100 forcing cycles, and moments for the asymmetric solutions are averaged with respect to all observed outcomes. Later in Section 4.4, we will explore in greater detail the validity of temporal homogeneity and ergodicity for both regular and chaotic response types.

ω	0^+	50	100	150
5	P	P	P	P
2.5	P	AP	3P	3P
1	P	3P	2P	C
0.5	P	AP	C	C

F

P	Periodic steady state
AP	Asymmetric periodic
NP	Period N-tupling
C	Chaotic

Table 4.1: Qualitative FRS solution behavior for the Duffing oscillator at sixteen discrete points in the forcing parameter space $F \in (0, 150] \times \omega \in [0.5, 5]$ for which moments amongst τ_i^n and $\tilde{u}_k^m$ are calculated directly.

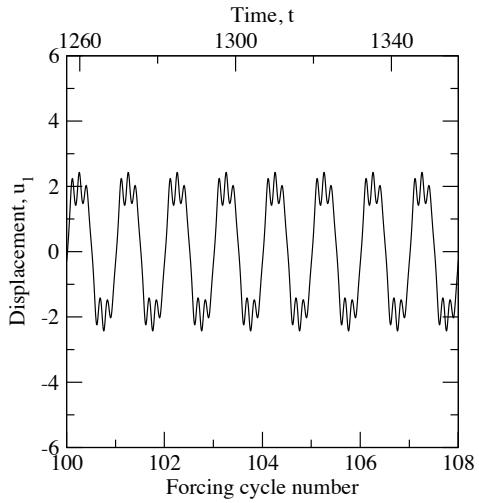

(a) $F = 10$ and $\omega = 0.5$: Periodic

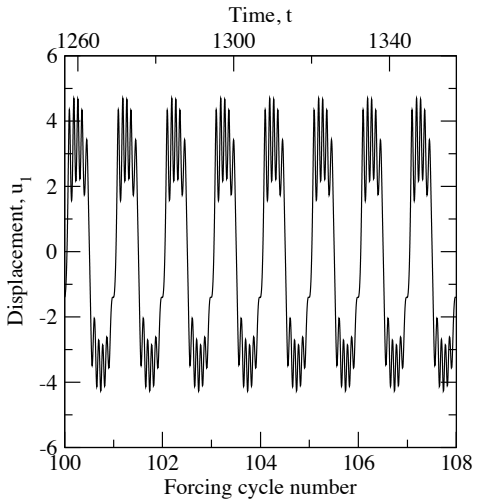

(b) $F = 50$ and $\omega = 0.5$: Asymmetric

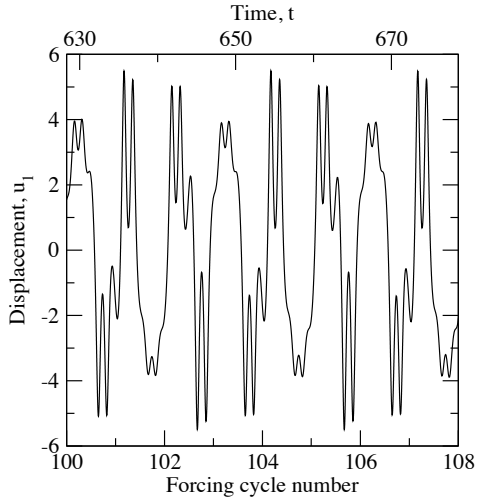

(c) $F = 50$ and $\omega = 1.0$: Period tripling

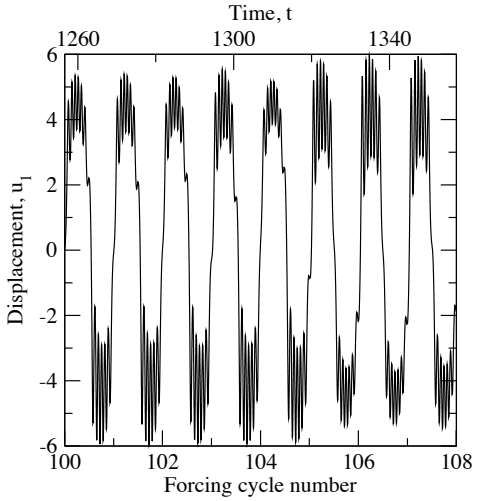

(d) $F = 100$ and $\omega = 0.5$: Chaotic

Figure 4.4: Time history of FRS solutions for the Duffing oscillator with a select number of forcing parameters. Transients have decayed for periodic solutions as each simulation is evolved beyond 100 forcing cycles.

For the Duffing oscillator, we employ a local bilinear interpolation scheme to approximate the functional dependence of the moments with respect to F and ω. Two of these moments, for example, are shown in Figure 4.5. The subset of forcing parameters from Table 4.1 serve as interpolation nodes. Observe that the moments scale smoothly with respect to F and ω, which implies that the functional dependence can easily be characterized. Other moments required for the models scale in a similar manner with respect to F and ω. This finding is particularly interesting, if not

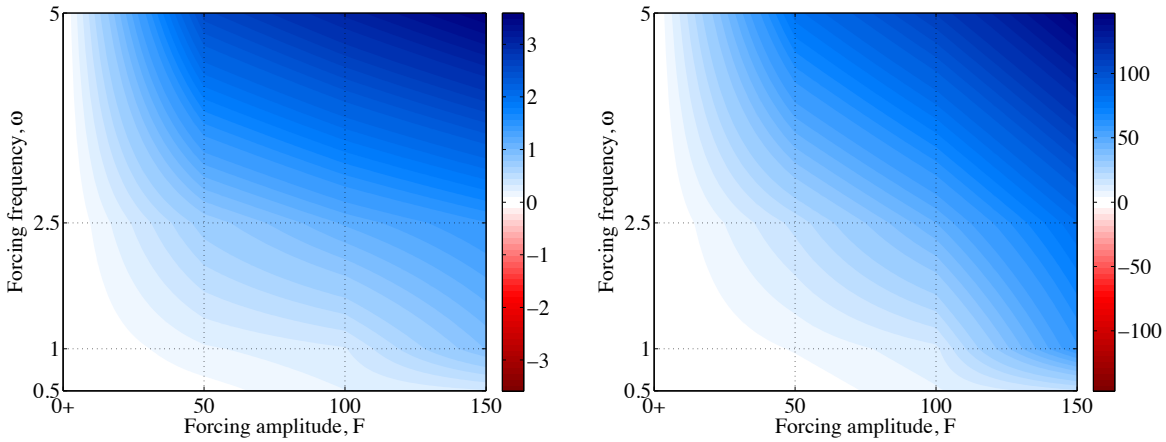

(a) $\langle \tau_1^n \tilde{u}_1^n \rangle$ (b) $\langle \tau_2^n \tilde{u}_2^n \rangle$

Figure 4.5: Estimated moments amongst τ_i^n and $\tilde{u}_k^m$ for the Duffing oscillator in the forcing parameter space $F \in (0, 150] \times \omega \in [0.5, 5]$. A local bilinear interpolation scheme is used to estimate the moments with nodes at $F = \{0^+, 50, 100, 150\}$ and $\omega = \{0.5, 1, 2.5, 5\}$, as indicated by the intersecting dotted lines. At each node, the moments are calculated directly from the FRS solutions in Table 4.1 with a consistent comb-type sampling filter for the IE scheme with coarse timestep of $\Delta t = 10^{-2}$.

surprising, considering a wide variety of trajectories were encountered, ranging in complexity from time-periodic to chaotic.

The required moments also scale smoothly with respect to the temporal grid, Δt, results for which are not shown here, as they resemble closely those for the nonlinear beam in Section 4.4. Note that additional FRS solutions need not be obtained to characterize the moments with respect to Δt; only the comb-type sampling filter needs to be modified. In this sense, characterizing the functional dependence of the moments with respect to Δt requires less effort than with respect to F and ω.

Estimated moments allow for efficient model construction. The number of FRS solutions (interpolation nodes) needed to characterize the moments should generally be influenced by the observed scaling behavior with respect to the parameters of interest. Smooth scaling, as in Figure 4.5, simplifies this task. Less smooth results (due to a more complicated functional dependence) would require additional nodes and/or higher-order interpolants. As shown in Table 4.2, the estimated moments in Figure 4.5 are quite accurate for a representative set of forcing parameters. When

Moment	Estimation	Direct calculation	Error
$\langle \tilde{u}_1^n \tilde{u}_1^n \rangle$	0.2171×10^2	0.2026×10^2	0.072
$\langle \tilde{u}_1^n \tilde{u}_1^{n-1} \rangle$	0.2168×10^2	0.2024×10^2	0.071
$\langle \tilde{u}_2^n \tilde{u}_2^n \rangle$	0.4098×10^3	0.3656×10^3	0.121
$\langle \tilde{u}_2^n \tilde{u}_2^{n-1} \rangle$	0.4107×10^3	0.3662×10^3	0.122
$\langle \tau_1^n \tilde{u}_1^n \rangle$	0.1936×10^1	0.1775×10^1	0.091
$\langle \tau_1^n \tilde{u}_1^{n-1} \rangle$	0.1952×10^1	0.1810×10^1	0.078
$\langle \tau_1^n \tilde{u}_2^n \rangle$	-0.3237×10^1	-0.3815×10^1	-0.152
$\langle \tau_1^n \tilde{u}_2^{n-1} \rangle$	-0.2648×10^1	-0.3215×10^1	-0.176

Table 4.2: Subgrid-scale moments for the Duffing oscillator with an arbitrarily chosen set of external forcing parameters ($F = 125$ and $\omega = 4.0$) for which the response is time-periodic and symmetric. Two methods of moment calculation are compared: direct calculation from an FRS solution obtained *a priori* (accurate but inefficient), and estimation (as shown in Figure 4.5). The moments are calculated for the IE scheme with a coarse timestep of $\Delta t = 10^{-2}$. Relative errors for the estimated moments are shown the final column.

compared to the moments obtained via direct calculation, the estimated moments in Table 4.2 vary by less than 20%.

Various choices can be made for the Duffing oscillator with regards to model construction. For the IE scheme, we select a linear stochastic estimate with two states and a two-point temporal stencil, which uses $(\mathcal{A}_i)^n$ and $(\mathcal{B}_{i\alpha})^{n\mu}$ with $M_S = 2$ and $M_T = 2$ in (2.15). This particular model is well-conditioned and provides a favorable combination of low *a priori* and *a posteriori* errors. For the HB scheme, we also select a linear stochastic estimate with two states, but we consider the effects of various stencils ($M_T = 1$, 2 and 3) when multiple harmonics are retained. The performance of a one-point cubic model will also be discussed briefly in Section 5.2. For this problem, the subgrid-scale models are based upon moment estimation for the IE scheme and direct calculation for the HB scheme.

4.3 Viscous Burgers flow characterization

For the viscous Burgers flow, we aim to characterize the subgrid-scale dynamics for the following flow parameter space:

$$Re \in [10^0, 10^3], \qquad St \in (0, 3]. \tag{4.5}$$

The properties of interest are spatiotemporal homogeneity, ergodicity, and scaling behavior with respect to the flow parameters (Re and St).

First we characterize the spatiotemporal dependence of the required multi-point moments for a representative set of flow parameters ($Re = 100$ and $St = 3$). An FRS solution is computed for these parameters using the RKCS scheme with a very fine grid ($\Delta x = 10^{-4}$ and $\Delta t = 10^{-8}$). Due to the parabolic nature of the governing PDE and the time-periodic inflow BCs, temporal homogeneity and ergodicity are found to be excellent assumptions when the flow is given time to convect downstream and the mean operator is taken over one period of oscillation. Both the single-point and multi-point moments are found to vary significantly in space, however, as shown in Figures 4.6, 4.7 and 4.8.

Observe in Figure 4.6 that the mean of $\tilde{u}_j^n$ grows slightly as the flow convects downstream, whereas the second moment is relatively homogeneous and the higher moments of the flow dissipate. In addition to the single-point moments shown in Figure 4.6, multi-point moments amongst $\tilde{u}_j^n$ may be required for the subgrid-scale models. For brevity, it is sufficient to state through observation that the multi-point moments amongst $\tilde{u}_j^n$ vary in a similar manner to those in Figure 4.6.

Multi-point (in time) moments amongst the velocity and subgrid-scale acceleration are shown in Figure 4.7. The mean of α_j^n is effectively zero, but the moments amongst $\tilde{u}_j^n$ and α_j^n are relatively large upstream. As the flow convects downstream, the time scales become less important and the moments decay. Note that the information

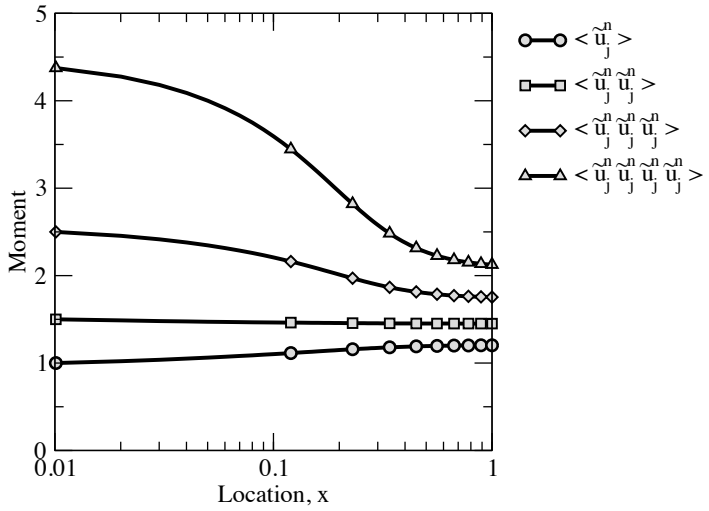

Figure 4.6: Spatial variation in select moments amongst the filtered velocity field $\tilde{u}_j^n$ for the Burgers flow with $Re = 100$ and $St = 3$. The FRS solution is filtered in space and time with a consistent comb-type sampling filter for the BTCS scheme with $\Delta x = 10^{-2}$ and $\Delta t = 10^{-2}$. Temporal homogeneity is assumed as the time domain for the mean operator is taken over one period of oscillation, whereas the spatial domain is infinitesimally small.

shown in Figure 4.7 is all that needs to be known about α to construct a spatially heterogeneous model for OPTROM with a linear stochastic estimate on a three-point backward temporal stencil.

Multi-point (in space) moments amongst the velocity and subgrid-scale force are shown in Figure 4.8. Observe that the mean of γ_j^n is greatest far upstream, where convection is dominant and the spatial scales are most complex. The multi-point moments amongst $\tilde{u}_j^n$ and γ_j^n display an even greater degree of functional dependence on the spatial location. Such variation all but necessitates the use of heterogeneous subgrid-scale models. The information shown in Figure 4.8 is all that needs to be known about γ in order to construct a heterogeneous model for OPSROM with a quadratic stochastic estimate with diagonal coefficients and a three-point spatial stencil. Previous research in optimal LES [69, 70, 104, 105] has suggested that quadratic estimates may in fact be necessary to accurately model subgrid-scale convection terms.

The next step is to characterize the functional dependence of the required moments

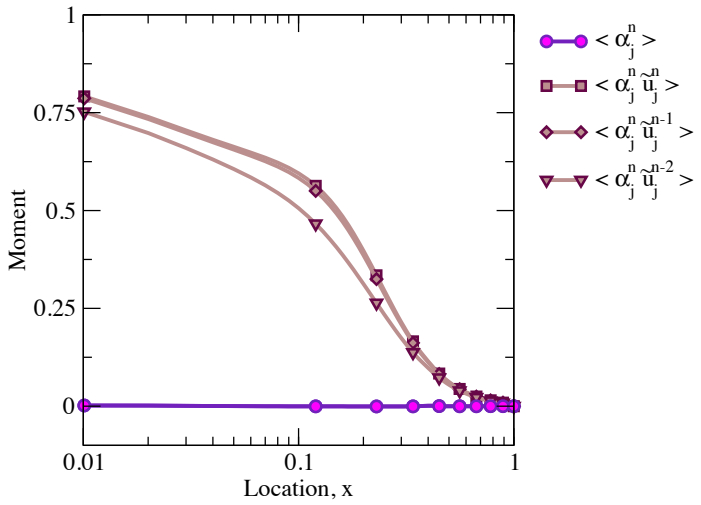

Figure 4.7: Spatial variation in select moments amongst the filtered velocity field $\tilde{u}_j^n$ and subgrid-scale acceleration α_j^n on a three-point temporal stencil for the Burgers flow with $Re = 100$ and $St = 3$. The FRS solution is filtered in space and time with a consistent comb-type sampling filter for the BTCS scheme with $\Delta x = 10^{-2}$ and $\Delta t = 10^{-2}$. Temporal homogeneity is assumed as the time domain for the mean operator is taken over one period of oscillation, whereas the spatial domain is infinitesimally small.

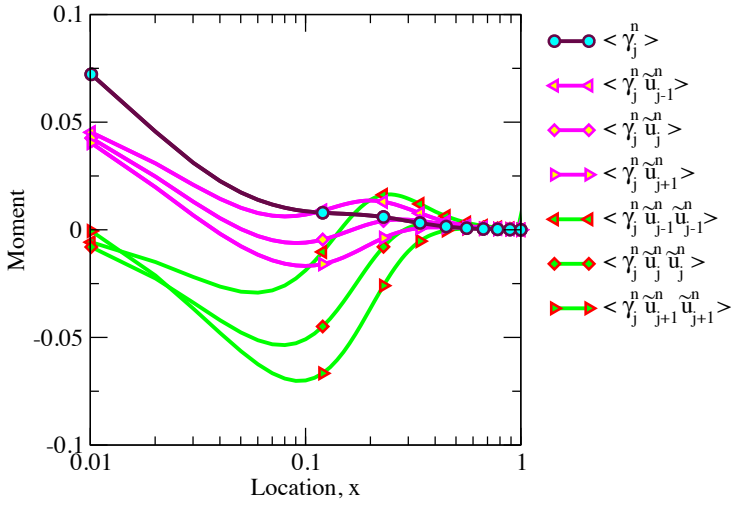

Figure 4.8: Spatial variation in select moments amongst the filtered velocity field $\tilde{u}_j^n$ and subgrid-scale force γ_j^n on a three-point spatial stencil for the Burgers flow with $Re = 100$ and $St = 3$. The FRS solution is filtered in space and time with a consistent comb-type sampling filter for the BTCS scheme with $\Delta x = 10^{-2}$ and $\Delta t = 10^{-2}$. Temporal homogeneity is assumed as the time domain for the mean operator is taken over one period of oscillation, whereas the spatial domain is infinitesimally small.

with respect to the flow parameters. To this end, FRS solutions are obtained for the sixteen possible combinations of the following Reynolds and Strouhal numbers: $Re = \{10^0, 10^1, 10^2, 10^3\}$ and $St = \{0^+, 0.75, 1.5, 3.0\}$. Four of these solutions are shown in Figure 4.9. The moments required for the subgrid-scale models are then calculated directly from the FRS solutions. Temporal homogeneity is assumed, but spatial dependence is preserved. A local bilinear interpolation scheme is then used to estimate the moments in the continuous flow parameter space. Hence, the sixteen discrete values of flow parameters serve as interpolation nodes.

Representative sets of estimated moments amongst $\tilde{u}_j^n$, α_j^n, and γ_j^n are shown in Figures 4.10, 4.11 and 4.12 at the $x = 0.5$ spatial location. Observe that the moments amongst $\tilde{u}_j^n$ in Figure 4.10 vary smoothly with respect to Re and St, which allows for the functional dependence to be easily characterized. Moments amongst $\tilde{u}_j^n$, α_j^n and γ_j^n in Figures 4.11 and 4.12 also display a similar type of scaling with respect to the flow parameters. The subgrid-scale accelerations in Figure 4.11 appear to be significant unless the flow is heavily damped ($Re \to 0$) and slowly fluctuating ($St \to 0$). The subgrid-scale forces in Figure 4.12 are also greatest for large Reynolds numbers, but seem to be affected less by the Strouhal number.

In order to determine the accuracy of the estimated moments in Figures 4.10, 4.11 and 4.12, one additional FRS solution is obtained for a new set of flow parameters ($Re = 50$ and $St = 2.25$). Several of the multi-point moments required for model construction are compared in Table 4.3. The moments are obtained by means of estimation (sampled from the information in Figures 4.10, 4.11 and 4.12) and direct calculation from the FRS solution for $Re = 50$ and $St = 2.25$. As shown in Table 4.3, the estimated moments amongst the velocity are generally 95% accurate, whereas the moments amongst the subgrid-scale force and acceleration are found to be 80% accurate. We deem these to be good results considering additional forms of uncertainty are embedded within the stochastic estimate.

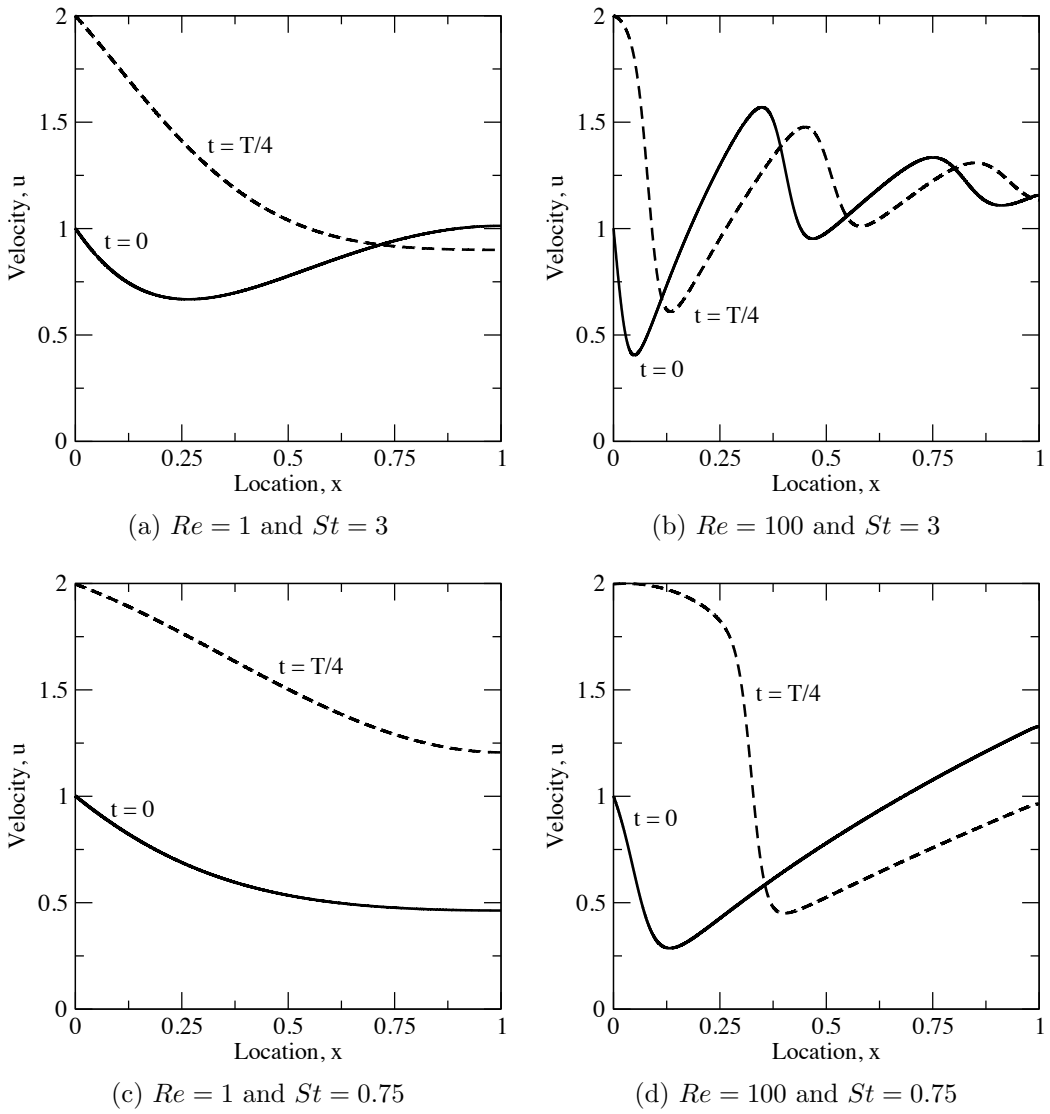

(a) $Re = 1$ and $St = 3$

(b) $Re = 100$ and $St = 3$

(c) $Re = 1$ and $St = 0.75$

(d) $Re = 100$ and $St = 0.75$

Figure 4.9: Snapshots of FRS solutions for the viscous Burgers flow with a select number of flow parameters. In each figure, the spatial distributions are shown at two different times during the inflow disturbance cycle: the beginning ($t = 0$, solid curve) and the peak ($t = T/4$, dashed curve).

The moments in Figures 4.10, 4.11 and 4.12 can also be tabulated for different grids by filtering the FRS data with different Δx and Δt values. Additional FRS data need not be obtained for such a task. For instance, when filtered with $\Delta x = 10^{-3}$ and $\Delta t = 10^{-3}$, the moments are also found to vary smoothly with respect to Re and St. Once tabulated, the moments can be interpolated with respect to the grid parameters Δx and Δt in addition to the flow parameters.

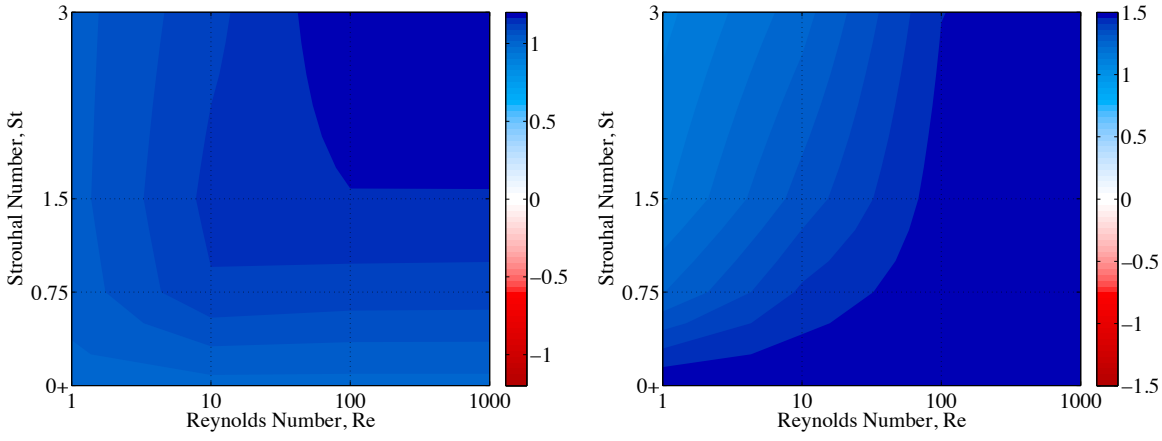

(a) $\langle \tilde{u}_j^n \rangle$ at $x = 0.5$ (b) $\langle \tilde{u}_j^n \tilde{u}_j^n \rangle$ at $x = 0.5$

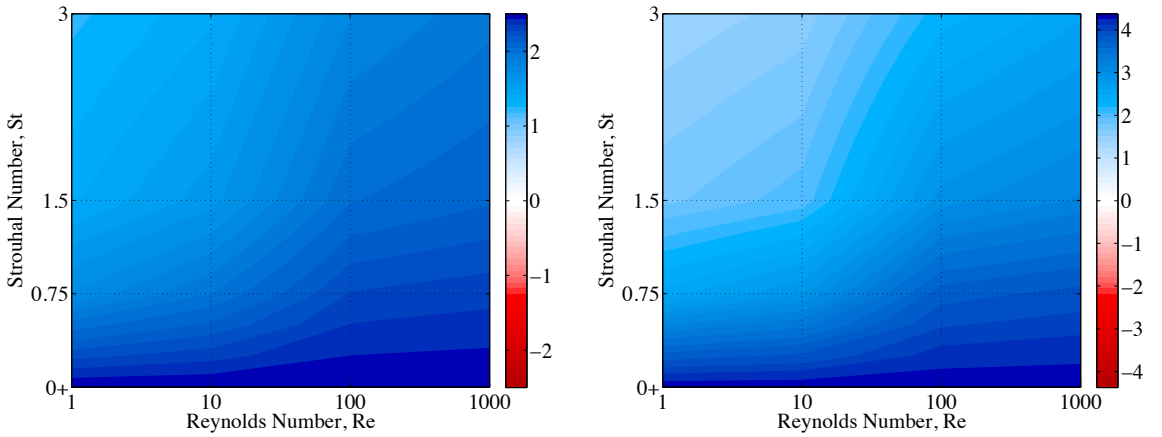

(c) $\langle \tilde{u}_j^n \tilde{u}_j^n \tilde{u}_j^n \rangle$ at $x = 0.5$ (d) $\langle \tilde{u}_j^n \tilde{u}_j^n \tilde{u}_j^n \tilde{u}_j^n \rangle$ at $x = 0.5$

Figure 4.10: Estimated moments amongst the filtered velocity $\tilde{u}_j^n$ for the Burgers flow in the flow parameter space $Re \in [10^0, 10^3] \times St \in (0^+, 3]$. A local bilinear interpolation scheme is used to estimate the moments with nodes at $Re = \{10^0, 10^1, 10^2, 10^3\}$ and $St = \{0^+, 0.75, 1.5, , 3\}$, as indicated by the intersecting dotted lines. One FRS solution is obtained at each of the sixteen nodes, and a consistent comb-type sampling filter is applied with $\Delta x = 10^{-2}$ and $\Delta t = 10^{-2}$ in order to characterize the moments. Temporal homogeneity is assumed, but spatial nonuniformity is considered as the mean operator is evaluated over an infinitesimal spatial domain and one cycle of oscillation. The moments here are compared at the $x = 0.5$ spatial location.

One of the objectives of this study is to determine which terms in the subgrid-scale dynamics are important for problems with spatiotemporal dependence. As such, we will model individually the subgrid-scale accelerations due to a coarse temporal grid (OPTROM) and the subgrid-scale forces due to a coarse spatial grid (OPSROM). When used in conjunction, the OPTROM and OPSROM models account for the

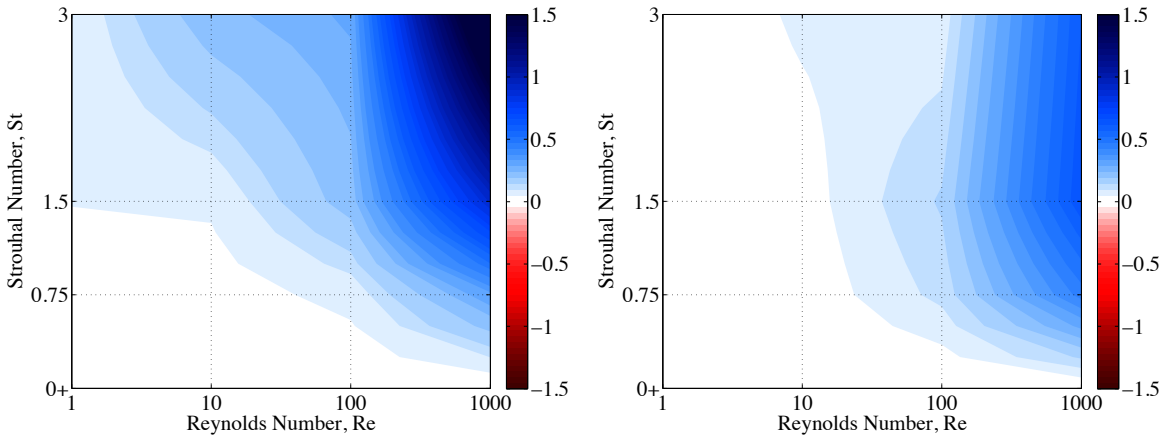

(a) $\langle \alpha_j^n \tilde{u}_j^n \rangle$ at $x = 0.25$

(b) $\langle \alpha_j^n \tilde{u}_j^n \rangle$ at $x = 0.5$

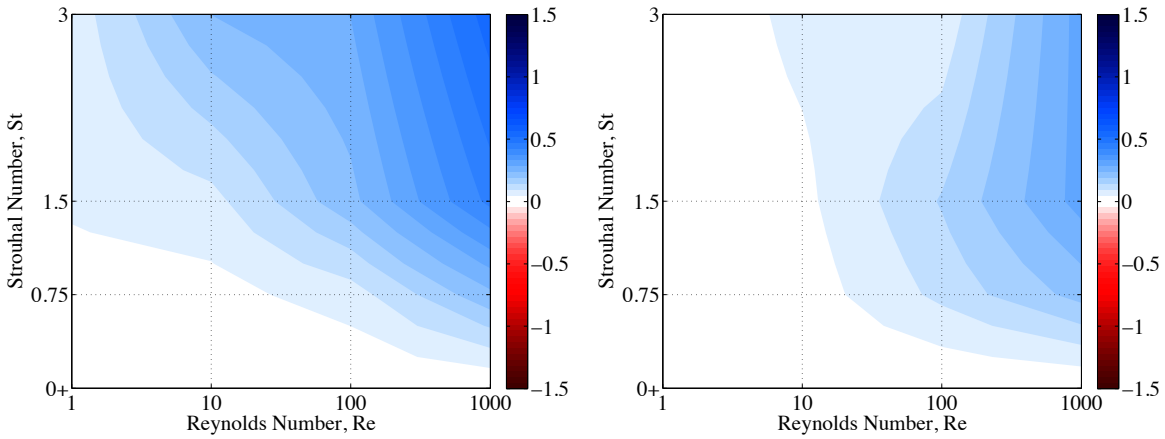

(c) $\left\langle \alpha_j^n \tilde{u}_j^{n-1} \right\rangle$ at $x = 0.25$

(d) $\left\langle \alpha_j^n \tilde{u}_j^{n-1} \right\rangle$ at $x = 0.5$

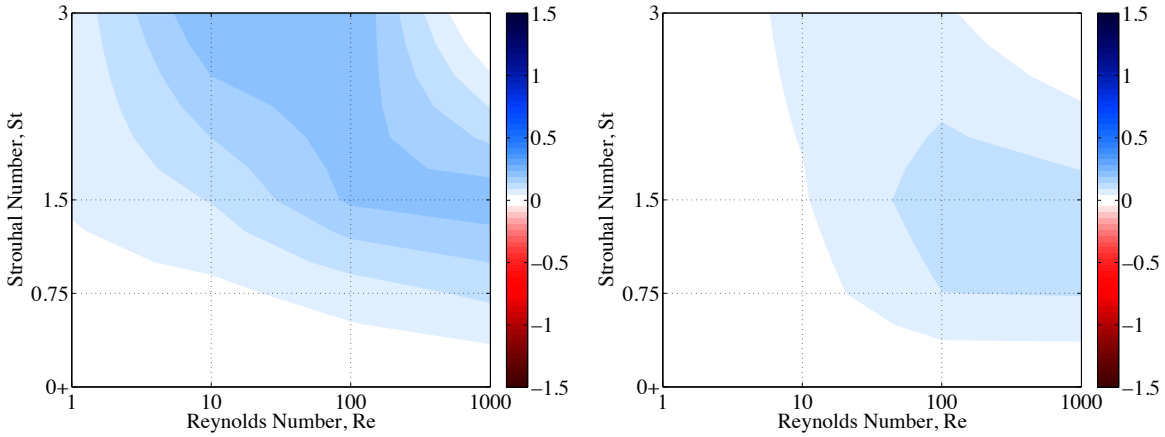

(e) $\left\langle \alpha_j^n \tilde{u}_j^{n-2} \right\rangle$ at $x = 0.25$

(f) $\left\langle \alpha_j^n \tilde{u}_j^{n-2} \right\rangle$ at $x = 0.5$

Figure 4.11: Estimated moments amongst the subgrid-scale acceleration, α_j^n, and filtered velocity, $\tilde{u}_j^n$, for the Burgers flow in the flow parameter space $Re \in [10^0, 10^3] \times St \in (0^+, 3]$. The moments here are compared at the $x = 0.25$ and $x = 0.5$ locations.

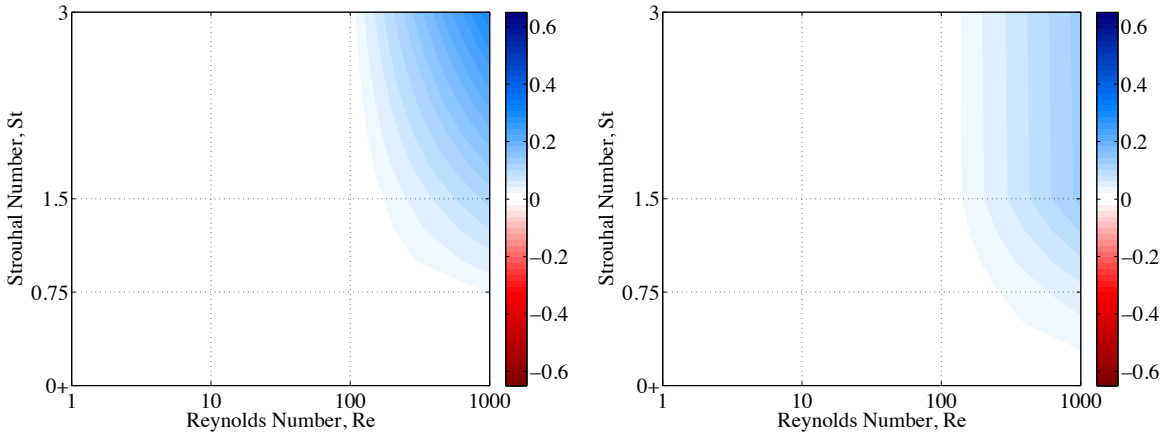

(a) $\langle \gamma_j^n \tilde{u}_{j-1}^n \rangle$ at $x = 0.25$

(b) $\langle \gamma_j^n \tilde{u}_{j-1}^n \rangle$ at $x = 0.5$

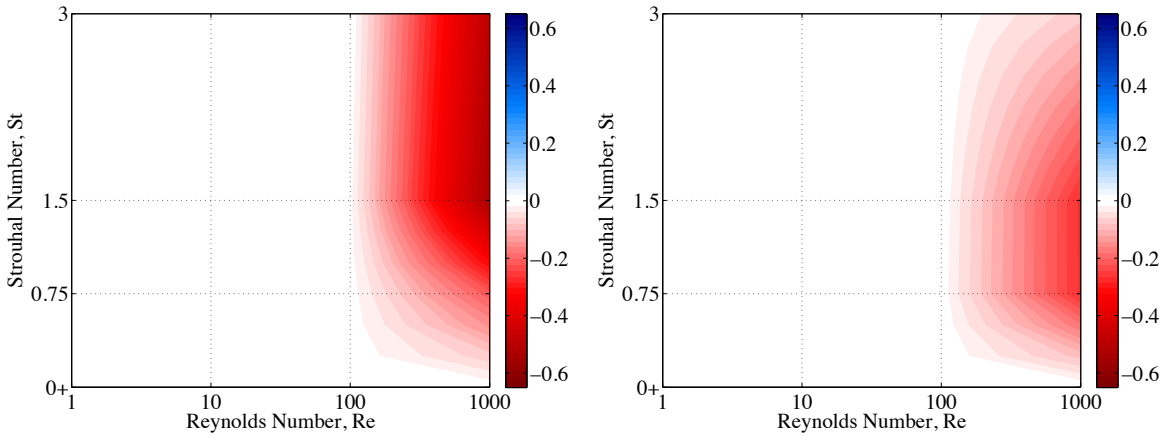

(c) $\langle \gamma_j^n \tilde{u}_j^n \rangle$ at $x = 0.25$

(d) $\langle \gamma_j^n \tilde{u}_j^n \rangle$ at $x = 0.5$

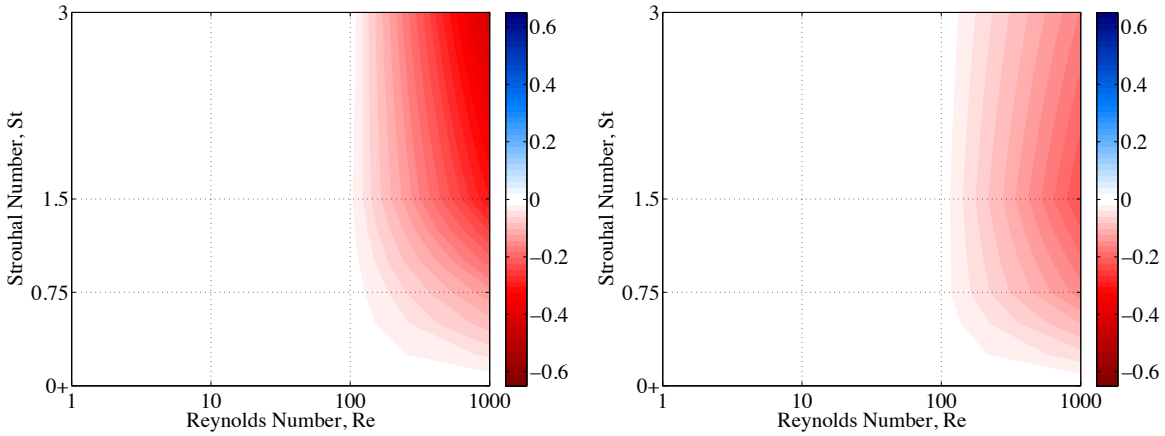

(e) $\langle \gamma_j^n \tilde{u}_{j+1}^n \rangle$ at $x = 0.25$

(f) $\langle \gamma_j^n \tilde{u}_{j+1}^n \rangle$ at $x = 0.5$

Figure 4.12: Estimated moments amongst the subgrid-scale force, γ_j^n, and filtered velocity, $\tilde{u}_j^n$, for the Burgers flow in the flow parameter space $Re \in [10^0, 10^3] \times St \in (0^+, 3]$. The moments here are compared at the $x = 0.25$ and $x = 0.5$ locations.

Moment	Estimation	Direct calculation	Error
$\langle \tilde{u}_j^n \rangle$	0.11501×10^{1}	0.11819×10^{1}	0.026
$\langle \tilde{u}_j^n \tilde{u}_j^n \rangle$	0.13682×10^{1}	0.14323×10^{1}	0.044
$\langle \tilde{u}_j^n \tilde{u}_j^{n-1} \rangle$	0.13677×10^{1}	0.14318×10^{1}	0.044
$\langle \tilde{u}_j^n \tilde{u}_j^{n-2} \rangle$	0.13660×10^{1}	0.14305×10^{1}	0.045
$\langle \tilde{u}_j^n \tilde{u}_{j-1}^n \rangle$	0.13680×10^{1}	0.14320×10^{1}	0.044
$\langle \tilde{u}_j^n \tilde{u}_{j+1}^n \rangle$	0.13678×10^{1}	0.14319×10^{1}	0.044
$\langle \tilde{u}_j^n \tilde{u}_j^n \tilde{u}_j^n \rangle$	0.16839×10^{1}	0.17771×10^{1}	0.052
$\langle \tilde{u}_j^n \tilde{u}_j^n \tilde{u}_j^n \tilde{u}_j^n \rangle$	0.21441×10^{1}	0.22535×10^{1}	0.048
$\langle \alpha_j^n \tilde{u}_j^n \rangle$	0.53069×10^{-1}	0.43953×10^{-1}	0.207
$\langle \alpha_j^n \tilde{u}_j^{n-1} \rangle$	0.52217×10^{-1}	0.43650×10^{-1}	0.196
$\langle \alpha_j^n \tilde{u}_j^{n-2} \rangle$	0.45786×10^{-1}	0.41569×10^{-1}	0.101
$\langle \gamma_j^n \tilde{u}_{j-1}^n \rangle$	0.12074×10^{-2}	0.15192×10^{-2}	0.205
$\langle \gamma_j^n \tilde{u}_j^n \rangle$	0.96578×10^{-3}	0.12604×10^{-2}	0.233
$\langle \gamma_j^n \tilde{u}_{j+1}^n \rangle$	0.87746×10^{-3}	0.10049×10^{-2}	0.126

Table 4.3: Subgrid-scale moments for the Burgers flow with an arbitrarily chosen set of flow parameters ($Re = 50$ and $St = 2.25$) at the $x = 0.5$ midfield location. Two different methods of moment calculation are compared: direct calculation from an FRS solution (accurate but inefficient) and estimation (as shown in Figures 4.10, 4.11 and 4.12). The moments are calculated for a coarse computational grid with $\Delta x = 10^{-2}$ and $\Delta t = 10^{-2}$. Relative errors for the estimated moments are shown the final column.

complete subgrid-scale spatiotemporal statistical structure (OPSTROM). All of the models will be spatially heterogeneous. For the subgrid-scale accelerations, we select a linear stochastic estimate with a three-point temporal stencil, which uses $(\mathcal{A}_i)_j^n$ and $(\mathcal{B}_{i\alpha})_{j\xi}^{n\mu}$ with $M_N = 1$ and $M_T = 3$ in (2.15). For the subgrid-scale forces, we select a quadratic stochastic estimate with a three-point spatial stencil, which uses $(\mathcal{A}_i)_j^n$, $(\mathcal{B}_{i\alpha})_{j\xi}^{n\mu}$ and $(\mathcal{C}_{i\alpha\beta})_{j\xi\eta}^{n\mu\nu}$ with $M_N = 3$ and $M_T = 1$ in (2.15). Only the diagonal quadratic coefficients are retained to avoid ill-conditioning. In other words, $(\mathcal{C}_{i\alpha\beta})_{j\xi\eta}^{n\mu\nu} = 0$ if $\xi \neq \eta$. This particular quadratic model is chosen (i) to match the functional form of the subgrid-scale convection in (3.16), and (ii) due to its superior performance in comparison to linear models for this problem.

4.4 Nonlinear beam characterization

For the nonlinear beam, we characterize the subgrid-scale dynamics with respect to the external forcing amplitude F and frequency ω. Unless otherwise stated, the BCs will be SS. Analogous to focusing on one physical beam specimen, the slenderness ratio Λ and damping ratio ζ will be fixed. To align with the work of Hall and Hanagud [109], Holmes [95], and Abhyankar [114], we consider the following parametric values:

$$\begin{aligned} \Lambda &= 442368 \qquad & F &\in (0, 15] \\ \zeta &= 1.0 & \omega &\in [1, 15]. \end{aligned} \tag{4.6}$$

For verification, the values of Λ and ζ are consistent with the computational study of Hall and Hanagud [109] in which solutions for $F \in (0, 10]$ and $\omega = 3.76$ were explored. The frequency range in (4.6) is chosen to surpass the first natural frequency of the linearized SS beam model, $\omega_1 = \pi^2$ [18], while the range of forcing amplitudes renders an assortment of highly nonlinear solutions.

FRS solutions for the beam are obtained with the explicit RKCS scheme with a fine computational grid ($\Delta x = 5{\times}10^{-3}$ and $\Delta t = 10^{-6}$). As shown by the grid convergence study in Appendix D, the RKCS scheme is able to fully resolve all spatiotemporal spectra to within $\epsilon < 10^{-6}$. However, the RKCS is a poor choice for ROM simulations due to numerical instability with coarse timesteps. As such, the unconditionally stable BTCS scheme will be used in Section 5.4 for ROM simulations that are under-resolved in space and under-resolved in time (USUT), as described in Figure 1.2. Also shown in Appendix D, the BTCS scheme can be used to compute USUT solutions several orders of magnitude faster than the FRS.

A variety of beam trajectories will be encountered in this study. In the time history of the response, we may find periodicity, asymmetry, period N-tupling, intermittency and chaos. Weak turbulence [115, 116], which for this problem implies

simultaneous spatial irregularity and temporal chaos, is not observed for the SS BCs in (3.20) and parameters in (4.6). To uncover a few of these trajectories, we sweep the forcing amplitude $F \in (0, 15]$ with a fixed frequency of $\omega = 3.76$. FRS solutions for six of these forcing amplitudes are shown in Figure 4.13. For small forcing amplitudes ($F \ll 1$), the response is nearly identical to the result of linear Euler-Bernoulli beam theory. For example, two peaks can be seen in the Figure 4.13a response for $F = 0.1$. As F increases, the nonlinearities become important and bifurcations occur. The first bifurcation appears around $F = 0.15$, whereupon a mode of local vibration is added to the response for a total of six peaks. A second bifurcation occurs near $F = 1.0$ and the response gains yet another mode of vibration for a total of ten peaks, as shown in Figure 4.13b. For larger forcing amplitudes, a variety of response types emerge, including asymmetric periodicity (Figure 4.13c), period doubling (Figure 4.13d), higher period N-tupling and chaos (Figure 4.13e). Chaotic regions act as a transitional phase in which two or more asymmetric branches merge to form a symmetric branch of a higher mode [109]. As shown in Figure 4.13e and 4.13f, increasing F can sometimes increase or decrease the complexity of solutions.

First we address the extent to which spatial homogeneity applies by studying the subgrid-scale dynamics for the FRS solution in Figure 4.13f for $F = 10$ and $\omega = 3.76$. The normalized moments amongst $\boldsymbol{\tau}$ and $\tilde{\mathbf{u}}$ are shown in Figure 4.14 on a three-point temporal stencil (t^n, t^{n-1}, t^{n-2}). The time domain for the mean operator is taken to be one steady state forcing cycle while the spatial domain is taken to be infinitesimally small, i.e. one spatial node, which enables us to observe any spatial variation in the moments. Very little spatial variation (at most 8% in the x-direction) can be seen in the Figure 4.14 normalized moments, which indicates that spatial homogeneity should be an inexact yet excellent assumption for models with multi-point temporal stencils. In addition to the time-periodic solution studied in Figure 4.14, similar results are observed for asymmetric and chaotic solutions.

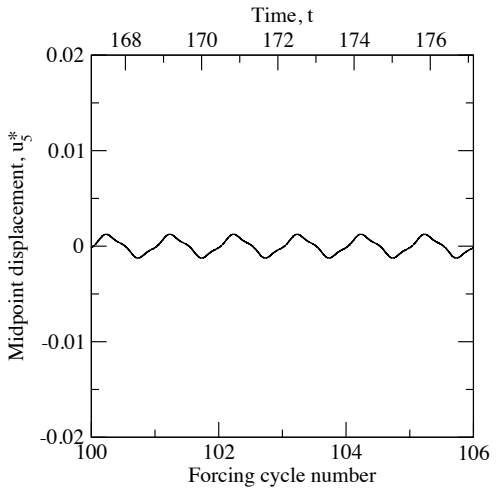

(a) $F = 0.1$: Periodic

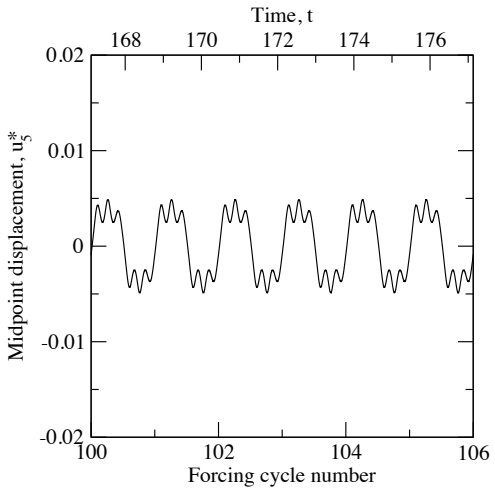

(b) $F = 1$: Periodic

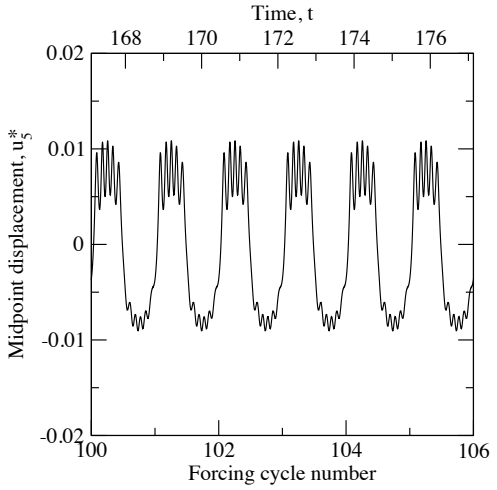

(c) $F = 7$: Asymmetric periodic

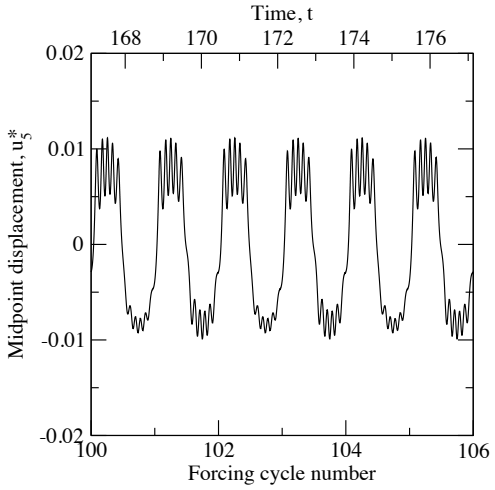

(d) $F = 7.5$: Period doubling

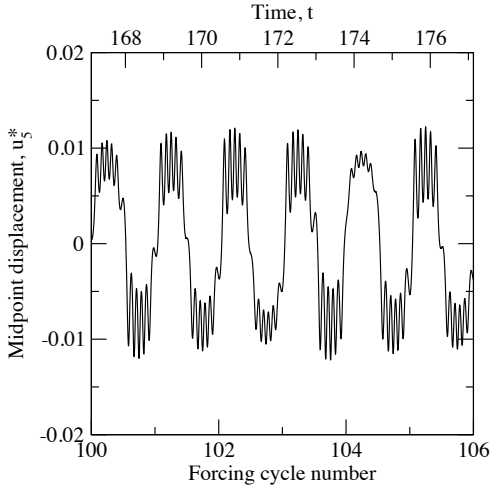

(e) $F = 8.5$: Chaotic

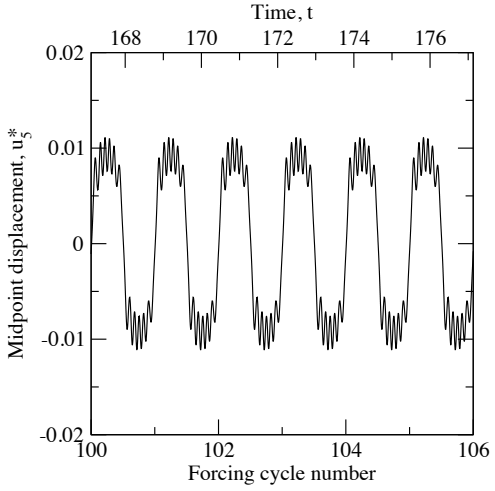

(f) $F = 10$: Periodic

Figure 4.13: Time history of FRS solutions for the midpoint displacement of the SS beam for a select number of forcing amplitudes with a fixed forcing frequency of $\omega = 3.76$. Transients have decayed for periodic solutions as each simulation is evolved beyond 100 forcing cycles.

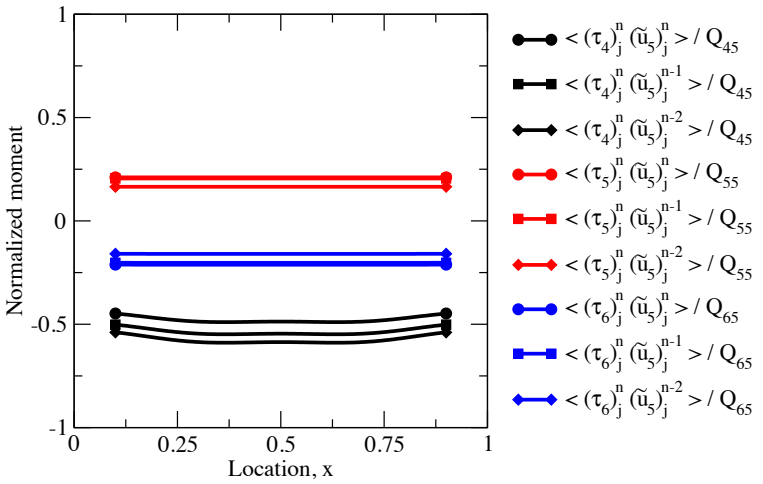

Figure 4.14: Spatial variation in select moments amongst $(\tau_i)_j^n$ and $(\tilde{u}_k)_p^m$ on a three-point backward temporal stencil ($M_T = 3$) for the SS beam with an external forcing of $F = 10$ and $\omega = 3.76$. The periodic FRS solution for this case is filtered in space and time with $\Delta x = 1.0{\times}10^{-1}$ and $\Delta t = 1.0{\times}10^{-2}$. Temporal homogeneity is assumed as the mean operator $\langle\cdot\rangle$ is taken over the 100^{th} forcing cycle $t \in [100(2\pi/\omega), 101(2\pi/\omega)]$, whereas the spatial domain is infinitesimally small $x \in (x_j - \Delta x, x_j + \Delta x)$.

Now consider the normalized moments amongst $\boldsymbol{\tau}$ and $\tilde{\mathbf{u}}$ on a three-point spatial stencil (x_{j-1}, x_j, x_{j+1}) shown in Figure 4.15. A high degree of spatial dependence can be seen, especially near the boundaries where the beam is simply supported and the displacement is zero, thus rendering the spatial homogeneity assumption invalid for multi-point spatial stencils. For example, the $\left\langle (\tau_4)_j^n (\tilde{u}_5)_{j-1}^n \right\rangle / \mathrm{Q}_{45}$ moments vary between 0 and -0.832 in the x-direction. This finding does not necessarily prohibit the analyst from constructing a homogeneous model with a multi-point spatial stencil, although one could expect perhaps less than optimal results.

Temporal variation in the normalized moments for $F = 10$ and $\omega = 3.76$ are shown in Figures 4.16 and 4.17. The beam is driven from its equilibrium position at $t = 0$ (zero initial conditions), and the moments are calculated at the beginning of each forcing cycle as the system undergoes a transient response. Hence, the domain for the mean operator is taken to be $t \in [t^n - 2\pi/\omega, t^n]$ and $x \in [0, 1]$. Eventually the transient vibrations dissipate and the system reaches a periodic steady state response

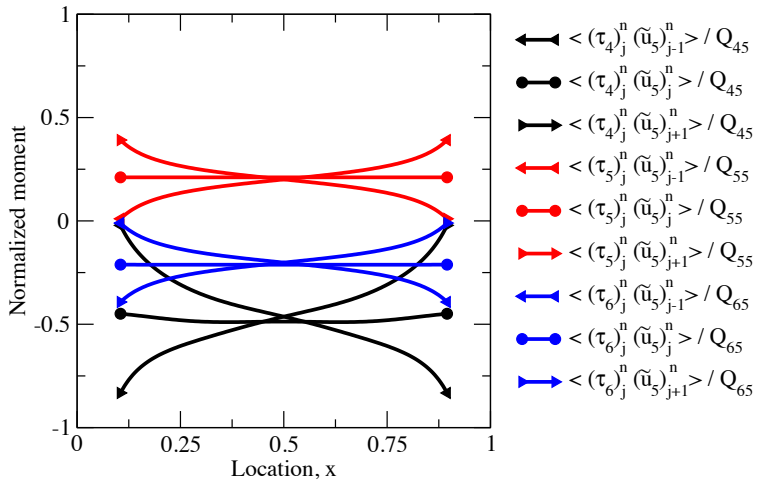

Figure 4.15: Spatial variation in select moments amongst $(\tau_i)_j^n$ and $(\tilde{u}_k)_p^m$ on a three-point central spatial stencil ($M_N = 3$) for the SS beam with an external forcing of $F = 10$ and $\omega = 3.76$. The moments are calculated with the same parameters as Figure 4.14.

well before the 100$^{\text{th}}$ forcing cycle. Temporal homogeneity is an exact assumption for the periodic response over one forcing cycle; this is true regardless of the chosen stencil (M_S, M_N, M_T). Temporal homogeneity is also an exact assumption over N forcing cycles when the beam undergoes period N-tupling for different loads.

Moments for chaotic solutions must be treated somewhat differently. Consider, for example, the FRS solution in Figure 4.13e for a forcing combination of $F = 8.5$ and $\omega = 3.76$. Temporal variations in the moments are shown in Figures 4.18 and 4.19 with various stencils. In both figures, the spatial domain for the mean operator is taken to be $x \in [0, 1]$. First we consider Figures 4.18a and 4.19a in which the time domain for the mean operator is taken to be one forcing cycle. The signature feature of chaos here resembles noise in the subgrid-scale dynamics. As seen in Figures 4.18b and 4.19b, extending the time domain for the mean operator to ten forcing cycles filters out much of the apparent noise. For example, when the mean operator is calculated over one forcing cycle, the $\left\langle (\tau_5)_j^n (\tilde{u}_5)_j^n \right\rangle / \mathrm{Q}_{55}$ moments vary between 0.081 and 0.316 as a function of time. By extending the time domain for the mean operator to ten forcing cycles, the same moments vary between 0.195 and 0.264 as a function of time.

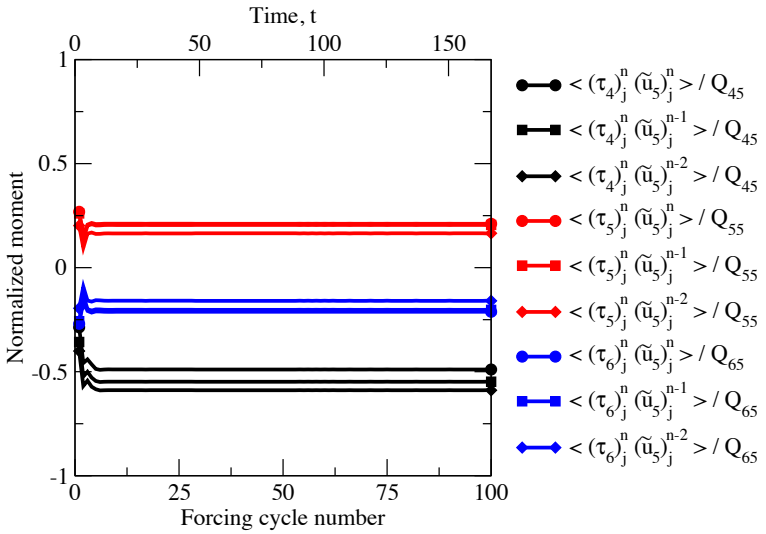

Figure 4.16: Temporal variation in select moments amongst $(\tau_i)_j^n$ and $(\tilde{u}_k)_p^m$ on a three-point backward temporal stencil ($M_T = 3$) for the SS beam with an external forcing of $F = 10$ and $\omega = 3.76$. The FRS solution is filtered with $\Delta x = 1.0{\times}10^{-1}$ and $\Delta t = 1.0{\times}10^{-2}$. The mean operator $\langle\cdot\rangle$ is taken over the entire spatial domain $x \in [0, 1]$ and one transient forcing cycle $t \in [t^n - 2\pi/\omega, t^n]$.

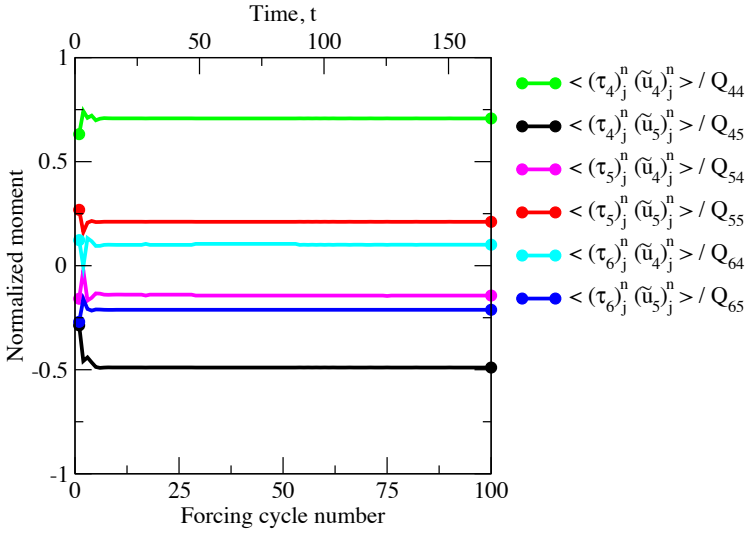

Figure 4.17: Temporal variation in select moments amongst $(\tau_i)_j^n$ and $(\tilde{u}_k)_p^m$ on a two-state stencil ($M_S = 2$) for the SS beam with an external forcing of $F = 10$ and $\omega = 3.76$. The moments are calculated with the same parameters as Figure 4.16.

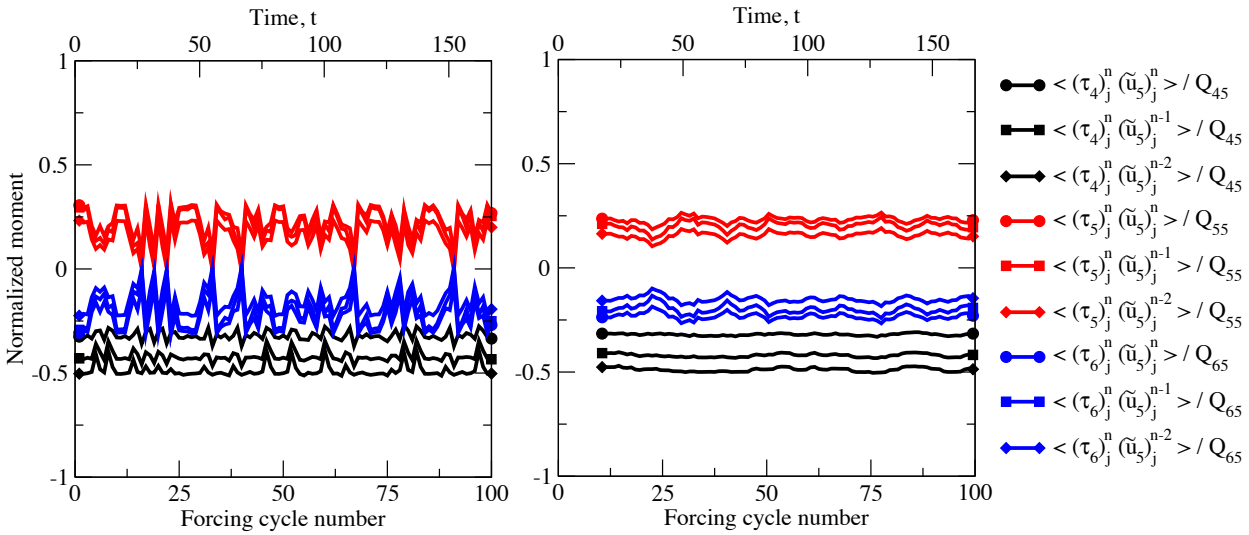

(a) Mean taken over one forcing cycle (b) Mean taken over ten forcing cycles

Figure 4.18: Temporal variation in select moments amongst $(\tau_i)_j^n$ and $(\tilde{u}_k)_p^m$ on a three-point backward temporal stencil ($M_T = 3$) for the SS beam with an external forcing of $F = 8.5$ and $\omega = 3.76$. The FRS solution is filtered with $\Delta x = 1.0{\times}10^{-1}$ and $\Delta t = 1.0{\times}10^{-2}$. The mean operator $\langle\cdot\rangle$ is taken over the entire spatial domain $x \in [0, 1]$ and over one or ten chaotic forcing cycles ($t \in [t^n - 2\pi/\omega, t^n]$ or $t \in [t^n - 10(2\pi/\omega), t^n]$).

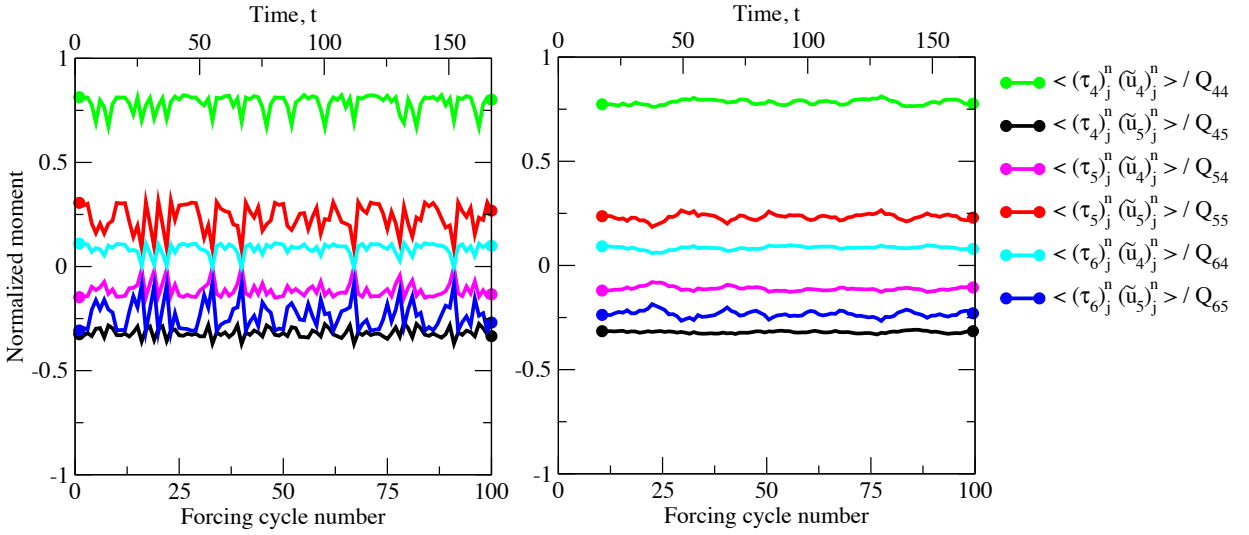

(a) Mean taken over one forcing cycle (b) Mean taken over ten forcing cycles

Figure 4.19: Temporal variation in select moments amongst $(\tau_i)_j^n$ and $(\tilde{u}_k)_p^m$ on a two-state stencil ($M_S = 2$) for the SS beam with an external forcing of $F = 8.5$ and $\omega = 3.76$. The moments are calculated with the same parameters as Figure 4.18.

By further extending the time domain to 100 forcing cycles, the same moments vary between 0.231 and 0.233 (less than 1% variation) for all time. In summary, temporal homogeneity appears to be a valid assumption so long as the trajectories remain on the same attractor and the mean is evaluated over $t \in [0, \infty)$. To be practical, in this study, $t \to \infty$ is approximated as 100 forcing cycles.

In summary, spatial homogeneity and temporal homogeneity are both found to be excellent (sometimes exact) assumptions for multi-point temporal and multi-state moments. The multi-point spatial moments, however, appear to be nonhomogeneous for this problem. This is true for both regular and chaotic response types. With these assumptions, a subgrid-scale model with a one-point spatial stencil can be used at every grid location (x_j and t^n), which greatly simplifies model construction and implementation. Ergodicity would further suggest that the required moments are invariant to ICs. This is in fact true for symmetric periodic solutions and approximately true for chaotic solutions in a long-term sense. Asymmetric periodic solutions, however, are sensitive to ICs. Fortunately, differences in the moments for asymmetric solutions (not shown) are subtle. Given these observations, and considering the higher level of difficulty required to develop models which are sensitive to ICs, we hereafter assume the evolution of the random filtered field to be an ergodic process for the purpose of model construction. For the case of asymmetric solutions, the moments are calculated based upon the expected value of all observed outcomes. In Section 5.4.4, it will be demonstrated that simulations with models constructed in this manner are able to predict asymmetric solution branches which are sensitive to ICs.

With the limitations of spatiotemporal homogeneity and ergodicity understood, the next step is to determine how the subgrid-scale moments scale with respect to the parameters of interest. In particular, we are interested in characterizing the functional dependence of the required moments with respect to the forcing parameters (F and ω) and grid parameters (Δx and Δt).

ω						
	15	P	AP	AP	C	P
	10	P	AP	3P	2P	3P
	6.5	P	AP	P	C	C
	3.76	P	P	P	P	P
	1	P	P	P	P	P
		0^+	3	6	10	15
				F		

P	Periodic steady state
AP	Asymmetric periodic
NP	Period N-tupling
C	Chaotic

Table 4.4: Qualitative FRS solution behavior for the SS beam at discrete points in the forcing space $F \in (0, 15] \times \omega \in [1, 15]$ for which moments amongst $(\tau_i)_j^n$ and $(\tilde{u}_k)_p^m$ are obtained via direct calculation. The indicated values of F and ω serve as interpolation nodes for estimated moments.

In order to characterize the functional dependence of the moments with respect to the forcing parameters, FRS solutions are obtained for the twenty-five combinations of F and ω shown in Table 4.4. Each solution is evolved beyond 100 forcing cycles. Periodicity, asymmetry, period N-tupling and chaos are all observed. The required moments are then calculated for each FRS solution. We employ a local bilinear interpolation scheme to approximate the functional dependence of the moments with respect to the forcing parameters. The discrete values of F and ω in Table 4.4 serve as the interpolation nodes. Twelve of these moments, for example, are shown in Figures 4.20 and 4.21. Observe that the moments vary smoothly with respect to F and ω, which implies that the functional dependence can easily be characterized with a relatively small amount of FRS data. As with the Duffing oscillator, this finding is interesting, considering the variety of response types encountered for the beam.

In addition to the forcing parameters, interpolants are also used to characterize the functional dependence of the required moments with respect to the grid parameters (Δx and Δt). Grids within $\Delta x \in [5.0 \times 10^{-3}, 2.5 \times 10^{-1}]$ and $\Delta t \in [10^{-6}, 10^{-2}]$ are considered. Additional FRS solutions need not be obtained for this task; only the comb-type sampling filter needs to be modified. In this sense, developing model dependence for Δx and Δt is much simpler than F and ω. As shown in Figure 4.22, the required moments for $F = 10$ and $\omega = 3.76$ are easily characterized with respect

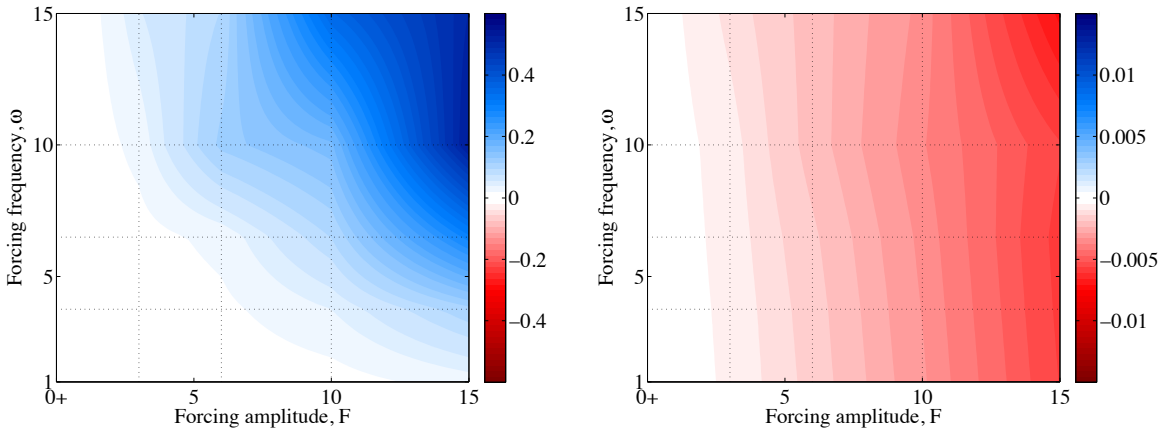

(a) $\left\langle (\tau_4)_j^n (\tilde{u}_4)_j^n \right\rangle$

(b) $\left\langle (\tau_4)_j^n (\tilde{u}_5)_j^n \right\rangle$

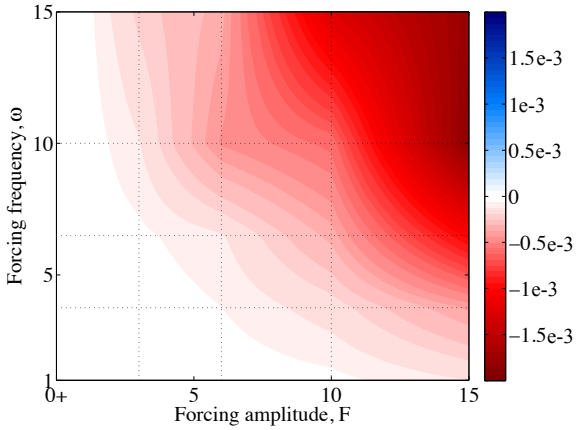

(c) $\left\langle (\tau_5)_j^n (\tilde{u}_4)_j^n \right\rangle$

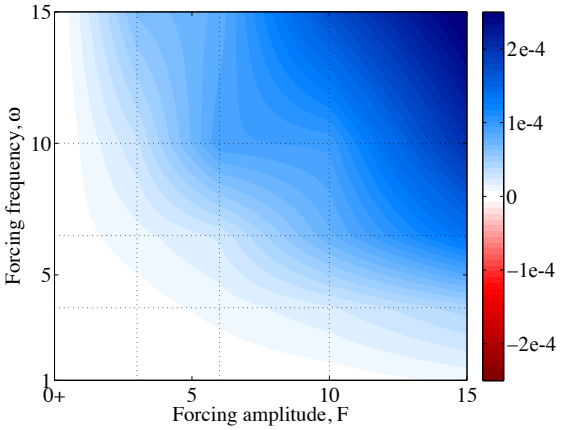

(d) $\left\langle (\tau_5)_j^n (\tilde{u}_5)_j^n \right\rangle$

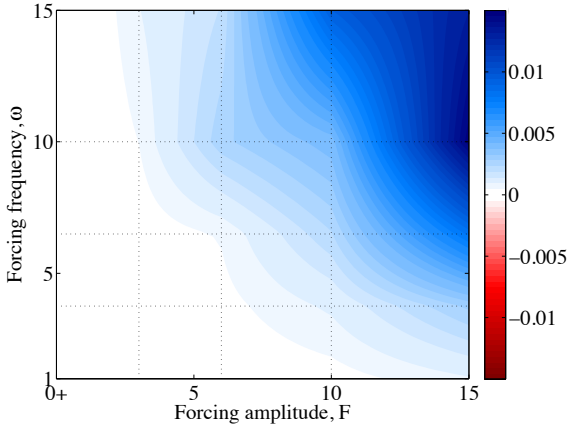

(e) $\left\langle (\tau_6)_j^n (\tilde{u}_4)_j^n \right\rangle$

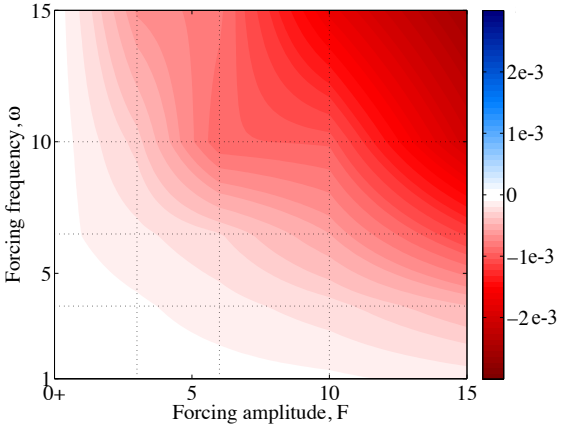

(f) $\left\langle (\tau_6)_j^n (\tilde{u}_5)_j^n \right\rangle$

Figure 4.20: Estimated moments amongst $(\tau_i)_j^n$ and $(\tilde{u}_k)_p^m$ for the SS beam on a two-state stencil ($M_S = 2$) in the forcing space $F \in (0, 15] \times \omega \in [1, 15]$. The FRS solutions are filtered with $\Delta x = 1.0 \times 10^{-1}$ and $\Delta t = 1.0 \times 10^{-2}$. A local bilinear interpolation scheme is used to model the moments with nodes at $F = \{0^+, 3, 6, 10, 15\}$ and $\omega = \{1, 3.76, 6.5, 10, 15\}$, indicated by the intersecting dotted lines.

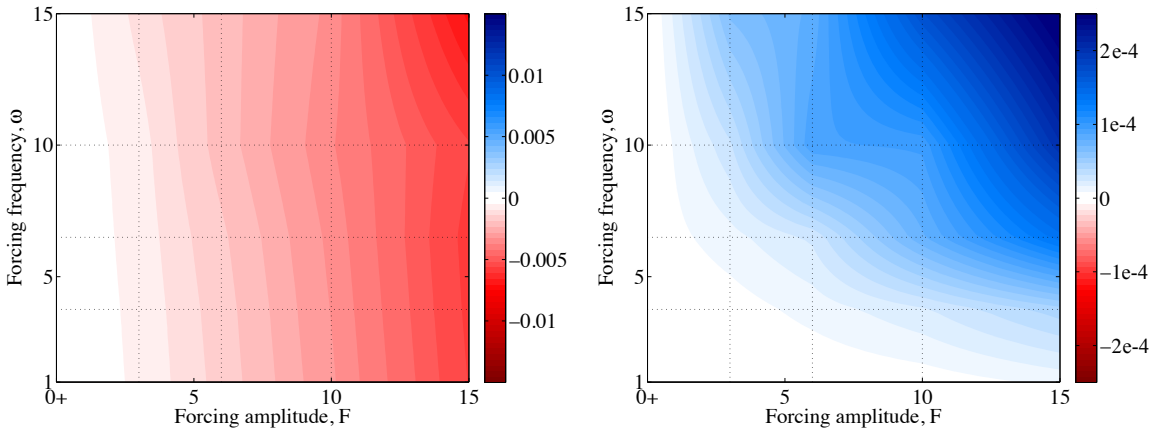

(a) $\left\langle (\tau_4)_j^n (\tilde{u}_5)_j^n \right\rangle$ (b) $\left\langle (\tau_5)_j^n (\tilde{u}_5)_j^n \right\rangle$

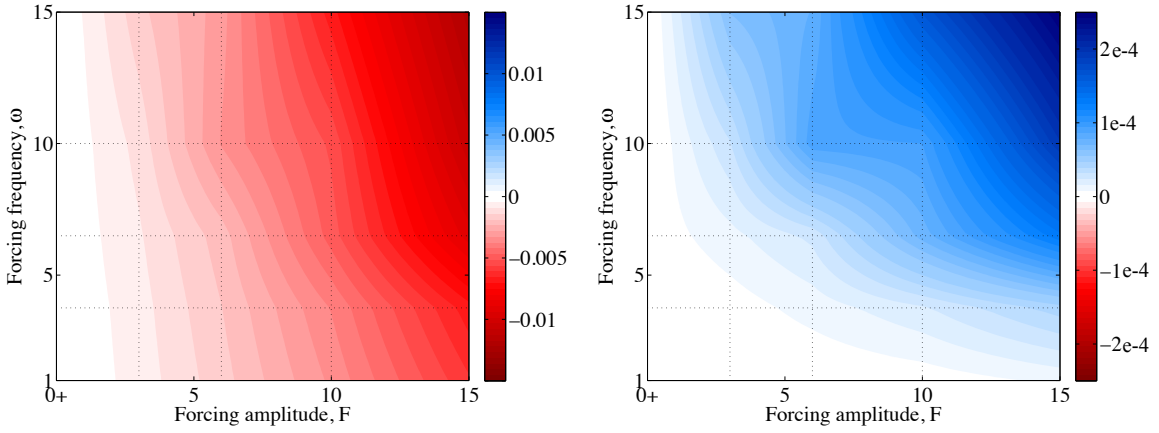

(c) $\left\langle (\tau_4)_j^n (\tilde{u}_5)_j^{n-1} \right\rangle$ (d) $\left\langle (\tau_5)_j^n (\tilde{u}_5)_j^{n-1} \right\rangle$

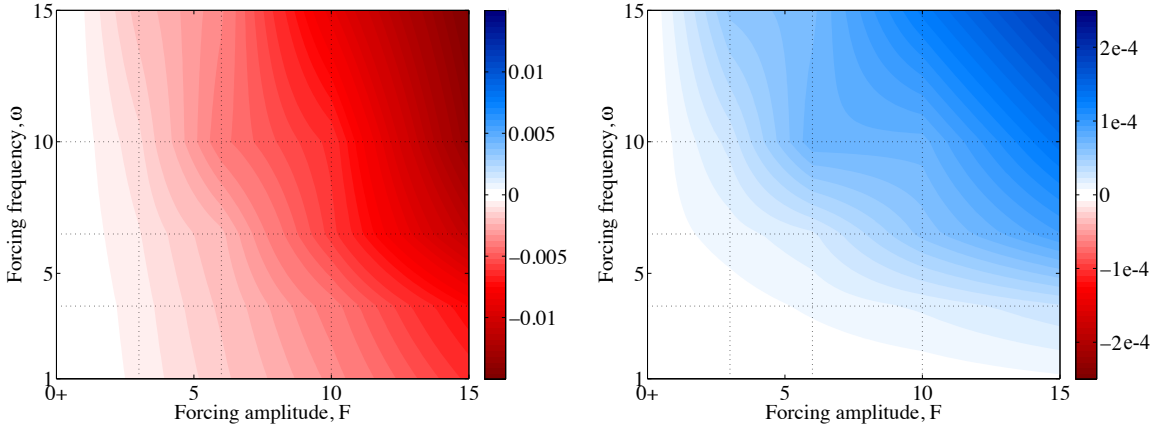

(e) $\left\langle (\tau_4)_j^n (\tilde{u}_5)_j^{n-2} \right\rangle$ (f) $\left\langle (\tau_5)_j^n (\tilde{u}_5)_j^{n-2} \right\rangle$

Figure 4.21: Estimated moments amongst $(\tau_i)_j^n$ and $(\tilde{u}_k)_p^m$ for the SS beam on a three-point temporal stencil ($M_T = 3$) in the forcing space $F \in (0, 15] \times \omega \in [1, 15]$. The moments are calculated with the same parameters as Figure 4.20.

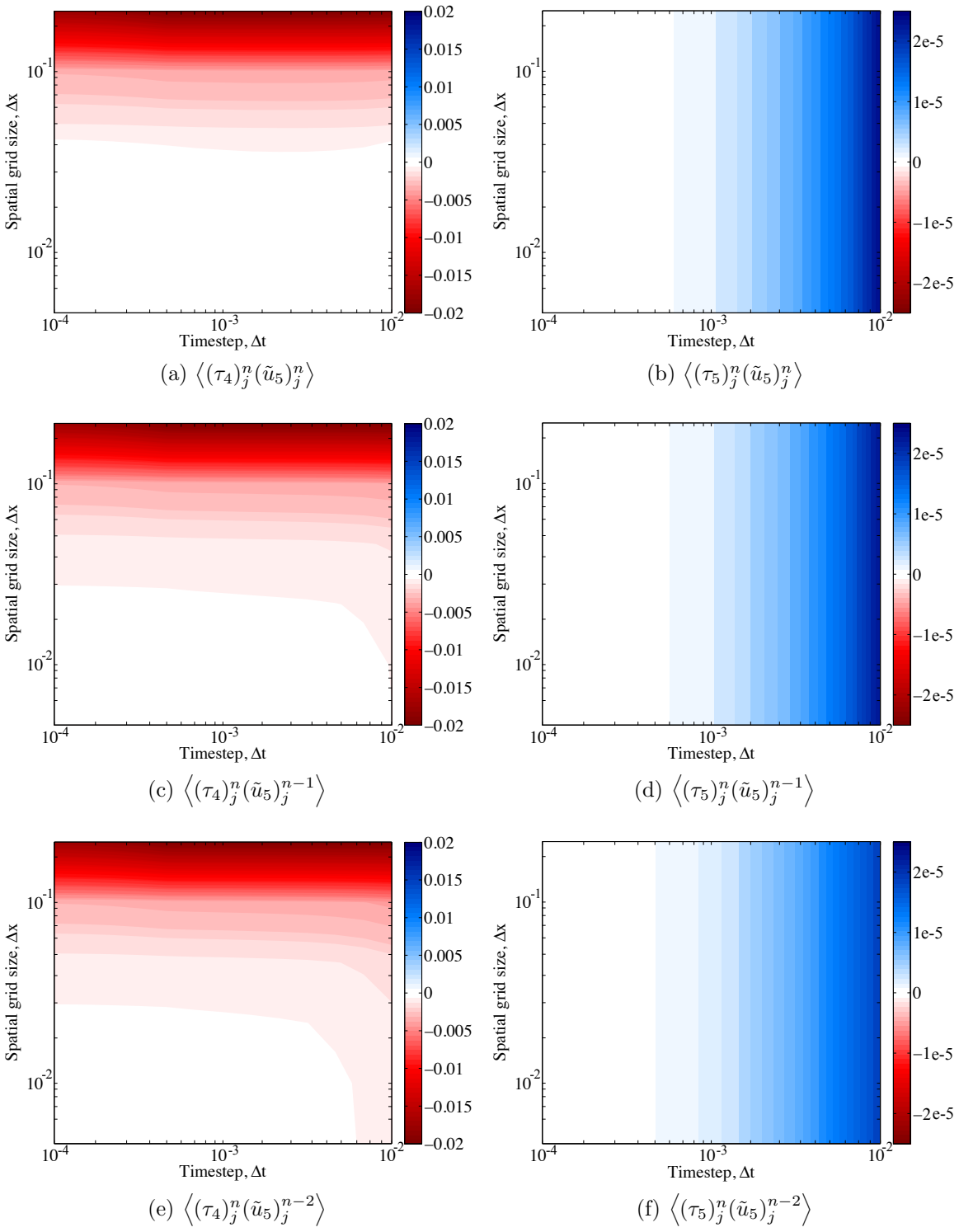

(a) $\left\langle (\tau_4)_j^n (\tilde{u}_5)_j^n \right\rangle$ (b) $\left\langle (\tau_5)_j^n (\tilde{u}_5)_j^n \right\rangle$

(c) $\left\langle (\tau_4)_j^n (\tilde{u}_5)_j^{n-1} \right\rangle$ (d) $\left\langle (\tau_5)_j^n (\tilde{u}_5)_j^{n-1} \right\rangle$

(e) $\left\langle (\tau_4)_j^n (\tilde{u}_5)_j^{n-2} \right\rangle$ (f) $\left\langle (\tau_5)_j^n (\tilde{u}_5)_j^{n-2} \right\rangle$

Figure 4.22: Estimated moments amongst $(\tau_i)_j^n$ and $(\tilde{u}_k)_p^m$ for the SS beam on a three-point temporal stencil ($M_T = 3$) with one state for an external forcing of $F = 10$ and $\omega = 3.76$ and various grids (Δx and Δt). Similar models are constructed for all forcing parameters in Table 4.4.

to the grid parameters. Similar results are computed for all FRS solutions shown in Table 4.4. Observe that moments for the subgrid-scale dynamics can be simplified in the following limiting cases: $\boldsymbol{\tau} \rightarrow \boldsymbol{\alpha}$ as $\Delta x \rightarrow \Delta x_{\text{FRS}}$ and $\boldsymbol{\tau} \rightarrow \boldsymbol{\gamma}$ as $\Delta t \rightarrow \Delta t_{\text{FRS}}$. Hence, the moments in Figure 4.22 can be used to construct subgrid-scale models for the OPTROM, OPSROM and OPSTROM variants.

With the subgrid-scale dynamics now characterized with respect to F, ω, Δx, and Δt for the SS set of BCs in (3.20), the next task is to explore the extent to which universality applies (if at all). Scaling and universality are in fact twin concepts [79]: the moments are either sensitive to a certain parameter, in which case the functional dependence could be characterized, or the moments are invariant, in which case the models are universal with respect to that parameter.

In our search for universality, we are looking for a lack of functional dependence in the subgrid-scale dynamics with respect to the BCs and the remaining physical parameters (Λ and ζ). Consider, for example, the CC set of BCs described in (3.21) and the CF set of BCs in (3.22). We compute FRS solutions for each of these BCs with an external forcing of $F = 10$ and $F = 8.5$ with $\omega = 3.76$. From the FRS solutions, a select number of temporal moments are compared in Figures 4.23 and 4.24. Based upon these moments, the subgrid-scale dynamics do in fact appear to be sensitive to the BCs. First observe the stronger correlations amongst $\boldsymbol{\tau}$ and $\mathbf{u}$ for the CC case. Also note the decreased sensitivity to the three-point temporal stencil for the CC and CF moments, which is evident by the narrower separation between the curves in Figures 4.23 and 4.24. These differences suggest that a subgrid-scale model developed for the SS beam may not be applicable to the CC and CF beams. A unique subgrid-scale model may be required for each set of BCs, and in this sense, the models are not universal with respect to the BCs.

Universality with respect to BCs is a common feature in the microscale dynamics of turbulent flows [79]. To help rationalize the observed lack of universality with

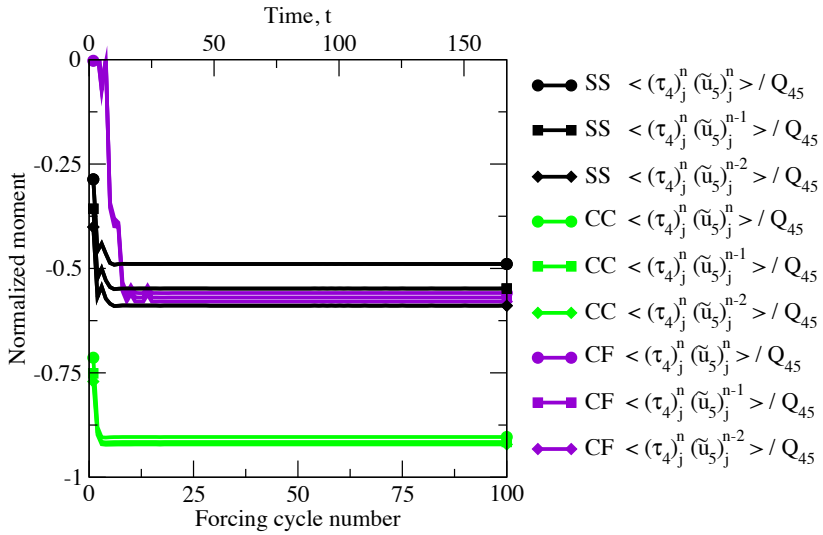

Figure 4.23: Temporal variation in moments amongst $(\tau_i)_j^n$ and $(\tilde{u}_k)_p^m$ for the SS, CC and CF beams on a three-point backward temporal stencil for an external forcing of $F = 10$ and $\omega = 3.76$. The response evolves to a periodic steady state for the SS, CC and CF boundary conditions. FRS solutions are filtered with $\Delta x = 1.0 \times 10^{-1}$ and $\Delta t = 1.0 \times 10^{-2}$. The mean operator $\langle \cdot \rangle$ is taken over the the entire spatial domain $x \in [0, 1]$ and one transient forcing cycle $t \in [t^n - 2\pi/\omega, t^n]$.

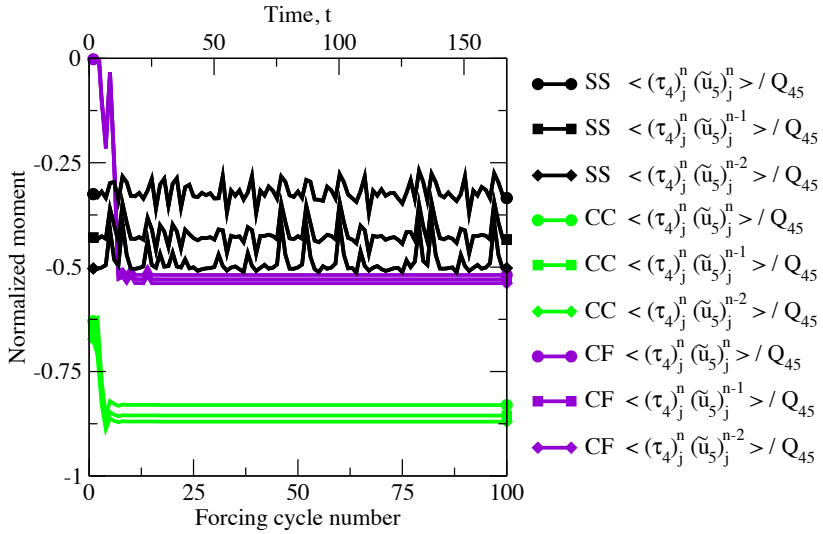

Figure 4.24: Temporal variation in select moments amongst $(\tau_i)_j^n$ and $(\tilde{u}_k)_p^m$ for the SS, CC and CF beams on a three-point backward temporal stencil for an external forcing of $F = 8.5$ and $\omega = 3.76$. The SS response is chaotic, whereas the CC and CF responses evolve to a periodic steady state. FRS solutions are filtered with $\Delta x = 1.0 \times 10^{-1}$ and $\Delta t = 1.0 \times 10^{-2}$. The mean operator $\langle \cdot \rangle$ is taken over the the entire spatial domain $x \in [0, 1]$ and one transient forcing cycle $t \in [t^n - 2\pi/\omega, t^n]$.

respect to BCs for this beam problem, turbulence has been described as a mechanism for the microscale dynamics to "forget" about the BCs through a loss of large-scale spatial correlation [116]. For this beam problem, however, only temporal chaos is observed. Spatial chaos (or weak turbulence [115, 116]) is not found for the range of parameters considered in this study. Without turbulence, and the subsequent loss of spatial correlation, we infer that the microscale structures may be sensitive to the BCs throughout the entire system.

Additional FRS simulations are computed in order to determine that the subgrid-scale dynamics are also sensitive to Λ and ζ. Besides the fixed values in (4.6), each of the moments amongst $\boldsymbol{\tau}$ and $\tilde{\mathbf{u}}$ are found to vary with respect to $\Lambda = \{10^5, 10^6, 10^7\}$ and $\zeta = \{0.01, 0.1\}$. Hence, the moments are not universal with respect to Λ and ζ, but if desired, empirical functions could also be constructed to estimate the moments as a function of these parameters. Such a task is outside the scope of this dissertation.

Accurate subgrid-scale models can be constructed efficiently with the knowledge we have learned about the subgrid-scale behavior of the nonlinear beam. Various choices can be made with regards to model construction, including the functional form of the model, the number of states, and the extent of support in space and time. As shown in Appendix E, the subgrid-scale models described in Table 4.5 provide the best combination of *a priori* and *a posteriori* error minimization and simplicity for this particular beam problem. Note the grid limitations in Table 4.5 for the OPTROM and OPSTROM variants: multi-point temporal models cannot be realized for a very small Δt. This is due in part to the subgrid-scale accelerations tending toward zero as the temporal resolution improves and also in part to the close proximity between neighboring timesteps. Hence, the difference between multi-point temporal moments approaches machine precision. Choosing instead a one-point stencil to avoid ill-conditioning does not improve predictions. This could in fact signal a diminishing need to model subgrid-scale accelerations.

Variant	Stochastic estimate	States	Grid limitations
OPSROM	$[M_S, M_N, M_T] = [2, 1, 1]$	$(u_4)_j^n$, $(u_5)_j^n$	None
OPTROM	$[M_S, M_N, M_T] = [1, 1, 3]$	$(u_5)_j^n$, $(u_5)_j^{n-1}$, $(u_5)_j^{n-2}$	$\Delta t \lesssim 5.0\times10^{-4}$ †
OPSTROM	$[M_S, M_N, M_T] = [1, 1, 3]$	$(u_5)_j^n$, $(u_5)_j^{n-1}$, $(u_5)_j^{n-2}$	$\Delta t \lesssim 5.0\times10^{-4}$ †

† Models are ill-conditioned as the moments amongst $(\tilde{u}_5)_j^n$, $(\tilde{u}_5)_j^{n-1}$ and $(\tilde{u}_5)_j^{n-2}$ become indistinguishable with double machine precision.

Table 4.5: Subgrid-scale models for the nonlinear beam with OPSROM, OPTROM and OPSTROM. For this particular beam problem, a linear stochastic estimate with homogeneous coefficients (in space and time) and the stencils above provides the best combination of accuracy and simplicity.

4.5 Summary of characterization of subgrid-scale dynamics

In this chapter, we characterized the subgrid-scale dynamics for the four nonlinear dynamical systems. With regards to the statistical moments required as inputs for model construction, we explored the extent to which the following properties are valid: spatial homogeneity, temporal homogeneity, ergodicity, scaling with respect to the system parameters, and universality. For all of the problems considered in this dissertation, temporal and ergodicity were found to be excellent assumptions for the purpose of model construction. For the canonical van der Pol and Duffing oscillators, the required statistical moments were also found to scale smoothly with respect to the system parameters. These observed properties enabled efficient construction of linear subgrid-scale models based upon estimated moments with multi-point temporal stencils. For the viscous Burgers flow, the required moments were found to be spatially dependent as the flow convected downstream. Smooth scaling was observed with respect to the Reynolds number and Strouhal number. For the (mass normalized) subgrid-scale forces, we selected a spatially heterogeneous quadratic model based upon estimated moments with a three-point spatial stencil, whereas for the subgrid-scale accelerations, we selected a spatially heterogeneous linear model based upon estimated

moments with a three-point temporal stencil. For the nonlinear beam problem, the required moments were found to be homogeneous in space to a large extent, with the exception of multi-point spatial moments. Smooth scaling was observed with respect to the external forcing and grid parameters. For the beam, we constructed spatially homogeneous linear models based upon estimated moments with a one-point spatial stencil and a three-point temporal stencil. The models were not found to be universal, however, with respect to the BCs for the chosen physical parameters, grid parameters, and nondimensionalization procedure. Therefore, unique subgrid-scale models were developed for the SS, CC and CF beam problems. The performance of all of these models will be tested in the following chapter.

CHAPTER 5

Performance of optimal reduced order models

In this chapter, we aim to determine which of the general ROM approaches described in Chapter 2 (standard ROM, OPTROM, OPSROM or OPSTROM) provide the best trade off between computational expense and accuracy for the nonlinear dynamical systems described in Chapter 3. We consider ROMs that are under-resolved in space (when applicable) and under-resolved in time (USUT), as illustrated in Figure 1.2. Several variants of the subgrid-scale models constructed in Chapter 4 will be tested to determine which ones are best for each problem. FRS solutions will be used as a baseline for comparison.

The canonical van der Pol and Duffing oscillators in Sections 5.1 and 5.2 contain time dependence only. As such, under-resolved simulations in time will be performed with the IE time-marching and HB time-spectral schemes. We denote standard ROM and OPTROM simulations with the IE scheme as IE and IE+OPTROM, respectively. The timestep Δt chosen for the IE scheme will be indicated in all figures. Standard ROM and OPTROM simulations with the HB scheme are denoted as HBN_H and HBN_H+OPTROM, where N_H indicates the number of harmonics retained.

The viscous Burgers flow and forced nonlinear beam problems to be studied in Sections 5.3 and 5.4 contain spatiotemporal dependence. USUT simulations for these problems will be performed with the BTCS scheme and a coarse spatiotemporal grid. Standard ROM, OPTROM, OPSROM and OPSTROM simulations are denoted as USUT, USUT+OPTROM, USUT+OPSROM and USUT+OPSTROM, respectively. The chosen spatial grid Δx and timestep Δt will be indicated in all figures.

Various tools and measures will be used to detect improvement in the OPTROM, OPSROM and OPSTROM solutions, including time history plots for displacement and velocity, snapshots of the spatial configuration, Poincaré maps, phase portraits, Fourier transformations for spatial and temporal spectra, bifurcation diagrams and Lyapunov exponents. Each of the *a posteriori* error measures defined in Section 2.10 will also be used when FRS data is available.

All simulations in this study are processed on a computer with a 2.6GHz central processing unit (CPU) and 4GB of random access memory (RAM). Absolute simulation times will be reported with respect to the processing time for this machine, measured in minutes, hours or days. For some problems, the simulation times will also be normalized by the time required to compute an equivalent FRS solution. We denote the normalized simulation times as $\mathcal{T}$.

5.1 Van der Pol oscillator results

For the autonomous van der Pol oscillator, all nonzero initial trajectories evolve to self-sustained LCOs. For each simulation, we specify the strength of the nonlinearity α and choose a coarse temporal grid (Δt or N_H). With the IE scheme, we specify nonzero ICs and evolve the system long enough for transients to decay. Equivalently, with the HB scheme, we provide an initial guess for the steady state LCO and drive the residual to zero. The quantities of interest for this problem are the displacement u_1, velocity u_2, and unknown frequency of oscillation ω. As described in Section 4.1, for the subgrid-scale models, we use a linear stochastic estimate with two states and a two-point temporal stencil.

5.1.1 Time-marching solutions

Time-marching solutions for a representative nonlinearity value ($\alpha = 10$) are shown in Figure 5.1 with a coarse timestep of $\Delta t = 10^{-2}$. When compared to the FRS result

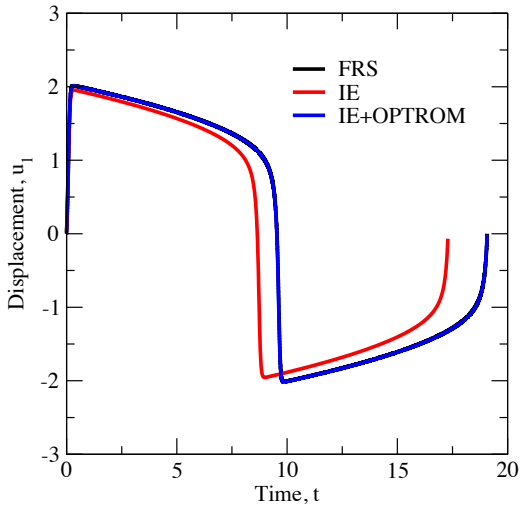

Figure 5.1: Time-marching solutions for displacement of the van der Pol oscillator with a fixed nonlinearity of $\alpha = 10$: FRS (black), standard IE with a coarse timestep of $\Delta t = 10^{-2}$ (red) and IE with OPTROM and $\Delta t = 10^{-2}$ (blue).

(RK4 with $\Delta t = 10^{-6}$), the standard IE solution under-predicts the displacement and velocity (not shown explicitly in Figure 5.1) and over-predicts the frequency of oscillation. However, when the subgrid-scale model is used during the simulation, the OPTROM solution is nearly identical to the FRS result. Hence, the subgrid-scale model has accomplished exactly what it was designed for: capturing the effects of the subgrid-scale dynamics on the coarse-grained solution.

The unknown frequency of oscillation is one of the most important features in the study of autonomous systems. LCO frequency curves for the van der Pol oscillator can be generated by plotting solutions for ω as a function of the nonlinearity. In Figure 5.2, we compare frequencies for $\alpha \in (0, 20]$ with increments of $\Delta\alpha = 0.1$. The standard IE solutions with $\Delta t = 10^{-2}$ over-predict the frequency for all α, whereas the OPTROM solutions are consistently accurate. It should be noted that the unknown frequency of oscillation is not explicitly solved for in the IE equations. In other words, the subgrid-scale model was designed to improve the evolution of u_1 and u_2, not ω. Improvement in the frequency is an indirect result of predicting the resolved states more accurately. Moreover, the consistent comb-type sampling filter used to

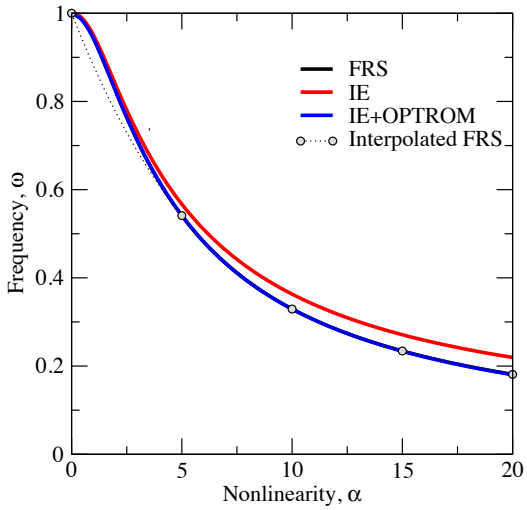

Figure 5.2: Time-marching solutions for the fundamental frequency of the van der Pol oscillator versus the nonlinearity $\alpha \in (0, 20]$: FRS (black), interpolated FRS with a fourth-order Lagrange polynomial (dotted), standard IE with a coarse timestep of $\Delta t = 10^{-2}$ (red) and IE with OPTROM and $\Delta t = 10^{-2}$ (blue).

derive the subgrid-scale model implicitly assumes that the frequencies of the FRS and OPTROM solutions are identical. The FRS and OPTROM frequencies in Figure 5.2 are in fact close but not identical. Despite the frequencies being incommensurate, we deduce that the comb-type filtering operation need not be modified.

It is worth mentioning here that as an alternative to OPTROM, one could choose to interpolate FRS solutions. We test this idea by interpolating the FRS solutions for ω with the same basis functions used to estimate the moments in Section 4.1, i.e. a fourth-order Lagrange polynomial with nodes at $\alpha = \{0^+, 5, 10, 15, 20\}$. The interpolated FRS frequencies, shown in Figure 5.2, are actually less accurate than the OPTROM results. The analyst could also interpolate FRS solutions for $u_1(t)$ and $u_2(t)$, but this would prove to be a more difficult and less profitable task. These findings support our preference for the OPTROM approach.

Frequency and displacement errors for the IE solutions with $\Delta t = 10^{-2}$ are shown in Figure 5.3. Including the subgrid-scale model in the governing equations reduces the errors by roughly two orders of magnitude for large α. There are two instances

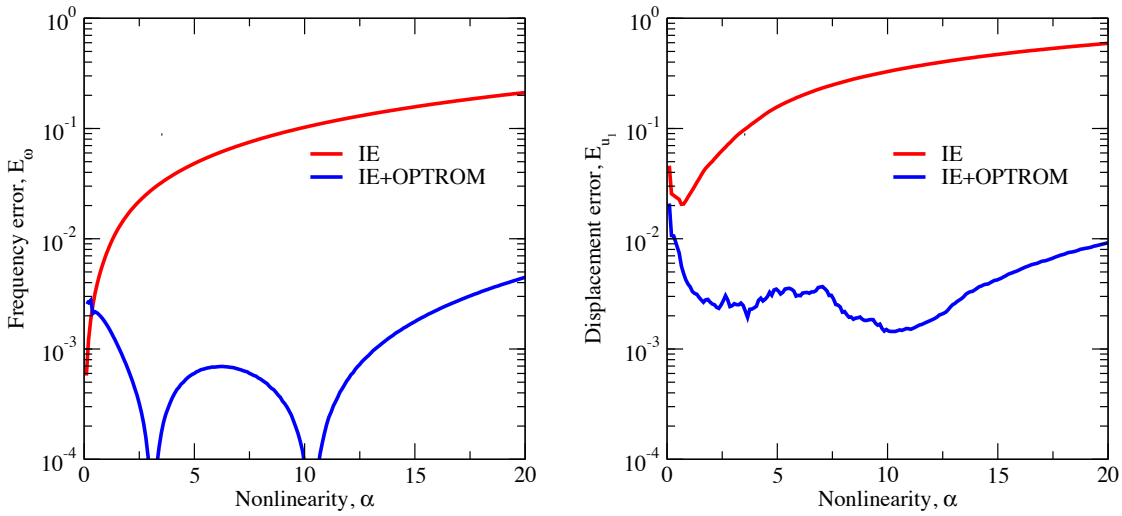

(a) Frequency errors

(b) Displacement errors

Figure 5.3: Errors for the van der Pol oscillator versus the nonlinearity $\alpha \in (0, 20]$: standard IE scheme with a coarse timestep of $\Delta t = 10^{-2}$ (red) and IE with OPTROM and $\Delta t = 10^{-2}$ (blue).

in which the frequency error E_ω for the OPTROM scheme is fortuitously zero. This does not occur at the interpolation nodes used to estimate the moments, i.e., the subgrid-scale model is not exact.

Recall that the subgrid-scale models for the IE scheme were developed in Section 4.1 as bivariate functions of α and Δt. Now we investigate the performance of the models by computing a large set of IE solutions for $\alpha \in (0, 20]$ with increments of 0.1 and $\Delta t \in [10^{-3}, 10^{-1}]$ with increments of 10^{-3}. Contours for the frequency and displacement errors are shown in Figures 5.4 and 5.5 on the same scale. Errors for the standard IE solutions are greatest for large α and Δt. This is also when the greatest error reduction occurs with OPTROM. Therefore, the subgrid-scale models are most needed, and most effective, when a coarse-grid is used and the nonlinearity is large.

The blank regions marked with a $*$ in Figures 5.4 and 5.5 indicate that the NR scheme, which is used to solve the IE equations at every timestep, failed to converge for that particular combination of α and Δt. Observe that the subgrid-scale models somewhat improve the convergence of the NR scheme: the size of the non-convergent

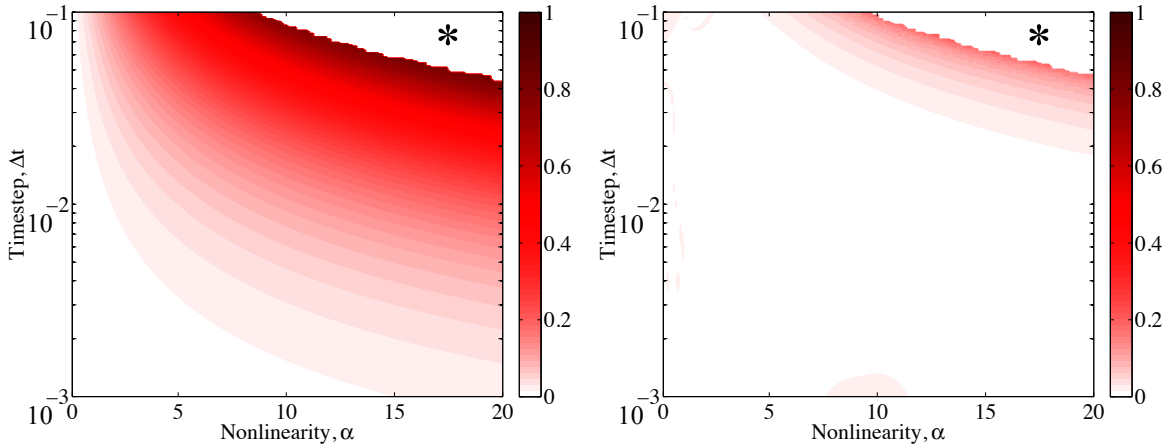

(a) IE (b) IE+OPTROM

Figure 5.4: Frequency error contours for the van der Pol oscillator with the IE time-marching scheme. The blank region marked with a $*$ indicates that the NR scheme (used to solve the IE equations at each timestep) failed to converge for the chosen parameters.

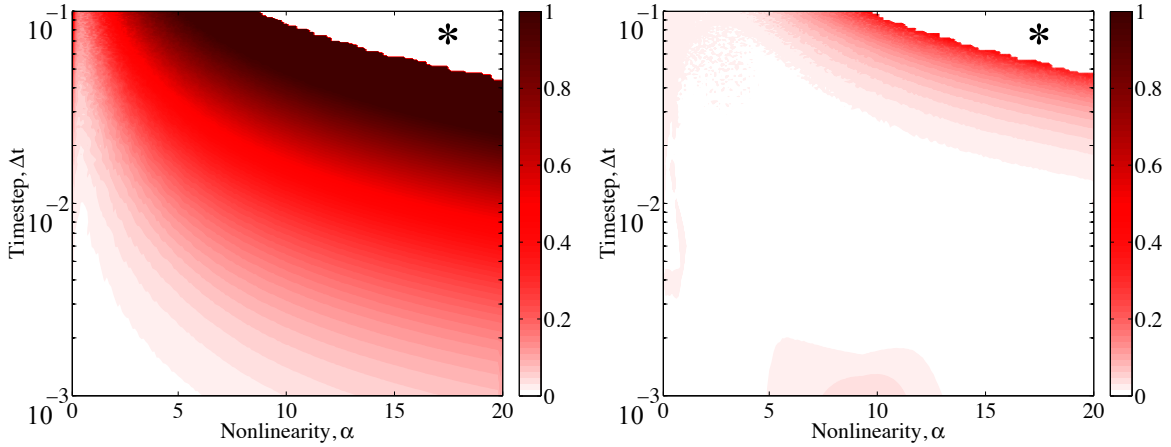

(a) IE (b) IE+OPTROM

Figure 5.5: Displacement error contours for the van der Pol oscillator with the IE time-marching scheme. The blank region marked with a $*$ indicates that the NR scheme (used to solve the IE equations at each timestep) failed to converge for the chosen parameters.

regions in Figures 5.4 and 5.5 are slightly decreased and the average number of NR iterations required for convergence (not shown) are reduced. While this particular observation of improved convergence for the IE scheme is quite encouraging, it should not be considered a generalization for all time-marching schemes.

5.1.2 Time-spectral solutions

The number of harmonics to be retained in the HB scheme is left to the analyst. Recall from Figure 4.1b that the even harmonic amplitudes are effectively zero for the van der Pol oscillator. For this reason, an odd number of harmonics will be retained. Only a small number of harmonics are required for a coarse-grained solution, and in this sense, the HB approach may be considered a computationally efficient alternative to time-marching. However, the accuracy is somewhat limited due to the assumed Fourier mode shapes. When a high fidelity solution is desired, a large number of harmonics may be required, in which case it can become more economical to evolve the system to a steady state solution with a time-marching scheme.

Reduced order HB solutions (HB1, HB3 and HB5) are shown in Figure 5.6 for a representative nonlinearity value of $\alpha = 10$. Observe that the standard HB results are unreliable, primarily due to the erroneous frequencies. When the subgrid-scale models are included in the governing equations, significant improvement can be seen in the HB+OPTROM solutions.

The HB1+OPTROM solution in Figure 5.6 is exact with respect to the frequency and first mode of the FRS solution. This result occurs for two reasons: First, the direct subgrid-scale model for HB1 is exact (contains zero *a priori* error as shown in Appendix C). Second, the models based upon estimated moments use $\alpha = 10$ as an interpolation node. The HB3+OPTROM and HB5+OPTROM solutions for displacement may be considered more accurate overall than HB1+OPTROM due to the increased number of modes, but the first modes and frequencies are not exact.

HB solutions for the frequency are compared in Figure 5.7 for all $\alpha \in (0, 20]$. The standard HB1 scheme incorrectly renders the linear solution ($\omega = 1$) regardless of the nonlinearity. When more harmonics are retained and the nonlinearity is small, the standard HB scheme provides fairly accurate solutions for the frequency. As the nonlinearity increases, however, the standard HB frequencies diverge from the

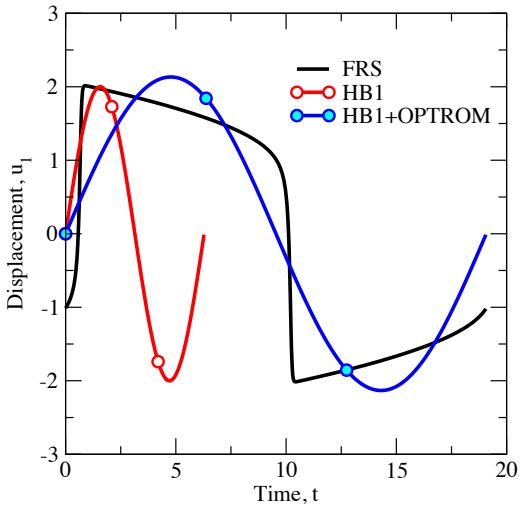

(a) One harmonic

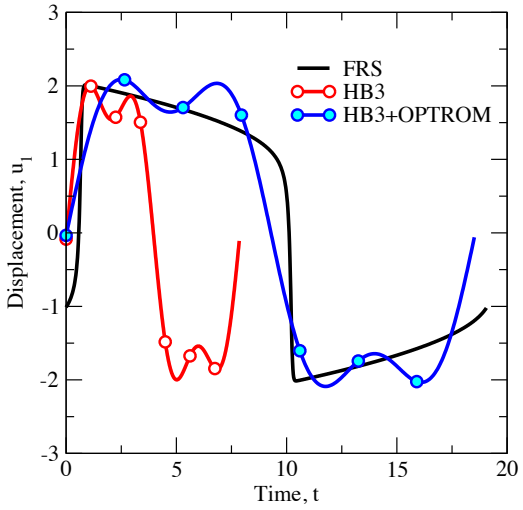

(b) Three harmonics

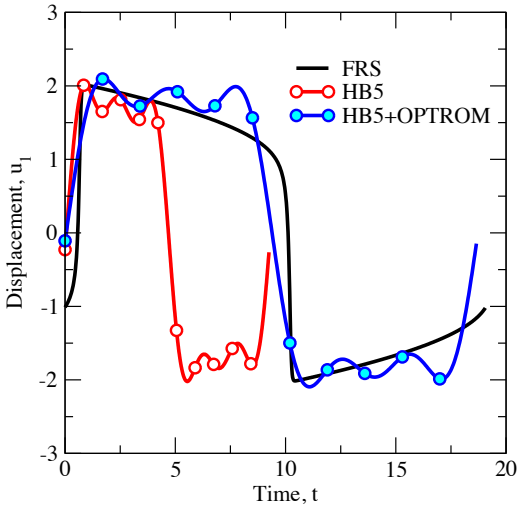

(c) Five harmonics

Figure 5.6: Harmonic balance (and FRS) solutions for displacement of the van der Pol oscillator with a fixed nonlinearity of $\alpha = 10$: standard HB (red) and HB with OPTROM (blue). The choice of N_H harmonics corresponds to $N_T = 2N_H + 1$ evenly spaced timesteps (dots) for one steady state period.

FRS result and asymptotically approach some irrational number. Also shown in Figure 5.7, the frequencies improve when the subgrid-scale models are included in the simulations. The HB1+OPTROM solutions for ω are exact at the model interpolation nodes ($\alpha = \{0^+, 5, 10, 15, 20\}$) and very close to the FRS result everywhere else.

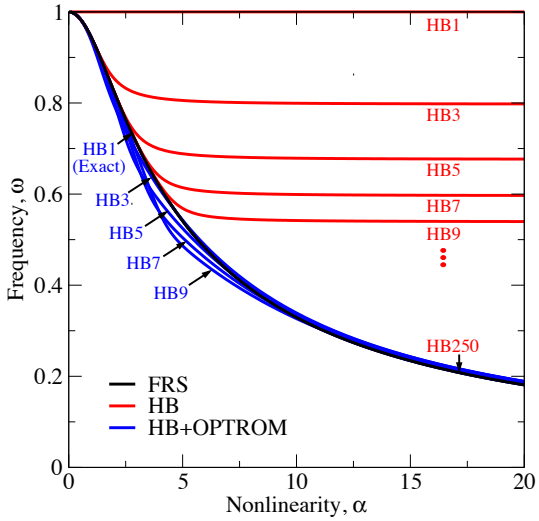

Figure 5.7: Harmonic balance solutions for the fundamental frequency of the van der Pol oscillator versus the nonlinearity $\alpha \in (0, 20]$: FRS (black), standard HB (red) and HB with OPTROM (blue). The HB1+OPTROM frequencies are exact with respect to the FRS at the Lagrange interpolation nodes (where the direct model is exact).

Frequency and displacement errors for the HB solutions are shown in Figure 5.8. When the nonlinearity is very small, the standard HB scheme is quite reliable when several harmonics are retained. As α increases, however, the standard HB scheme suffers from large errors. Including the subgrid-scale models in the simulations reduces the frequency errors E_ω by about two orders of magnitude and the displacement errors E_{u_1} by nearly one order of magnitude. The error reduction in Figure 5.8 indicates that subgrid-scale models are most needed, and most effective, with the HB scheme when the system is highly nonlinear.

5.1.3 Summary of results for the van der Pol oscillator

The autonomous van der Pol oscillator served as a testbed for OPTROM with the IE time-marching and HB time-spectral schemes. For large nonlinearities, the standard IE and HB schemes proved to be unreliable as large errors occurred in the displacement and fundamental frequency of oscillation. However, when the subgrid-scale models were included in the simulations, *a posteriori* errors for the solutions were

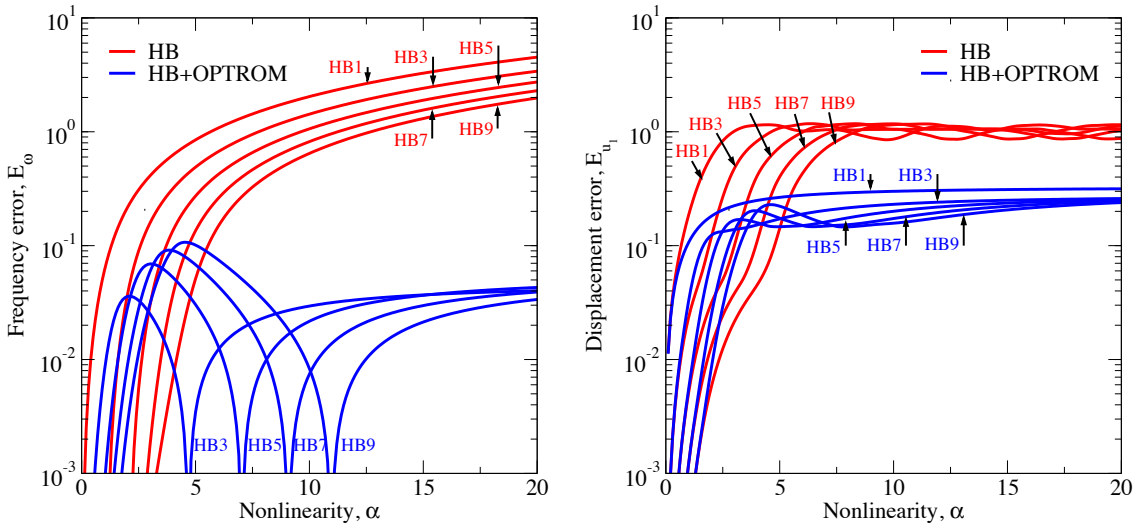

(a) Frequency errors

(b) Displacement errors

Figure 5.8: Frequency and displacement errors for the van der Pol oscillator versus the nonlinearity $\alpha \in (0, 20]$: standard HB (red) and HB with OPTROM (blue). The frequency errors for HB1+OPTROM (not shown due to scale) are zero at the model interpolation nodes.

reduced by one to two orders of magnitude. Despite not being taken into account when developing the subgrid-scale models, the greatest error reduction occurred in solutions for the unknown frequency of oscillation. This improvement is believed to be an indirect result of predicting the resolved states (displacement and velocity) more accurately. As expected from the analysis in Appendix C, OPTROM solutions with the HB scheme were exact (produced first mode of FRS) with one harmonic retained.

5.2 Duffing oscillator results

Depending on the selected physical parameters (F, ω and ζ), the Duffing oscillator may undergo regular or chaotic response types, as shown in Table 4.1. The robust IE time-marching scheme will be used to explore the entire forcing parameter space defined in (4.4). Only for regular response types is the Duffing oscillator well-suited for HB analysis. As such, we use the HB time-spectral scheme to explore a much smaller forcing parameter space for which we expect the response to be time-periodic.

5.2.1 Time-marching solutions

Time marching solutions for the response are compared in Figures 5.9 and 5.10 for two sets of forcing parameters with various resolutions. The FRS solutions (RK4 with $\Delta t = 10^{-6}$) are assumed to be exact, whereas the coarse IE results (both standard and OPTROM with $M_S = 2$ and $M_T = 2$) contain errors, but are faster to compute by several orders of magnitude. Several types of plots for these two quantities are shown in Figures 5.9 and 5.10, including the time histories for displacement and velocity, phase portraits, uniform sampling Poincaré maps, zero velocity Poincaré maps, and temporal spectra obtained by discrete Fourier transformation. The uniform sampling Poincaré maps record the values of displacement and velocity at the beginning of each forcing cycle, and are useful in detecting chaos and period N-tupling sequences. The zero velocity Poincaré maps record the configurations for which the system experiences zero velocity, and are useful in detecting the development of high frequency content.

Considered first in Figure 5.9 are symmetric time-periodic solutions for an external forcing of $F = 125$ and $\omega = 1.25$. IE results (standard and OPTROM) are calculated with a coarse timestep of $\Delta t = 10^{-2}$. The system is driven from its equilibrium position at $t = 0$ and transients are allowed to decay as each solution is evolved beyond 100 forcing cycles. Observe in the time history plots (Figures 5.9a and 5.9b) and phase portrait (Figure 5.9f) that OPTROM significantly improves predictions for the transverse displacement and velocity. This improvement can be seen more clearly in the Poincaré maps (Figures 5.9c and 5.9d), where the OPTROM results are three times closer to the FRS. Note that the finite number of points in the Poincaré sections is a signature feature of periodicity. Improvement in the Poincaré maps is primarily due to the ability OPTROM to resolve more accurately a wide range of time scales, such as the 9^{th} and 17^{th} modes of the temporal spectra (Figure 5.9e).

In addition to regular solutions, OPTROM can also improve predictions for chaotic response types. Figure 5.10 shows a chaotic FRS solution for an external forcing of

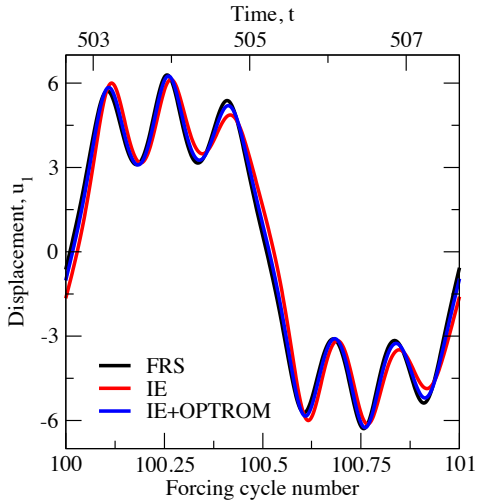

(a) Displacement time history

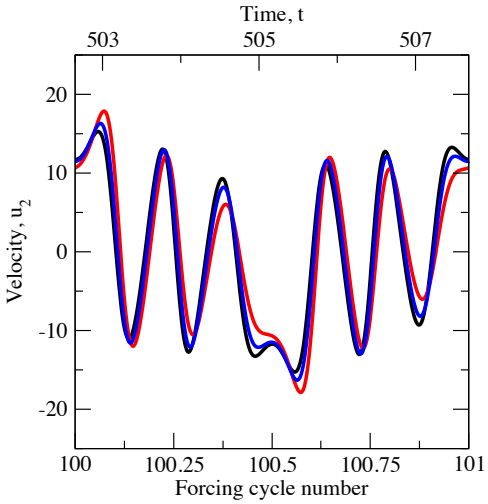

(b) Velocity time history

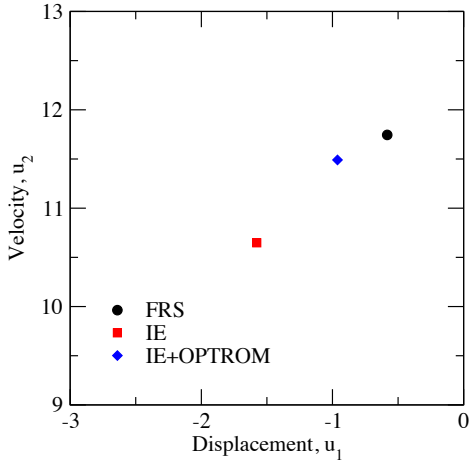

(c) Uniform sampling Poincaré map

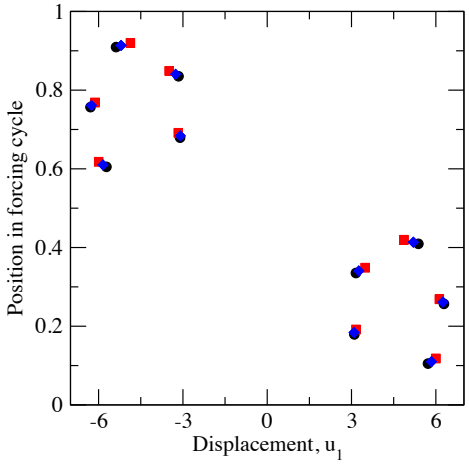

(d) Zero velocity Poincaré map

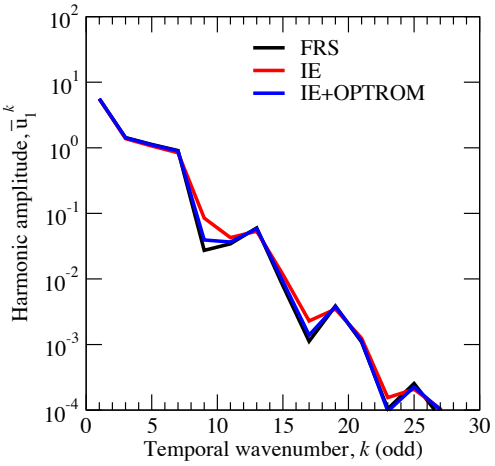

(e) Temporal spectra

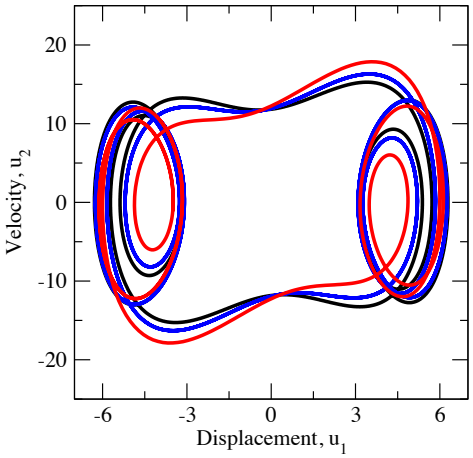

(f) Phase portrait

Figure 5.9: FRS, standard IE and OPTROM solutions for the Duffing oscillator with an external forcing of $F = 125$ and $\omega = 1.25$. ROM solutions are obtained using the IE scheme with a coarse timestep of $\Delta t = 10^{-2}$.

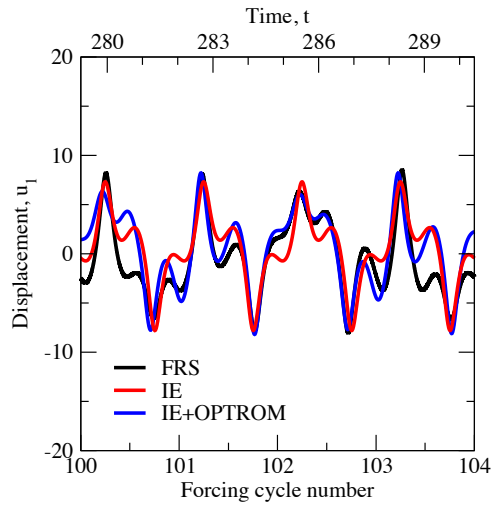

(a) Displacement time history

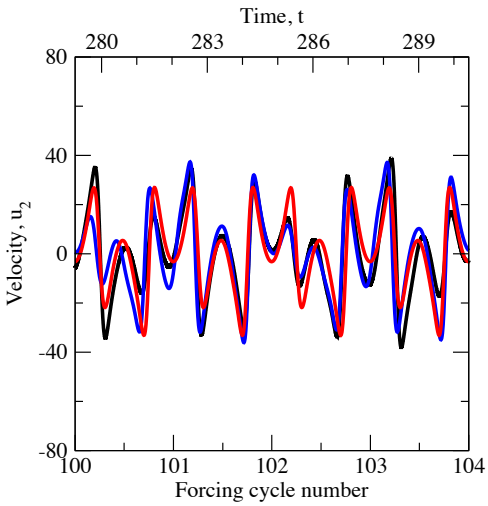

(b) Velocity time history

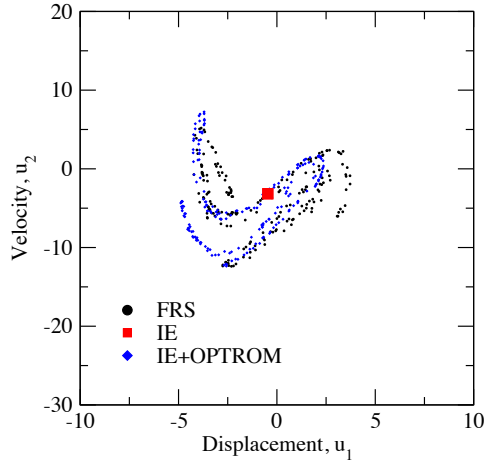

(c) Uniform sampling Poincaré map

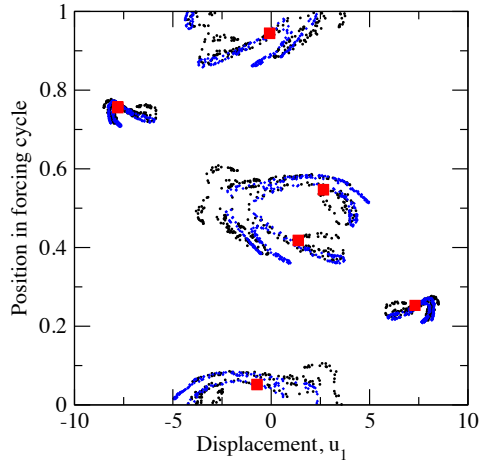

(d) Zero velocity Poincaré map

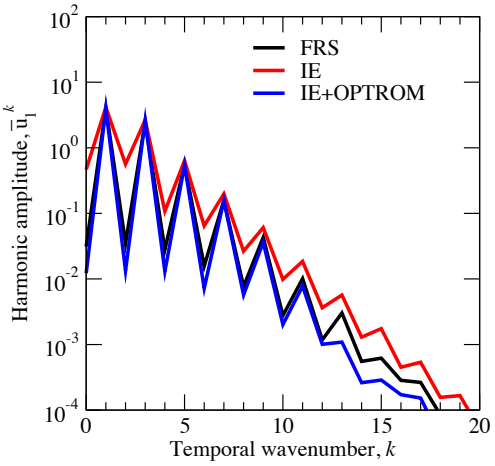

(e) Temporal spectra

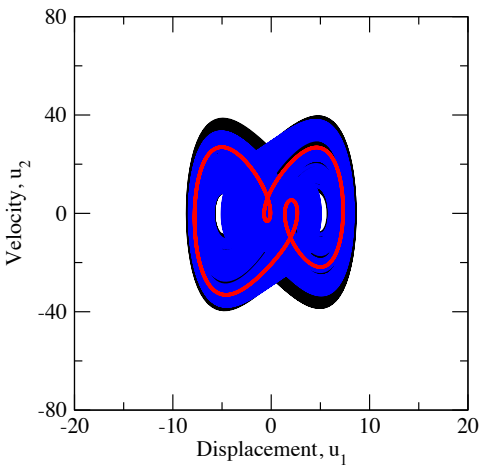

(f) Phase portrait

Figure 5.10: FRS, standard IE and OPTROM solutions for the Duffing oscillator with an external forcing of $F = 125$ and $\omega = 2.25$. ROM solutions are obtained using the IE scheme with a coarse timestep of $\Delta t = 10^{-2}$.

$F = 10$ and $\omega = 15$ alongside IE results (standard and OPTROM). Most notably, observe that the OPTROM solution is rightfully chaotic, whereas the standard IE result is artificially periodic and asymmetric. As the system evolves, orbits for the FRS and OPTROM solutions completely cover subsets of the phase plane, which is one of the classic signs of chaos. No two trajectories are exactly alike, and an infinite number of points are possible within certain sections of the Poincaré maps. The standard IE scheme, however, falsely produces only six points of zero velocity and returns to the same state at the beginning of each forcing cycle. The FRS and OPTROM spectra are in excellent agreement, whereas the even IE spectra are over-predicted due to the asymmetric periodic response.

5.2.2 Lyapunov exponents

Our next task is to determine for a large forcing parameter space when the Duffing oscillator will undergo stable oscillations (regularity) or unstable oscillations (chaos) as it evolves. There is, however, no universally accepted definition for chaos. For practical matters, we defer to the widely accepted definition of chaos [1] as long-term aperiodic behavior in a deterministic system that exhibits sensitive dependence to initial conditions. To this end, Lyapunov exponents have been used extensively throughout the literature [1] to discriminate between regular and chaotic response types. A variety of numerical methods have been developed to calculate Lyapunov exponents for both discrete and continuous nonlinear dynamical systems [117].

We consider the fate of two infinitesimally close phase trajectories. As the system evolves in time, the trajectories will either coalesce (an indication of regularity) or diverge (an indication of chaos) at an exponential rate. This rate of convergence or divergence is known as the Lyapunov exponent, λ, where

$$\|\delta_i(t)\| \cong \|\delta_i^0\| e^{\lambda t} \tag{5.1}$$

and $(\delta_i)_j(t)$ are the infinitesimal separations for each state. In this work, we compute the local Lyapunov exponents (local in phase space) for displacement by following two infinitesimally close trajectories for ten forcing cycles. A total of three simulations are required for each λ computation: First we perform a simulation in which transients are driven out of the system as it evolves to a nearby basin of attraction. Then we perform a nominal simulation in which the system is driven for ten forcing cycles with initial conditions on the basin of attraction, followed by a perturbed simulation in which the initial conditions for displacement are perturbed by $\delta_1^0 = 10^{-9}$. A linear least squares curve fit is then used to approximate the exponential rate of separation in (5.1). While it is typical to consider the maximal Lyapunov exponent [117] when predicting chaos for a high dimensional system, here we focus on the local Lyapunov exponents for displacement. We ignore the exponents for velocity as they typically share the same sign with those for displacement in a long-term sense [118].

A negative Lyapunov exponent ($\lambda < 0$) is a strong indication of regularity, whereas a positive exponent ($\lambda > 0$) is a sign of (but does not guarantee) chaos. For certain system parameters and ICs, it may be possible for a trajectory to undergo transient chaos [119] or intermittency before eventually reaching one of many regular orbits, in which case the Lyapunov exponents may be positive in the short-term, whereas the long-term behavior of the system may be regular.

For the Duffing oscillator, we aim to determine which combinations of F and ω produce regular or chaotic behavior. A large solution space needs to be explored, and it is not feasible to obtain FRS solutions for every simulation. Instead, we employ the efficient IE scheme (standard and OPTROM) with various timesteps. To provide a baseline for comparison, we also compute the exponents with the highly accurate RK4 scheme with a timestep of $\Delta t = 10^{-4}$. The RK4 results, shown in Figure 5.11, indicate that the majority of the forcing parameter space (about 82%) is dominated by regular behavior, whereas the remainder (about 18%) is populated with concentrated

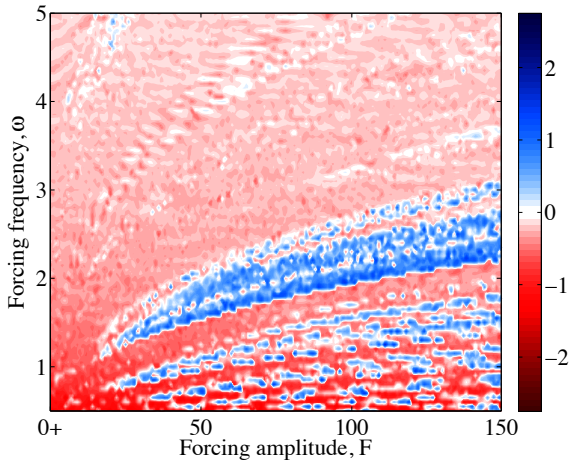

Figure 5.11: Highly resolved Lyapunov exponent map for the Duffing oscillator in the forcing parameter space $F \in (0, 150] \times \omega \in [0.5, 5.0]$ with increments $\Delta F = 1$ and $\Delta\omega = 0.05$. A total of 13,741 simulations are shown. Solutions are calculated with the RK4 scheme with $\Delta t = 10^{-4}$. Regions of blue indicate chaos whereas regions of red indicate regularity.

regions of chaos. Such maps have been aptly described in the nonlinear dynamics literature [118] as self-similar "islands of chaos" embedded in large "seas of regularity". In general, but not without exception, the Lyapunov exponents of largest magnitude (both positive and negative) live in the lower frequency space.

Given the computational resources allocated for this study, the RK4 results in Figure 5.11 required 107 hours of simulation time. Fully resolved simulations with a timestep of $\Delta t = 10^{-6}$ would require more than a year to compute. As shown in Figure 5.12 and Table 5.5, similar results can be obtained orders of magnitude faster with the IE schemes (standard and OPTROM) with a coarse timestep.

The standard IE results in Figures 5.12a, 5.12c and 5.12e suggest that the islands of chaos tend to disappear as the timestep is coarsened. We infer this result is due to increased numerical damping, which impedes the development of higher temporal modes. Previous research [97] has found that increased physical damping also tends to decrease the likelihood of a chaotic response.

Results for the IE scheme with OPTROM in Figures 5.12b, 5.12d and 5.12f indicate that the subgrid-scale models significantly improve the accuracy of predictions

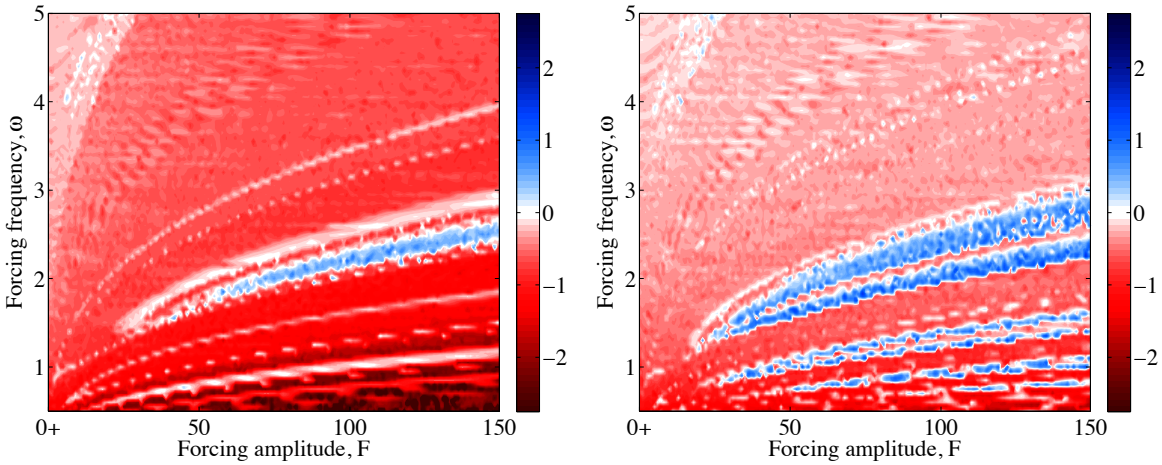

(a) IE with $\Delta t = 10^{-2}$

(b) OPTROM with $\Delta t = 10^{-2}$

(c) IE with $\Delta t = 10^{-3}$

(d) OPTROM with $\Delta t = 10^{-3}$

(e) IE with $\Delta t = 10^{-4}$

(f) OPTROM with $\Delta t = 10^{-4}$

Figure 5.12: Coarse Lyapunov exponent maps for the Duffing oscillator in the forcing parameter space $F \in (0, 150] \times \omega \in [0.5, 5.0]$ with increments $\Delta F = 1$ and $\Delta\omega = 0.05$. A total of 13,741 simulations are shown in each map.

Timestep	RK4	IE	OPTROM
$\Delta t = 10^{-2}$	—	2.7	3.2
$\Delta t = 10^{-3}$	—	26.1	28.2
$\Delta t = 10^{-4}$	107.2	215.4	221.3

Table 5.1: Computation times (in terms of hours of CPU time) required to produce the Lyapunov exponents for the Duffing oscillator in Figures 5.11 and 5.12.

Timestep	RK4	IE	OPTROM
$\Delta t = 10^{-2}$	—	3.44%	13.00%
$\Delta t = 10^{-3}$	—	14.10%	14.95%
$\Delta t = 10^{-4}$	17.78%	17.49%	17.71%

Table 5.2: Percentage of the $F \times \omega$ forcing parameter space for which the Lyapunov exponents for the Duffing oscillator are positive in Figures 5.11 and 5.12.

for the Lyapunov exponents. Fewer regions of artificial regularity occur, as shown for a representative set of forcing parameters in Figure 5.10. This improved accuracy is quantified in Table 5.2, where we record the percentage of the forcing parameter space for which the exponents are positive. With a coarse timestep of $\Delta t = 10^{-2}$, the IE scheme with OPTROM predicts 13% of the space to be chaotic in contrast to 3% with the standard IE scheme.

5.2.3 Time-spectral solutions

In this section, HB time-spectral solutions (standard and OPTROM) will be compared to the FRS results in Fourier space. We first consider solutions for a fixed forcing amplitude of $F = 1.25$ with various forcing frequencies within the range $\omega \in (0, 2.40]$. A frequency marching procedure will be used to generate solution branches for the harmonic amplitudes below the resonant frequency, which are commonly referred to throughout the literature as backbone curves [1, 96]. With the frequency marching procedure, the forcing amplitude is fixed, the frequency is incrementally advanced

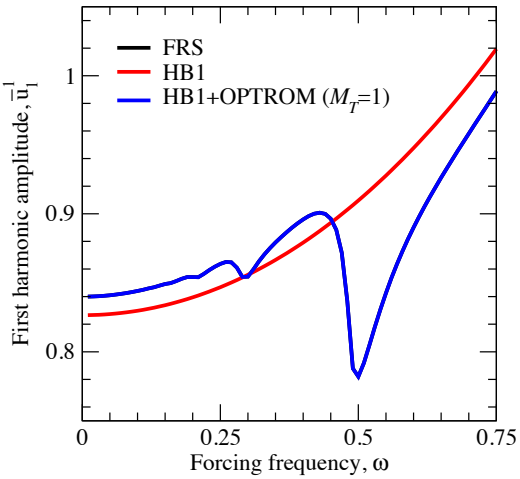

Figure 5.13: HB1 solutions for the Duffing oscillator generated by frequency marching with a fixed forcing amplitude of $F = 1.25$: FRS (black), standard HB1 (red), and HB1 with OPTROM (blue).

forward or backward, and the solution from the previous simulation is used as the initial guess for the NR solver. Backbone curves are produced by extracting the harmonic amplitudes from each solution. Only the odd harmonic amplitudes will be presented since the even (and zero$^{\text{th}}$) harmonics are effectively zero for this problem.

HB1 solutions for the first harmonic amplitude $\bar{u}_1^1$ are shown in Figure 5.13. First note that the FRS solution for $\bar{u}_1^1$ contains what appear to be a number of resonant structures below the natural frequency ($\omega = 1$ for the linearized system and $\omega = 2.40$ for the nonlinear system). These structures are referred to throughout the literature as undertones or subharmonics and are known to be rich in spectral content [96]. Next, observe that the standard HB1 scheme is incapable of picking up any subharmonic structures. When the direct subgrid-scale model is included in the HB1 simulation, the solutions for $\bar{u}_1^1$ are identical to the FRS result. Recall from Section 4.2 that the subgrid-scale model developed for the HB1 scheme is exact (contains zero *a priori* error as shown in Appendix C), and is based upon a linear stochastic estimate with two states ($M_S = 2$) and a one-point temporal stencil ($M_T = 1$). Multi-point temporal stencils are not realizable for HB1 as the models are ill-conditioned.

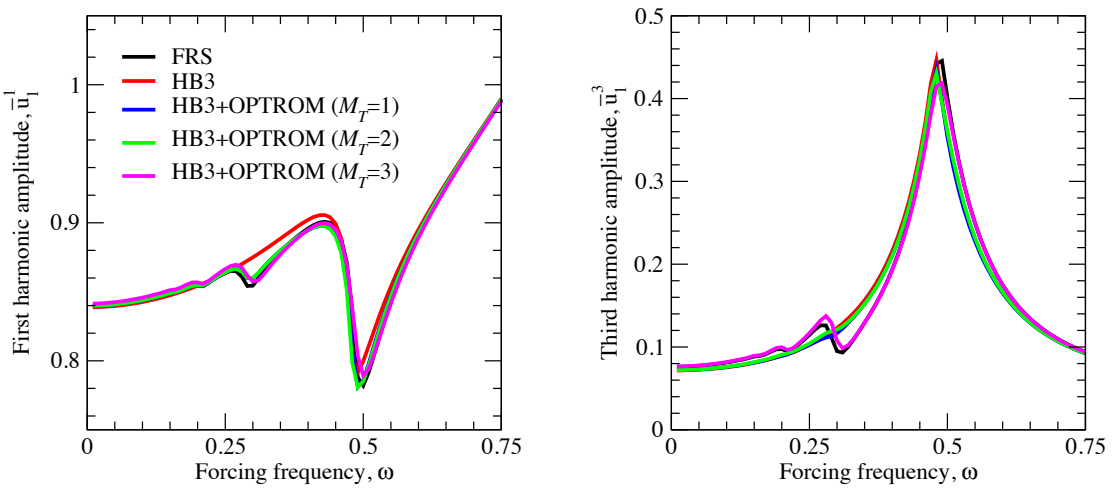

(a) First harmonic amplitude

(b) Third harmonic amplitude

Figure 5.14: HB3 solutions for the Duffing oscillator generated by frequency marching with a fixed forcing amplitude of $F = 1.25$.

The HB3 solutions in Figure 5.14 resolve the first and third harmonic amplitudes, $\bar{u}_1^1$ and $\bar{u}_1^3$. First note that the standard HB3 scheme successfully picks up the first subharmonic near $\omega = 0.5$, but does not detect any of the lower subharmonics. Several subgrid-scale models are tested with the HB3 scheme, all of which are based upon a linear stochastic estimate with two states ($M_S = 2$). The first model uses a one-point temporal stencil ($M_T = 1$), the second a two-point temporal stencil ($M_T = 2$) and the third a three point temporal stencil ($M_T = 3$). None of these models are exact for the HB3 scheme. Each OPTROM model is successful in predicting additional subharmonic structures in $\bar{u}_1^1$, but only the three-point model improves predictions for $\bar{u}_1^3$. This observation suggests that multi-point temporal stencils may, at times, be necessary to improve the accuracy of fine time scales.

HB5 solutions for $\bar{u}_1^1$, $\bar{u}_1^3$ and $\bar{u}_1^5$ are shown in Figure 5.15. The standard HB5 scheme accurately predicts the first two subharmonics. This trend of picking up additional structures continues as more modes are retained. From the exploded view in Figure 5.15c, it can be seen that only the three-point OPTROM model improves $\bar{u}_1^5$, similar to what was observed for $\bar{u}_1^3$ with HB3. The differences between the HB5

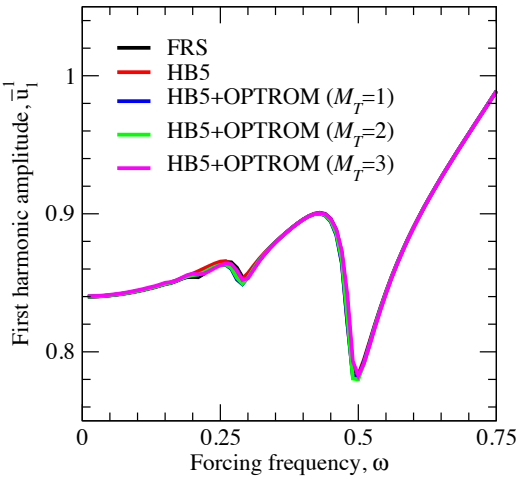

(a) First harmonic amplitude

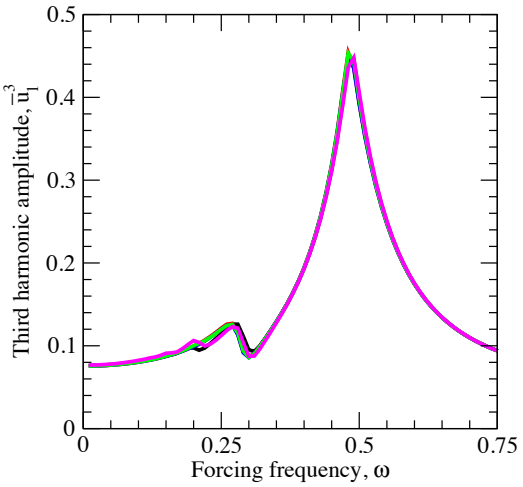

(b) Third harmonic amplitude

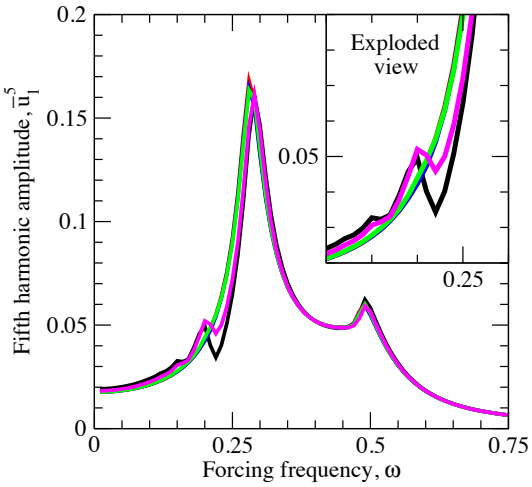

(c) Fifth harmonic amplitude

Figure 5.15: HB5 solutions for the Duffing oscillator generated by frequency marching with a fixed forcing amplitude of $F = 1.25$.

solutions and the FRS are less noticeable here compared to the HB1 and HB3 results, which indicates (i) an overall improvement in the fidelity of the solution as more modes are retained and (ii) a diminishing need for OPTROM.

We now examine the average *a posteriori* errors for the harmonic amplitudes across the backbone curves. Recall that the error for the k^{th} harmonic amplitude of the i^{th} state $\bar{E}_i^k$ is defined in (2.27). Here we average the $\bar{E}_i^k$ quantities across the entire backbone curve; for $F = 1.25$ the average is taken over $\omega \in (0, 2.40]$. Shown in Figure 5.16 are $\bar{E}_1^1$, $\bar{E}_1^3$ and $\bar{E}_1^5$ as a function of N_H for each scheme. Notice the errors

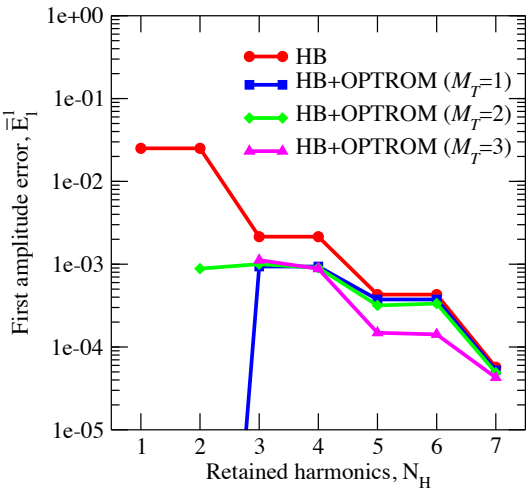

(a) First amplitude error, $\bar{E}_1^1$

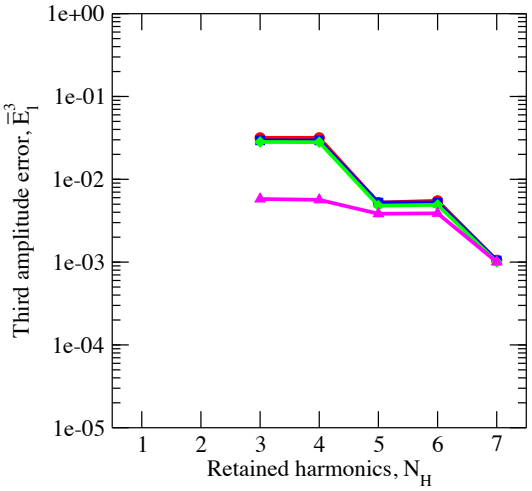

(b) Third amplitude error, $\bar{E}_1^3$

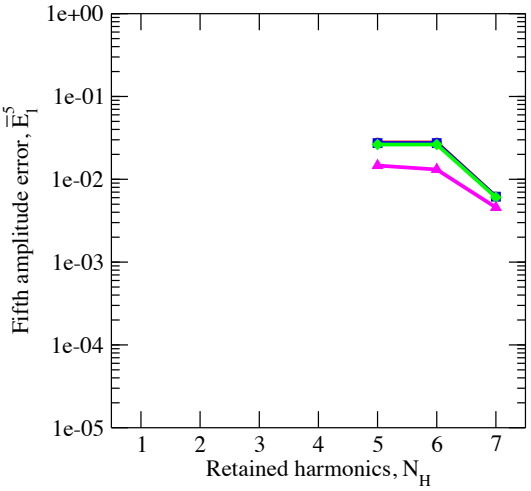

(c) Fifth amplitude error, $\bar{E}_1^5$

Figure 5.16: *A posteriori* errors for the HB solutions for the Duffing oscillator in Figures 5.13–5.15. Each amplitude error $\bar{E}_1^k$ shown here represents the average value over the backbone curve $\omega \in (0, 2.40]$ for $F = 1.25$.

for all schemes tend to zero as more harmonics are retained. The step-like convergence behavior is due to the fact that the even amplitudes are practically zero. Therefore, retaining an even number of modes does not significantly improve the accuracy. The vast majority of the error occurs in the subharmonic region.

All three OPTROM models in Figure 5.16 improve the accuracy of the HB scheme, but the greatest example of error reduction can be seen in Figure 5.16a. When one or two harmonics are retained, the one-point OPTROM model is exact, thus rendering

the $\bar{E}_1^1$ error zero. As more harmonics are retained, however, the $\bar{E}_1^3$ and $\bar{E}_1^5$ errors in Figures 5.16b and 5.16c experience marginal improvement at best with the one-point model. Only the three-point model significantly reduces the $\bar{E}_1^3$ and $\bar{E}_1^5$ errors. This observation is due to the fact that only the three-point model was able to pick up additional structures in $\bar{u}_1^3$ and $\bar{u}_1^5$. When a moderate number of harmonics are retained, the three-point model renders the best results. As more harmonics are retained (beyond $N_H = 7$), it becomes difficult to discern improvement in the accuracy of the resolved Fourier modes. From this observation, we can infer that the OPTROM models are most beneficial for this problem with low to moderate resolutions.

In addition to the multi-point models based upon a linear stochastic estimate, a one-point cubic model was also investigated, the results for which will not be shown here. For the HB1 and HB2 schemes, the one-point cubic model improves solutions for $\bar{u}_1^1$, but not to the same degree as the one-point linear model. When three or more harmonics are retained, the cubic model actually worsens the HB result. A rationale for the poor performance of this model is as follows: When a cubic approximation is used in (2.15) and (2.16), higher-order moments among $\tilde{u}_i^n$ and τ_i^n (up to sixth-order) are required to compute the estimation coefficients. These higher-order moments turn out to be orders of magnitude smaller than the first-order and second-order moments required for the linear model. So, in essence, the poor performance of the cubic model is due to the use of poorly correlated data [65, 66, 68].

As a final demonstration for the Duffing oscillator, we investigate the ability of the OPTROM models to predict subharmonic structures for variable forcing amplitudes and frequencies. To this end, we generate surfaces for the first harmonic amplitude $\bar{u}_1^1$ in the forcing parameter space $F \in (0, 1.25] \times \omega \in (0, \omega_p]$, where ω_p is the peak frequency of the backbone. The surfaces for $\bar{u}_1^1$ are compared in Figure 5.17. The FRS and HB1 solutions with OPTROM in Figures 5.17a and 5.17c are identical. In contrast, the standard HB1 solution in Figure 5.17b fails to predict any subharmonics.

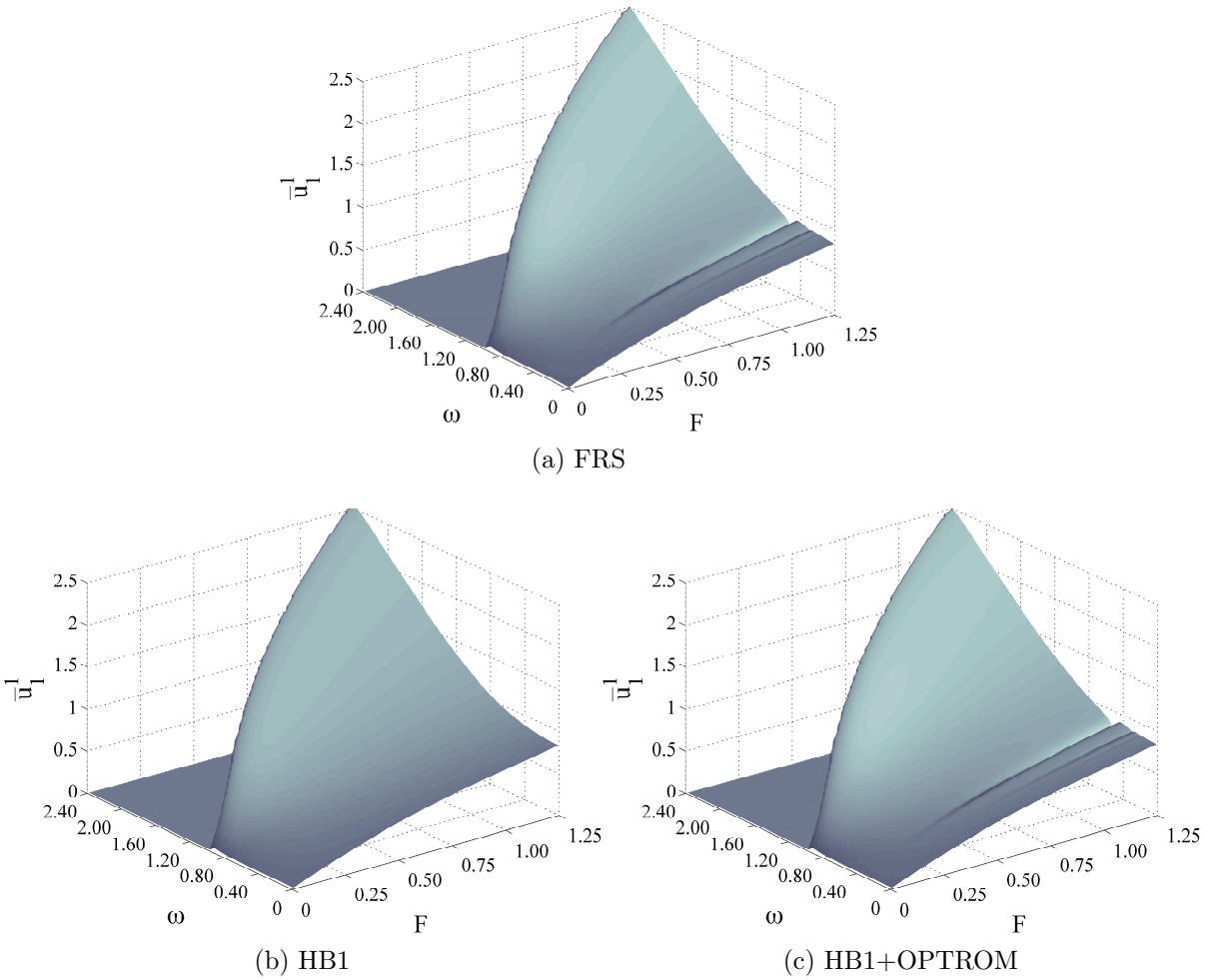

(a) FRS

(b) HB1

(c) HB1+OPTROM

Figure 5.17: Surfaces for the first harmonic amplitude $\bar{u}_1^1$ of the Duffing oscillator in the forcing space $F \in (0, 1.25] \times \omega \in (0, \omega_p]$ with $\Delta F = 0.01$ and $\Delta\omega = 0.01$.

5.2.4 Summary of results for the Duffing oscillator

The Duffing oscillator allowed us to investigate the OPTROM approach for a system in which the response may be regular or chaotic. The subgrid-scale models developed for the IE time-marching scheme were found to improve the reliability of under-resolved predictions for both regular and chaotic response types. By reducing discretization errors in the form of strong numerical damping, the models were able to prevent the occurrence of artificial regularity.

The subgrid-scale models were also found to significantly improve the accuracy of under-resolved predictions for Lyapunov exponents. Simulations for the Lyapunov

exponents were carried out in a large forcing parameter space with three different time-marching methods: a highly resolved RK4 scheme, a coarse standard IE scheme, and a coarse IE scheme with OPTROM. The RK4 scheme proved to be accurate but expensive, as simulations required several days of processing time. The coarse IE simulations (standard and OPTROM) were both computed up to 50 times faster, but the OPTROM results were found to be four times more reliable.

Several different types of subgrid-scale models were tested with the HB time-spectral scheme for computing time-periodic solutions. The model based upon a linear stochastic estimate with two states and one-point temporal model once again proved to be exact (zero *a priori* and *a posteriori* errors) for the HB scheme with one harmonic retained. When a moderate number of harmonics were retained, multi-point subgrid-scale models were found to be most effective for accurately predicting subharmonic structures. For this problem, the need for OPTROM, and its efficacy, proved to be greatest for low to moderate resolutions with the HB scheme.

5.3 Viscous Burgers flow results

For the viscous Burgers flow, we compute USUT simulations with the BTCS scheme for two sets of flow parameters. For the first set of parameters ($Re = 100$ and $St = 3$), we investigate the performance of three different subgrid-scale models calculated directly from the FRS solution. We model individually the subgrid-scale accelerations due to a coarse temporal grid (OPTROM) and the (mass normalized) subgrid-scale forces due to a coarse spatial grid (OPSROM). When these models are used in conjunction, they account for the complete subgrid-scale spatiotemporal statistical structure (OPSTROM). For the second set of parameters ($Re = 50$ and $St = 2.25$), we test the performance of the subgrid-scale models based upon estimated moments constructed in Section 4.3.

5.3.1 Performance of direct models

Fully evolved solutions for a flow with $Re = 100$ and $St = 3$ are shown in Figure 5.18. The FRS solution is calculated with the explicit RKCS scheme and a very fine grid ($\Delta x = 10^{-4}$ and $\Delta t = 10^{-8}$) to resolve all scales within 10^{-6} absolute error. The ROM solutions (standard USUT, OPTROM, OPSROM and OPSTROM) are all calculated with the implicit BTCS scheme and a very coarse grid ($\Delta x = 10^{-2}$ and $\Delta t = 10^{-2}$). Substantial errors can be seen in the standard USUT solution as the velocity field appears to be over-damped as it convects downstream.

The remaining solutions in Figure 5.18 are obtained with various types of models, all of which are nonhomogeneous in space and homogeneous in time. The first type of model, OPSROM, is similar to those used in OLES in the sense that it considers only the subgrid-scale convection and diffusion due to the use of a coarse spatial grid. This particular OPSROM model is based upon a quadratic stochastic estimate with diagonal coefficients and a central three-point spatial stencil (uses $\tilde{u}_{j-1}^n$, $\tilde{u}_j^n$ and $\tilde{u}_{j+1}^n$ to predict γ). The results in Figure 5.18 indicate that OPSROM provides only marginal improvement, likely due to the unaddressed numerical damping associated with the coarse timestep. Both the spatial and temporal spectra appear to be largely unaffected by OPSROM alone.

The second type of model in Figure 5.18, OPTROM, considers only the subgrid-scale acceleration due to the use of a coarse temporal grid. This particular OPTROM model is based upon a linear stochastic estimate with a backward three-point temporal stencil (uses $\tilde{u}_j^{n-2}$, $\tilde{u}_j^{n-1}$ and $\tilde{u}_j^n$ to predict α). The results in Figure 5.18 indicate that the OPTROM model reduces the numerical damping associated with a coarse timestep, but errors are still present as the downstream velocities are under-predicted. Moderate improvement can be seen in the spatial and temporal spectra, especially in the lower mode numbers.

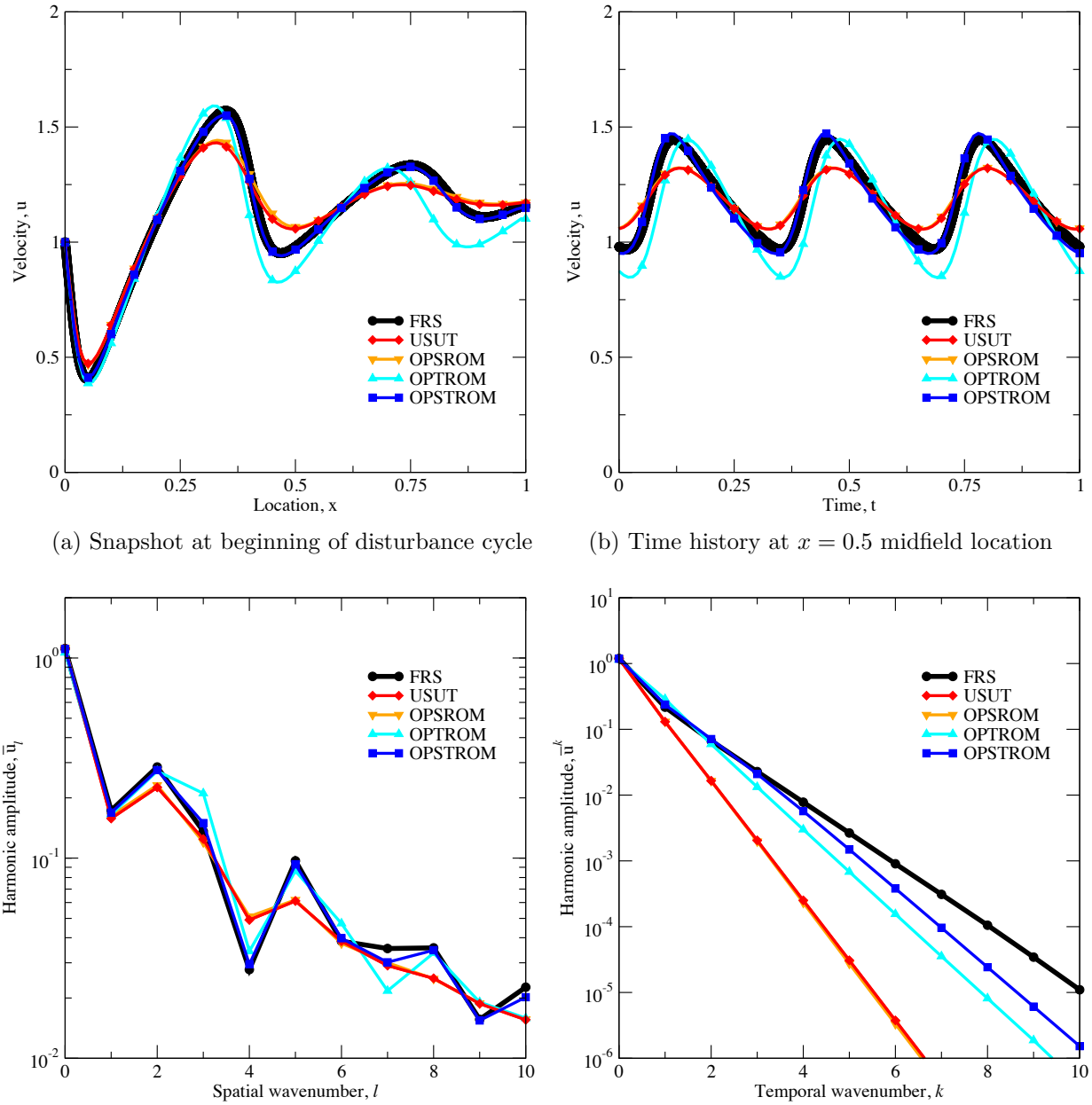

(a) Snapshot at beginning of disturbance cycle

(b) Time history at $x = 0.5$ midfield location

(c) Spatial spectra for Figure 5.18a

(d) Temporal spectra for Figure 5.18b

Figure 5.18: Velocity profile for the Burgers flow with $Re = 100$ and $St = 3$ calculated with various resolutions. The FRS solution is calculated using the explicit RKCS scheme with a fine grid ($\Delta x = 10^{-4}$ and $\Delta t = 10^{-8}$). All other simulations (standard USUT, OPSROM, OPTROM and OPSTROM) are under-resolved in space and time and are calculated using the implicit BTCS scheme with a coarse grid ($\Delta x = 10^{-2}$ and $\Delta t = 10^{-2}$). The under-resolved simulations are obtained nearly four orders of magnitude faster than the FRS. Including the subgrid-scale models adds a small amount of expense (less than 20%) to the simulations.

When used individually, both the OPTROM and OPSROM models in Figure 5.18 appear to be insufficient for eliminating the discretization errors, which suggests that the subgrid spatial and temporal scales are both important and need to be considered. To this end, the OPSTROM model is designed to account for the complete subgrid-scale spatiotemporal structure. The OPSTROM solution in Figure 5.18 is in excellent agreement with the FRS result throughout the entire spatial domain. Enrichment can be seen in nearly all of the spatiotemporal spectra.

5.3.2 Performance of models based upon estimated moments

Fully evolved solutions for a new flow with $Re = 50$ and $St = 2.25$ are shown in Figure 5.19. The FRS solution is again calculated with a very fine grid ($\Delta x = 10^{-4}$ and $\Delta t = 10^{-8}$), and the ROM solutions (standard USUT and OPSTROM) are calculated with a very coarse grid ($\Delta x = 10^{-2}$ and $\Delta t = 10^{-2}$). Again, the USUT solution appears to be over-damped as the flow convects downstream. Two different types of OPSTROM models are compared. The first model is calculated directly from the FRS solution, whereas the second is constructed from estimated moments in Section 4.3. Both OPSTROM models are found to significantly improve the accuracy solutions throughout the entire domain. Enrichment can be seen in virtually all modes of the spatial and temporal spectra.

As discussed in Chapter 2, the subgrid-scale models are formulated to preserve the underlying spatiotemporal statistical structure. As a final result, we explore the extent to which the statistical moments are actually preserved in the ROM solutions. Compared in Table 5.3 are selected moments amongst the velocities for the FRS, standard USUT, and OPSTROM (with models based upon estimated moments) solutions from Figure 5.19. The errors, stated in parenthesis, are generally greatest for the higher-order moments. When compared to the FRS moments, the OPSTROM approach is typically five times more accurate than the standard USUT scheme.

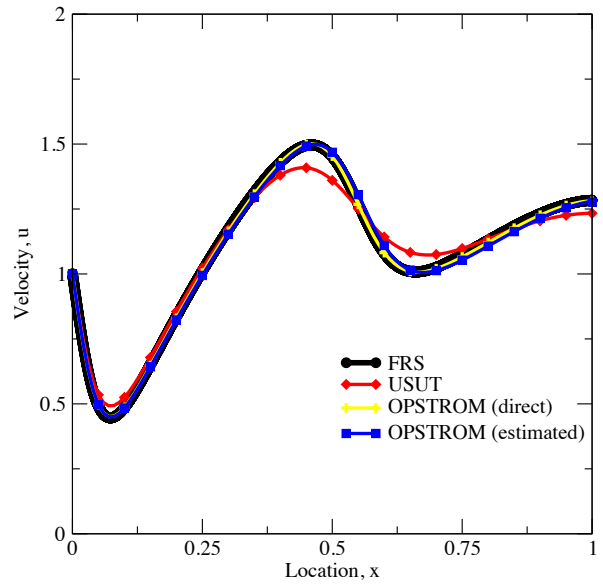

(a) Snapshot at beginning of disturbance cycle

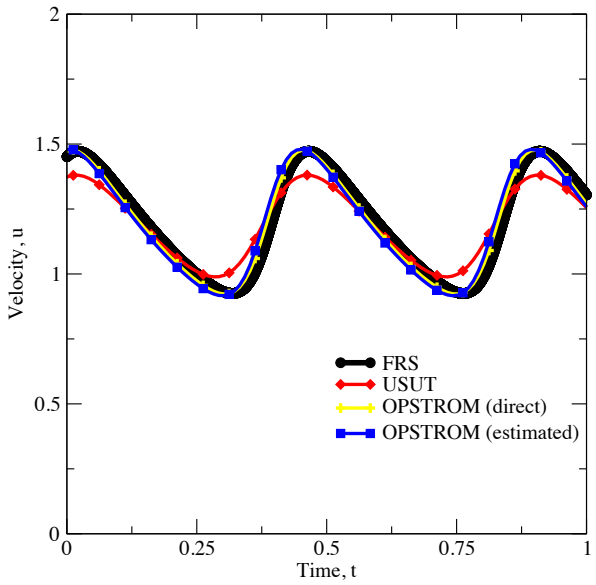

(b) Time history at $x = 0.5$ midfield location

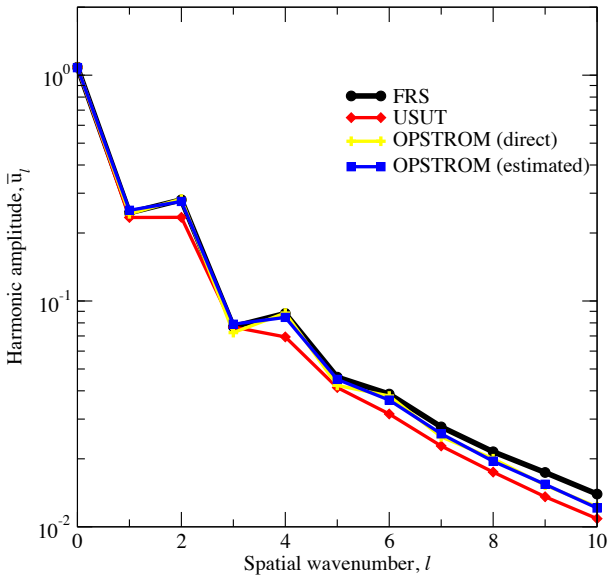

(c) Spatial spectra for Figure 5.19a

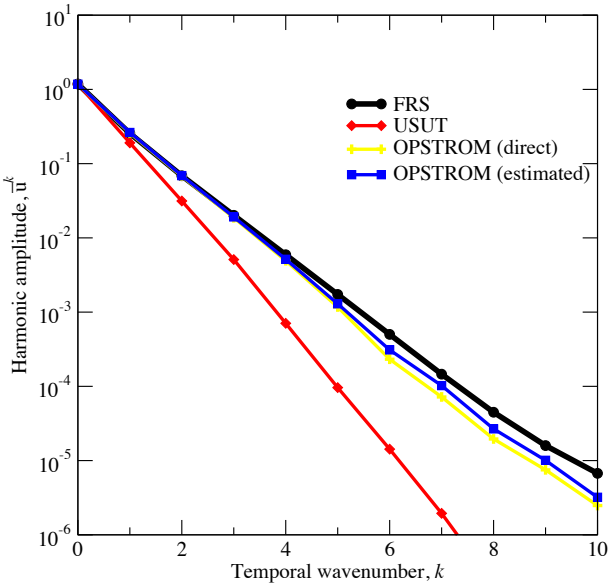

(d) Temporal spectra for Figure 5.19b

Figure 5.19: Velocity profile for the Burgers flow with $Re = 50$ and $St = 2.25$ calculated with various resolutions. The FRS solution is calculated using the explicit RKCS scheme with a fine grid ($\Delta x = 10^{-4}$ and $\Delta t = 10^{-8}$). All other simulations (standard USUT and OPSTROM) are under-resolved in space and time and are calculated using the implicit BTCS scheme with a coarse grid ($\Delta x = 10^{-2}$ and $\Delta t = 10^{-2}$). Two different types of subgrid-scale models are derived for OPSTROM: one calculated directly from the FRS solution shown in the figures (accurate but impractical) and the other derived from the estimated moments shown in Figures 4.10, 4.11 and 4.12. The under-resolved simulations are obtained nearly four orders of magnitude faster than the FRS. Including the subgrid-scale models adds a small amount of expense (less than 20%) to the simulations.

Moment	FRS	OPSTROM (error)	USUT (error)
$\langle \tilde{u}_j^n \rangle$	1.1819	1.1807 (0.0010)	1.1779 (0.0034)
$\langle \tilde{u}_j^n \tilde{u}_j^n \rangle$	1.4323	1.4268 (0.0038)	1.4060 (0.0184)
$\langle \tilde{u}_j^n \tilde{u}_j^{n-1} \rangle$	1.4318	1.4263 (0.0038)	1.4057 (0.0182)
$\langle \tilde{u}_j^n \tilde{u}_j^{n-2} \rangle$	1.4305	1.4252 (0.0037)	1.4046 (0.0181)
$\langle \tilde{u}_j^n \tilde{u}_{j-1}^n \rangle$	1.4320	1.4265 (0.0038)	1.4058 (0.0183)
$\langle \tilde{u}_j^n \tilde{u}_{j+1}^n \rangle$	1.4319	1.4265 (0.0038)	1.4057 (0.0183)
$\langle \tilde{u}_j^n \tilde{u}_j^n \tilde{u}_j^n \rangle$	1.7771	1.7607 (0.0092)	1.7001 (0.0433)
$\langle \tilde{u}_j^n \tilde{u}_j^n \tilde{u}_j^n \tilde{u}_j^n \rangle$	2.2535	2.2219 (0.0140)	2.0809 (0.0766)

Table 5.3: *A posteriori* moment comparison for FRS and ROM (standard USUT and estimated OPSTROM) solutions for the Burgers flow in Figure 5.19. Relative errors for the standard USUT and OPSTROM simulations are stated in parenthesis.

5.3.3 Summary of results for the viscous Burgers flow

For the viscous Burgers flow, we tested the performance of the various subgrid-scale models by comparing ROM solutions (standard USUT, OPTROM, OPSROM and OPSTROM) to the FRS. Solutions with the OPSROM scheme (which accounts for the subgrid spatial structure only and is analogous to OLES for turbulent flows) appeared to be significantly overdamped as the flow convected downstream. Solutions with the OPTROM scheme (which accounts for the subgrid temporal structure only) were also found to be under-predicted. As such, the OPSROM and OPTROM models alone were found to be insufficient for error reduction. The full OPSTROM solutions, however, were in excellent agreement with the FRS. Enrichment was observed in both the spatial and temporal spectral modes. OPSTROM models based upon estimated moments were found to be approximately five times more accurate than the standard USUT scheme in preserving the underlying spatiotemporal statistical structure for a given resolution.

5.4 Nonlinear beam results

In this fourth and most extensive example, we compute USUT simulations with the BTCS scheme for the geometrically nonlinear beam under the influence of time-periodic external forcing. Depending on the selected physical parameters, the beam response may undergo symmetric time-periodicity, asymmetry, period N-tupling, chaos and intermittency. Such behavior makes the beam an excellent problem for OPSTROM. The SS beam will be the focus of this analysis, although CC and CF beams will also be considered briefly. First we investigate the performance of various direct subgrid-scale models for both chaotic and regular response types. Spatially homogeneous, linear models will be used with $M_S = 1$, $M_N = 1$ and $M_T = 3$, as constructed in Section 4.4. Direct models alone are often not practical for use as they require *a priori* knowledge of moments calculated from FRS solutions. To address the issue of practical application, the performance of models based upon estimated moments will also be tested. Following validation of the models based upon estimated moments, we demonstrate the ability of the OPSTROM approach to accurately and efficiently trace bifurcation diagrams, map the temporal complexity of solutions, and predict regions of chaos and regularity in a large forcing parameter space.

5.4.1 Performance of direct models

We first investigate the accuracy and computational efficiency of the direct subgrid-scale models for the SS beam. We consider several combinations of external forcing parameters (F and ω) for which the response may be regular or chaotic. FRS and USUT solutions for the SS beam are compared in Figures 5.20–5.24 with various types of models and resolutions. Solutions for the CC and CF beams are also shown in Figures 5.25 and 5.26. In each figure, the response is characterized by the transverse velocity and displacement at the midpoint location, written as u_4^* and u_5^*, respectively.

Six different types of plots for these two quantities are shown in Figures 5.20–5.26, including the time histories, phase portraits, uniform sampling Poincaré maps, zero velocity Poincaré maps, and temporal spectra obtained by discrete Fourier transformation. The uniform sampling Poincaré maps record the values of u_4^* and u_5^* at the beginning of each forcing cycle, and are useful in detecting chaos and period N-tupling sequences. The zero velocity Poincaré maps record the configurations for which the beam experiences zero midpoint velocity, and are useful in detecting the development of high frequency content in the response.

Considered first in Figure 5.20 are time-periodic solutions for the SS beam with an external forcing of $F = 10$ and $\omega = 3.76$. USUT results (standard and OPSTROM) are calculated with a moderate spatial grid ($\Delta x = 10^{-1}$) and a very coarse timestep ($\Delta t = 10^{-2}$). The beam is driven from its equilibrium position at $t = 0$ and transients are allowed to decay as each solution is evolved beyond 100 forcing cycles. Observe in the time history plots (Figures 5.20a and 5.20b) that OPSTROM significantly improves predictions for the transverse displacement and velocity. This improvement can be seen more clearly in the uniform sampling Poincaré map (Figure 5.20c), where u_4^* and u_5^* obtained with FRS and OPSTROM are in close agreement at the beginning of each forcing cycle. The zero velocity Poincaré map (Figure 5.20d) reveals 22 occasions for which the FRS and OPSTROM schemes predict zero transverse velocity; the standard USUT scheme falsely predicts only 10 such occasions. The finite number of points in the Poincaré sections is a signature feature of periodicity. Improvement in the zero velocity Poincaré map is primarily due to the model's ability to predict additional time scales, which can be seen in the temporal spectra (Figure 5.20e). In particular, note the improved resolution of the secondary peak at the 13^{th} temporal mode, which is primarily responsible for the majority of zero velocity points.

Results for the same set of forcing parameters ($F = 10$ and $\omega = 3.76$) are shown in Figure 5.21, but with a moderate spatial grid ($\Delta x = 10^{-1}$) and a moderate timestep

($\Delta t = 10^{-3}$). For this resolution, the FRS and OPSTROM results are in excellent agreement. Standard USUT results have improved as well (compared to the very coarse results in Figure 5.20), but errors are still prevalent, particularly in the uniform sampling Poincaré map (Figure 5.21c) and phase portrait (Figure 5.21f). The temporal spectra in Figure 5.21e indicate that OPSTROM has almost completely resolved all temporal modes, even those below the FRS threshold in Appendix D ($\epsilon < 10^{-6}$). Hence, for a fraction of the computation time ($\mathcal{T} = 1.02 \times 10^{-3}$ for this set of grid parameters), OPSTROM is nearly identical to the FRS.

OPSTROM can also prevent the onset of artificial chaos. Figure 5.22 shows USUT results for the SS beam with the same forcing parameters ($F = 10$ and $\omega = 3.76$), but with a very coarse spatial grid ($\Delta x = 2.5 \times 10^{-1}$) and a very fine timestep ($\Delta t = 10^{-5}$). Note the application of OPSROM (models the subgrid-scale force only) as the complete OPSTROM model cannot be realized for the highly resolved Δt (recall the grid limitations in Table 4.5). This combination of grid parameters is actually a poor choice, as the solutions in Figure 5.22 are less accurate than those in Figures 5.20 and 5.21, and the computation times are more expensive by one to two orders of magnitude. Artificial chaos occurs with the standard USUT scheme, an erroneous result characterized by the fully populated section of the phase plane and an uncountable number of points in the Poincaré maps. Artificial chaos also gives rise to even modes in the temporal spectra, which are not shown in Figure 5.22e for clarity. OPSROM is more reliable, as the response is rightfully periodic.

In addition to regular solutions, OPSTROM can also improve predictions for chaotic dynamics. Figure 5.23 shows a chaotic FRS solution for the SS beam with a new set of external forcing parameters ($F = 10$ and $\omega = 15$) alongside USUT results (standard and OPSTROM). Most importantly, observe that the OPSTROM solution is rightfully chaotic, whereas the standard USUT result is artificially periodic. As the system evolves, orbits for the FRS and OPSTROM solutions completely cover subsets

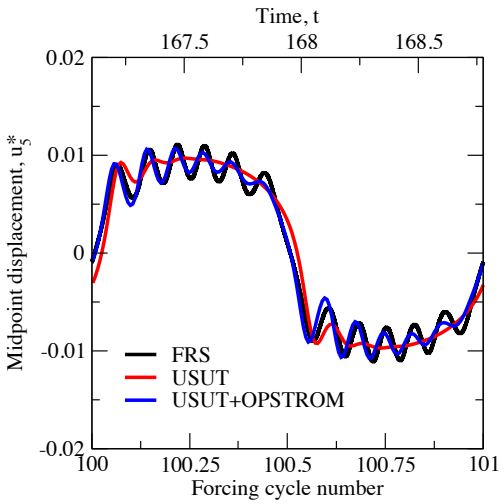

(a) Displacement time history

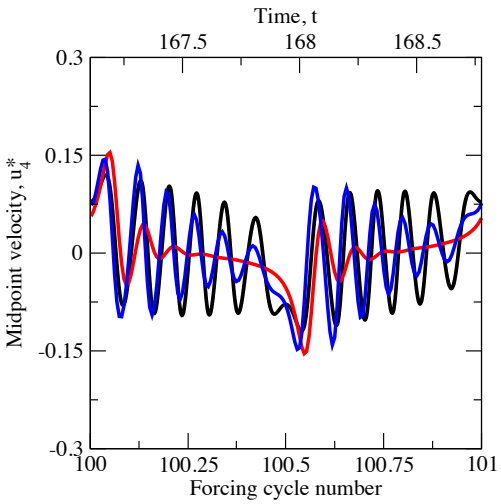

(b) Velocity time history

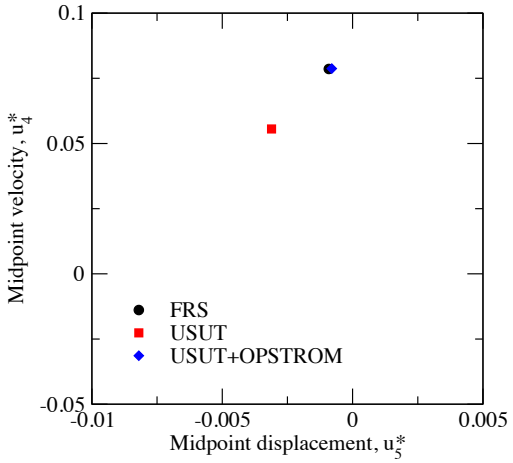

(c) Uniform sampling Poincaré map

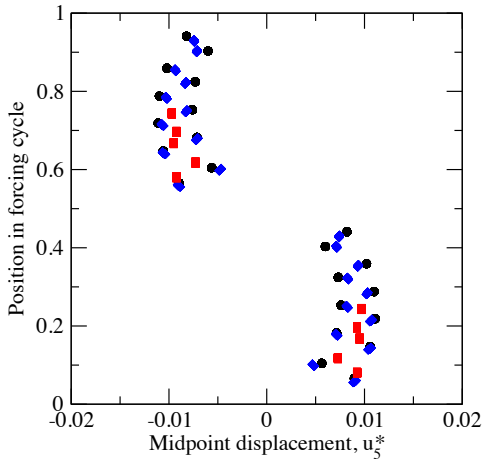

(d) Zero velocity Poincaré map

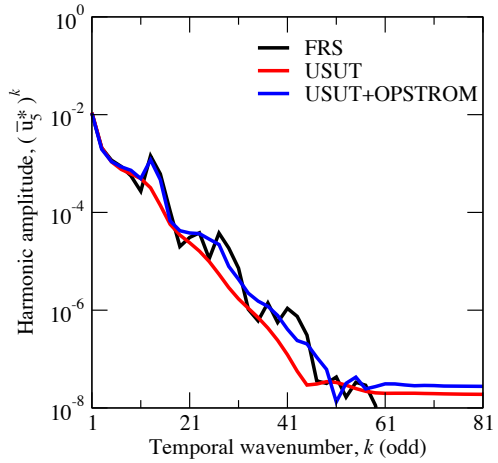

(e) Temporal spectra

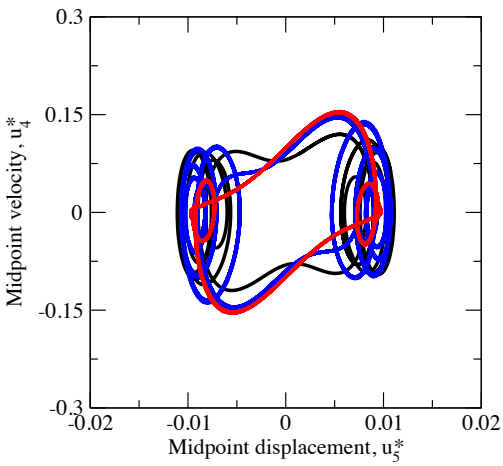

(f) Phase portrait

Figure 5.20: USUT solutions (standard and OPSTROM) for the SS beam with an external forcing of $F = 10$ and $\omega = 3.76$ with a moderate spatial grid (Δx=1.0×10^{-1}) and a very coarse timestep (Δt=1.0×10^{-2}).

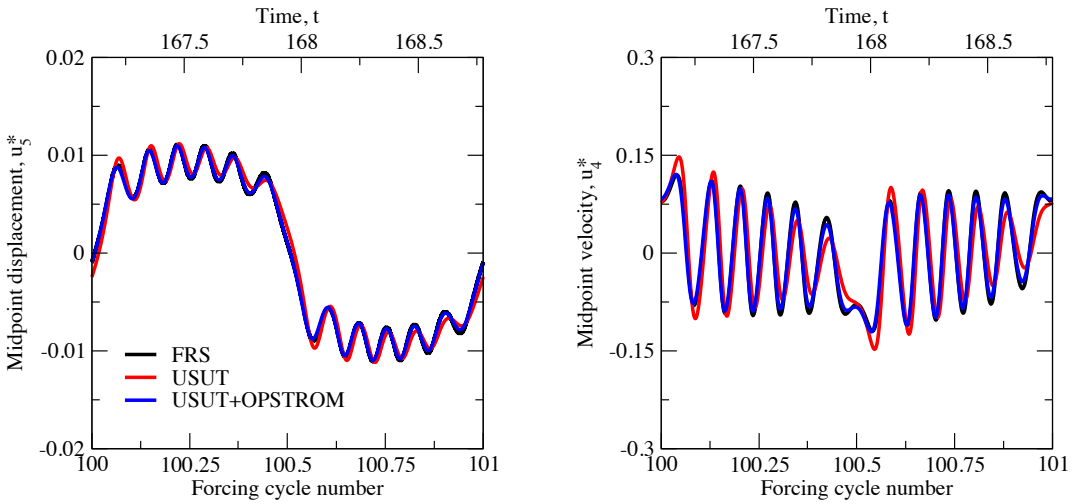

(a) Displacement time history

(b) Velocity time history

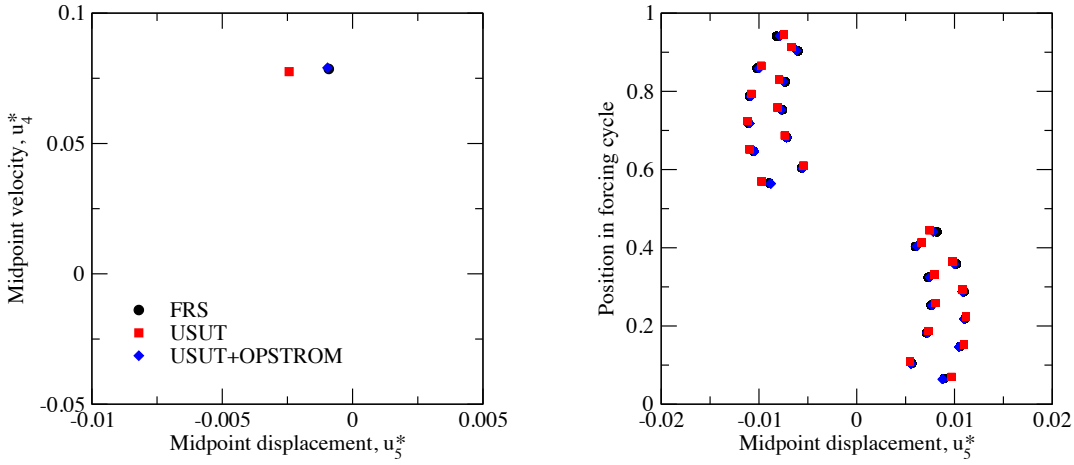

(c) Uniform sampling Poincaré map

(d) Zero velocity Poincaré map

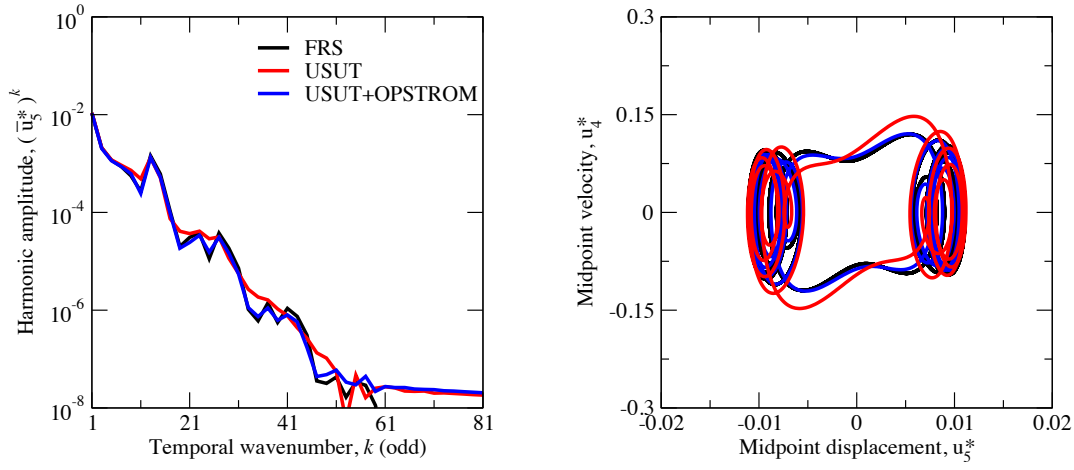

(e) Temporal spectra

(f) Phase portrait

Figure 5.21: USUT solutions (standard and OPSTROM) for the SS beam with an external forcing of $F = 10$ and $\omega = 3.76$ with a moderate spatial grid (Δx=1.0×10^{-1}) and a moderate timestep (Δt=1.0×10^{-3}).

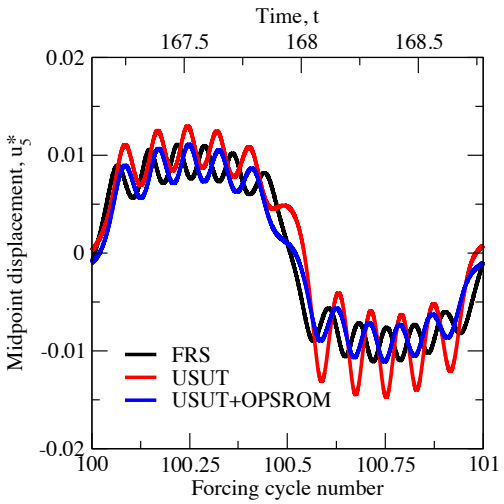

(a) Displacement time history

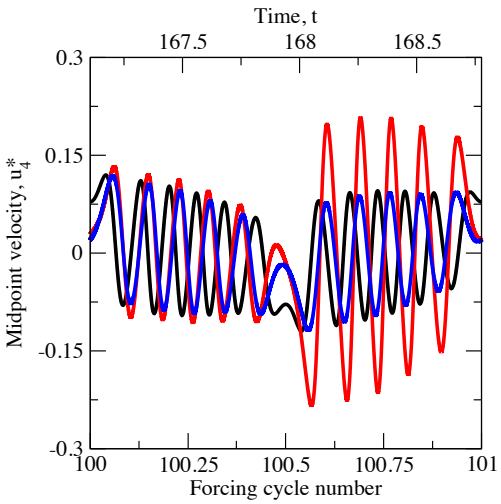

(b) Velocity time history

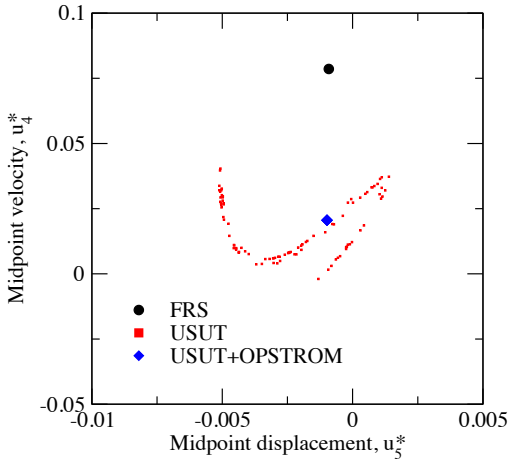

(c) Uniform sampling Poincaré map

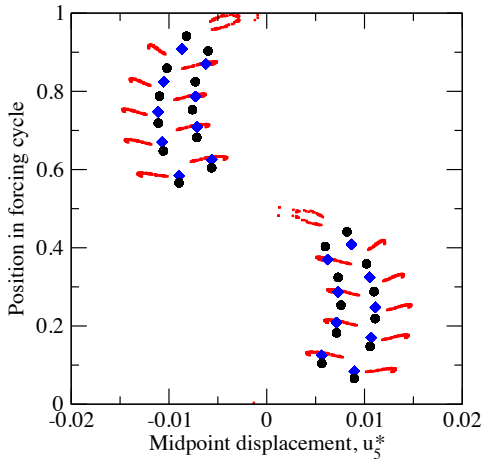

(d) Zero velocity Poincaré map

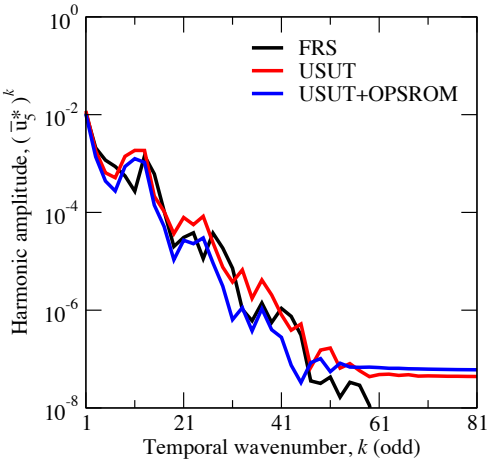

(e) Temporal spectra

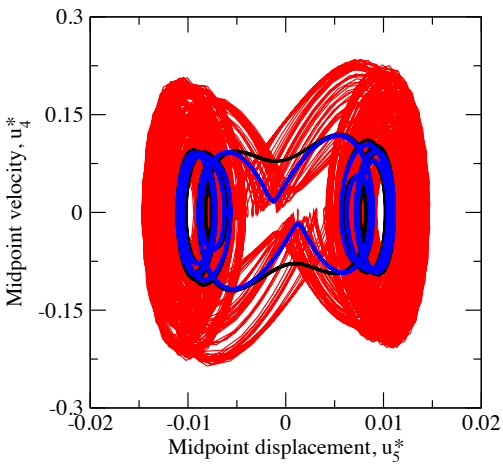

(f) Phase portrait

Figure 5.22: USUT solutions (standard and OPSROM) for the SS beam with an external forcing of $F = 10$ and $\omega = 3.76$ with a very coarse spatial grid (Δx=2.5×10^{-1}) and a very fine timestep (Δt=1.0×10^{-5}).

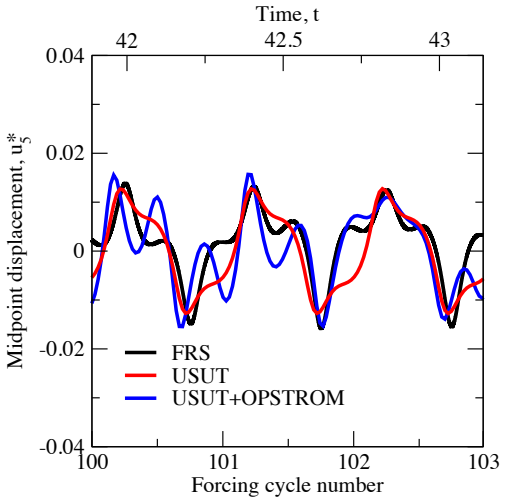

(a) Displacement time history

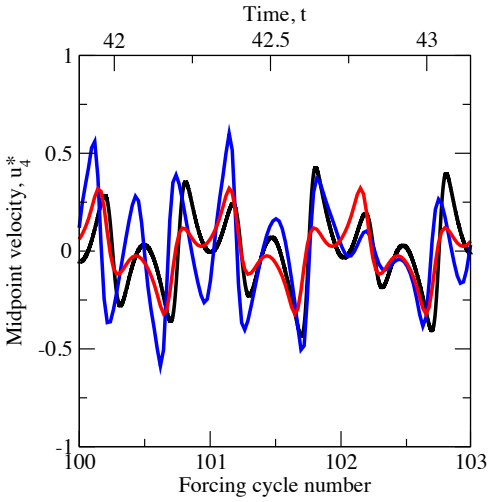

(b) Velocity time history

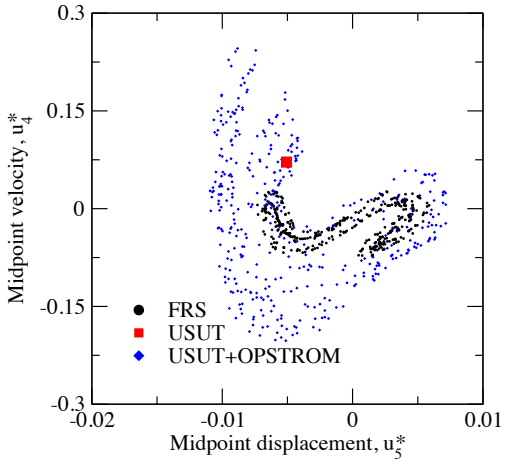

(c) Uniform sampling Poincaré map

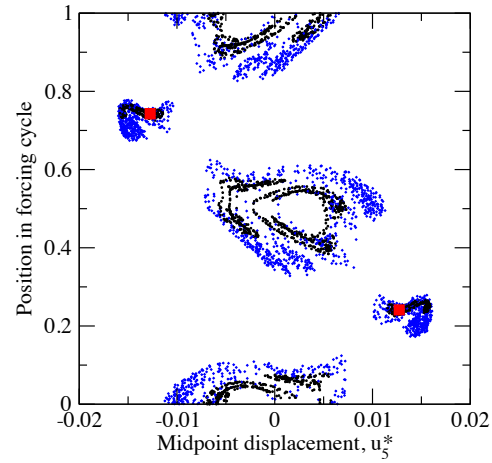

(d) Zero velocity Poincaré map

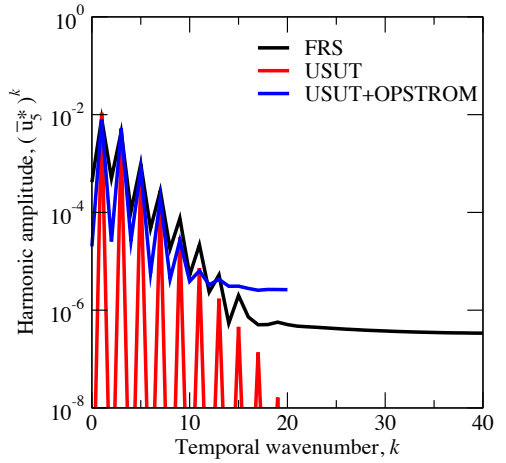

(e) Temporal spectra

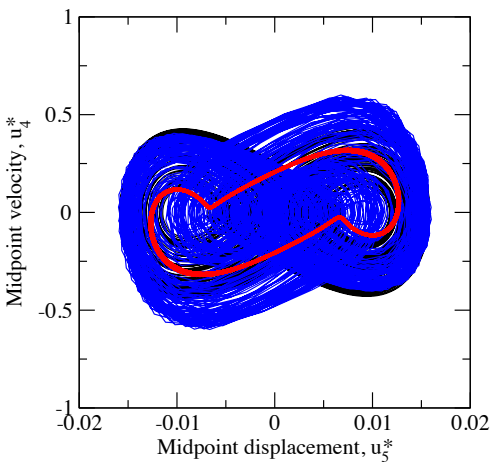

(f) Phase portrait

Figure 5.23: USUT solutions (standard and OPSTROM) for the SS beam with an external forcing of $F = 10$ and $\omega = 15$ with a moderate spatial grid (Δx=1.0×10^{-1}) and a very coarse timestep (Δt=1.0×10^{-2}).

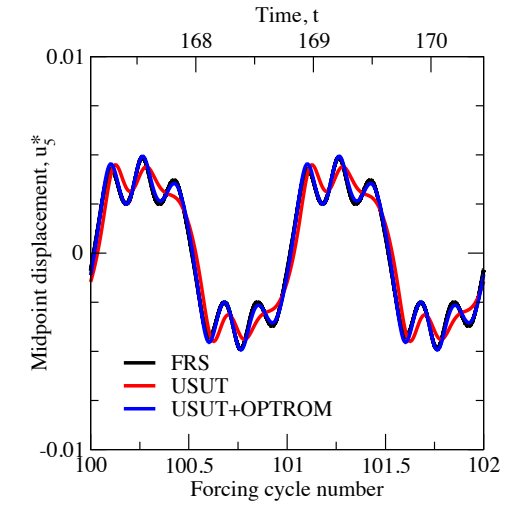

(a) Displacement time history

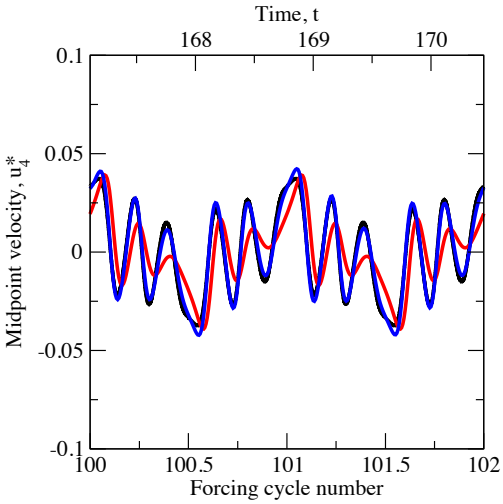

(b) Velocity time history

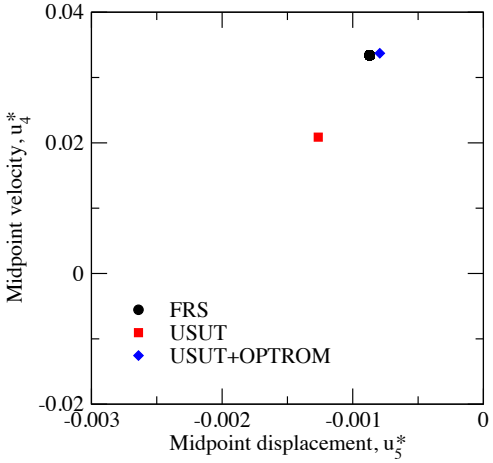

(c) Uniform sampling Poincaré map

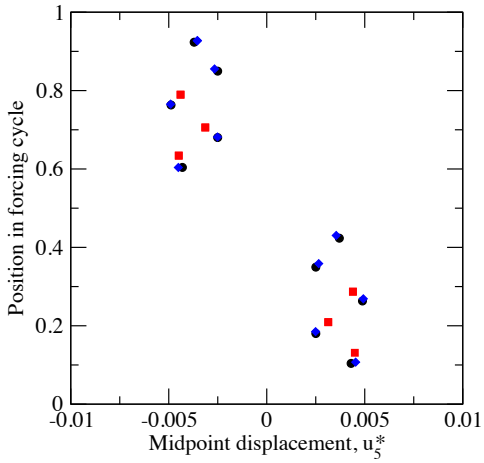

(d) Zero velocity Poincaré map

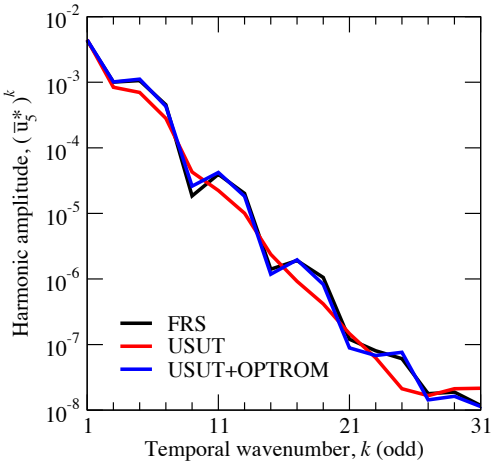

(e) Temporal spectra

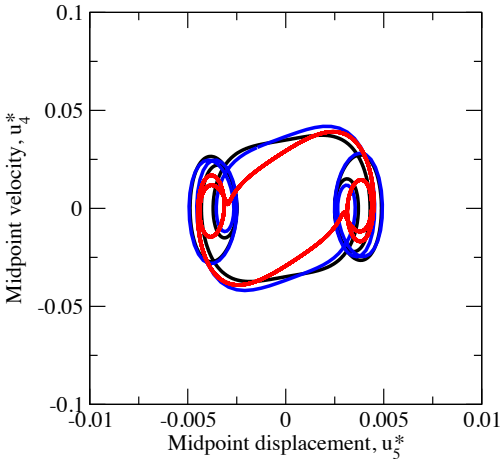

(f) Phase portrait

Figure 5.24: USUT solutions (standard and OPTROM) for the SS beam with an external forcing of $F = 1$ and $\omega = 3.76$ with a moderate spatial grid (Δx=1.0×10^{-1}) and a very coarse timestep (Δt=1.0×10^{-2}).

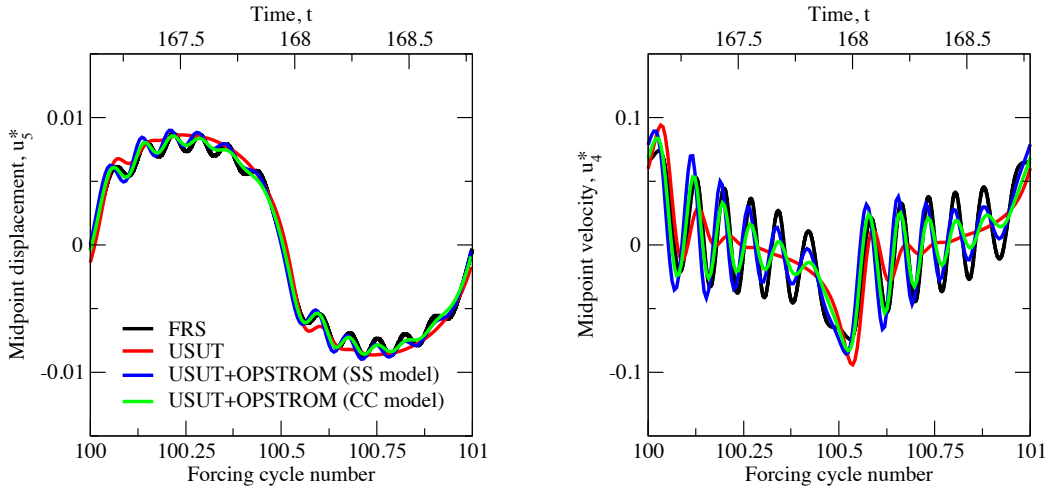

(a) Displacement time history

(b) Velocity time history

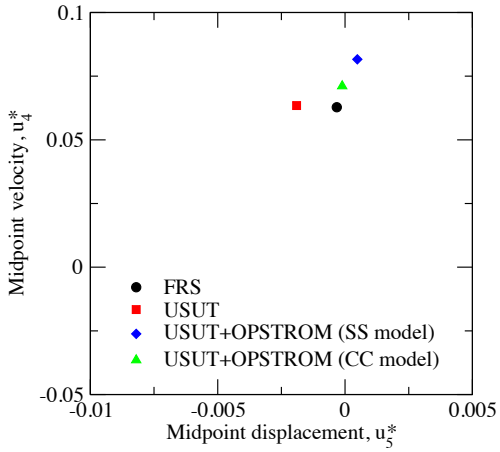

(c) Uniform sampling Poincaré map

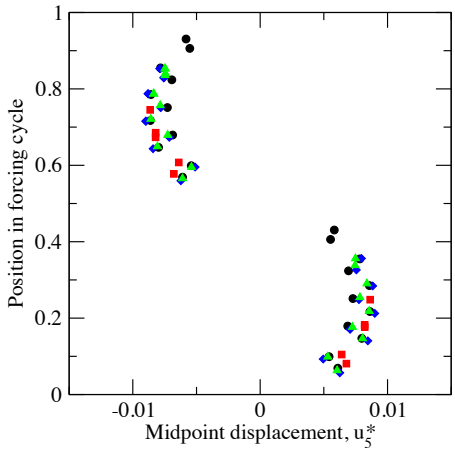

(d) Zero velocity Poincaré map

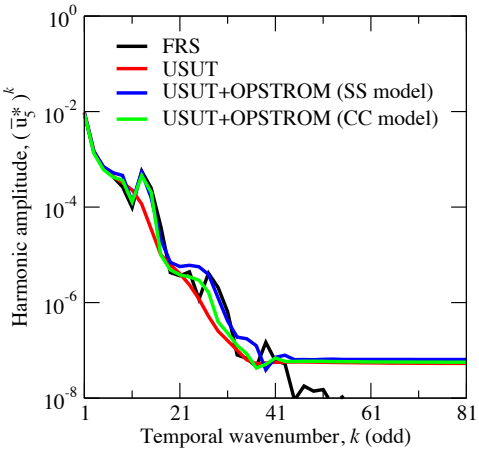

(e) Temporal spectra

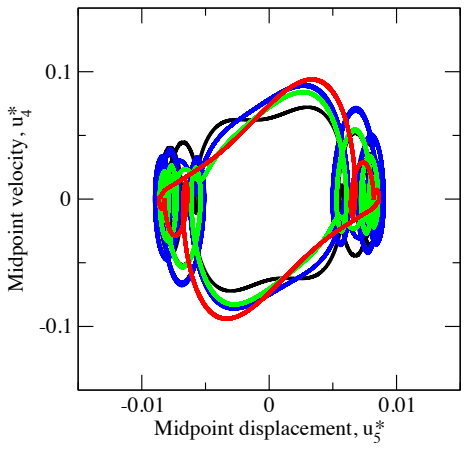

(f) Phase portrait

Figure 5.25: USUT solutions (standard and OPSTROM) for the CC beam with an external forcing of $F = 10$ and $\omega = 3.76$ with a moderate spatial grid (Δx=1.0×10^{-1}) and a very coarse timestep (Δt=1.0×10^{-2}).

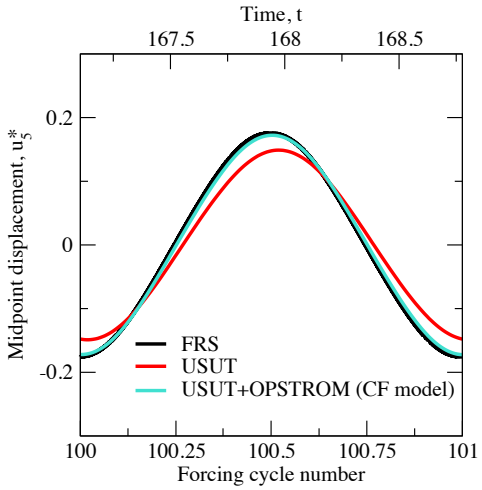

(a) Displacement time history

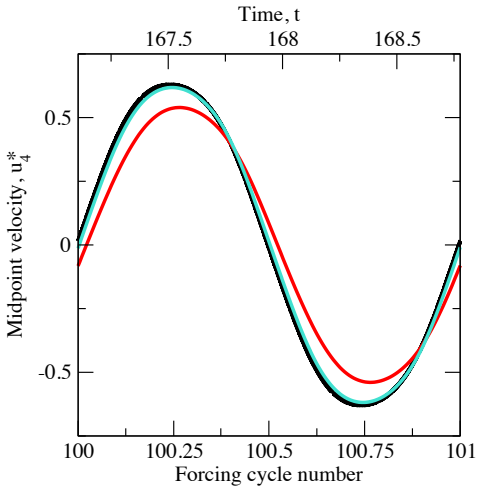

(b) Velocity time history

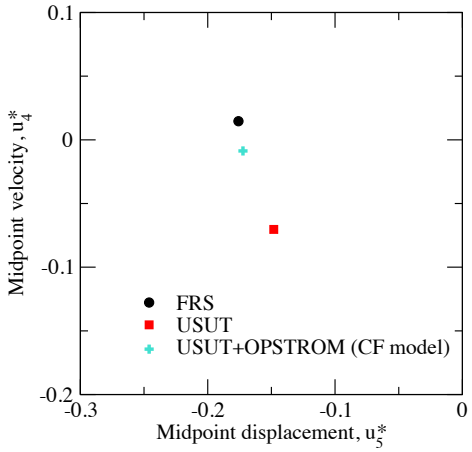

(c) Uniform sampling Poincaré map

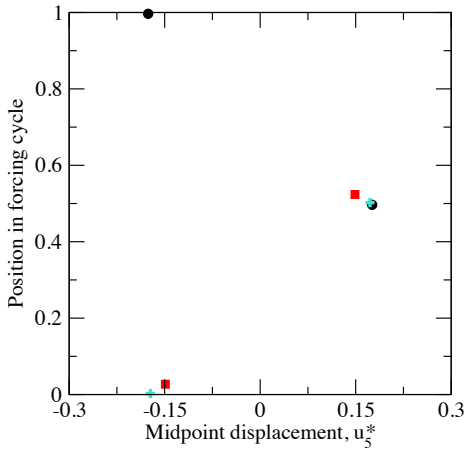

(d) Zero velocity Poincaré map

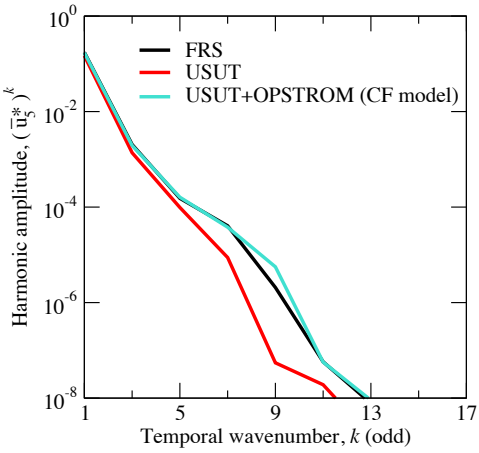

(e) Temporal spectra

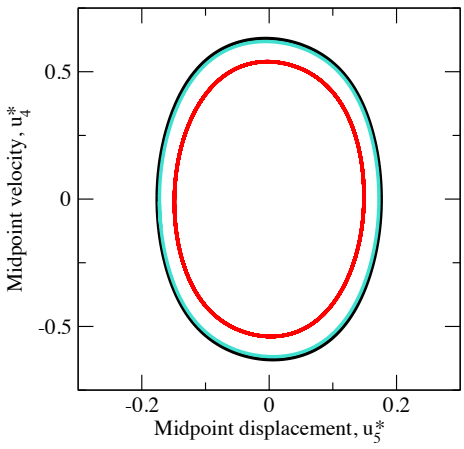

(f) Phase portrait

Figure 5.26: USUT solutions (standard and OPSTROM) for the CF beam with an external forcing of $F = 2$ and $\omega = 3.76$ with a moderate spatial grid (Δx=1.0×10^{-1}) and a very coarse timestep (Δt=1.0×10^{-2}).

of the phase plane, which is one of the classic signs of chaos. No two trajectories are exactly alike, and an infinite number of points are possible within certain sections of the Poincaré maps. The standard USUT scheme, however, falsely produces only two points of zero velocity and returns to the same state at the beginning of each forcing cycle. The FRS and OPSTROM solutions contain odd and even spectra, whereas the standard USUT spectra are simply odd. Notice the USUT spectra are cut off at the 20^{th} mode due to the choice of $\omega = 15$ and $\Delta t = 10^{-2}$.

Depending on the problem and chosen grid, OPTROM or OPSROM models alone may sometimes be sufficient for error reduction. Consider, for example, the external forcing amplitude shown in Figure 5.24 ($F = 1$), which is smaller in magnitude than those in Figures 5.20–5.23. As such, there are fewer spatial and temporal scales to resolve. Nevertheless, the standard USUT solution in Figure 5.24 experiences large errors in the form of increased numerical damping with a moderate spatial grid ($\Delta x = 10^{-1}$) and a very coarse timestep ($\Delta t = 10^{-2}$). The phase portrait for the standard USUT solution is also missing a loop in Figure 5.24f. Hence, the winding number [120] for the standard USUT solution is two in contrast to three for the FRS solution. The OPTROM solution, however, is in excellent agreement with the FRS. With OPTROM, errors for the temporal spectra in Figure 5.24e are generally reduced by one order of magnitude. Although subgrid spatial and temporal scales both exist for this set of forcing parameters, the subgrid temporal scales are far more significant. This observation explains, in part, why OPTROM is so effective.

Although the assumption of universality with respect to BCs was found to be weak in the previous chapter, the performance of models based on this assumption will nevertheless be investigated here. Considered first in Figure 5.25 are OPSTROM results for the CC beam with $F = 10$ and $\omega = 3.76$. All solutions are time-periodic. OPSTROM results are compared for two different subgrid-scale models: one derived from the SS solution (shown not to be universal) and the other derived from the CC

solution (the "correct" model). Observe that, as expected, the OPSTROM results with the CC model compare favorably to the FRS. Somewhat surprisingly, the SS model still does a good job of predicting both the large-scale and small-scale behavior compared to the standard USUT result. One can infer that at least some of the subgrid-scale structures for the CC beam are accurately predicted by the SS model.

As a final example, in Figure 5.26, we compare OPSTROM results for the CF beam with $F = 2$ and $\omega = 3.76$. All solutions are time-periodic. Compared to the FRS result, the standard USUT solution appears to be overdamped as it is smaller in magnitude and lagging in phase. Again, two different types of subgrid-scale models are investigated: one derived from the SS solution (shown not to be universal) and the other derived from the CF solution (the "correct" model). Results for the SS model are not shown because the NR scheme does not converge, even when the FRS result is provided as an initial guess at coincidental grid points. The OPSTROM solution with the CF model, however, is in excellent agreement with the FRS result.

5.4.2 Computational efficiency

For a given computational grid, Figures 5.20–5.26 suggest that OPSTROM is more reliable than the standard USUT approach with a coarse grid. Before running a large number of simulations, however, it is worthwhile to determine which computational grids provide the maximum computational efficiency for this particular problem.

Our next task is to determine which combination(s) of Δx and Δt provide the greatest accuracy with respect to the computation time for the SS beam. This will be done for the standard USUT scheme in addition to the OPSROM, OPTROM and OPSTROM variants. For each scheme, a number of simulations are run for an external forcing of $F = 10$ and $\omega = 3.76$ with various grids. Shown in Figures 5.27–5.30 are intersecting contours for the *a posteriori* errors in velocity and displacement (shaded in gray and defined in Part I) and normalized computation times (lines of constant $\mathcal{T}$)

as a function of Δx and Δt. For each scheme, the maximum computational efficiency is found by tracing a curve through which the *a posteriori* errors are minimized with respect to the computation time. Any combination of Δx and Δt on or near these efficiency curves would be a good choice for a simulation. Any other grid would be inefficient and wasteful.

For this problem, OPSTROM is the most efficient scheme for fast simulations, as shown in Figure 5.31. A specified level of accuracy can be achieved one order of magnitude faster with OPSTROM when a moderate or large Δt is chosen. When the performance of arbitrary grids are compared, as opposed to the most efficient grids in Figure 5.31, the benefits of OPSTROM become even more pronounced. OPSTROM remains the most efficient option in Figure 5.31 until a very small Δt is used, at which point subgrid-scale accelerations become difficult to model. For a very small Δt, the subgrid-scale accelerations are effectively numerical noise, and OPSROM then becomes the most efficient scheme. OPSROM is more accurate than standard USUT with respect to the grid, but not always with respect to the computation time, as the subgrid-scale models add a small amount of expense to the simulations.

It should be noted that the computational efficiency results in Figures 5.27–5.30 are generated with respect to simulations computed using fixed order schemes and double floating point precision. As such, more comprehensive results could in fact be obtained if both the scheme order and precision were varied. While the issue of interpolation order has been given significant attention in the numerical analysis literature, the impact of floating point precision on the accuracy and efficiency of simulation has only recently been investigated [121, 122]. Questions regarding the impact of floating point precision on computational efficiency curves such as those generated in Figures 5.27–5.30 would appear to be still unanswered for many problems in nonlinear dynamics, including the modeling of turbulent flows.

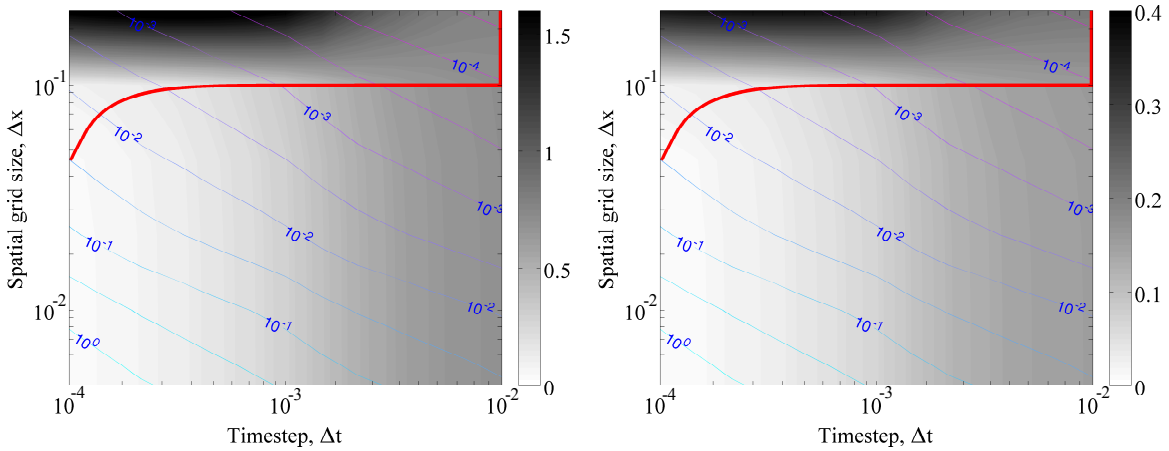

(a) USUT velocity errors, E_{u_4} (b) USUT displacement errors, E_{u_5}

Figure 5.27: Computational efficiency of the standard USUT scheme with various grids (Δx and Δt) for the SS beam with an external forcing of $F = 10$ and $\omega = 3.76$. The contours shaded in gray indicate the *a posteriori* errors for velocity E_{u_4} and displacement E_{u_5}. The intersecting contour lines (unshaded) indicate the normalized computation times, $\mathcal{T}$. The maximum computational efficiency is found by tracing a curve (red) through which the *a posteriori* errors are minimized for a given computation time. Large errors occur for $\Delta x = 2.5\times10^{-1}$ and small Δt as a result of artificial chaos (see Figure 5.22), an effect prevented with larger values of Δt due to increased numerical damping.

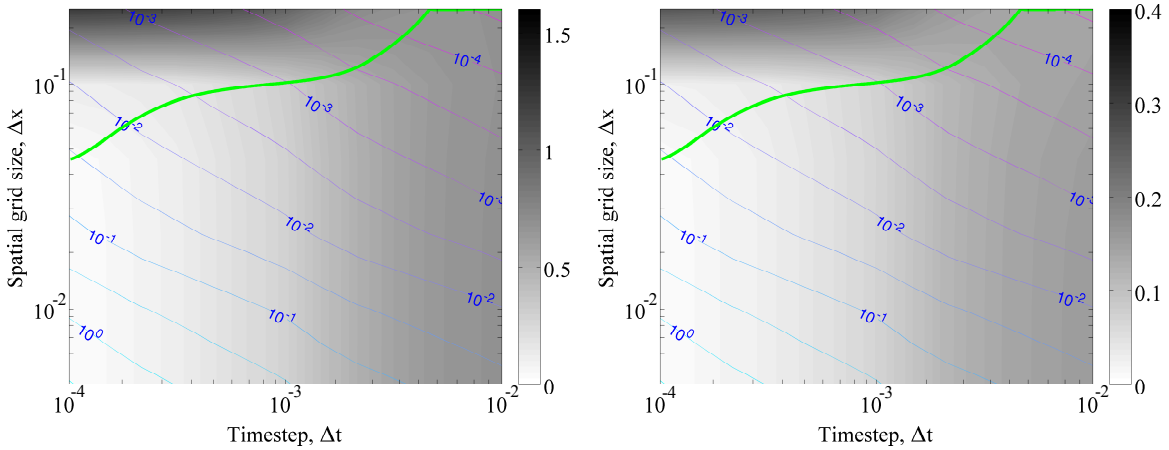

(a) USUT+OPSROM velocity errors, E_{u_4} (b) USUT+OPSROM displacement errors, E_{u_5}

Figure 5.28: Computational efficiency of the USUT scheme with OP**S**ROM ($\boldsymbol{\mathcal{M}}$ models $\boldsymbol{\gamma}$ only) and various grids (Δx and Δt) for the SS beam with an external forcing of $F = 10$ and $\omega = 3.76$. The maximum computational efficiency is traced with the green curve. All steady state solutions are rightfully periodic; artificial chaos does not occur. The OPSROM technique is more accurate than the standard USUT scheme with respect to the grid, but not necessarily with respect to $\mathcal{T}$, as the models add a small amount of computational expense.

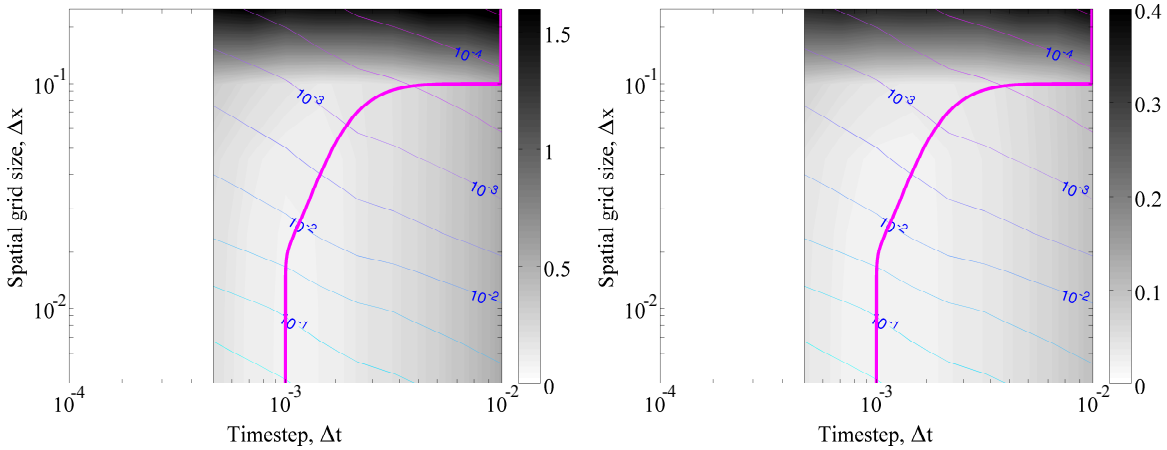

(a) USUT+OPTROM velocity errors, E_{u_4} (b) USUT+OPTROM displacement errors, E_{u_5}

Figure 5.29: Computational efficiency of the USUT scheme with OP**T**ROM ($\boldsymbol{\mathcal{M}}$ models $\boldsymbol{\alpha}$ only) and various grids (Δx and Δt) for the SS beam with an external forcing of $F = 10$ and $\omega = 3.76$. The maximum computational efficiency is traced with the magenta curve. Artificial chaos occurs for $\Delta x = 2.5{\times}10^{-1}$ and all values of Δt as the OPTROM model improves the apparent temporal resolution from the standard USUT scheme in Figure 5.27. Hence, the errors are actually worse for $\Delta x = 2.5{\times}10^{-1}$ and large Δt. The OPTROM technique does, however, improve predictions for small Δx and large Δt when a subgrid-scale model can be realized. The chosen model cannot be realized for $\Delta t \lesssim 5.0{\times}10^{-4}$ due to the grid limitation in Table 4.5.

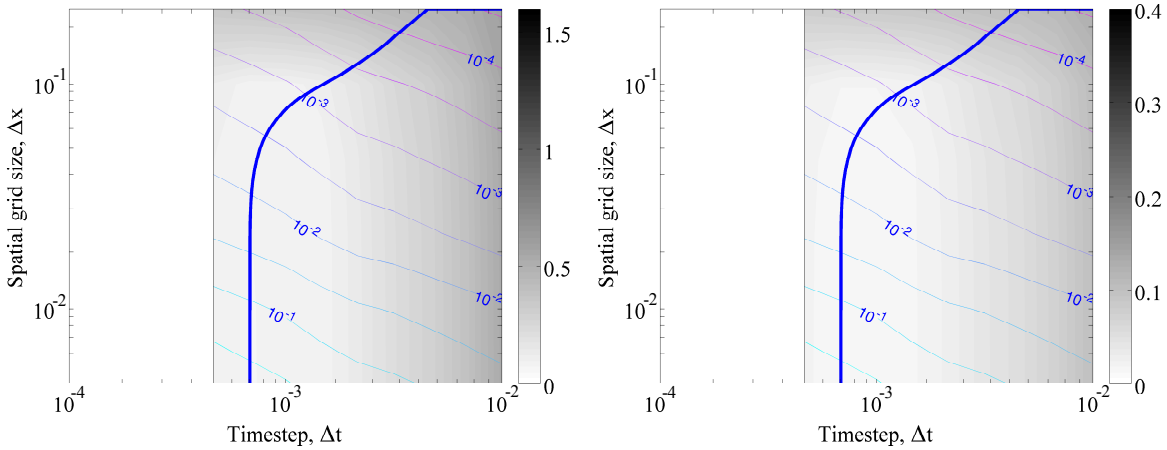

(a) USUT+OPSTROM velocity errors, E_{u_4} (b) USUT+OPSTROM displacement errors, E_{u_5}

Figure 5.30: Computational efficiency of the USUT scheme with OP**ST**ROM ($\boldsymbol{\mathcal{M}}$ models $\boldsymbol{\alpha}$ and $\boldsymbol{\gamma}$) and various grids (Δx and Δt) for the SS beam with an external forcing of $F = 10$ and $\omega = 3.76$. The maximum computational efficiency is traced with the blue curve. All steady state solutions are rightfully periodic. The OPSTROM technique outperforms all other schemes when a subgrid-scale model can be realized. The chosen model cannot be realized for $\Delta t \lesssim 5.0{\times}10^{-4}$ due to the grid limitation in Table 4.5.

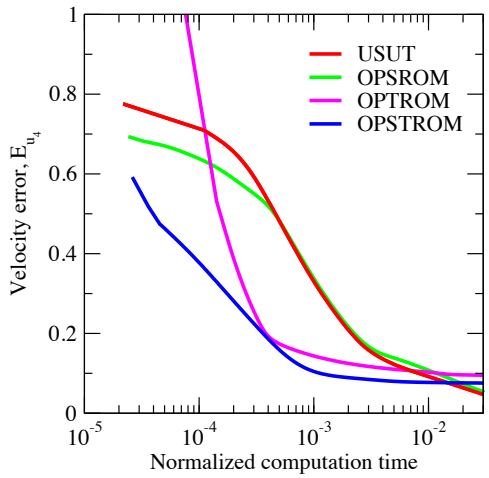

(a) Minimum velocity errors

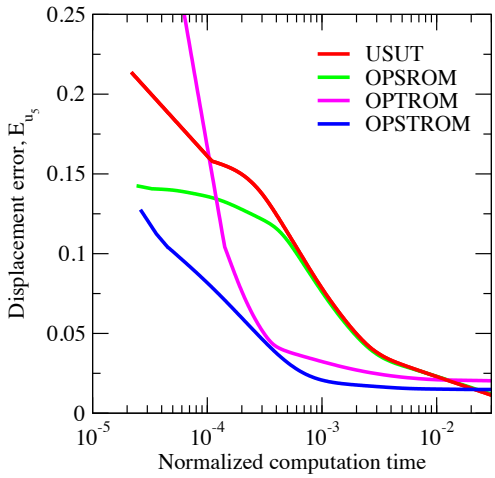

(b) Minimum displacement errors

Figure 5.31: Maximum computational efficiency curves for the USUT schemes in Figures 5.27–5.30 for the SS beam with an external forcing of $F = 10$ and $\omega = 3.76$. A specified level of accuracy can be achieved approximately one order of magnitude faster with OPSTROM than with the standard USUT scheme when a moderate or large Δt is chosen.

5.4.3 Performance of models based upon estimated moments

In order to validate the subgrid-scale models based upon estimated moments, we compare USUT results (standard and OPSTROM) to a FRS solution for the SS beam with an arbitrary set of forcing parameters ($F = 11.5$ and $\omega = 9.5$). As shown in Figure 5.32, the FRS solution indicates that the beam undergoes a chaotic response for this particular set of forcing parameters. Observe that the standard USUT result with a coarse grid falsely predicts a symmetric time-periodic solution. This can be seen clearly in the uniform sampling Poincaré map as the standard USUT response returns to the same state at the beginning of each forcing cycle. Exactly six instances of zero velocity per steady state forcing cycle can be seen in the uniform sampling Poincaré map for the standard USUT response. The OPSTROM simulation, however, correctly predicts a chaotic response as an infinite number of points appear to be possible in sections of the Poincaré maps. The dominant modes in the temporal spectra are also in excellent agreement with the FRS.

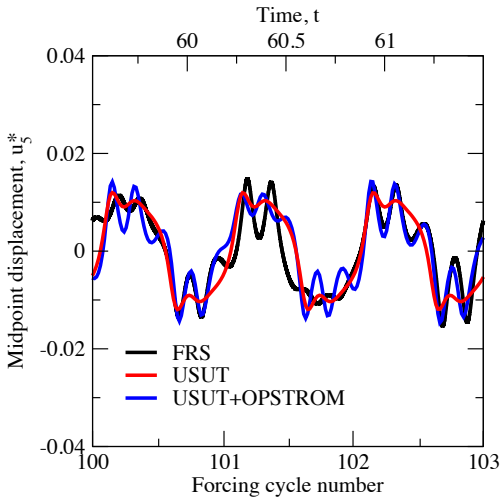

(a) Displacement time history

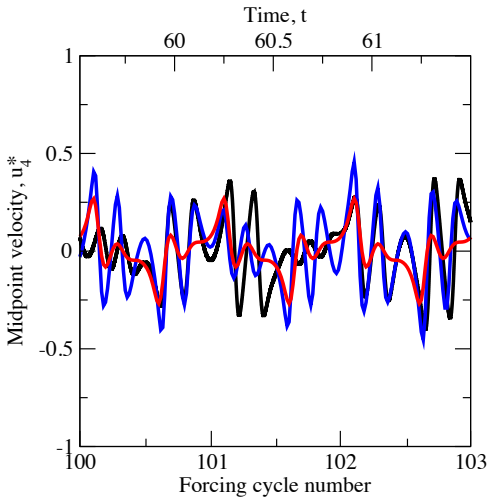

(b) Velocity time history

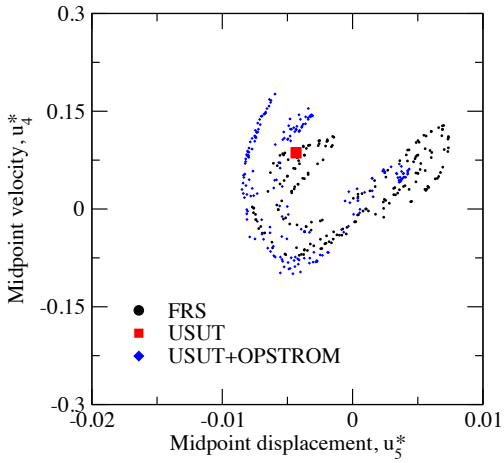

(c) Uniform sampling Poincaré map

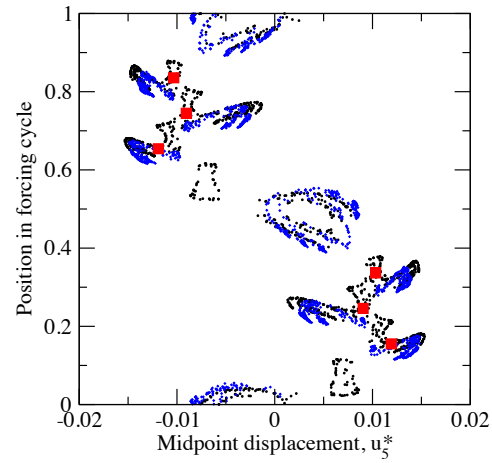

(d) Zero velocity Poincaré map

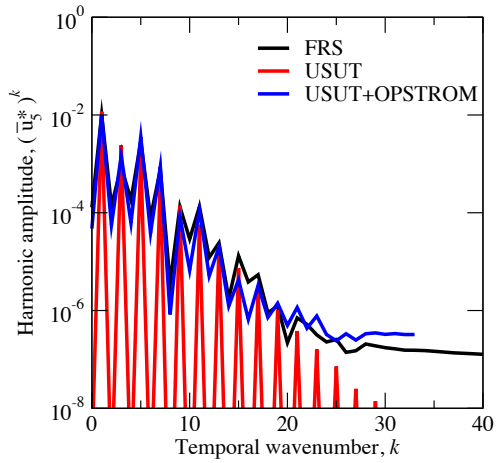

(e) Temporal spectra

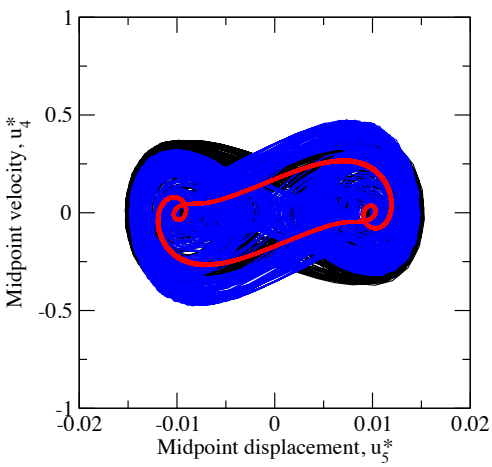

(f) Phase portrait

Figure 5.32: USUT solutions (standard and OPSTROM) for the SS beam with an external forcing of $F = 11.5$ and $\omega = 9.5$ with a moderate spatial grid (Δx=1.0×10^{-1}) and a very coarse timestep (Δt=1.0×10^{-2}).

Again, we emphasize that the FRS solution in Figure 5.32 is shown strictly for the sake of comparison. In other words, the FRS data in Figure 5.32 was not used to construct the subgrid-scale model. Estimated moments, two of which are shown in in Figure 4.21, were used instead to construct the model. The OPSTROM results to be presented in Sections 5.4.4–5.4.6 are based upon models with estimated moments.

5.4.4 Tracing bifurcations

In order to analyze the complex bifurcation behavior of the beam response, we sweep the forcing amplitude $F \in (0, 15]$ with a fixed frequency of $\omega = 15$. Simulations are carried out with three schemes: standard USUT with a coarse grid (fast), USUT with OPSTROM and a coarse grid (fast), and standard USUT with a fine grid (slow but presumably accurate). Recorded in Figure 5.33 are bifurcations that occur in the midpoint velocity at the beginning of each forcing cycle. As shown by the computation times in Figure 5.33, the coarse USUT simulations (standard and OPSTROM) are two orders of magnitude faster than the fine USUT simulation.

Some of the forcing amplitudes in Figure 5.33 appear to generate well-defined branches for regular orbits in addition to chaotic attractors. This observation can be attributed to one of two possibilities: First, it may in fact be possible for regular and chaotic attractors to coexist for certain parameters, in which case the fate of any one trajectory depends heavily on the choice of ICs [1]. The second scenario involves the selection of physical parameters for which only regular attractors exist, but the response undergoes transient chaos [119] or intermittency before eventually reaching one of many regular orbits. Such orbits, if plotted in phase space, may nearly intersect at the basin boundaries but not become entangled with them [119]. Depending on the ICs, there may be enough energy in the transient response for the trajectory to jump from one potential well to another, thus displaying characteristics of chaos until dissipation drives the system to a regular orbit. Distinguishing between these two

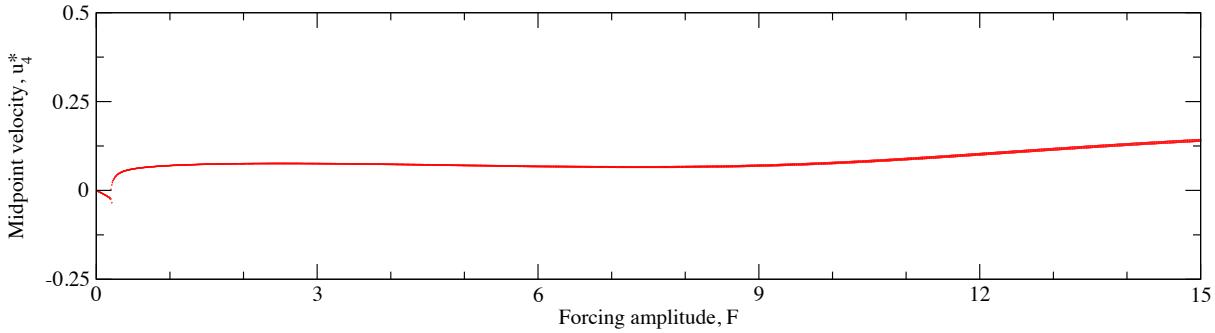

(a) Coarse USUT with $\Delta x = 1.0 \times 10^{-1}$ and $\Delta t = 1.0 \times 10^{-2}$ (5.4 hours)

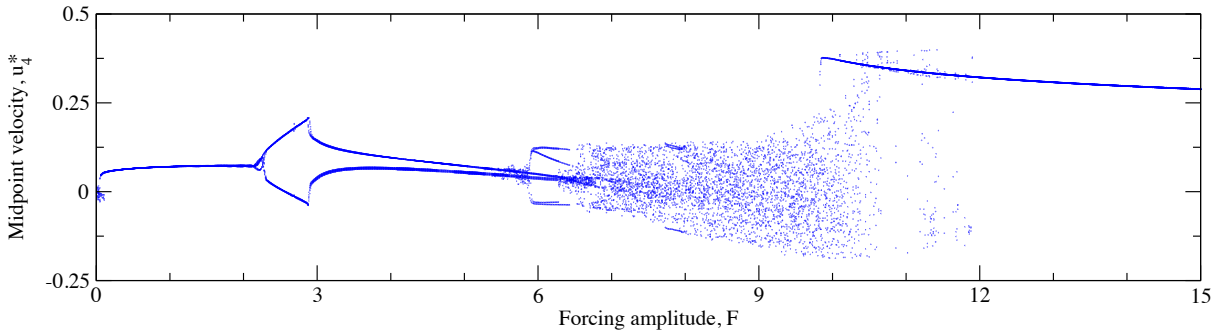

(b) Coarse USUT+OPSTROM with $\Delta x = 1.0 \times 10^{-1}$ and $\Delta t = 1.0 \times 10^{-2}$ (6.2 hours)

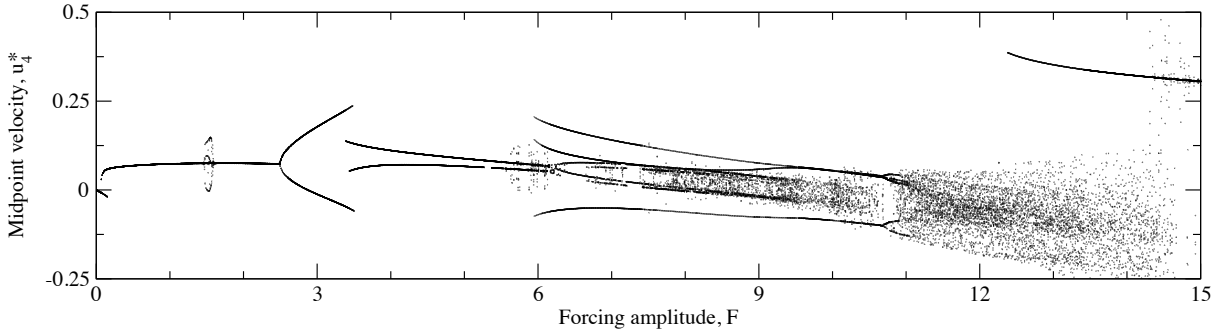

(c) Fine USUT with $\Delta x = 1.0 \times 10^{-1}$ and $\Delta t = 1.0 \times 10^{-4}$ (18 days)

Figure 5.33: Forcing amplitude bifurcations for the midpoint velocity u_4^* of the SS beam (recorded at the beginning of each forcing cycle) with a fixed forcing frequency of $\omega = 15$. The conglomeration of dots represent 1,500 solutions evolved for 100 forcing cycles with initial conditions sampled from $(u_4)_j^0 = V \sin(\pi x_j)$ with $V \in [-0.5, 0.5]$. Predictions are compared for three different simulations: coarse USUT (red), coarse USUT with OPSTROM (blue), and fine USUT (black). Computation times are stated in parenthesis. Similar FRS bifurcations would require years of simulation time, and therefore, are not feasible given the computational resources allocated for this study.

cases is difficult; the only way to be certain is to simulate all possible ICs and evolve all possible trajectories for infinite time.

As demonstrated in Figure 5.33a, the coarse USUT scheme fails to predict any bifurcations for the entire range of forcing parameters. All trajectories evolve to a symmetric periodic response, one of which can be found in Figure 5.23 for $F = 10$. Strong numerical damping due to the coarse grid impedes the development of higher modes which are primarily responsible for the bifurcated motions.

The bifurcation diagrams for the coarse OPSTROM and fine USUT schemes in Figures 5.33b and 5.33c are qualitatively similar, the primary difference being the forcing amplitudes at which the bifurcations occur. As we progress through the range of forcing amplitudes, we record the value of F at which the bifurcations occur with the fine USUT solution followed by the value of F for the OPSTROM solution in parenthesis, i.e. F and (F). Small forcing amplitudes produce symmetric periodic solutions until $F = 2.6$ (2.2), at which point the first bifurcation gives rise to asymmetric solutions. One qualitative exception occurs with the fine USUT solution: a brief pocket of multi-period motions can be found between $F = 1.5$ and $F = 1.6$. Beyond $F = 5.9$ (5.7), a variety of trajectories emerge, including period N-tupling (up to octupling), transient chaos and intermittency. Full-fledged chaos eventually takes over until $F = 12.3$ (9.9); beyond this point symmetric periodic solutions begin to appear for some ICs. Transient chaos ultimately dies out and this new branch of symmetric solutions persists beyond $F = 15$ (15). Similar bifurcation cycles occur for higher forcing amplitudes. As stated by Hall and Hanagud [109], chaos acts as a transitional mechanism with which two or more asymmetric branches merge to form a symmetric branch of a higher mode. Increasing F can sometimes increase or decrease the complexity of solutions.

5.4.5 Temporal complexity

Consider a scenario in which the analyst needs to predict the number of times the total kinetic energy in a system goes to zero. To this end, we record the number of zero velocity points (peaks) N_P in the response normalized by the forcing period $T = 2\pi/\omega$. This quantity (N_P/T) is also somewhat indicative of the dominant temporal modes. If the higher temporal modes (e.g. the thirteenth mode for $F = 10$ and $\omega = 3.76$ in Figures 5.20 and 5.21) have significant amplitudes, many peaks will appear in the response. Note that the quantity N_P/T indicates the number of temporal modes resolved by the scheme as opposed to the true number of temporal modes, unless of course a FRS is used, in which case they may be considered one and the same.

Contours for the quantity N_P/T are mapped in Figure 5.34 for the continuous forcing space $F \in (0, 15] \times \omega \in [1, 15]$. Simulations are performed with $\Delta x = 10^{-1}$ and three timesteps: $\Delta t = 10^{-2}$, 10^{-3} and 10^{-4}. Results for the standard USUT and OPSTROM schemes (OPSROM for $\Delta t = 10^{-4}$) are compared side-by-side in Figure 5.34. Observe that increasing F and ω can sometimes increase or decrease the temporal complexity. A sudden change in contrast indicates an abrupt shift in the response behavior. Grainy regions are generally a sign of chaos. Convergence with respect to the timestep is apparent, and moreover, the subgrid-scale models appear to accelerate this convergence. Notice in particular the discrepancies between the coarse and fine USUT predictions in Figures 5.34a and 5.34e. Assuming the fine USUT results in Figure 5.34e are more accurate, the coarse OPSTROM results in Figure 5.34b appear to be quite reliable.

The computation times required to produce the temporal complexity maps in Figure 5.34 are summarized in Table 5.5. Note that the coarse OPSTROM simulation in Figure 5.34b is nearly two orders of magnitude faster than the fine USUT simulation in Figure 5.34e, and yet the results are quite similar.

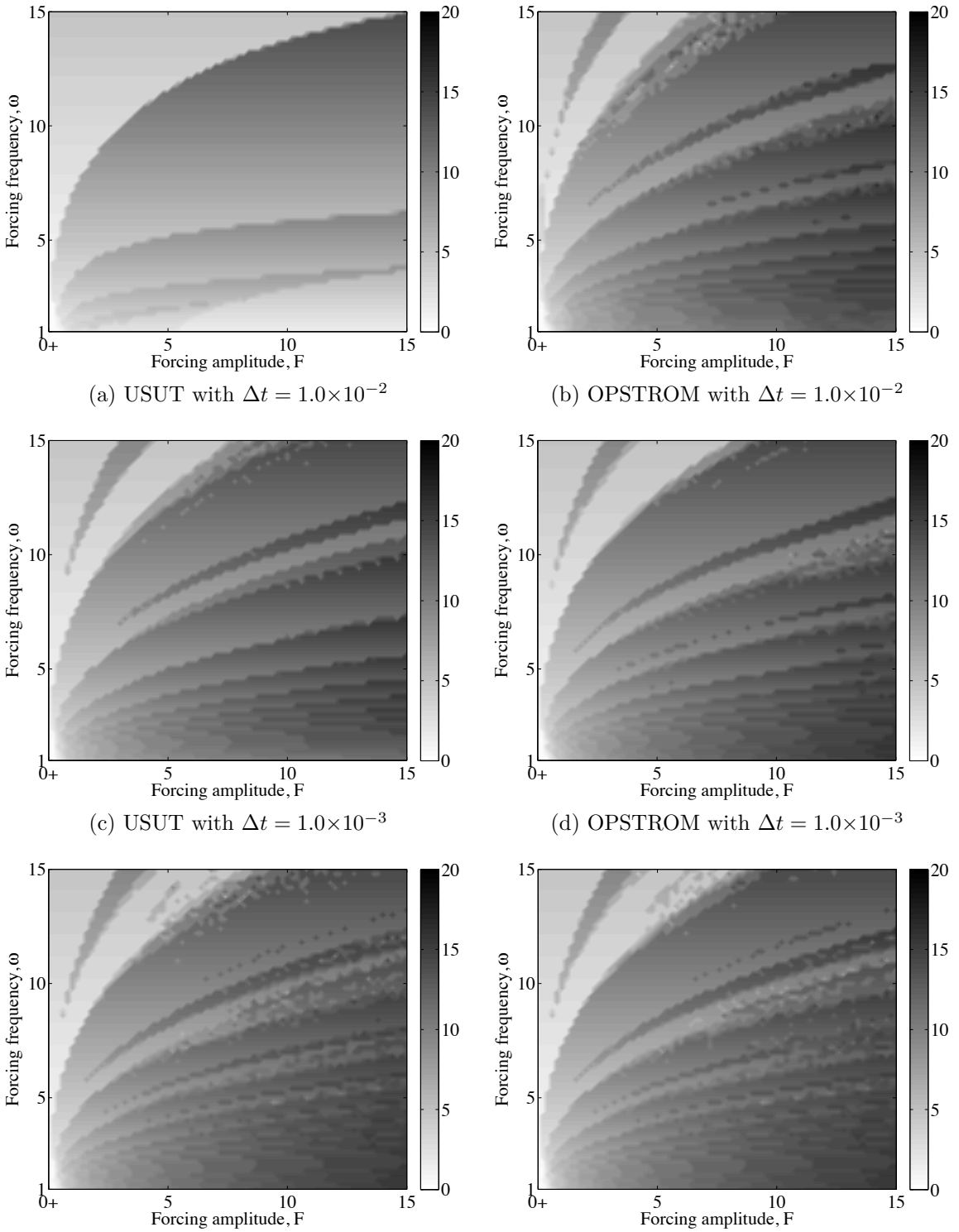

(a) USUT with $\Delta t = 1.0\times10^{-2}$

(b) OPSTROM with $\Delta t = 1.0\times10^{-2}$

(c) USUT with $\Delta t = 1.0\times10^{-3}$

(d) OPSTROM with $\Delta t = 1.0\times10^{-3}$

(e) USUT with $\Delta t = 1.0\times10^{-4}$

(f) OPSROM with $\Delta t = 1.0\times10^{-4}$

Figure 5.34: Number of zero velocity points N_P per forcing period T for the SS beam in the forcing parameter space $F \in (0, 15] \times \omega \in [1, 15]$ with increments of $\Delta F = 0.2$ and $\Delta\omega = 0.2$. The beam is driven from its equilibrium position for 20 forcing cycles. A total of 5,396 simulations are shown in each map.

Timestep	USUT	OPSTROM
$\Delta t = 10^{-2}$	3.9	4.5
$\Delta t = 10^{-3}$	34.2	35.7
$\Delta t = 10^{-4}$	321.6	326.4

Table 5.4: Computation times (in terms of hours of CPU time) required to produce the temporal complexity maps for the SS beam in Figure 5.34 with $\Delta x = 10^{-1}$ and the indicated Δt values. Similar FRS results for this problem would require several years of simulation.

5.4.6 Lyapunov exponents

In this section, we will investigate which combinations of F and ω result in regular or chaotic behavior. To this end, we compute Lyapunov exponents for the beam in the same manner as the Duffing oscillator in Section 5.2.2. For this beam problem, we compute the local Lyapunov exponents for the midpoint transverse displacement by following the uniform sampling Poincaré sections of two infinitesimally close trajectories for ten forcing cycles. Two simulations are required for each λ computation: first, a nominal simulation in which the beam is driven from its equilibrium position with $(u_i)_j^0 = 0$, and then a perturbed simulation in which the beam is given an initial displacement of $(u_5)_j^0 = (\delta_5)_j^0 = D\sin(\pi x_j)$ with $D = 10^{-9}$. A linear least squares curve fit is then applied to approximate the exponential rate of separation in (5.1).

As described in Section 5.2.2, a positive Lyapunov exponent is a very good, but inexact, predictor of chaos. For certain parameters and ICs, a trajectory may undergo transient chaos [119] or intermittency before eventually reaching one of many regular orbits, in which case the Lyapunov exponents may be positive in the short-term, whereas the long-term behavior of the system may be regular. While it is typical to consider the maximal Lyapunov exponent [117] for high dimensional systems, here we focus on the local Lyapunov exponents for the midpoint displacement as they are found to be equivalent to the maximal Lyapunov exponents in a long-term sense.

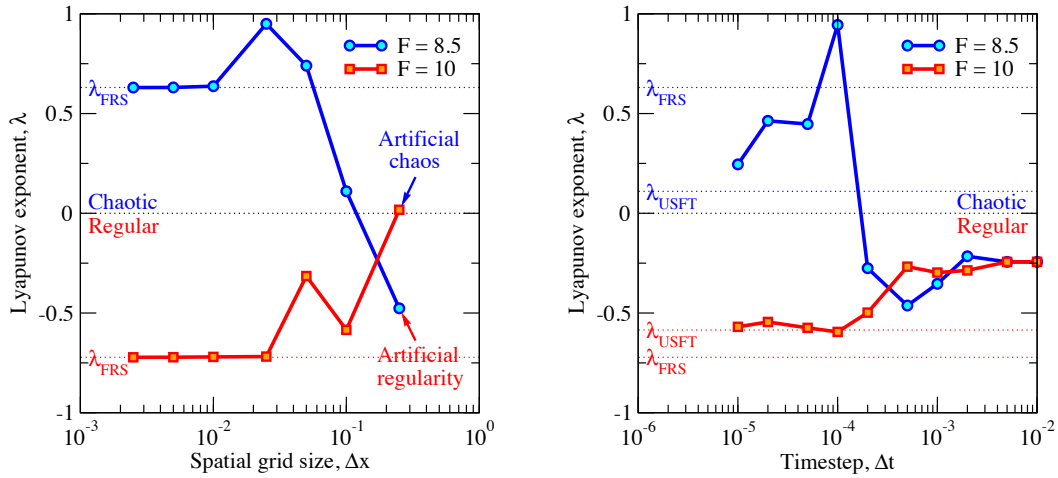

(a) USFT exponents

(b) USUT exponents with $\Delta x = 10^{-1}$

Figure 5.35: Convergence of Lyapunov exponents for the SS beam with $F = 10$ (regular) and $F = 8.5$ (chaotic) with $\omega = 3.76$. USFT exponents in Figure 5.35a converge to the FRS result as the spatial grid is refined to $\Delta x = 5.0{\times}10^{-3}$. USUT exponents in Figure 5.35b converge to the USFT result with $\Delta x = 10^{-1}$ as the timestep is refined.

Lyapunov exponents for the beam are found to converge slowly with respect to the grid parameters. Figure 5.35 shows examples of these exponents for two trajectories, one regular ($F = 10$ and $\omega = 3.76$) and the other chaotic ($F = 8.5$ and $\omega = 3.76$), computed with the standard USFT and USUT schemes. As the spatial grid is refined, the USFT exponents converge to the FRS result. Artificial chaos and regularity are possible with a coarse Δx. As expected, USUT exponents converge (albeit slowly) toward the USFT result for $\Delta x = 10^{-1}$ as $\Delta t \to \Delta t_{\text{FRS}}$. For a sufficiently large Δt, numerical dissipation in the USUT scheme overpowers the physics, thus preventing the onset of chaos for $F = 8.5$.

Maps for the Lyapunov exponents are shown in Figure 5.36 for the continuous forcing parameter space $F \in (0, 15] \times \omega \in [1, 15]$. Similar to what we saw for the Duffing oscillator, the maps in Figure 5.36 can be described as self-similar "islands of chaos" embedded in large "seas of regularity" [118]. Several USUT schemes (standard, OPSTROM and OPSROM) are used to calculate the exponents with a fixed spatial grid ($\Delta x = 10^{-1}$) and various timesteps ($\Delta t = 10^{-2}$, 10^{-3} and 10^{-4}). We assume that

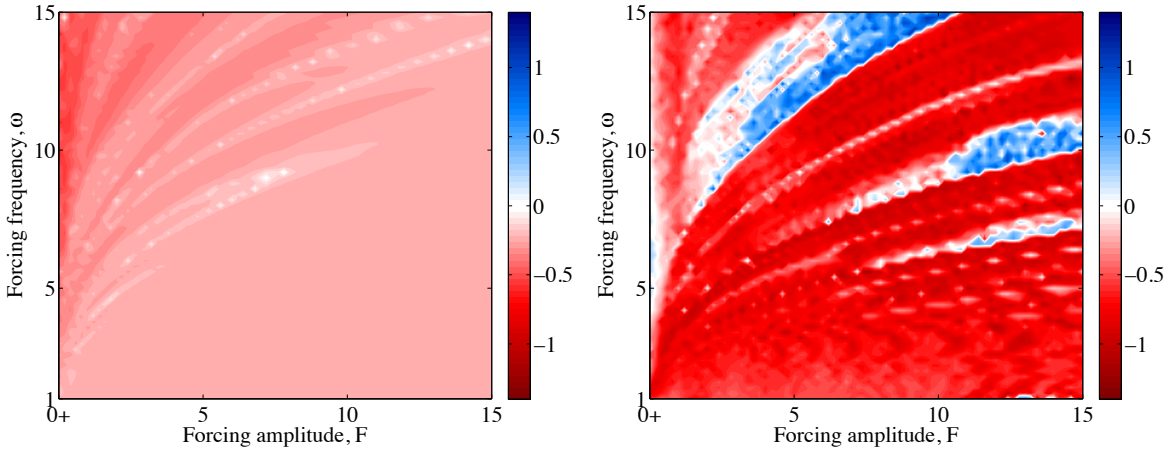

(a) USUT with $\Delta t = 1.0\times10^{-2}$

(b) OPSTROM with $\Delta t = 1.0\times10^{-2}$

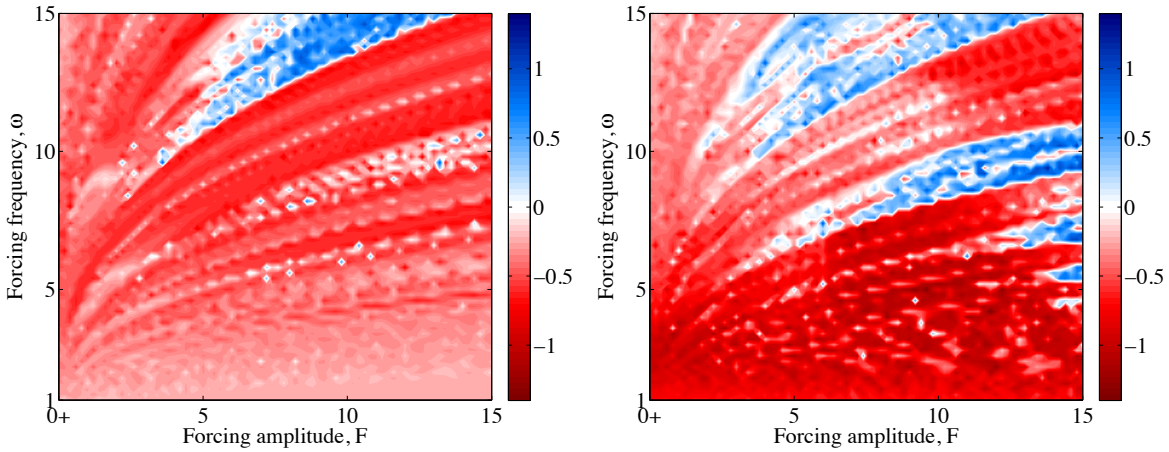

(c) USUT with $\Delta t = 1.0\times10^{-3}$

(d) OPSTROM with $\Delta t = 1.0\times10^{-3}$

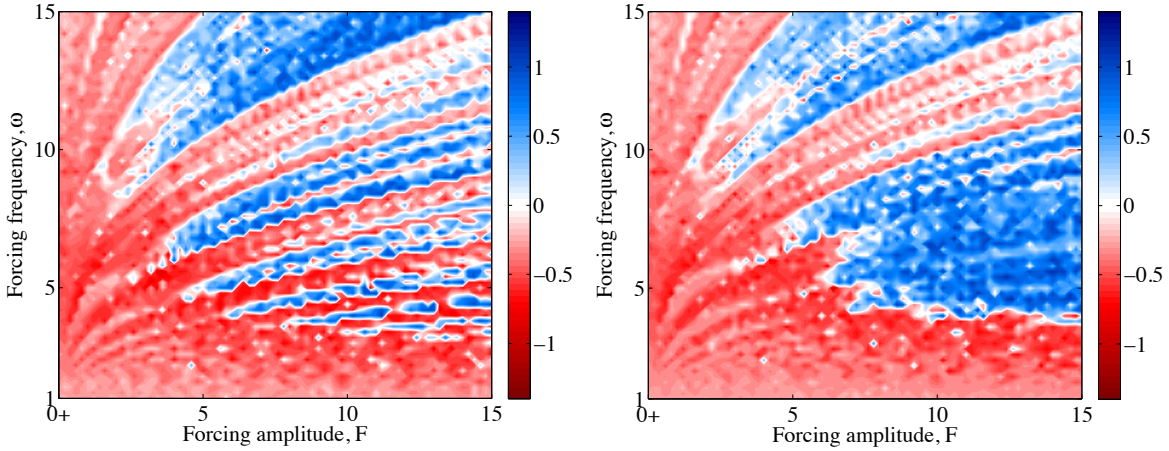

(e) USUT with $\Delta t = 1.0\times10^{-4}$

(f) OPSROM with $\Delta t = 1.0\times10^{-4}$

Figure 5.36: Lyapunov exponent maps for the SS beam in the forcing parameter space $F \in (0, 15] \times \omega \in [1, 15]$ with increments of $\Delta F = 0.2$ and $\Delta\omega = 0.2$. A total of 5,396 simulations are shown in each map. Additional chaotic regions may appear as the resolution is refined.

Timestep	USUT	OPSTROM
$\Delta t = 10^{-2}$	3.9	4.5
$\Delta t = 10^{-3}$	34.2	35.7
$\Delta t = 10^{-4}$	321.6	326.4

Table 5.5: Computation times (in terms of hours of CPU time) required to produce the Lyapunov exponent maps for the SS beam in Figure 5.34 with $\Delta x = 10^{-1}$ and the indicated Δt values. Similar FRS results for this problem would require several years of simulation.

the Lyapunov exponents for the standard USUT scheme in Figures 5.36a, 5.36c and 5.36e become more accurate as the Δt is refined from 10^{-2} to 10^{-3} and 10^{-4}. With this assumption, the OPSTROM (and OPSROM) results in Figures 5.36b, 5.36d and 5.36f appear to be more reliable. While the prediction of chaos is admittedly an inexact process, for a given resolution, the OPSTROM models appear to improve the reliability of the USUT predictions for the Lyapunov exponents.

The computation times required to produce the Lyapunov exponent maps in Figure 5.34 are summarized in Table 5.5. Given the computational resources allocated for this study, similar FRS results would require several years of simulation. As shown in Table 5.5, simulations with the USUT scheme (both standard and OPSTROM) can be carried out in a matter of hours.

5.4.7 Summary of results for the nonlinear beam

We demonstrated the capabilities of OPSTROM through a computational study of a simply supported nonlinear beam under the influence of time-periodic external forcing. We studied the performance of various ROM simulations (standard USUT, OPTROM, OPSROM and OPSTROM) with a coarse computational grid in space and time. Two different types of subgrid-scale models were investigated. For the first type of model, the required moments were calculated directly from FRS solutions. The second type of model was based upon estimated moments. Both models were based

upon a spatially homogeneous stochastic estimate with a one-point spatial stencil and a three-point temporal stencil.

Analysis of the direct subgrid-scale models allowed for appraisal by comparison with FRS solutions. Substantial errors were found in the standard ROM solutions for the beam response. The OPSTROM approach significantly improved predictions for all states, including the transverse displacement and velocity. Results in the form of Poincaré maps, phase portraits and temporal spectra compared favorably with the FRS. For certain parameters, the models were even able to prevent the onset of artificial chaos and regularity. All three variants of the direct models were investigated, including OPTROM, OPSROM and OPSTROM. In general, the OPSTROM model rendered the best performance of the three. For very small timesteps, however, the subgrid-scale accelerations diminished and became difficult to model. OPSROM then became the best option available.

Results for the models based upon estimated moments focused on three scenarios in which it is both practical and profitable to develop subgrid-scale models *a priori*. Each case involved the exploration of a large forcing parameter space. For the first scenario, bifurcation diagrams were accurately traced with a highly resolved standard ROM in 18 days. With a sweep of the forcing amplitude, symmetric periodic orbits split off into branches for asymmetric and multi-period orbits, followed by transient chaos, intermittency and full-fledged chaos. For larger forcing amplitudes, the chaotic trajectories eventually returned to symmetric orbits. An OPSTROM scheme qualitatively captured all of this behavior with a coarse grid in about six hours. The standard ROM failed to predict any bifurcations with the same grid. In the second scenario, contours for the number of zero velocity points per forcing cycle were accurately predicted with OPSTROM in a matter of hours as opposed to weeks with the standard ROM. A similar amount of computational savings were observed in the third and final scenario where OPSTROM was found to accurately predict regions

of chaos and regularity. Given the constraints on computational resources for this study, similar FRS predictions would require several years of processing time.

CHAPTER 6

Conclusion

In closing, we summarize the salient features of the proposed theoretical framework and provide a recap of the results for the four nonlinear dynamical systems. We also identify some areas for future research, most of which pertain to the development of efficient techniques for model construction.

6.1 Summary of proposed theoretical framework

In this dissertation, we presented a new data-driven reduced order modeling (ROM) framework called optimal spatiotemporal reduced order modeling (OPSTROM) for nonlinear dynamical systems. With the proposed framework, the governing equations for a general system are modified for an under-resolved simulation with an arbitrary discretization scheme and a coarse grid in space and time. Basic filtering concepts are used to derive residual terms referred to as subgrid-scale dynamics, which are typically neglected in standard ROMs. With the OPSTROM approach, these subgrid-scale dynamics are modeled using the optimal prediction formalism, which is based upon principles of mean-square error minimization, conditional expectations and stochastic estimation. These subgrid-scale models are designed to provide closure and reduce discretization errors by interacting with the coarse variables as the system evolves in space and time. As most multiscale models include some kind of knowledge or assumptions about the interactions between resolved scales and unresolved scales, the proposed models are formulated to include statistical information that is consistent with the underlying spatiotemporal statistical structure. This is the distinguishing

feature of the proposed OPSTROM framework.

The OPSTROM approach has practical application for a wide range of multiscale problems in computational physics and engineering. When a fully resolved simulation (FRS) is not feasible, the OPSTROM approach can be used to expedite simulations by coarsening the computational grid in space and time with an appropriate scheme (one that is stable, consistent and convergent) while maintaining reliable predictions for the quantities of interest. Several variants of the technique are in fact conceivable: standard ROM (which neglects the subgrid spatiotemporal structure), OPTROM (which accounts for the subgrid temporal structure), OPSROM (which accounts for the subgrid spatial structure), and OPSTROM (which accounts for the complete subgrid spatiotemporal structure). The OPTROM and OPSTROM variants are new, whereas OPSROM is analogous to the numerical method known as optimal large-eddy simulation (OLES) for turbulent flows.

Model construction requires inputs in the form of multi-point statistical moments amongst the state variables and subgrid-scale dynamics. In order to provide a sound derivation, we have assumed *a priori* knowledge of the required moments. We suggest such information can in principle be obtained from statistical analysis of fully resolved simulations, theory, experiments, or reconstructions from multiple sources. Practical utility of the proposed models is enhanced when the required moments display to some degree the following properties: spatiotemporal homogeneity, ergodicity, universality and smooth scaling with respect to the system parameters and computational grid. Spatiotemporal homogeneity, if observed, would imply that the same model can be used at every grid point and timestep in a simulation. Should smooth scaling be found, subgrid-scale models can be efficiently constructed by characterizing (or estimating) the required moments with empirical functions (or interpolants) based upon a select number of realizations. Once a model is established for a system, the OPSTROM approach can easily be implemented into any solver.

6.2 Summary of results for selected systems

Four nonlinear dynamical systems served as testbeds for the OPSTROM framework. The van der Pol and Duffing oscillators enabled us to focus exclusively on OPTROM and the effects of subgrid time scales. The viscous Burgers flow and nonlinear beam allowed us to test the OPTROM, OPSROM and OPSTROM variants for problems with spatiotemporal dependence. For each of the four systems, the objectives were (i) to characterize the subgrid-scale dynamics, and (ii) to determine which general ROM approach (standard ROM, OPTROM, OPSROM or OPSTROM) provides the best trade off between computational expense and accuracy. For the van der Pol and Duffing oscillators, fully resolved simulations were performed with an explicit fourth-order accurate time-marching scheme, whereas ROM simulations were carried out with a time spectral method and an implicit first-order accurate time-marching scheme. For the viscous Burgers flow and nonlinear beam problems, a second-order accurate central differencing scheme was used for spatial semi-discretization. In the time domain, fully resolved simulations were performed with an explicit fourth-order accurate time-marching scheme, and ROM simulations were also carried out with an implicit first-order accurate time-marching scheme.

Our study of the van der Pol oscillator demonstrated that the OPTROM approach is effective for autonomous systems. Temporal homogeneity and ergodicity were found to be excellent assumptions for the required statistical moments. Subgrid-scale models based upon direct calculation from FRS solutions and moment estimation were found to improve the accuracy of coarse time-marching and time-spectral simulations by one to two orders of magnitude. Solutions for the unknown frequency of oscillation experienced the greatest improvement, despite not being taken into account when deriving the models. This improvement is an indirect result of evolving the resolved states (displacement and velocity) more accurately. A special case was also discovered

for the time-spectral scheme: an exact subgrid-scale model (one with zero *a priori* and *a posteriori* error) can be derived when one harmonic is retained in the analysis. No other schemes with this property have been found.

Analysis of the forced Duffing oscillator revealed that the OPTROM approach is also effective for systems excited by external forcing. The subgrid-scale dynamics were characterized easily and accurately by means of moment estimation with respect to external forcing parameters. Temporal homogeneity and ergodicity were found to be excellent assumptions for the required statistical moments for both regular and chaotic response types. Time-marching simulations for the Duffing oscillator were expedited by coarsening the temporal grid. Substantial errors occurred in the form of strong numerical damping (which impedes the development of high frequency modes) and artificial regularity (in place of a true chaotic response). The OPTROM approach was shown to improve the reliability of predictions for both regular and chaotic response types. Time-spectral simulations were also carried out with subgrid-scale models based upon single-point and multi-point temporal stencils. As with the van der Pol oscillator, an exact subgrid-scale model was derived with one harmonic retained in the analysis. For higher fidelity simulations with multiple harmonics retained, models based upon multi-point temporal stencils performed best with respect to their ability to predict subharmonic structures (also referred to as undertones) in the response. For the time-marching and time-spectral schemes, the OPTROM approach provided the best trade off between computational expense and accuracy.

Numerical simulation of the viscous Burgers equation (nonlinear wave propagation with diffusion) allowed us to demonstrate application of the OPSTROM approach to a fluid dynamics problem with spatiotemporal dependence. Large-amplitude inflow disturbances were prescribed to excite the flow. Characterization of the subgrid-scale dynamics revealed spatial variation of the required multi-point moments and smooth scaling with respect to the flow parameters (Reynolds number and Strouhal number).

These observed properties enabled efficient construction of spatially heterogeneous subgrid-scale models with a relatively small amount of FRS data (sixteen solutions). We investigated the performance of the models by comparing various ROM solutions (standard ROM, OPTROM, OPSROM and OPSTROM) to the FRS. When used independently, simulations with the OPTROM and OPSROM models were found to be insufficient for error reduction. When used in conjunction, however, simulations with the OPSTROM models were in excellent agreement with the FRS. Enrichment was observed in both the spatial and temporal spectral modes. The best model for the subgrid spatial scales was found to be a quadratic estimate with a three-point central spatial stencil, whereas the best model for the subgrid temporal scales was found to be a linear estimate with a three-point backward temporal stencil. Simulations with OPSTROM models based upon estimated moments were found to be five times more accurate than the standard ROM in preserving the underlying spatiotemporal statistical structure for a given resolution in space and time.

In our most extensive example, we investigated the nonlinear structural dynamics of a geometrically nonlinear beam under the influence of time-dependent external forcing. The response of the beam with simply supported boundary conditions was the primary focus of the study, although we also considered briefly the response with clamped-clamped and clamped-free boundary conditions. A variety of trajectories were encountered in a parametric study of the beam dynamics, including symmetric time-periodicity, asymmetry, period N-tupling and chaos.

Through a characterization of the subgrid-scale dynamics for the nonlinear beam, the required statistical moments displayed a large degree of temporal homogeneity. A large degree of spatial homogeneity was also observed in the single-point, but not multi-point, spatial moments. It was also determined that the evolution of the random filtered field could be assumed to be an ergodic process for the purpose of model construction. The study of the multi-point correlations also determined

that the functional relationship between the spatiotemporal correlations and system parameters (both physical and computational) could be represented accurately with approximating functions constructed using a limited amount of FRS data (twenty-five solutions) and local bilinear interpolation. This finding is particularly noteworthy since, as previously mentioned, a variety of different trajectories were encountered in the parameter space, ranging in complexity from time-periodic periodic to chaotic. Finally, the required moments were found to depend on the form of the boundary conditions, and in this sense, the developed subgrid-scale models cannot be considered universal with respect to these problem constraints.

In order to determine the best ROM approach for the nonlinear beam, several types of subgrid-scale models were tested. Simulations with the standard ROM were found to be unreliable, often leading to large errors and incorrect predictions in the form of artificial chaos and regularity. Simulations with the OPTROM, OPSROM and OPSTROM variants improved the reliability of predictions for all states, including the transverse displacement and velocity. Results in the form of Poincaré maps, phase portraits and temporal spectra compared favorably with the FRS. For certain parameters, the models even prevented the onset of artificial chaos and regularity. Homogeneous models (in space and time) based upon a linear stochastic estimate with a three-point temporal and one-point spatial stencil were found to provide the best combination of accuracy and simplicity. Out of all the ROMs considered in this study, OPSTROM emerged as the best option available with a coarse spatiotemporal grid. As the temporal grid was refined, however, the subgrid-scale accelerations diminished and became difficult to model, in which case OPSROM became the best option.

With the best models established for the nonlinear beam, we conducted a series of numerical experiments designed to capture the complex bifurcation behavior of the dynamic response in a large forcing parameter space. For the first experiment, bifurcation diagrams were accurately traced with a highly resolved standard ROM

in eighteen days. With a sweep of the forcing amplitude, symmetric periodic orbits split off into branches for asymmetric and multi-period orbits, followed by transient chaos, intermittency and full-fledged chaos. For larger forcing amplitudes, the chaotic trajectories eventually returned to symmetric orbits. An OPSTROM scheme with a much coarser grid and subgrid-scale models based upon estimated moments captured all of this behavior in about six hours. The standard ROM failed to predict any bifurcations with the same grid. In the second numerical experiment, maps for the number of zero velocity points per forcing cycle were accurately predicted with OPSTROM in a matter of hours, as opposed to weeks with the standard ROM. In the third and final experiment, maps for the Lyapunov exponents were drawn with a specified level of accuracy one to two orders of magnitude faster with OPSTROM.

In summary, the subgrid-scale dynamics were easily characterized for each of the nonlinear dynamical systems with a small amount of FRS data. Model construction was greatly simplified for each problem due to the observed levels of spatiotemporal homogeneity and predictable scaling behavior in the required multi-point statistical moments with respect to the system parameters. Out of the four ROM variants (standard ROM, OPTROM, OPSROM, and OPSTROM), the OPSTROM approach was found to provide the best overall performance with a coarse computational grid.

6.3 Areas for future research

The theoretical advancements made in this dissertation have created some exciting opportunities for future research in the field of multiscale modeling. The OPSTROM approach has proven to be robust, versatile, and widely applicable to any nonlinear dynamical system. In this regard, an immediate impact can be made for a number of multiphysics problems which are gathering substantial interest in both industry and academia [123–125]. Fluid-structure interaction (FSI) problems [126, 127], for example, often require high-fidelity simulations (which are expensive to perform) and

could benefit greatly from the OPSTROM approach. In Appendix F, we demonstrate how the OPSTROM approach can be extended to enhance the reliability and efficiency of under-resolved simulations for FSI problems. First we discuss implementation with FSI problems in general, then we specialize the approach for an aeroelastic problem related to the field of flapping flight. In Appendix F, subgrid spatial and temporal scales are considered for both the fluid and structure. Details for discretization and dynamic coupling are also discussed.

Future work by the author and his advisors will concentrate on application of OPSTROM to large-scale problems in the fields of nonlinear fluid and structural dynamics. In particular, we are interested in applications to turbulent flows and nonlinear structural dynamical systems in which weak turbulence may occur. In the field of turbulent flows, it would be considered a major advancement if one could show that the OPSTROM approach may, in certain cases, be more effective than OLES (or OPSROM) in terms of computational efficiency and error reduction.

In addition to its intended application, it may be possible to modify or extend the OPSTROM framework for the purpose of nonlinear system identification [128, 129]. Such an approach would begin with *a priori* knowledge of the system response from measured experimental data. In order to derive a set of governing PDEs, one could assume a general system of the form $A\mathbf{u} = \boldsymbol{\mathcal{M}}$. Note the absence of the nonlinear force vector $\mathbf{R}$ in comparison to the general system in (2.1). Instead, we leave it to the stochastic estimate $\boldsymbol{\mathcal{M}}$ to determine which terms (both linear and nonlinear) should be retained in the governing equations. In order to determine the unknown stochastic estimation coefficients, we follow the direct calculation approach developed in Chapter 2, with the exception that the statistical moments required for model construction come from measured experimental data instead of an FRS solution. In this sense, it may be possible to derive a set of governing equations with the optimal prediction formalism as an alternative to physical laws and assumptions, as illustrated

in Figure 1.1. With this approach, it may also be possible to reduce epistemic errors with the nonlinear system identification approach in addition to discretization errors with OPSTROM. As an example to support what may seem to be an adventurous proposal, a number of studies in the field of LES [130–133] have used measured experimental data from turbulent flows to derive (or tune) the unknown coefficients for Smagorinsky-type subgrid-scale viscosity models [38, 39].

The remainder of this concluding section will discuss a number of unanswered questions which remain in regards to the construction of optimal subgrid-scale models. First of all, additional work can be done to identify trends and perhaps establish some general rules for choosing the functional form of the stochastic estimate. In other words, for a given system, it would be helpful to know *a priori* which model design parameters, including the power series order (linear, quadratic, cubic) and stencil sizes (M_S, M_T, M_S), are likely to provide the best estimates. Furthermore, there exists a need to determine the conditions under which one may assume a model to be spatially homogeneous and perhaps universal. For some systems, it may be possible to obtain the multi-point statistical moments required for model construction from theory as an alternative to FRS simulations or experimental data. Finally, from a continuum mechanics perspective, it may also be possible to construct a unified subgrid-scale model for the general field equations as a function of the constitutive parameters.

With regards to the order of the stochastic estimate, the obvious choice would be to choose a model which matches the highest order of the nonlinear terms in the governing PDEs. For example, in order to model the subgrid-scale convection in the viscous Burgers flow (which contains a second-order nonlinearity), we selected a quadratic stochastic estimate, owing to the observation of its superior performance in comparison to a linear stochastic estimate. This choice aligns with the quadratic estimates selected in previous works [69, 70] to model the subgrid-scale convection for OLES of turbulent flows. Langford and Moser stated [67] that quadratic estimates

should in general be required for the Navier-Stokes equations. However, Langford and Moser also stated [67] that multi-point linear estimates may at times be sufficient if it can be shown that the flow is Galilean invariant. A number of *a priori* testing procedures have also been proposed by Meneveau [130] in order to determine the correct functional form of subgrid-scale models.

The choice of the order for the stochastic estimate is not always straightforward, however, as we recall our study of the Duffing oscillator for which a linear estimate was found to perform better than a cubic estimate, despite the third-order nonlinearity in the restoring force. This surprising result was attributed to the use of poorly correlated data required as inputs for the high-order models [65, 66, 68]. Similarly, for the nonlinear beam problem, a linear estimate was found to provide the best predictions, despite the third-order nonlinearities in the restoring force. In addition to our previous explanation, it may also help to consider the *dominant* order of the nonlinearity in the governing equations. For example, given the small transverse displacements for the nonlinear beam ($u \ll 1$), the first-order components of the restoring force are orders of magnitude stronger than third-order components. This in fact may be the primary cause for the poorly correlated data in the higher-order models. Future work could be done to clarify this issue.

The spatial stencil size chosen for a subgrid-scale model should be influenced by several issues, including (i) the spatial domain of influence on the subgrid-scale dynamics, (ii) the amount of information used in the spatial discretization scheme, (iii) the computational expense required for a given stencil, and (iv) the amount of pre-processing required to obtain the required inputs. In general, the subgrid-scale dynamics may be influenced by the entire spatial domain. For many systems, though, one might expect a stronger functional dependence on information from nearby spatial locations. Nevertheless, issue (i) is certainly problem-dependent. With regards to issue (ii), a good choice for the stencil size may be to match that of the spatial

discretization scheme. Such a choice would also correspond to a consistent filter used to derive the subgrid-scale dynamics. In this dissertation, for example, a second-order accurate central differencing scheme (a three-point spatial stencil) was used for the viscous Burgers flow. Coincidentally, a three-point spatial stencil was found to provide the best estimate for the subgrid-scale convection and diffusion. For the nonlinear beam problem, however, we avoided the use of multi-point spatial stencils in order to construct a spatially homogeneous model. For the beam, a one point model was found to provide reasonable predictions, perhaps due to the relative lack of spatial complexity. Previous works in OLES have used various multi-point spatial stencils to model subgrid-scale convection and diffusion, including one-point [67], two-point [65], three-point [70], and even up to 125-point ($5\times5\times5$) stencils [68,134]. Efforts have also been taken [70,134] to design skew-symmetric stencils [135] with symmetry-preserving properties in order to avoid numerical pathologies such as instability. Finally, the detrimental effects associated with issues (iii) and (iv) could influence one to avoid using excessively large spatial stencils.

Similarly, the temporal stencil size chosen for the model could include any portion of the history from zero to present time. Including non-Markovian memory effects has been shown to improve predictions for some systems [62,105]. In this work, it was found that increasing the multi-point temporal stencil size improved predictions for the subgrid-scale accelerations with a coarse temporal grid. There are complications, however, with using too much data in the estimate [65,66,68]. Retaining information from distant timesteps can lead to poorly correlated data and worsen the estimate. Moreover, for the nonlinear beam problem, the multi-point temporal moments became indistinguishable as the temporal grid was refined. From a computational standpoint, the memory required for storing information from previous timesteps can also become prohibitive for high dimensional systems. Future work could perhaps shed some light on the chosen stencil size in both space and time.

As discussed in the previous section, universal behavior [79] was not found in the subgrid-scale models for the nonlinear beam. The multi-point moments required for model construction appeared to be sensitive to the boundary conditions throughout the entire spatial domain. We hypothesized that weak turbulence [115, 116], and the subsequent loss of spatial correlation, may in some cases be required for universal behavior in nonlinear structural dynamical systems. Even with weak turbulence, however, one might still expect the subgrid-scale dynamics to be spatially nonhomogeneous near the structural boundaries. This hypothesis is similar in concept to wall effects in turbulent flows [2]. Previous research in LES for turbulent flows has addressed the need for spatially heterogeneous models near wall boundaries [136, 137]. Similar methods could be developed for the OPSTROM approach with nonlinear structural dynamical systems.

Finally, from a continuum mechanics perspective, it may be possible to construct universal subgrid-scale models for the general field equations [138]. Such a task would effectively remove the problem-dependence from the model construction process. The models would simply depend on each of the system parameters in addition to the chosen discretization scheme. For example, a three-dimensional anisotropic Hookean material would in general require characterization with respect to 21 independent constitutive parameters [138]. Material symmetries would decrease this functional dependence to 9 parameters (orthotropic), 5 parameters (transverse isotropic), and 2 parameters (isotropic). Of course, materials with nonlinear, viscous, and plastic behavior would introduce additional complexities. External forcing parameters should also be taken into account. Some degree of spatial homogeneity and universal behavior would also be required if such models are to be independent of problem geometry. We acknowledge that this final proposal for future research may seem like a daunting task, but we also emphasize from an interdisciplinary perspective the tremendous value such models could potentially provide.

Bibliography

[1] S. H. Strogatz. *Nonlinear dynamics and chaos: with applications to physics, biology, chemistry, and engineering*. Perseus Books, Cambridge, MA, 1994.

[2] S. B. Pope. *Turbulent Flows*. Cambridge University Press, Cambridge, 2000.

[3] J. Fish. Bridging the scales in nano engineering and science. *Journal of Nanoparticle Research*, 8:577–594, 2006.

[4] W. L. Oberkampf, Sharon M DeLand, B. M. Rutherford, Kathleen V. Diegert, and Kenneth F. Alvin. Error and uncertainty in modeling and simulation. *Reliability Engineering and System Safety*, 75:333–357, 2002.

[5] J. Kaipo and E. Somersalo. *Statistical and Computational Inverse Problems*. Springer, New York, 2005.

[6] D. Calvetti and E. Somersalo. *Introduction to Bayesian Scientific Computing*. Springer, New York, 2007.

[7] P. J. Roache. Verification of codes and calculations. *AIAA Journal*, 36(5):696–702, 1998.

[8] J. C. Butcher. *Numerical Methods for Ordinary Differential Equations*. John Wiley & Sons, New York, 2003.

[9] T. Belytschko. *Nonlinear Finite Elements for Continua and Structures*. John Wiley and Sons, 2000.

[10] J. C. Tannehill, D. A. Anderson, and R. H. Pletcher. *Computational Fluid Mechanics and Heat Transfer*. Taylor and Francis, Philadelphia, PA, second edition, 1997.

[11] W. Cheney and D. Kincaid. *Numerical Mathematics and Computing*. Brooks/Cole, Belmont, CA, 2004.

[12] R. W. Hamming. *Numerical Methods for Scientists and Engineers*. McGraw-Hill, New York, 1973.

[13] W. E, B. Engquist, X. Li, W. Ren, and E. Vanden-Eijnden. Heterogeneous multiscale methods: A review. *Communications in Computational Physics*, 2(3):367–450, 2007.

[14] M. F. Horstemeyer. Multiscale modeling: A review. *Practical Aspects of Computational Chemistry*, pages 87–135, 2009.

[15] Z. Bai, P. M. Dewilde, and R. W. Freund. Reduced-order modeling. *Numerical Analysis Manuscript No. 02-4-13, Bell Laboratories*, 2002.

[16] D. J. Lucia, P. S. Beran, and W. A. Silva. Reduced-order modeling: New approaches for computational physics. *Progress in Aerospace Sciences*, 40:51–117, 2004.

[17] J. N. Reddy. *Energy Principles and Variational Methods in Applied Mechanics*. John Wiley & Sons, New Jersey, second edition, 2002.

[18] D. J. Inman. *Engineering Vibration*. Prentice Hall, New Jersey, third edition, 2008.

[19] N. Kryloff and N. Bogoliuboff. *Introduction to Nonlinear Mechanics*. Princeton University Press, Princeton, NJ, 1947.

[20] G. Dimitriadis. Continuation of higher-order harmonic balance solutions for nonlinear aeroelastic systems. *Journal of Aircraft*, 45(2):523–537, 2008.

[21] G. Berkooz, P. Holmes, and J. L. Lumley. The proper orthogonal decomposition in the analysis of turbulent flows. *Annual Review of Fluid Mechanics*, 25:539–575, 1993.

[22] J. P. Boyd. *Chebyshev and Fourier Spectral Methods*. Springer-Verlag, Berlin, 1989.

[23] P. S. Symonds and T. X. Yu. Counterintuitive behavior in a problem of elastic-plastic beam dynamics. *Journal of Applied Mechanics*, 52:517–522, 1985.

[24] R. D. Cook, D. S. Malkus, M. E. Plesha, and R. J. Witt. *Concepts and Applications of Finite Element Analysis*. John Wiley & Sons, New York, fourth edition, 2002.

[25] W. K. Liu and H. S. Park. Bridging scale methods for computational nanotechnology. In *Handbook of Theoretical and Computational Nanotechnology*. 2005.

[26] W. K. Liu, E. G. Karpov, and H. S. Park. *Nano Mechanics and Materials: Theory, Multiscale Methods and Applications*. John Wiley & Sons, 2006.

[27] T. Belytschko and X. Xiao. Coupling methods for continuum model with molecular model. *International Journal for Multiscale Computational Engineering*, 1:115–126, 2003.

[28] G. J. Wagner and W. K. Liu. Coupling of atomistic and continuum simulations using a bridging scale decomposition. *Journal of Computational Physics*, 190(1):249–274, 2003.

[29] W. K. Liu, H. S. Park, D. Qian, E. G. Karpov, H. Kadowaki, and G. J. Wagner. Bridging scale methods for nanomechanics and materials. *Computer Methods in Applied Mechanics and Engineering*, 195(23):1407–1421, 2006.

[30] H. Kadowaki and W. K. Liu. Bridging multi-scale method for localization problems. *Computer Methods in Applied Mechanics and Engineering*, 193:3267–3302, 2004.

[31] W. Ren and W. E. Heterogeneous multiscale method for the modeling of complex fluids and microfluidics. *Journal of Computational Physics*, 204(1):1–26, 2005.

[32] B. Perthame. Second order Boltzmann-type schemes for compressible Euler equations in one and two space dimensions. *SIAM Journal on Numerical Analysis*, 29:1–19, 1992.

[33] K. Xu and K. H. Pendergast. Numerical Navier-Stokes solutions from gas kinetic theory. *Journal of Computational Physics*, 114:9–17, 1994.

[34] P. Moin and K. Mahesh. Direct numerical simulation: A tool for turbulence research. *Annual Review of Fluid Mechanics*, 30:539–578, 1998.

[35] M. Lesieur and O. Metais. New trends in large-eddy simulations of turbulence. *Annual Review of Fluid Mechanics*, 28:45–82, 1996.

[36] S. Ghosal. An analysis of numerical errors in large-eddy simulations of turbulence. *Journal of Computational Physics*, 125:187–206, 1996.

[37] A. N. Kolmogorov. The local structure of turbulence in incompressible viscous fluid for very large reynolds numbers. *Dokl. Akad. Nauk SSSR*, 30:299–303, 1941.

[38] J. Smagorinsky. General circulation experiments with the primitive equations. *Monthly Weather Review*, 91:99–164, 1963.

[39] M. Germano, U. Piomelli, P. Moin, and W. H. Cabot. A dynamic subgrid-scale eddy viscosity model. *Physics of Fluids*, 3:1760–1765, 1991.

[40] T. J. R. Hughes, G. R. Feijoo, L. Mazzei, and J. B. Quincy. The variational multiscale method—a paradigm for computational mechanics. *Computer Methods in Applied Mechanics and Engineering*, 166:3–24, 1998.

[41] T. J. R. Hughes. Multiscale phenomena: Green's functions, the Dirichlet-to-Neumann formulation, subgrid scale models, bubbles and the origins of stabilized methods. *Computer Methods in Applied Mechanics and Engineering*, 127:387–401, 1995.

[42] T. J. R. Hughes and J. R. Steward. A space-time formulation for multiscale phenomena. *Journal of Computational and Applied Mathematics*, 74:217–229, 1996.

[43] W. K. Liu, Y. Chen, R. A. Uras, and C. T. Chang. Generalized multiple scale reproducing kernel methods. *Computer Methods in Applied Mechanics and Engineering*, 139(1):91–157, 1996.

[44] J. Fish, V. Filonova, and Z. Yuan. Reduced order computational continua. *Computer Methods in Applied Mechanics and Engineering*, 221–222:104–116, 2012.

[45] A. Abdulle and W. E. Finite difference heterogeneous multi-scale method for homogenization problems. *Journal of Computational Physics*, 191:18–39, 2003.

[46] B. Engquist and Y. H. Tsai. Heterogeneous multiscale methods for stiff ordinary differential equations. *Mathematics of Computation*, 74:1707–1742, 2005.

[47] R. Sharp, Y. H. Tsai, and B. Engquist. Multiple time scale methods for the inverted pendulum problem. *Proceedings of Convergence on Multiscale Methods in Science and Engineering, Lecture Notes in Computational Science and Engineering, Springer Verlag*, 44:233–244, 2005.

[48] W. E and X. Y. Yue. Analysis of multiscale methods for stochastic differential equations. *Communications on Pure and Applied Mathematics*, 58(11):1544–1585, 2005.

[49] E. Vanden-Eijnden. Numerical techniques for multiscale dynamical systems with stochastic effects. *Communications in Mathematical Sciences*, 1(2):385–391, 2003.

[50] P. Smolinski, T. Belytschko, and M. Neal. Multi-time-step integration using nodal partitioning. *International Journal for Numerical Methods in Engineering*, 26(2):349–359, 1998.

[51] A. Gravouil and A. Combescure. Multi-time-step and two-scale domain decomposition method for non-linear structural dynamics. *International Journal for Numerical Methods in Engineering*, 58:1545–1569, 2003.

[52] Q. Yu and J. Fish. Multiscale asymptotic homogenization for multiphysics problems with multiple spatial and temporal scales: a coupled thermo-viscoelastic example problem. *International Journal of Solids and Structures*, 39:6429–6452, 2002.

[53] C. L. Bottasso. Multiscale temporal integration. *Computer Methods in Applied Mechanics and Engineering*, 191:2815–2830, 2002.

[54] M. Slemrod and A. Acharya. Time-averaged coarse variables for multi-scale dynamics. *Quarterly of Applied Mathematics*, 70:793–803, 2012.

[55] A. Ammar, F. Chinesta, E. Cueto, and M. Doblaré. Proper generalized decomposition of time-multiscale models. *International Journal for Numerical Methods in Engineering*, 90(5):569–596, 2012.

[56] D. Givon, R. Kupferman, and A. Stuart. Extracting macroscopic dynamics: Model problems and algorithms. *Nonlinearity*, 17:55–127, 2004.

[57] H. Mori. Transport, collective motion and Brownian motion. *Progress of Theoretical Physics*, 33:423–450, 1965.

[58] R. Zwanzig. Nonlinear generalized Langevin equations. *Journal of Statistical Physics*, 9:215–220, 1973.

[59] A. J. Chorin, A. P. Kast, and R. Kupferman. Optimal prediction of underresolved dynamics. *Proceedings of the National Academy of Sciences of the United States of America*, 95(8):4094–4098, 1998.

[60] A. J. Chorin, O. H. Hald, and R. Kupferman. Optimal prediction and the Mori-Zwanzig representation of irreversible processes. *Proceedings of the National Academy of Sciences of the United States of America*, 97(7):2968–2973, 2000.

[61] A. J. Chorin, R. Kupferman, and D. Levy. Optimal prediction for Hamiltonian partial differential equations. *Journal of Computational Physics*, 162:267–297, 2000.

[62] A. J. Chorin, O. H. Hald, and R. Kupferman. Optimal prediction with memory. *Physica D*, 166:239–257, 2002.

[63] H. Grabert. *Projection Operator Techniques in Nonequilibrium Statistical Mechanics*. Springer, Berlin, 1982.

[64] E. Fick and G. Sauerman. *The Quantum Statistics of Dynamical Processes*. Springer, Berlin, 1990.

[65] R. Adrian, B. Jones, M. Chung, Y. Hassan, C. Nithianandan, and A. Tung. Approximation of turbulent conditional averages by stochastic estimation. *Physics of Fluids*, 1:992–998, 1989.

[66] R. Adrian. Stochastic estimation of subgrid-scale motions. *Applied Mechanics Review*, 43:214–218, 1990.

[67] J. Langford and R. D. Moser. Optimal LES formulations for isotropic turbulence. *Journal of Fluid Mechanics*, 398:321–346, 1999.

[68] P. S. Zandonade, J. A. Langford, and R. D. Moser. Finite volume optimal large-eddy simulation of isotropic turbulence. *Physics of Fluids*, 16:2255–2271, 2004.

[69] P. Vedula, R. D. Moser, and P. S. Zandonade. Validity of quasinormal approximation in turbulent channel flow. *Physics of Fluids*, 17(055106):1–9, 2005.

[70] P. Vedula, R. D. Moser, and R. J. Adrian. Optimal large-eddy simulation based on coarse sampling. *Unpublished report*, 2005.

[71] R. D. Moser, N. Malaya, H. Chang, P. S. Zandonade, P. Vedula, A. Bhattacharya, and A. Hasselbacher. Theoretically based optimal large-eddy simulation. *Physics of Fluids*, 21(105104), 2009.

[72] G. He, R. Rubinstein, and L. P. Wang. Effects of subgrid-scale modeling on the correlations in large eddy simulation. *Physics of Fluids*, 14:2186–2193, 2002.

[73] G. He, M. Wang, and S. K. Lele. On the computation of space-time correlations by large eddy simulation. *Physics of Fluids*, 16:3859–3867, 2004.

[74] A. LaBryer, P. J. Attar, and P. Vedula. An optimal prediction method for underresolved time-marching and time-spectral schemes. *International Journal for Multiscale Computational Engineering*, accepted article in press.

[75] A. LaBryer, P. J. Attar, and P. Vedula. A framework for optimal temporal reduced order modeling of nonlinear dynamical systems. *Journal of Sound and Vibration*, 332(4):993–1010, 2013.

[76] A. LaBryer, P. J. Attar, and P. Vedula. Optimal spatiotemporal reduced order modeling, Part I: Proposed framework. *Computational Mechanics*, accepted article in press.

[77] A. LaBryer, P. J. Attar, and P. Vedula. Optimal spatiotemporal reduced order modeling, Part II: Application to a nonlinear beam. *Computational Mechanics*, accepted article in press.

[78] A. LaBryer, P. J. Attar, and P. Vedula. Characterization of subgrid-scale dynamics for a nonlinear beam. *Journal of Computers and Structures*, under review.

[79] L. P. Kadanoff. Scaling and universality in statistical physics. *Physica A*, 163:1–14, 1990.

[80] T. J. R. Hughes, L. Mazzei, and K. E. Jansen. Large eddy simulation and the variational multiscale method. *Computing and Visualization in Science*, 3:47–59, 2000.

[81] G. Düring, C. Josserand, and S. Rica. Weak turbulence for a vibrating plate: can one hear a Kolmogorov spectrum? *Physical Review Letters*, 97(2):025503, 2006.

[82] F. M. Najjar and D. K. Tafti. Study of discrete test filters and finite difference approximations for the dynamic subgrid-scale stress model. *Physics of Fluids*, 8(4):1076–1088, 1996.

[83] G. D. Birkhoff. What is the ergodic theorem? *The American Mathematical Monthly*, 49(4):222–226, 1942.

[84] C. C. Moore. Ergodicity of flows on homogeneous spaces. *American Journal of Mathematics*, 88(1):154–178, 1966.

[85] L. Liu, J. P. Thomas, E. H. Dowell, and P. Attar. A comparison of classical and high dimensional harmonic balance approaches for a Duffing oscillator. *Journal of Computational Physics*, 215:298–320, 2006.

[86] K. C. Hall, J. P. Thomas, and W. S. Clark. Computation of unsteady nonlinear flows in cascades using a harmonic balance technique. *AIAA Journal*, 40(5):879–886, 2002.

[87] J. P. Thomas, J. P. Dowell, and K. C. Hall. Nonlinear inviscid aerodynamic effects on transonic divergence, flutter, and limit cycle oscillations. *AIAA Journal*, 40(4):638–646, 2002.

[88] A. LaBryer and P. J. Attar. A harmonic balance approach for large-scale problems in nonlinear structural dynamics. *Journal of Computers and Structures*, 88(17–18):1002–1017, 2010.

[89] L. Liu, E. H. Dowell, and K. C. Hall. A novel harmonic balance analysis for the van der Pol oscillator. *International Journal of Non-Linear Mechanics*, 42:2–12, 2007.

[90] S. A. Orszag. On the elimination of aliasing in finite difference schemes by filtering high-wavenumber components. *Journal of Atmospheric Sciences*, 28:1074, 1971.

[91] A. LaBryer and P. J. Attar. High dimensional harmonic balance dealiasing techniques for a Duffing oscillator. *Journal of Sound and Vibration*, 324:1016–1038, 2009.

[92] B. van der Pol. On relaxation oscillations. *The London, Edinburgh and Dublin Philosophical Magazine & Journal of Science*, 2(7):978–992, 1927.

[93] U. Parlitz and W. Lauterborn. Period-doubling cascades and devil's staircases of the driven van der Pol oscillator. *Physical Review A*, 36(3):1428–1434, 1987.

[94] G. Duffing. *Erzwungene Schwingungen bei veranderlicher Eigenfrequenz und ihre technische Bedeutung*. Heft 41/42, Braunschweig, 1918.

[95] P. Holmes. A nonlinear oscillator with a strange attractor. *Philosophical Transactions of the Royal Society*, 292(1394):419–448, 1979.

[96] L. N. Virgin. *Introduction to Experimental Nonlinear Dynamics*. Cambridge University Press, Cambridge, 2000.

[97] T. Kalmar-Nagy and B. Balachandran. Forced harmonic vibration of the Duffing oscillator with linear viscous damping. In I. Kovacic and M. Brennan, editors, *Duffing's Equation: Non-linear Oscillators and their Behaviour*. Wiley, 2011.

[98] J. M. Burgers. A mathematical model illustrating the theory of turbulence. *Advances in Applied Mechanics*, 1:171–199, 1948.

[99] E. Hopf. The partial differential equation $u_t + uu_x = \mu u_{xx}$. *Communications on Pure and Applied Mathematics*, 3:201–230, 1950.

[100] M. J. Lighthill. Viscosity effects in sound waves of finite amplitude. *Surveys in Mechanics*, pages 249–350, 1956.

[101] D. T. Blackstock. Convergence of the Keck-Boyer perturbation solution for plane waves of finite amplitude in a viscous fluid. *Journal of the Acoustical Society of America*, 39:411–413, 1966.

[102] J. P. Bouchaud, M. Mezard, and G. Parisi. Scaling and intermittency in Burgers turbulence. *Physical Review E*, 52:3656–3674, 1995.

[103] R. C. Maple, P. I. King, J. M. Wolff, and P. D. Orkwis. Split-domain harmonic balance solutions to Burgers' equation for large-amplitude disturbances. *AIAA Journal*, 206(2):206, 2003.

[104] A. Das and R. D. Moser. Optimal large-eddy simulation of forced Burgers equation. *Physics of Fluids*, 14(12):4344–4351, 2002.

[105] D. Bernstein. Optimal prediction of Burgers's equation. *Multiscale Modeling & Simulation*, 6:27–52, 2007.

[106] D. Givoli. Non-reflecting boundary conditions. *Journal of Computational Physics*, 94:1–29, 1991.

[107] M. R. M. Crespo da Silva. Non-linear flexural-flexural-torsional-extensional dynamics of beams - I. Formulation. *International Journal of Solids and Structures*, 24(12):1225–1234, 1988.

[108] M. R. M. Crespo da Silva. Non-linear flexural-flexural-torsional-extensional dynamics of beams - II. Response analysis. *International Journal of Solids and Structures*, 24(12):1235–1242, 1988.

[109] E. K. Hall and S. V. Hanagud. Chaos in a single equilibrium point system: finite deformations. *Nonlinear Dynamics*, 2:157–170, 1991.

[110] M. R. M. Crespo da Silva. Non-linear flexural-flexural-torsional dynamics of inextensional beams - I. Equations of motion. *Journal of Structural Mechanics*, 6(4):437–448, 1978.

[111] M. R. M. Crespo da Silva. Non-linear flexural-flexural-torsional dynamics of inextensional beams - II. Forced motions. *Journal of Structural Mechanics*, 6(4):449–461, 1978.

[112] B. A. Freno and P. G. A. Cizmas. An investigation into the significance of the non-linear terms in the equations of motion for a cantilevered beam. *International Journal of Non-Linear Mechanics*, 47:84–95, 2012.

[113] A. Papoulis and S. Unnikrishna Pillai. *Probability, Random Variables and Stochastic Processes*. McGraw-Hill, New York, 2002.

[114] N. S. Abhyankar. *Studies in nonlinear structural dynamics: Chaotic behavior and Poynting effect*. PhD thesis, Georgia Institute of Technology, 2001.

[115] P. Manneville. *Dissipative structures and weak turbulence*. Academic Press, Boston MA, 1990.

[116] R. R. Reynolds, L. N. Virgin, and E. H. Dowell. High-dimensional chaos can lead to weak turbulence. *Nonlinear Dynamics*, 4:531–546, 1993.

[117] S. Rugonyi and K. J. Bathe. An evaluation of the Lyapunov characteristic exponent of chaotic continuous systems. *International Journal for Numerical Methods in Engineering*, 56:145–163, 2003.

[118] A. R. Zeni and J. A. C. Gallas. Lyapunov exponents for a Duffing oscillator. *Physica D*, 89:71–82, 1995.

[119] E. H. Dowell and C. Pezeshki. On necessary and sufficient conditions for chaos to occur in Duffing's equation: a heuristic approach. *Journal of Sound and Vibration*, 121(2):195–200, 1988.

[120] J. R. Munkres. *Topology*. Prentice Hall, New Jersey, second edition, 1999.

[121] P. F. Wang, G. Huang, and Z. Z. Wang. Analysis and application of multiple precision computation and round-off error for nonlinear dynamical systems. *Advances in Atmospheric Sciences*, 23:758–766, 2006.

[122] S. Chakraborty, U. Frisch, W. Pauls, and S. S. Ray. Nelkin scaling for the Burgers equation and the role of high-precision calculations. *Physical Review E*, 85(015301):1–4, 2012.

[123] W. B. J. Zimmerman. *Multiphysics Modeling with Finite Elements*. World Scientific Publishing Co., London, 2006.

[124] D. A. Bader. *Petascale Computing: Algorithms and Applications*. Chapman & Hall, Boca Raton, FL, 2008.

[125] R. I. Borja. *Multiscale and Multiphysics Processes in Geomechanics*. Springer-Verlag, Berlin, 2011.

[126] H. J. Bungartz and M. Schafer. *Fluid-Structure Interaction: Modelling, Simulation, Optimization*. Springer-Verlag, Berlin, 2006.

[127] M. P. Paidoussis, S. J. Price, and E. de Langre. *Fluid-Structure Interactions: Cross-Flow Induced Instabilities*. Cambridge University Press, New York, first edition, 2011.

[128] O. Nelles. *Nonlinear System Identification*. Springer-Verlag, Berlin, first edition, 2000.

[129] G. Kerschen, K. Worden, A. F. Vakakis, and J. C. Golinval. Past, present and future of nonlinear system identification in structural dynamics. *Mechanical Systems and Signal Processing*, 20:505–592, 2006.

[130] C. Meneveau. Statistics of turbulence subgrid-scale stresses: Necessary conditions and experimental tests. *Physics of Fluids*, 6:353–833, 1994.

[131] J. Kleissl, M. B. Parlange, and C. Meneveau. Field experimental study of dynamic Smagorinsky models in the atmospheric surface layer. *Journal of Atmospheric Sciences*, 61(18):2296–2307, 2004.

[132] E. Bou-Zeid, C. Meneveau, and M. Parlange. A scale-dependent Lagrangian dynamic model for large eddy simulation of complex turbulent flows. *Physics of Fluids*, 17(025105):1–18, 2005.

[133] E. Bou-Zeid, N. Vercauteren, M. B. Parlange, and C. Meneveau. Scale dependence of subgrid-scale model coefficients: an a priori study. *Physics of Fluids*, 20(115106):1–6, 2008.

[134] J. A. Langford and R. D. Moser. Breakdown of continuity in large-eddy simulation. *Physics of Fluids*, 13:1524–1528, 2001.

[135] R. W. C. P. Verstappen and A. E. P. Veldman. Symmetry-preserving discretization of turbulent flow. *Journal of Computational Physics*, 187:343–368, 2003.

[136] S. Ghosal and P. Moin. The basic equations for the large-eddy simulation of turbulent flows in complex geometries. *Journal of Computational Physics*, 118:24–37, 1995.

[137] O. V. Vasilyev, T. S. Lund, and P. Moin. A general class of commutative filters for LES in complex geometries. *Journal of Computational Physics*, 146:82–104, 1998.

[138] Y. C. Fung. *A First Course in Continuum Mechanics*. Prentice Hall, New Jersey, third edition, 1994.

[139] F. M. White. *Viscous Fluid Flow*. McGraw-Hill, New York, third edition, 2006.

[140] E. H. Dowell. *A Modern Course in Aeroelasticity*. Kluwer Academic Publishers, The Netherlands, fourth edition, 2004.

[141] J. R. Wright and J. E. Cooper. *Introduction to Aircraft Aeroelasticity and Loads*. John Wiley and Sons, England, 2007.

[142] M. D. Greenberg. *Advanced Engineering Mathematics*. Prentice Hall, Englewood Cliffs, NJ, second edition, 1998.

[143] J. B. Frandsen. Numerical bridge deck studies using finite elements, Part I: Flutter. *Journal of Fluids and Structures*, 19:171–191, 2004.

[144] T. Weis-Fogh. Quick estimates of flight fitness in hovering animals, including novel mechanisms for lift production. *Journal of Experimental Biology*, 59:169–230, 1973.

[145] W. Nachtigall. *Insects in Flight*. McGraw-Hill, New York, 1974.

[146] S. Ho, H. Nassef, N. Pornsinsirirak, Y. C. Tai, and C. M. Ho. Unsteady aerodynamics and flow control for flapping wing flyers. *Progress in Aerospace Sciences*, 39:635–681, 2003.

[147] M. Lighthill. Hydromechanics of aquatic animal propulsion. *Annual Review of Fluid Mechanics*, 1:413–445, 1969.

[148] J. Rayner. Thrust and drag in flying birds: Applications to birdlike micro air vehicles hydromechanics of aquatic animal propulsion. In *Fixed and Flapping Wing Aerodynamics for Micro Air Vehicle Applications*, volume 195, pages 217–230. AIAA, Reston, VA, 2001.

[149] J. S. Lee. *Numerical Study on Flapping-Airfoil Design and Unsteady Mechanism of Two-Dimensional Insect Wing*. PhD thesis, Seoul National University, 2006.

[150] K. Isogai, Y. Shinmoto, and Y. Watanabe. Effects of dynamic stall on propulsive efficiency and thrust of flapping airfoil. *AIAA Journal*, 37(10):1145–1151, 1999.

[151] K. Hall and S. Hall. A rational engineering analysis of the efficiency of flapping flight. In *Fixed and Flapping Wing Aerodynamics for Micro Air Vehicle Applications*, volume 195, pages 217–230. AIAA, Reston, VA, 2001.

[152] S. Heathcote, Z. Wang, and I. Gursul. Effect of spanwise flexibility on flapping wing propulsion. *Journal of Fluids and Structures*, 24:183–199, 2008.

[153] S. Heathcote and I. Gursul. Flexible flapping airfoil propulsion. *AIAA Journal*, 45(5):1066–1079, 2007.

[154] Y. Lian, W. Shyy, D. Viieru, and B. Zhang. Membrane wing aerodynamics for micro air vehicles. *Progress in Aerospace Sciences*, 39:425–465, 2003.

[155] W. Shyy, P. Ifju, and D. Viieru. Membrane wing-based micro air vehicles. *Applied Mechanics Reviews*, 58:283–301, 2005.

[156] R. Gordnier. High fidelity computational simulation of a membrane wing airfoil. *Journal of Fluids and Structures*, 5:897–917, 2009.

[157] M. R. Visbal and R. Gordnier. High-fidelity simulations of moving and flexible airfoils at low reynolds numbers. In *Animal Locomotion*. Springer-Verlag, Berlin, 2010.

[158] J. Hron and S. Turek. A monolithic FEM/multigrid solver for ALE formulation of fluid-structure interaction with application in biomechanics. In *Fluid-Structure Interaction: Modelling, Simulation, Optimization*. Springer-Verlag, Berlin, 2006.

[159] C. Farhat, K. G. van der Zee, and P. Geuzaine. Provably second-order time-accurate loosely-coupled solution algorithms for transient nonlinear computational aeroelasticity. *Computer Methods in Applied Mechanics and Engineering*, 195:1973–2001, 2006.

[160] M. Hell. An efficient solver for the fully coupled solution of large-displacement fluid-structure interaction problems. *Computer Methods in Applied Mechanics and Engineering*, 193:1–23, 2004.

[161] K. J. Bathe and H. Zhang. Finite element developments for general fluid flows with structural interactions. *International Journal for Numerical Methods in Engineering*, 60:213–232, 2004.

[162] H. Matthies and J. Steindorf. Partitioned strong coupling algorithms for fluid-structure interaction. *Computers and Structures*, 81:805–812, 2003.

[163] H. Matthies, R. Niekamp, and J. Steindorf. Algorithms for strong coupling procedures. *Computer Methods in Applied Mechanics and Engineering*, 195:2028–2049, 2006.

[164] K. J. Bathe and G. A. Ledezma. Benchmark problems for incompressible fluid flows with structural interactions. *Computers and Structures*, 85:628–644, 2007.

[165] C.W. Hirt, A.A Amsden, and J. L. Cook. An arbitrary Lagrangian-Eulerian computing method for all flow speeds. *Journal of Computational Physics*, 14(3):227–253, 1974.

[166] A. L. R. Thomas, G.K. Taylor, R.B. Srgley, R. L. Nudds, and R. J. Bomphrey. Dragonfly flight: Free-flight and tethered flow visualizations reveal a diverse array of unsteady lift-generating mechanisms, controlled primarily via angle of attack. *Journal of Experimental Biology*, 207:4299–4323, 2004.

[167] P. J. Attar. Some results for approximate strain and rotation tensor formulations in geometrically non-linear reissner-mindlin plate theory. *International Journal of Non-Linear Mechanics*, 43(2):81–99, 2008.

[168] T. von Kármán. Festigkeitsprobleme in maschinenbau. *Encyclopedia of Mathematics*, IV/4C:311–385, 1910.

[169] L. Bao, J. Hu, Y. L. Yu, P. Cheng, B. Q. Xu, and B. G. Tong. Viscoelastic constitutive model related to deformation of insect wing under loading in flapping motion. *Journal of Applied Mathematics and Mechanics*, 26(6):741–748, 2006.

[170] F. M. Bos, D. Lentink, B. W. van Ouheusden, and H. Bijl. Influence of wing kinematics on aerodynamic performance in hovering insect flight. *Journal of Fluid Mechanics*, 594:341–368, 2008.

[171] G. J. Berman and Z. J. Wang. Energy-minimizing kinematics in hovering insect flight. *Journal of Fluid Mechanics*, 582:153–168, 2007.

[172] S. N. Fry, R. Sayaman, and M. H. Dickinson. The aerodynamics of free-flight maneuvers in Drosophila. *Science*, 300:495–498, 2003.

[173] M. R. Visbal and D. V. Gaitonde. High-order accurate methods for complex unsteady subsonic flows. *AIAA Journal*, 37(10):1231–1239, 1999.

[174] M. R. Visbal. High-fidelity simulation of transitional flows past a plunging airfoil. *AIAA Journal*, 47(11):2685–2697, 2009.

Appendix A – Conditional average

From a statistical perspective [113], the purpose of the subgrid-scale model $\boldsymbol{\mathcal{M}}$ is to estimate one random variable $\boldsymbol{\tau}$ in terms of another random variable $\tilde{\mathbf{u}}$. We seek a function of $\tilde{\mathbf{u}}$, written as $\boldsymbol{\mathcal{M}}(\tilde{\mathbf{u}})$, to approximate $\boldsymbol{\tau}$ such that the mean-square error is minimal; hence,

$$\mathbf{e} = \left\langle [\boldsymbol{\tau} - \boldsymbol{\mathcal{M}}(\tilde{\mathbf{u}})]^2 \right\rangle = \int_{-\infty}^{\infty} \int_{-\infty}^{\infty} [\boldsymbol{\tau} - \boldsymbol{\mathcal{M}}(\tilde{\mathbf{u}})]^2 \boldsymbol{f}(\boldsymbol{\tau}, \tilde{\mathbf{u}}) \, d\boldsymbol{\tau} d\tilde{\mathbf{u}}, \tag{A.1}$$

where $\boldsymbol{f}(\boldsymbol{\tau}, \tilde{\mathbf{u}})$ is the joint PDF of $\tilde{\mathbf{u}}$ and $\boldsymbol{\tau}$. Knowledge of $\boldsymbol{f}$ is not required, but can be found given $\mathbf{u}$ and $\tilde{\mathbf{u}}$. From the definition of a conditional PDF, $\boldsymbol{f}(\boldsymbol{\tau}, \tilde{\mathbf{u}}) = \boldsymbol{f}(\boldsymbol{\tau}|\tilde{\mathbf{u}}) \boldsymbol{f}(\tilde{\mathbf{u}})$, and (A.1) becomes

$$\mathbf{e} = \int_{-\infty}^{\infty} \boldsymbol{f}(\tilde{\mathbf{u}}) \int_{-\infty}^{\infty} [\boldsymbol{\tau} - \boldsymbol{\mathcal{M}}(\tilde{\mathbf{u}})]^2 \boldsymbol{f}(\boldsymbol{\tau}|\tilde{\mathbf{u}}) \, d\boldsymbol{\tau} d\tilde{\mathbf{u}}. \tag{A.2}$$

Since $\boldsymbol{f}$ must be positive everywhere, both integrands are positive. The mean-square error is minimized with respect to $\tilde{\mathbf{u}}$ if

$$\frac{\partial \mathbf{e}}{\partial \boldsymbol{\mathcal{M}}} = 0 = \int_{-\infty}^{\infty} \boldsymbol{f}(\tilde{\mathbf{u}}) \int_{-\infty}^{\infty} 2 [\boldsymbol{\tau} - \boldsymbol{\mathcal{M}}(\tilde{\mathbf{u}})] \boldsymbol{f}(\boldsymbol{\tau}|\tilde{\mathbf{u}}) \, d\boldsymbol{\tau} d\tilde{\mathbf{u}}, \tag{A.3}$$

which holds if the inner integral evaluates to zero. That is, if

$$\boldsymbol{\mathcal{M}}(\tilde{\mathbf{u}}) = \int_{-\infty}^{\infty} \boldsymbol{\tau} \boldsymbol{f}(\boldsymbol{\tau}|\tilde{\mathbf{u}}) \, d\boldsymbol{\tau} = \langle \boldsymbol{\tau}|\tilde{\mathbf{u}} \rangle . \tag{A.4}$$

Hence, out of all possible representations for $\boldsymbol{\mathcal{M}}(\tilde{\mathbf{u}})$, the mean-square error is minimized when the model is equal to the mean of $\boldsymbol{\tau}$ conditional on $\tilde{\mathbf{u}}$.

Appendix B – Stochastic estimate

A stochastic estimate [65] for the model $\boldsymbol{\mathcal{M}}$ can be found by expanding the conditional average in the form of a multivariate power series about the event $\tilde{\mathbf{u}} = 0$. Since the expansion must be truncated at some level, terms up to quadratic are retained in (2.15). The unknown coefficients $\boldsymbol{\mathcal{A}}$, $\boldsymbol{\mathcal{B}}$ and $\boldsymbol{\mathcal{C}}$ are determined by minimizing the mean-square error between the power series and the conditional average:

$$(e_i)_j^n = \left\langle \left[(\mathcal{M}_i)_j^n - (\mathcal{A}_i)_j^n - \sum_{\alpha}^{M_S} \sum_{\xi}^{M_N} \sum_{\mu}^{M_T} (\mathcal{B}_{i\alpha})_{j\xi}^{n\mu} (\tilde{u}_\alpha)_\xi^\mu - \sum_{\alpha,\beta}^{M_S} \sum_{\xi,\eta}^{M_N} \sum_{\mu,\nu}^{M_T} (\mathcal{C}_{i\alpha\beta})_{j\xi\eta}^{n\mu\nu} (\tilde{u}_\alpha)_\xi^\mu (\tilde{u}_\beta)_\eta^\nu \right]^2 \right\rangle . \tag{B.1}$$

The orthogonality principle [113] states that each term in the mean-square error (B.1) must be statistically uncorrelated with the known data in the domain of interest. For the quadratic estimate, the following inner products must be orthogonal:

$$0 = \left\langle \left[(\mathcal{M}_i)_j^n - (\mathcal{A}_i)_j^n - \sum_{\alpha}^{M_S} \sum_{\xi}^{M_N} \sum_{\mu}^{M_T} (\mathcal{B}_{i\alpha})_{j\xi}^{n\mu} (\tilde{u}_\alpha)_\xi^\mu - \sum_{\alpha,\beta}^{M_S} \sum_{\xi,\eta}^{M_N} \sum_{\mu,\nu}^{M_T} (\mathcal{C}_{i\alpha\beta})_{j\xi\eta}^{n\mu\nu} (\tilde{u}_\alpha)_\xi^\mu (\tilde{u}_\beta)_\eta^\nu \right], 1 \right\rangle \tag{B.2}$$

$$0 = \left\langle \left[(\mathcal{M}_i)_j^n - (\mathcal{A}_i)_j^n - \sum_{\alpha}^{M_S} \sum_{\xi}^{M_N} \sum_{\mu}^{M_T} (\mathcal{B}_{i\alpha})_{j\xi}^{n\mu} (\tilde{u}_\alpha)_\xi^\mu - \sum_{\alpha,\beta}^{M_S} \sum_{\xi,\eta}^{M_N} \sum_{\mu,\nu}^{M_T} (\mathcal{C}_{i\alpha\beta})_{j\xi\eta}^{n\mu\nu} (\tilde{u}_\alpha)_\xi^\mu (\tilde{u}_\beta)_\eta^\nu \right], (\tilde{u}_\gamma)_\phi^\lambda \right\rangle$$

$$0 = \left\langle \left[(\mathcal{M}_i)_j^n - (\mathcal{A}_i)_j^n - \sum_{\alpha}^{M_S} \sum_{\xi}^{M_N} \sum_{\mu}^{M_T} (\mathcal{B}_{i\alpha})_{j\xi}^{n\mu} (\tilde{u}_\alpha)_\xi^\mu - \sum_{\alpha,\beta}^{M_S} \sum_{\xi,\eta}^{M_N} \sum_{\mu,\nu}^{M_T} (\mathcal{C}_{i\alpha\beta})_{j\xi\eta}^{n\mu\nu} (\tilde{u}_\alpha)_\xi^\mu (\tilde{u}_\beta)_\eta^\nu \right], (\tilde{u}_\gamma)_\phi^\lambda (\tilde{u}_\delta)_\psi^\rho \right\rangle$$

The system in (B.2) can be simplified to the form in (2.16) first by letting $\boldsymbol{\mathcal{M}} = \langle \boldsymbol{\tau} | \tilde{\mathbf{u}} \rangle$, then by expanding the inner products, commuting the mean operator through additive terms, assuming constant coefficients and rearranging the final result. The stochastic estimation coefficients can be found with knowledge of the moments amongst $\boldsymbol{\tau}$ and $\tilde{\mathbf{u}}$, assuming they form a linearly independent system in (2.16).

Appendix C – An exact subgrid-scale model

As a special case, an exact subgrid-scale model (one with zero *a priori* error) can be constructed for the HB scheme if (and only if) one harmonic is retained in the analysis (also referred to throughout the literature as the describing function method). Necessary conditions apply: the governing system of equations must contain odd polynomial-type nonlinearities in $\mathbf{R}$ and the response must be time-periodic. Hence, the fully resolved solution for such a system contains only odd temporal harmonics in (2.32). Following the application of a consistent spectral cutoff filter to $\mathbf{u}(t)$, the filtered solution can be written as

$$\tilde{\mathbf{u}}(t) = \hat{\mathbf{u}}^0 + \hat{\mathbf{u}}^1 \cos(\omega t) + \hat{\mathbf{u}}^2 \sin(\omega t). \tag{C.1}$$

An analytical expression for $\boldsymbol{\tau}$ can be derived by substituting the expansions for $\mathbf{u}$ and $\tilde{\mathbf{u}}$ into (2.6) and simplifying the result using the appropriate power-reduction and product-to-sum trigonometric identities. The subgrid-scale force (for a third-order nonlinearity) can then be written as

$$\boldsymbol{\tau}(t) = \hat{\boldsymbol{\tau}}^0 + \hat{\boldsymbol{\tau}}^1 \cos(\omega t) + \hat{\boldsymbol{\tau}}^2 \sin(\omega t) + \hat{\boldsymbol{\tau}}^5 \cos(3\omega t) + \hat{\boldsymbol{\tau}}^6 \sin(3\omega t). \tag{C.2}$$

Higher-order terms (from the FRS) are truncated by the spectral cutoff filter. For the subgrid-scale model, we choose a linear estimate with arbitrary spatially dependent coefficients

$$\boldsymbol{\mathcal{M}}(t) = \hat{\boldsymbol{\mathcal{A}}} + \sum^{M_S} \sum^{M_N} \hat{\boldsymbol{\mathcal{B}}}^1 \hat{\mathbf{u}}^1 \cos(\omega t) + \sum^{M_S} \sum^{M_N} \hat{\boldsymbol{\mathcal{B}}}^2 \hat{\mathbf{u}}^2 \sin(\omega t). \tag{C.3}$$

Now consider the *a priori* error in (2.25), which is based on the subgrid-scale quantities averaged over $\Delta\mathbf{x}$ and Δt (2.22–2.24). Recall from (2.37), the timestep corresponding to the choice of one harmonic ($N_H = 1$) is $\Delta t = 2\pi/3\omega$. If we integrate $\boldsymbol{\tau}$ from t to $t + \Delta t$, the time-averaged result can be written as

$$\langle \boldsymbol{\tau} \rangle_{\Delta\mathbf{x}}^{\Delta t} = \hat{\boldsymbol{\eta}}^0 + \hat{\boldsymbol{\eta}}^1 \cos(\omega t) + \hat{\boldsymbol{\eta}}^2 \sin(\omega t), \tag{C.4}$$

where the coefficients $\hat{\boldsymbol{\eta}}^0$, $\hat{\boldsymbol{\eta}}^1$ and $\hat{\boldsymbol{\eta}}^2$ depend only on $\hat{\mathbf{u}}^0$, $\hat{\mathbf{u}}^1$ and $\hat{\mathbf{u}}^2$. The third harmonic terms in $\langle \boldsymbol{\tau} \rangle_{\Delta\mathbf{x}}^{\Delta t}$ vanish due to integration over $\Delta t = 2\pi/3\omega$. Similarly, the time-averaged model becomes

$$\langle \boldsymbol{\mathcal{M}} \rangle_{\Delta\mathbf{x}}^{\Delta t} = \hat{\boldsymbol{\mu}}^0 + \hat{\boldsymbol{\mu}}^1 \cos(\omega t) + \hat{\boldsymbol{\mu}}^2 \sin(\omega t), \tag{C.5}$$

where the coefficients $\hat{\boldsymbol{\mu}}^0$, $\hat{\boldsymbol{\mu}}^1$ and $\hat{\boldsymbol{\mu}}^2$ are functions of $\hat{\boldsymbol{\mathcal{A}}}$, $\hat{\boldsymbol{\mathcal{B}}}^1$, $\hat{\boldsymbol{\mathcal{B}}}^2$, $\hat{\mathbf{u}}^0$, $\hat{\boldsymbol{u}}^1$ and $\hat{\boldsymbol{u}}^2$. Observe that the basis functions for $\langle \boldsymbol{\tau} \rangle_{\Delta\mathbf{x}}^{\Delta t}$ and $\langle \boldsymbol{\mathcal{M}} \rangle_{\Delta\mathbf{x}}^{\Delta t}$ are identical, and they form a complete orthogonal set. Like terms can be equated. If the number of states in the model M_S is equal to the number of states in the system N_S, the estimation coefficients can be solved for in terms of $\hat{\mathbf{u}}^0$, $\hat{\mathbf{u}}^1$ and $\hat{\mathbf{u}}^2$. We can also express $\langle \boldsymbol{\tau} \rangle_{\Delta\mathbf{x}}^{\Delta t}$ in terms of the estimation coefficients. There are no unresolved terms. This is the reason an exact subgrid-scale model (zero *a priori* error) can be achieved with the describing function method. Higher-order HB schemes do not enjoy the same properties since $\langle \boldsymbol{\tau} \rangle_{\Delta\mathbf{x}}^{\Delta t}$ contains additional terms left unresolved by $\langle \boldsymbol{\mathcal{M}} \rangle_{\Delta\mathbf{x}}^{\Delta t}$.

We return to the generalized Langevin representation [60] of the HB subgrid-scale model in Section 2.9: The non-Markovian memory term in (2.24) must be zero for this particular model due to the selection of a one-point temporal stencil (meaning the dynamics are not projected onto past or future data). The Markovian contribution in (2.24) (the projection onto present data) is complete for the describing function method because we can express $\langle \boldsymbol{\tau} \rangle_{\Delta\mathbf{x}}^{\Delta t}$ exactly in terms of the estimation coefficients.

It naturally follows that the mean of the noise term (orthogonal dynamics) must be zero. Higher-order HB schemes give rise to components in $\langle \boldsymbol{\tau} \rangle_{\Delta \mathbf{x}}^{\Delta t}$ orthogonal to the data in $\langle \boldsymbol{\mathcal{M}} \rangle_{\Delta \mathbf{x}}^{\Delta t}$. In this sense, the nonzero *a priori* errors for higher-order HB schemes can be attributed to the unresolved noise.

Appendix D – Grid convergence for the nonlinear beam

The true response of the nonlinear beam could possibly cover an infinite range of spatiotemporal scales. For practical matters, a simulation may be considered fully resolved if the computational grid resolves all variables to within some tolerance, ϵ. The choice of ϵ is left to the analyst and may vary depending on the application. Influential factors may include precision limitations of the physical or computational variety. Our criterion for a FRS for the beam is straightforward: all spatiotemporal spectra must be converged to within $\epsilon < 10^{-6}$. Any scheme (stable, consistent and convergent) can produce a FRS if the grid parameters (Δx and Δt) are chosen to be sufficiently small. Otherwise, the simulation should be considered a standard ROM when the subgrid-scale models are excluded. The ROMs considered in this study may be under-resolved in space and under-resolved in time (USUT), fully resolved in space and under-resolved in time (FSUT), or under-resolved in space and fully resolved in time (USFT), as described in Figure 1.2.

The RKCS and BTCS schemes are both investigated with respect to their ability to achieve the four different resolutions in Figure 1.2. To this end, we apply a strong external forcing ($F = 10$ and $\omega = 3.76$) for which the beam evolves to a time-periodic response when transients are allowed to decay. In a sense, this task becomes a typical convergence study as shown in Figures D.1, D.2 and D.3. The end result of achievable resolutions are shown in Table D.1, along with the normalized computation times.

We first consider the explicit RKCS scheme, which is prone to numerical instability with coarse timesteps. For example, when the spatial grid is chosen to be $\Delta x = 5.0 \times 10^{-3}$, choosing a timestep of $\Delta t \gtrsim 10^{-6}$ renders the scheme unstable. Further decreasing Δt below 10^{-6} does not affect the outcome within the FRS tolerance.

Scheme	FRS	USFT	FSUT	USUT
RKCS	$\Delta x = 5.0\times10^{-3\star}$ $\Delta t = 1.0\times10^{-6\dagger}$ $\mathcal{T} = 1.0$	$\Delta x = 1.0\times10^{-1}$ $\Delta t = 1.0\times10^{-6\dagger}$ $\mathcal{T} = 5.81\times10^{-2}$	NP	NP
BTCS	NF	NF	$\Delta x = 5.0\times10^{-3\star}$ $\Delta t = 1.0\times10^{-2}$ $\mathcal{T} = 3.72\times10^{-2}$	$\Delta x = 1.0\times10^{-1}$ $\Delta t = 1.0\times10^{-2}$ $\mathcal{T} = 1.09\times10^{-4}$

$\star$	Required to satisfy FRS criteria
$\dagger$	Required for numerical stability
NP	Not possible due to instability with a coarse Δt
NF	Not feasible due to computational expense with required Δt

Table D.1: Resolutions achievable for the SS beam with the RKCS and BTCS schemes (FRS, USFT, FSUT and USUT) with corresponding computation times. Required grid values are in black; representative grid values are in red. The FRS completely resolves all spectra to within $\epsilon < 10^{-6}$ for $F = 10$ and $\omega = 3.76$. Computation times $\mathcal{T}$ are normalized by 0.325 hours, which is the time required to evolve a FRS for one forcing cycle on a computer with a 2.6GHz CPU and 4GB of RAM.

Hence, the stable timestep with $\Delta x = 5.0 \times 10^{-3}$ also happens to be converged. As shown in Table D.1, under-resolved timesteps with USUT and FSUT simulations are not possible with the RKCS scheme. However, as shown in Figure D.1, USFT and FRS results can be found by refining the spatial grid with Δt fixed. For each spatial grid, a time history of the midpoint displacement is shown alongside a snapshot of the quarter-forcing cycle (QFC) spatial configuration. A spectral breakdown of both the spatial and temporal signals reveals a response dominated by odd modes. Even modes are effectively zero and are omitted for clarity. Temporal structures are quite complex, but only three spatial modes exist within the threshold of interest. Despite this simple spatial structure, the RKCS scheme requires a fine spatial grid with $\Delta x = 5.0\times10^{-3}$ to resolve all spatiotemporal spectra to within FRS tolerance. This is due in part to the widespread coupling between microscale and macroscale spatiotemporal structures that occurs in nonlinear systems. In particular, notice a coarse Δx significantly affects both the resolved spatial and temporal spectra.

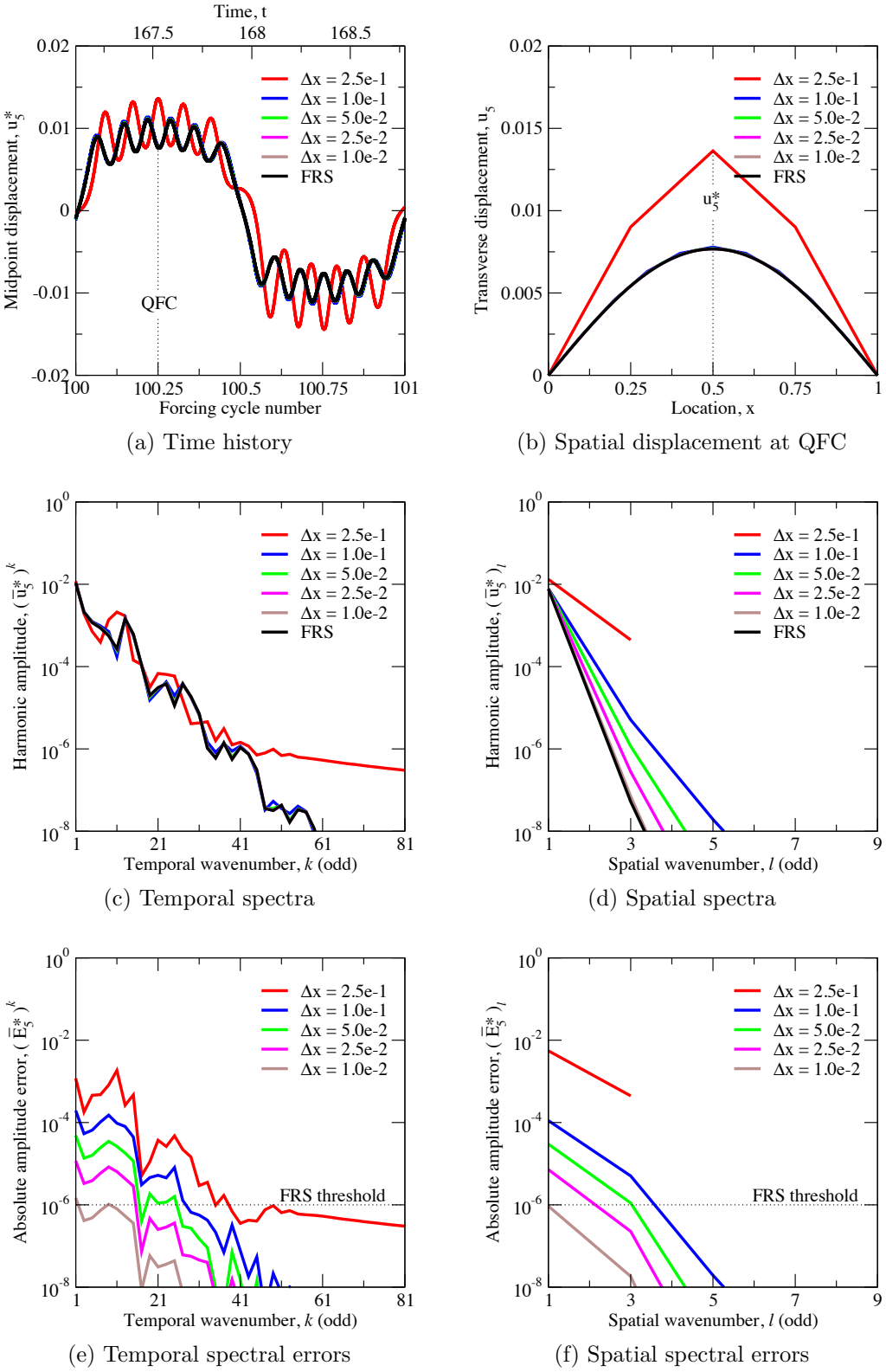

(a) Time history

(b) Spatial displacement at QFC

(c) Temporal spectra

(d) Spatial spectra

(e) Temporal spectral errors

(f) Spatial spectral errors

Figure D.1: Spectral breakdown of USFT and FRS solutions for the SS beam with an external forcing of $F = 10$ and $\omega = 3.76$. Results are obtained using the RKCS scheme in Table D.1 with $\Delta t = 10^{-6}$ and the indicated Δx values. Artificial chaos occurs with $\Delta x = 2.5{\times}10^{-1}$; all other simulations are rightfully time-periodic.

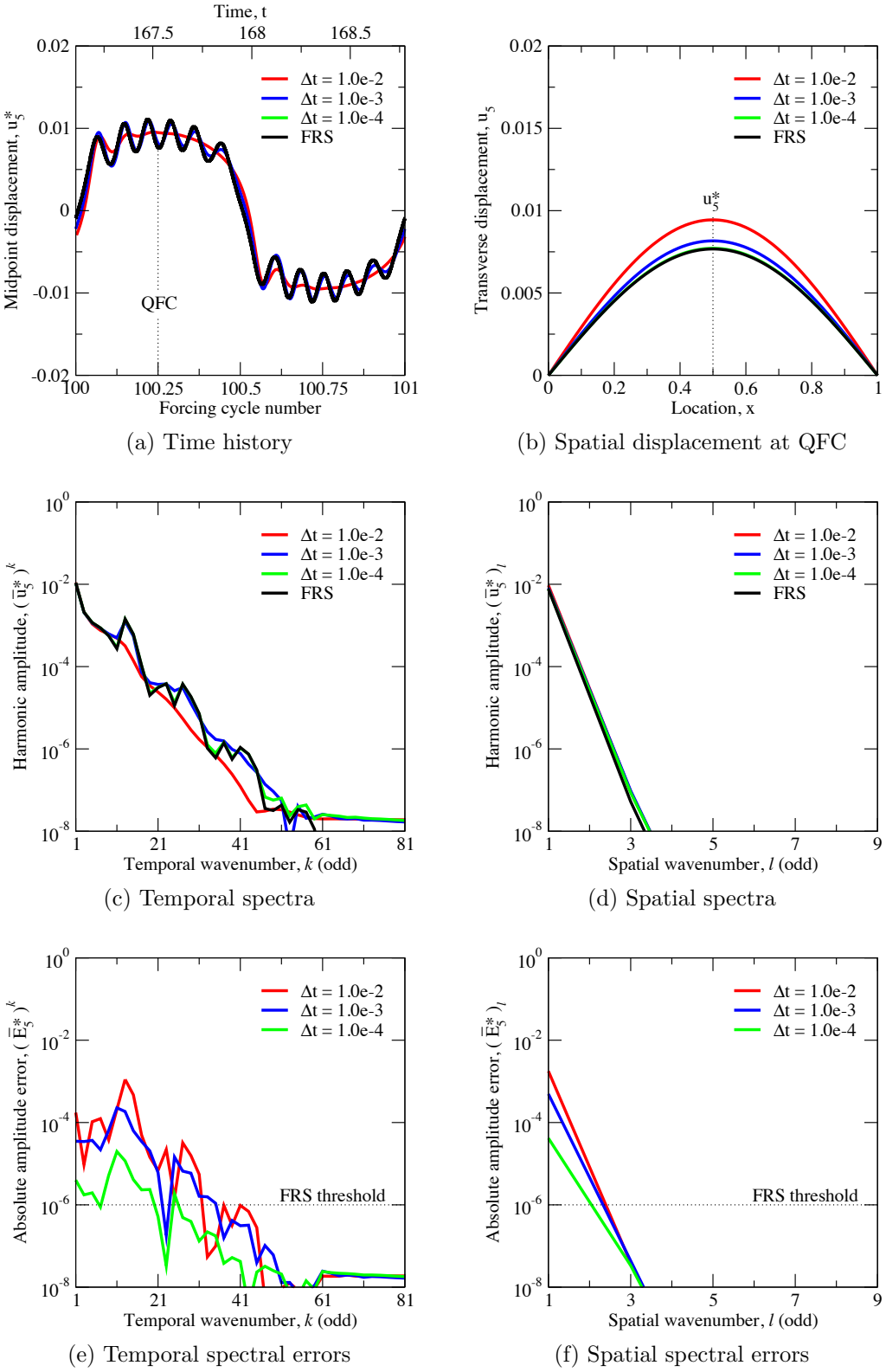

(a) Time history

(b) Spatial displacement at QFC

(c) Temporal spectra

(d) Spatial spectra

(e) Temporal spectral errors

(f) Spatial spectral errors

Figure D.2: Spectral breakdown of FSUT and FRS solutions for the SS beam with an external forcing of $F = 10$ and $\omega = 3.76$. Results are obtained using the schemes in Table D.1 with $\Delta x = 5.0{\times}10^{-3}$ and the indicated Δt values. All simulations are rightfully time-periodic.

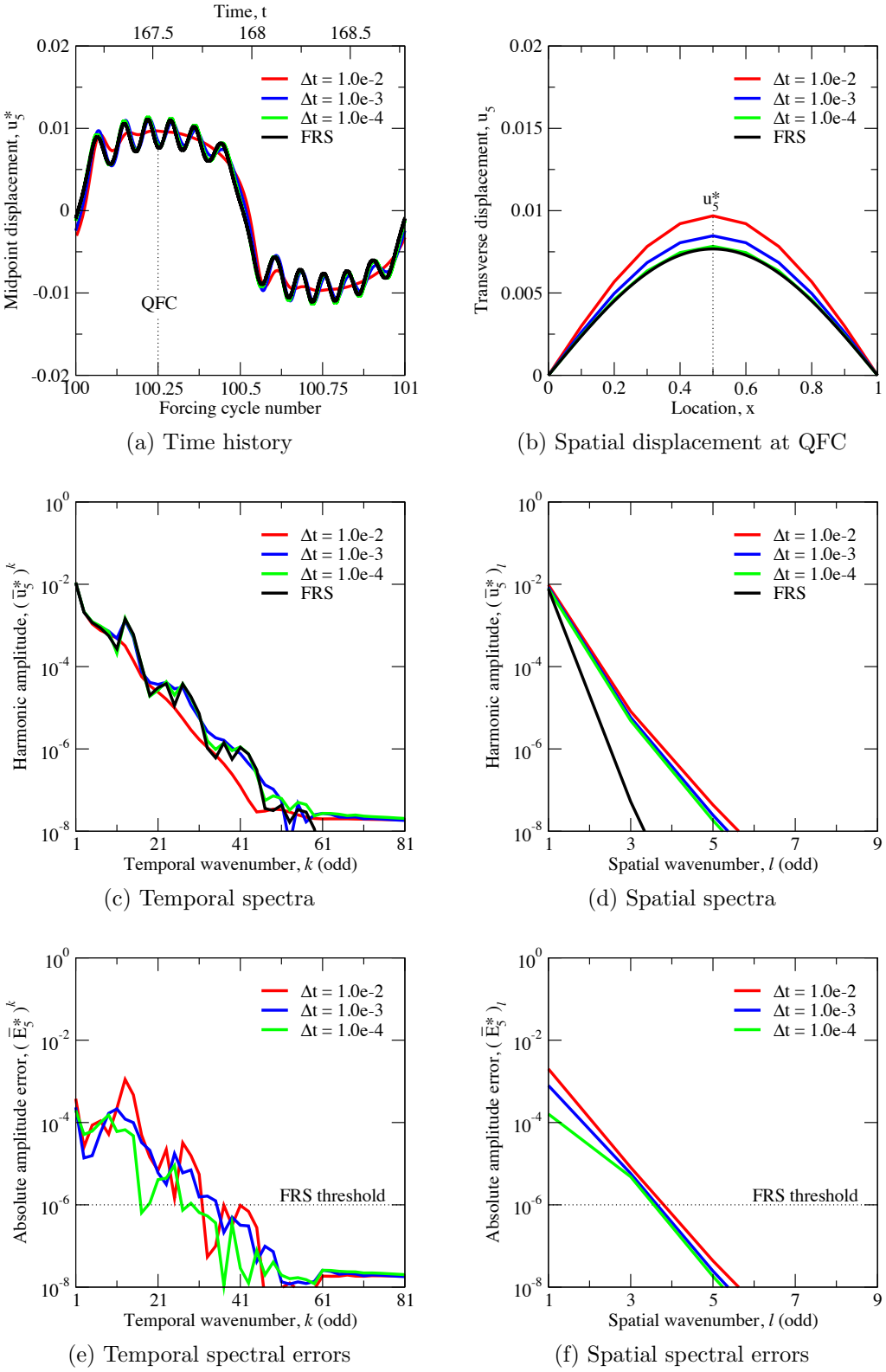

(a) Time history

(b) Spatial displacement at QFC

(c) Temporal spectra

(d) Spatial spectra

(e) Temporal spectral errors

(f) Spatial spectral errors

Figure D.3: Spectral breakdown of USUT and FRS solutions for the SS beam with an external forcing of $F = 10$ and $\omega = 3.76$. Results are obtained using the schemes in Table D.1 with $\Delta x = 1.0{\times}10^{-1}$ and the indicated Δt values. All simulations are rightfully time-periodic.

With the unconditionally stable BTCS scheme, an implicit set of equations must be solved at every timestep with an iterative root finding scheme. Hence, for the same computational grid (Δx and Δt), BTCS calculations are more expensive than RKCS. However, the ability to coarsen Δt allows the analyst to obtain affordable FSUT and USUT solutions with the BTCS scheme. Observe, for example, in Table D.1 that a USUT solution with $\Delta x = 10^{-1}$ and $\Delta t = 10^{-2}$ can be calculated four orders of magnitude faster than the FRS solution. While FRS and FSUT simulations are possible with the BTCS scheme, for this study the RKCS scheme is more efficient for these resolutions, and therefore, will be used to produce FRS solutions.

Returning to Figure 1.2, the coarsest (and fastest) USUT resolution is limited by the beam dimensions and convergence of the BTCS solver. For the beam spanning $x \in [0, 1]$, the largest spatial grid compatible with the chosen FD scheme is $\Delta x = 2.5\times10^{-1}$. The largest timestep is limited as convergence becomes difficult with the NR method for $\Delta t \gtrsim 10^{-2}$. Computational grids chosen from $\Delta x \in [5.0 \times 10^{-3}, 2.5 \times 10^{-1}]$ and $\Delta t \in [10^{-6}, 10^{-2}]$ are considered viable in this study.

FSUT solutions can be obtained with the BTCS scheme as shown in Figure D.2. The spatial grid is fixed at the FRS result $\Delta x = 5.0\times10^{-3}$, whereas the temporal grid is based upon coarse Δt values. Large errors in the temporal spectra indicate a high level of coupling between the microscale and macroscale temporal structures. The most significant errors occur in the thirteenth mode, which is primarily responsible for the secondary vibrations. The spatial spectra display a weaker degree of coupling.

USUT solutions can also be found with the BTCS scheme. Shown in Figure D.3 are solutions for a representative spatial grid of $\Delta x = 10^{-1}$ with the same Δt increments as Figure D.2. The choice of a coarse $\Delta x = 10^{-1}$ primarily affects the accuracy of the higher spatial modes, although some influence can be seen in the dominant temporal structures. The USUT scheme is the fastest of all ROMs for this problem, as shown in Table D.1, where the computation times are reduced by four orders of magnitude.

Appendix E – Subgrid-scale models for the nonlinear beam

Before solving a PDE with OPSTROM, the analyst should determine which subgrid-scale models are "best" for the problem at hand. Influential factors may include error measures, convergence and practical utility. For the nonlinear beam problem, we investigate the performance of several subgrid-scale models for a representative set of forcing parameters ($F = 10$ and $\omega = 3.76$) and grid parameters ($\Delta x = 10^{-1}$ and $\Delta t = 10^{-2}$). For appraisal criteria, we consider the *a priori* and *a posteriori* errors defined in Section 2.10 for transverse velocity and displacement, computation times, the average number of NR iterations per timestep required for convergence, and ease of implementation. Models under consideration include linear and quadratic estimates with one or two states (M_S) and multi-point stencils in space (M_N) and time (M_T). Temporal homogeneity is assumed as the solution for $F = 10$ and $\omega = 3.76$ is periodic. Both spatially homogeneous and nonhomogeneous models are compared. Performance is summarized in Table E.1.

The most basic model in Table E.1 uses a linear stochastic estimate with one state ($M_S = 1$) and a one-point stencil ($M_N = 1$ and $M_T = 1$). Out of all possible states, the transverse displacement $(u_5)_j^n$ renders the best predictions with the most basic model. For the values of F, ω, Δx and Δt considered here, including quadratic terms in the estimate does not improve upon the linear models as the quadratic coefficients are effectively zero. Using two states in the estimate ($M_S = 2$) with transverse displacement $(u_5)_j^n$ and velocity $(u_4)_j^n$ does in fact improve the predictions. Including additional states, however, is prohibited by the fact that $(u_5)_j^n$ and $(u_6)_j^n$ are almost perfectly (negatively) correlated, resulting in an ill-conditioned set of equations for the model coefficients. Moments amongst the longitudinal states ($(u_1)_j^n$, $(u_2)_j^n$ and $(u_3)_j^n$)

[*Model parameters*]	*A priori* errors, e_{u_4} | e_{u_5}	*A posteriori* errors, E_{u_4} | E_{u_5}	Computation time, $\mathcal{T}$	NR iters
Standard USUT				
[None]	1.000 | 1.000	0.709 | 0.157	1.09×10^{-4}	3.52
USUT with homogeneous linear OPSTROM $[(\mathcal{A}_i)^n_j, (\mathcal{B}_{i\alpha})^{n\mu}_{j\xi}]$				
$[M_S=1, M_N=1, M_T=1]$	0.701 | 0.817	0.681 | 0.146	1.18×10^{-4}	3.52
$[M_S=1, M_N=3, M_T=1]$	0.838 | 0.802	0.696 | 0.149	1.21×10^{-4}	3.55
$[M_S=2, M_N=1, M_T=1]$	0.401 | 0.808	0.560 | 0.110	1.25×10^{-4}	3.67
$[M_S=1, M_N=1, M_T=3]$	0.379 | 0.154	0.552 | 0.106	1.29×10^{-4}	3.84
USUT with spatially nonhomogeneous linear OPSTROM $[(\mathcal{A}_i)^n_j, (\mathcal{B}_{i\alpha})^{n\mu}_{j\xi}]$				
$[M_S=1, M_N=1, M_T=1]$	0.682 | 0.817	0.682 | 0.146	1.28×10^{-4}	3.52
$[M_S=1, M_N=3, M_T=1]$	0.699 | 0.672	0.650 | 0.137	1.36×10^{-4}	3.51
$[M_S=2, M_N=1, M_T=1]$	0.389 | 0.806	0.560 | 0.110	1.35×10^{-4}	3.68
$[M_S=1, M_N=1, M_T=3]$	0.369 | 0.153	0.550 | 0.105	1.89×10^{-4}	3.84
USUT with homogeneous quadratic OPSTROM $[(\mathcal{A}_i)^n_j, (\mathcal{B}_{i\alpha})^{n\mu}_{j\xi}, (\mathcal{C}_{i\alpha\beta})^{n\mu\nu}_{j\xi\eta}]$				
$[M_S=1, M_N=1, M_T=1]$	0.701 | 0.817	0.681 | 0.146	1.21×10^{-4}	3.52
$[M_S=2, M_N=1, M_T=1]$	0.401 | 0.808	0.560 | 0.110	1.36×10^{-4}	3.67
$[M_S=1, M_N=1, M_T=3]$	0.379 | 0.154	0.552 | 0.106	1.39×10^{-4}	3.84
USUT with spatially nonhomogeneous quadratic OPSTROM $[(\mathcal{A}_i)^n_j, (\mathcal{B}_{i\alpha})^{n\mu}_{j\xi}, (\mathcal{C}_{i\alpha\beta})^{n\mu\nu}_{j\xi\eta}]$				
$[M_S=1, M_N=1, M_T=1]$	0.682 | 0.817	0.682 | 0.147	1.30×10^{-4}	3.52
$[M_S=2, M_N=1, M_T=1]$	0.389 | 0.806	0.561 | 0.109	1.47×10^{-4}	3.67
$[M_S=1, M_N=1, M_T=3]$	0.369 | 0.153	0.549 | 0.106	1.99×10^{-4}	3.85

$[M_S=1, M_N=1, M_T=1]$ models use $[(u_5)^n_j]$
$[M_S=1, M_N=3, M_T=1]$ models use $[(u_5)^n_{j-1}, (u_5)^n_j, (u_5)^n_{j+1}]$
$[M_S=2, M_N=1, M_T=1]$ models use $[(u_4)^n_j, (u_5)^n_j]$
$[M_S=1, M_N=1, M_T=3]$ models use $[(u_5)^{n-2}_j, (u_5)^{n-1}_j, (u_5)^n_j]$

Table E.1: Appraisal metrics for various subgrid-scale models for the SS beam with an external forcing of $F=10$ and $\omega=3.76$. All models are developed for the BTCS scheme with the OPSTROM variant and a computational grid of Δx=1.0×10^{-1} and Δt=1.0×10^{-2}. Additional models are conceivable; however, increasing the order of the estimate, number states (M_S), spatial stencil (M_N) and temporal stencil (M_T) can produce an ill-conditioned (linearly dependent) system in the stochastic estimation equations. For this set of forcing parameters and resolution, the model highlighted in blue is considered to provide the best combination of accuracy, computational efficiency and simplicity.

are several orders of magnitude smaller, and therefore, relatively insignificant. We model $(\tau_1)_j^n$, $(\tau_2)_j^n$ and $(\tau_3)_j^n$, but $(u_1)_j^n$, $(u_2)_j^n$ and $(u_3)_j^n$ are not used in the estimate.

The spatially nonhomogeneous models in Table E.1 require unique moments and coefficients at each node, and as a result, implementation is more difficult in the pre-processing stage. Nevertheless, the nonhomogeneous models should theoretically provide more accurate predictions. This can be seen in Table E.1 where the *a priori* errors are marginally better for most nonhomogeneous models. Ultimately of greater importance, however, are the *a posteriori* errors, which in most cases vary by less than 1%. The three-point spatial models ($M_N = 3$) deserve some discussion as they are significantly affected by the spatial homogeneity assumption. Compared to the single-point model, the homogeneous three-point models actually *increase* the *a posteriori* errors. This result could have been foreseen given the correlations in Figure 4.15. The nonhomogeneous three-point models do, however, decrease the *a posteriori* errors, but not to the same degree as some of the other options. More sophisticated multi-point spatial models ($M_N > 1$ with $M_T > 1$ and/or $M_S > 1$) are not realizable. Given the longer computation times, lack of major benefit, and difficulty in implementation, we hereby restrict our consideration to spatially homogeneous models with a one-point spatial stencil. It should be made clear, however, that for some problems (such as the viscous Burgers flow), it can be expected that limiting models in this way will not be profitable.

For this problem, we consider the "best" subgrid-scale model for OPSTROM to be a linear stochastic estimate with a three-point backward temporal stencil ($M_T = 3$). The transverse displacements $(u_5)_j^n$, $(u_5)_j^{n-1}$ and $(u_5)_j^{n-2}$ provide the model with enough information to predict the velocity and acceleration at each timestep. Moreover, since $(u_5)_j^n$ is almost perfectly (negatively) correlated with $(u_6)_j^n$, the transverse curvature can also be known with a high degree of accuracy. All of this information is contained (in a statistical sense) in the stochastic estimate. The chosen OPSTROM

model is highlighted in blue in Table E.1. Additional models were investigated but are not shown here, some of which were found to produce an ill-conditioned set of equations for the model coefficients.

We repeat the analysis in Table E.1 to determine the "best" subgrid-scale models for OPSROM and OPTROM. For the OPTROM variant, we select a linear estimate based upon the transverse displacement with a three-point temporal stencil. For the OPSROM variant, we select a linear estimate based upon the transverse displacement and velocity with a one-point stencil. All models are homogeneous in space and time. The "best" models for each scheme are summarized in Table 4.5.

Appendix F – Potential application to fluid-structure interaction problems

In this Appendix, we draft a proposal for future research in which the OPSTROM framework may be used to enhance the reliability and efficiency of simulations for fluid-structure interaction (FSI) problems. We begin with a background discussion on the nature of FSI problems in Section F.1. Implementation of the OPSTROM approach will then be developed in a general manner. The Navier-Stokes equations for an isothermal, incompressible Newtonian flow are modified for OPSTROM in Section F.2, and the field equations for a generic solid continuum are modified for OPSTROM in Section F.3. Details regarding the dynamic coupling of the fluid and structure are discussed in Section F.4. Finally, in Section F.5, we propose for future research an engineering design problem involving high-fidelity aeroelastic simulation of a flapping dragonfly wing.

F.1 Background on fluid-structure interactions

Many engineering systems consist of solid structures that are in contact with at least one fluid. In general, the physics of the fluid and structure are strongly coupled. When a fluid flows around a structure, loads are exerted in the form of pressure and shear stress [139]. Such loads may result in structural deformation, which in turn alters the flow of the fluid. This feedback cycle is known throughout the literature as FSI, and often plays a pivotal role in engineering design [126, 127].

A special form of FSI known as aeroelasticity is commonly used to describe the mutual interaction among inertial, elastic, and aerodynamic forces [140]. The Collar diagram [140], illustrated in Figure F.1, is often used to visualize such interactions.

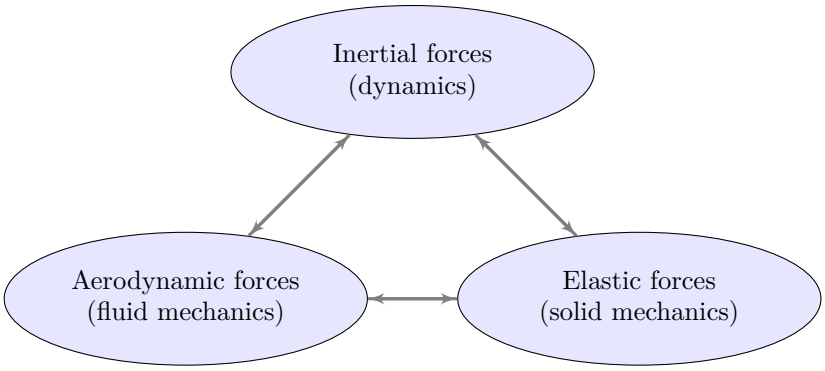

Figure F.1: The Collar diagram [140], which describes aeroelasticity as the mutual interaction amongst inertial, elastic, and aerodynamic forces.

Several aerospace engineering subdisciplines can be identified by pairing nodes in the Collar diagram. Flight dynamics, for example, considers the combination of dynamics and fluid mechanics. Structural dynamics considers dynamics and solid mechanics. Static aeroelasticity considers fluid mechanics and solid mechanics. The combined effect of all three subdisciplines is known as dynamic aeroelasticity.

Flutter is perhaps the most well-known aeroelastic phenomenon and arguably one the most difficult to predict [140, 141]. Flutter is characterized by self-excited vibrations in which a structure feeds upon energy extracted from a fluid. From a mathematical perspective, flutter is the result of a Hopf bifurcation [142] due to parameter modulation of the flow velocity. Below some critical flow velocity, which is also known as the flutter velocity, small perturbations to an aeroelastic system are dissipated through aerodynamic or structural damping. Above the flutter velocity, negative damping occurs, in which case small perturbations to the system result in stable or unstable oscillations. In many cases, such as the Tacoma Narrows bridge collapse [143], flutter can lead to catastrophic structural failures.

Other forms of FSI can be found outside the aerospace arena, including biomedical, civil, chemical, naval and petroleum engineering. To name a few, FSI simulations have been conducted for abdominal aortic aneurysms, heart valves, coronary stents, bridge decks, reactive surface flows, marine catenary risers and biological flyers [126, 127].

Recent demand has escalated for flapping-wing micro aerial vehicles (MAVs) with high maneuverability, portability and stealthiness, in addition to the ability to perch and hover. Such attributes would be ideal for covert operations in perilous situations. Inspiration has been drawn from biological flyers such as insects, birds, and bats, but their abilities to generate sufficient lift remains somewhat of a paradox [144–146]. A number of mechanisms have been identified to enable biological flyers, including dynamic stall, leading edge vortex shedding, and wake capturing [147–151]. With each of these phenomena, wing flexibility seems to play a very important role [152–155]. From a biomimicry perspective, these flight-enabling mechanisms need to be better understood for the purpose of MAV design.

Historically, the primary obstacle to high-fidelity aeroelastic simulation of flapping flight is computational expense [156, 157]. Nevertheless, the latest advancements in supercomputing infrastructure are leading to the possibility of solving the underlying FSI equations to the level of detail required to gain significant insight. Despite the remarkable progress made in supercomputing, innovative solution techniques are still needed to make high-fidelity simulations possible for such problems. In this regard, the author believes that the OPSTROM approach can play a pivotal role in future aeroelastic analysis of flapping flight.

F.2 Fluid dynamic equations of motion

The governing equations of motion for an isothermal, incompressible Newtonian flow are hereby modified for a FSI simulation with the OPSTROM approach. In place of the true velocity field $\mathbf{v}$ and pressure p, the Navier-Stokes equations [139] are written in terms of the filtered velocity field $\widetilde{\mathbf{v}}$ and pressure $\widetilde{p}$. There is no need to filter the fluid density ρ_{F}, as it is assumed to be constant. We consider the fluid to reside in the spatial domain $\boldsymbol{\Omega}_{\mathrm{F}}$, which is enclosed by the surface $\boldsymbol{\Gamma}_{\mathrm{F}} = \boldsymbol{\Gamma}_{\mathrm{F}}^{\mathrm{D}} \cup \boldsymbol{\Gamma}_{\mathrm{F}}^{\mathrm{N}} \cup \boldsymbol{\Gamma}_{\mathrm{FSI}}$, where $\boldsymbol{\Gamma}_{\mathrm{F}}^{\mathrm{D}}$ and $\boldsymbol{\Gamma}_{\mathrm{F}}^{\mathrm{N}}$ are the open surfaces on which Dirichlet and Neumann boundary conditions

are specified, respectively, and $\mathbf{\Gamma}_{\text{FSI}}$ denotes the fluid-structure interface (wetted area). The modified Navier-Stokes equations for the incompressible flow become

$$\rho_{\text{F}}\left(\frac{\partial\widetilde{\mathbf{v}}}{\partial t}+\left(\widetilde{\mathbf{v}}\cdot\nabla\right)\widetilde{\mathbf{v}}\right)=\nabla\cdot\widetilde{\boldsymbol{\sigma}}_{\text{F}}+\mathbf{b}_{\text{F}}+\boldsymbol{\tau}_{\text{F1}}\text{ in }\boldsymbol{\Omega}_{\text{F}} \tag{F.1}$$

$$\nabla\cdot\widetilde{\mathbf{v}}=\boldsymbol{\tau}_{\text{F2}}\text{ in }\boldsymbol{\Omega}_{\text{F}}. \tag{F.2}$$

The first equation in (F.1) represents conservation of momentum, whereas the second equation in (F.2) represents conservation of mass, or continuity. In the momentum equation, the first term on the left-hand side describes local acceleration, and the second term describes nonlinear convection. On the right-hand side of the momentum equation, $\widetilde{\boldsymbol{\sigma}}_{\text{F}}$ denotes the filtered fluid stress tensor, and $\mathbf{b}_{\text{F}}$ is the vector of body forces per unit volume, which in the presence of a gravitational field becomes $\mathbf{b}_{\text{F}}=\rho_{\text{F}}\mathbf{g}$. For an incompressible Newtonian fluid in which μ represents the dynamic viscosity, the true stress tensor is given by

$$\boldsymbol{\sigma}_{\text{F}}=-p\mathbf{I}+\mu\left(\nabla\mathbf{v}+\left(\nabla\mathbf{v}\right)^{\text{T}}\right), \tag{F.3}$$

whereas the filtered stress tensor in (F.1) takes on the following form

$$\widetilde{\boldsymbol{\sigma}}_{\text{F}}=-\widetilde{p}\mathbf{I}+\mu\left(\nabla\widetilde{\mathbf{v}}+\left(\nabla\widetilde{\mathbf{v}}\right)^{\text{T}}\right). \tag{F.4}$$

The final terms in the modified Navier-Stokes equations ($\boldsymbol{\tau}_{\text{F1}}$ and $\boldsymbol{\tau}_{\text{F2}}$) represent the subgrid-scale dynamics for OPSTROM, and are unique from what can be found in the fluids literature. Like the general system in (2.5), $\boldsymbol{\tau}_{\text{F1}}$ and $\boldsymbol{\tau}_{\text{F2}}$ in (F.1) and (F.2) can be split into subgrid-scale forces and accelerations. For the modified momentum equation in (F.1), the subgrid-scale dynamics are given by $\boldsymbol{\tau}_{\text{F1}}=\boldsymbol{\alpha}_{\text{F1}}+\boldsymbol{\gamma}_{\text{F1}}$, where

$$\boldsymbol{\alpha}_{\text{F1}}=\rho_{\text{F}}\left(\frac{\partial\widetilde{\mathbf{v}}}{\partial t}-\widetilde{\frac{\partial\mathbf{v}}{\partial t}}\right) \tag{F.5}$$

$$\boldsymbol{\gamma}_{\mathrm{F}1} = \rho_{\mathrm{F}} \left((\widetilde{\mathbf{v}} \cdot \nabla) \, \widetilde{\mathbf{v}} - \widetilde{(\mathbf{v} \cdot \nabla) \, \mathbf{v}} \right) + \left(\widetilde{\nabla \cdot \boldsymbol{\sigma}_{\mathrm{F}}} - \nabla \cdot \widetilde{\boldsymbol{\sigma}}_{\mathrm{F}} \right). \tag{F.6}$$

Similarly, for the modified continuity equation in (F.2), the subgrid-scale dynamics are given by $\boldsymbol{\tau}_{\mathrm{F}2} = \boldsymbol{\alpha}_{\mathrm{F}2} + \boldsymbol{\gamma}_{\mathrm{F}2}$, where

$$\boldsymbol{\alpha}_{\mathrm{F}2} = 0 \tag{F.7}$$

$$\boldsymbol{\gamma}_{\mathrm{F}2} = \nabla \cdot \widetilde{\mathbf{v}} - \widetilde{\nabla \cdot \mathbf{v}}. \tag{F.8}$$

Models for the subgrid-scale dynamics (F.1) and (F.2) can be constructed with the stochastic estimate in (2.15). For a compressible flow with thermal gradients [139], the modified Navier-Stokes equations must also include a third equation to describe conservation of energy. In addition to the terms in (F.5)–(F.8), one should also take into account the residual fields due to filtered density and energy for such a flow.

The modified Navier-Stokes equations in (F.1) and (F.2) are, in general, subject to the following three types of boundary conditions

$$\begin{aligned}
\widetilde{\mathbf{v}} &= \mathbf{v}_{\mathrm{F}}^{\mathrm{D}} + \boldsymbol{\beta}_{\mathrm{F}}^{\mathrm{D}} \text{ on } \boldsymbol{\Gamma}_{\mathrm{F}}^{\mathrm{D}} && \boldsymbol{\beta}_{\mathrm{F}}^{\mathrm{D}} = \widetilde{\mathbf{v}} - \mathbf{v} \\
\widetilde{\boldsymbol{\sigma}}_{\mathrm{F}} \cdot \widetilde{\mathbf{n}}_{\mathrm{F}} &= \mathbf{t}_{\mathrm{F}}^{\mathrm{N}} + \boldsymbol{\beta}_{\mathrm{F}}^{\mathrm{N}} \text{ on } \boldsymbol{\Gamma}_{\mathrm{F}}^{\mathrm{N}} && \boldsymbol{\beta}_{\mathrm{F}}^{\mathrm{N}} = \widetilde{\boldsymbol{\sigma}}_{\mathrm{F}} \cdot \widetilde{\mathbf{n}}_{\mathrm{F}} - \boldsymbol{\sigma}_{\mathrm{F}} \cdot \mathbf{n}_{\mathrm{F}} \\
\widetilde{\mathbf{v}} &= \frac{\partial \mathbf{u}_{\mathrm{FSI}}}{\partial t} + \boldsymbol{\beta}_{\mathrm{F}}^{\mathrm{FSI}} \text{ on } \boldsymbol{\Gamma}_{\mathrm{FSI}} && \boldsymbol{\beta}_{\mathrm{F}}^{\mathrm{FSI}} = \widetilde{\mathbf{v}} - \mathbf{v},
\end{aligned} \tag{F.9}$$

where $\mathbf{n}_{\mathrm{F}}$ is the outward unit normal vector to the fluid surface, $\tilde{\mathbf{n}}_{\mathrm{F}}$ is the filtered unit normal vector, $\mathbf{v}_{\mathrm{F}}^{\mathrm{D}}$ are the prescribed velocities on the Dirichlet surface, $\mathbf{t}_{\mathrm{F}}^{\mathrm{N}}$ are the prescribed tractions on the Neumann surface, and $\mathbf{u}_{\mathrm{FSI}}$ are the time-dependent structural displacements on the fluid-structure interface. For the latter boundary condition, we have assumed the contact surface to be impermeable and without slip. The final terms ($\boldsymbol{\beta}_{\mathrm{F}}^{\mathrm{FSI}}$, $\boldsymbol{\beta}_{\mathrm{F}}^{\mathrm{D}}$, and $\boldsymbol{\beta}_{\mathrm{F}}^{\mathrm{N}}$) represent the subgrid-scale boundary conditions for the fluid.

F.3 Structural dynamic equations of motion

We consider the solid structure to be a continuum governed by the field equations [138]. In place of the true displacement field $\mathbf{u}$, the field equations are written in terms of the filtered displacements $\widetilde{\mathbf{u}}$ and are modified for OPSTROM. The structure resides in the spatial domain $\mathbf{\Omega}_{\mathrm{S}}$ enclosed by the surface $\mathbf{\Gamma}_{\mathrm{S}} = \mathbf{\Gamma}_{\mathrm{S}}^{\mathrm{D}} \cup \mathbf{\Gamma}_{\mathrm{S}}^{\mathrm{N}} \cup \mathbf{\Gamma}_{\mathrm{FSI}}$, where $\mathbf{\Gamma}_{\mathrm{S}}^{\mathrm{D}}$ and $\mathbf{\Gamma}_{\mathrm{S}}^{\mathrm{N}}$ are the open surfaces on which Dirichlet and Neumann boundary conditions are specified. The fluid-structure interface is defined by $\mathbf{\Gamma}_{\mathrm{FSI}} = \mathbf{\Omega}_{\mathrm{F}} \cap \mathbf{\Omega}_{\mathrm{S}}$. The modified field equations for the structure become

$$\rho_{\mathrm{S}} \frac{\partial^2 \widetilde{\mathbf{u}}}{\partial t^2} = \nabla \cdot \widetilde{\boldsymbol{\sigma}}_{\mathrm{S}} + \mathbf{b}_{\mathrm{S}} + \boldsymbol{\tau}_{\mathrm{S}} \text{ in } \mathbf{\Omega}_{\mathrm{S}}, \tag{F.10}$$

where ρ_{S} represents the density of the structure. The left-hand side of (F.10) describes the inertial loads per unit volume. On the right-hand side, $\widetilde{\boldsymbol{\sigma}}_{\mathrm{S}}$ denotes the filtered stress tensor and $\mathbf{b}_{\mathrm{S}}$ is the vector of body forces per unit volume, which in the presence of a gravitational field becomes $\mathbf{b}_{\mathrm{S}} = \rho_{\mathrm{S}}\mathbf{g}$. The final term in the modified field equations, $\boldsymbol{\tau}_{\mathrm{S}} = \boldsymbol{\alpha}_{\mathrm{S}} + \boldsymbol{\gamma}_{\mathrm{S}}$, represents the subgrid-scale dynamics for OPSTROM, the components for which are given by

$$\boldsymbol{\alpha}_{\mathrm{S}} = \rho_{\mathrm{S}} \left(\frac{\partial^2 \widetilde{\mathbf{u}}}{\partial t^2} - \widetilde{\frac{\partial^2 \mathbf{u}}{\partial t^2}} \right) \tag{F.11}$$

$$\boldsymbol{\gamma}_{\mathrm{S}} = \left(\widetilde{\nabla \cdot \boldsymbol{\sigma}_{\mathrm{S}}} - \nabla \cdot \widetilde{\boldsymbol{\sigma}}_{\mathrm{S}} \right). \tag{F.12}$$

As with the modified fluid equations, both the filtered and unfiltered structural stress tensors are required to compute the subgrid-scale forces in (F.11) and (F.12). Such expressions depend only on the constitutive properties of the solid material, which may be elastic, viscoelastic or plastic [138].

The modified field equations for the structure in (F.10) are, in general, subject to

the following three types of boundary conditions

$$\begin{aligned}
\tilde{\mathbf{u}} &= \mathbf{u}_{\mathrm{S}}^{\mathrm{D}} + \boldsymbol{\beta}_{\mathrm{S}}^{\mathrm{D}} \text{ on } \boldsymbol{\Gamma}_{\mathrm{S}}^{\mathrm{D}} && \boldsymbol{\beta}_{\mathrm{S}}^{\mathrm{D}} = \tilde{\mathbf{u}} - \mathbf{u} \\
\widetilde{\boldsymbol{\sigma}}_{\mathrm{S}} \cdot \tilde{\mathbf{n}}_{\mathrm{S}} &= \mathbf{t}_{\mathrm{S}}^{\mathrm{N}} + \boldsymbol{\beta}_{\mathrm{S}}^{\mathrm{N}} \text{ on } \boldsymbol{\Gamma}_{\mathrm{S}}^{\mathrm{N}} && \boldsymbol{\beta}_{\mathrm{F}}^{\mathrm{N}} = \widetilde{\boldsymbol{\sigma}}_{\mathrm{S}} \cdot \tilde{\mathbf{n}}_{\mathrm{S}} - \boldsymbol{\sigma}_{\mathrm{S}} \cdot \mathbf{n}_{\mathrm{S}} \\
\widetilde{\boldsymbol{\sigma}}_{\mathrm{S}} \cdot \tilde{\mathbf{n}}_{\mathrm{S}} &= -\widetilde{\boldsymbol{\sigma}}_{\mathrm{F}} \cdot \tilde{\mathbf{n}}_{\mathrm{F}} + \mathbf{t}_{\mathrm{FSI}} + \boldsymbol{\beta}_{\mathrm{S}}^{\mathrm{FSI}} \text{ on } \boldsymbol{\Gamma}_{\mathrm{FSI}} && \boldsymbol{\beta}_{\mathrm{S}}^{\mathrm{FSI}} = \widetilde{\boldsymbol{\sigma}}_{\mathrm{S}} \cdot \tilde{\mathbf{n}}_{\mathrm{S}} - \boldsymbol{\sigma}_{\mathrm{S}} \cdot \mathbf{n}_{\mathrm{S}} + \widetilde{\boldsymbol{\sigma}}_{\mathrm{F}} \cdot \tilde{\mathbf{n}}_{\mathrm{F}} - \boldsymbol{\sigma}_{\mathrm{F}} \cdot \mathbf{n}_{\mathrm{F}},
\end{aligned} \tag{F.13}$$

where $\mathbf{n}_{\mathrm{S}}$ is the outward unit normal vector to the structural surface, $\tilde{\mathbf{n}}_{\mathrm{S}}$ is the filtered unit normal vector, $\mathbf{u}_{\mathrm{S}}^{\mathrm{D}}$ are the prescribed displacements on the Dirichlet surface, $\mathbf{t}_{\mathrm{S}}^{\mathrm{N}}$ are the prescribed tractions on the Neumann surface, and $\mathbf{t}_{\mathrm{FSI}}$ are the externally applied tractions to the fluid-structure interface. The final terms ($\boldsymbol{\beta}_{\mathrm{S}}^{\mathrm{FSI}}$, $\boldsymbol{\beta}_{\mathrm{S}}^{\mathrm{D}}$, and $\boldsymbol{\beta}_{\mathrm{S}}^{\mathrm{N}}$) represent the subgrid-scale boundary conditions for the structure.

F.4 Fluid-structure coupling

The governing equations for the fluid and structure in Sections F.2 and F.3 must be discretized and coupled in order to simulate FSI problems. Throughout the FSI literature [158–164], there exist two fundamentally different approaches for solving the coupled equations: monolithic and partitioned. The OPSTROM technique can be used to improve the reliability and efficiency of under-resolved simulations based upon either the monolithic or partitioned approach.

In the monolithic approach [158–161], the governing equations for the fluid and structure are solved simultaneously. The structural equations are typically recast into first-order form and semi-discretized in space. The resulting structural equations are then combined with the fluid equations, also semi-discretized in space, to form a single system of first order ODEs. The system is then fully discretized in time and solved using a preferred time-integration scheme. In order to eliminate the possibility of numerical instability, implicit time-marching schemes are often preferred [164]. One of the potential pitfalls to monolithic schemes is the requirement for both the fluid and structural subsystems to be integrated with the same resolution. In many cases,

however, the range of time scales for the fluid and structural subsystems may be quite different. Hence, in order to sufficiently resolve the physics for one subsystem, excessive computational resources may be wasted on the other.

In the partitioned approach [162–164], the governing equations for the fluid and structure are solved separately with different time-integration schemes and coupled in various ways as the subsystems evolve. Potential benefits to partitioning include (i) reduced computational expense with respect to memory and processing time, (ii) reduced number of subiterations per timestep, (iii) increased flexibility with respect to time-integration strategies, and (iv) increased modularity, which enables the use of pre-existing (off-the-shelf) software [159]. Potential drawbacks to partitioning include (i) increased computational expense with respect to networking time, (ii) increased difficulty in boundary condition enforcement, and (iii) decreased time-accuracy [159].

Whether a monolithic or partitioned framework is used, dynamic coupling is often complicated by the different frames of reference in which the fluid-structure interface is defined. Most CSD solvers use a Lagrangian frame of reference (which is attached to the structure) in $\boldsymbol{\Omega}_{\mathrm{S}}$, whereas CFD solvers typically use an Eulerian frame of reference (which is fixed in space) in $\boldsymbol{\Omega}_{\mathrm{F}}$. Should these frames of reference be used for the fluid and structure, the time-dependent boundary conditions on $\boldsymbol{\Gamma}_{\mathrm{FSI}}$ must be updated in their respective domains by means of coordinate transformation. This mapping can often lead to various numerical pathologies [159,164]. One of the most effective strategies to facilitate this coupling is to use an arbitrary Lagrangian-Eulerian (ALE) frame of reference for the fluid [158, 165]. With the ALE technique, the frame of reference is neither fixed in space or attached to the fluid. Instead, the computational mesh inside $\boldsymbol{\Omega}_{\mathrm{F}}$ is allowed to move arbitrarily to optimize performance, while the nodes on $\boldsymbol{\Gamma}_{\mathrm{FSI}}$ are fixed to the fluid-structure interface [158, 165]. Details for implementing the OPSTROM approach with the ALE technique are currently unknown and may be addressed by future research.

F.5 Aeroelastic analysis of a flapping dragonfly wing

In this Section, we set up a problem for future work in which the OPSTROM approach can be used to simulate a dragonfly in flight. Whereas a number of recent works have indeed investigated flying insects via aeroelastic simulation, we hereby propose an engineering design problem. Dragonflies have evolved to overcome physiological limitations such as muscle strength, endurance, joint flexibility, and wing constitutive properties. From a biomimicry perspective, MAVs need not be burdened by the same limitations. In this regard, the goal of MAV design should not be to imitate biological flyers, but rather to learn from their success and borrow inspiration.

The first step of this proposed research is to reproduce via aeroelastic simulation what dragonflies are able to achieve in the real world. The next step is to glean from the simulations as much as possible about the underlying physics and flight-enabling mechanisms. An engineering design problem can then be formulated in which, under certain constraints, the goal is to optimize performance metrics such as lift, endurance and maneuverability with respect to a number of design parameters such as the wing geometry, material properties and flapping kinematics. Such a task would require many high-fidelity simulations to explore an entire design space, in which case the OPSTROM approach may be the best option available.

Dragonflies are endowed with two pairs of strong transparent wings, and are able to achieve great maneuverability in flight. Lift mechanisms include classical lift at low angles of attack, supercritical lift at high angles of attack, and vortex shedding along the leading edge of the forewings [166]. Wing flexibility and aeroelastic effects seem to play an important role in lift generation [152–156]. Flapping is controlled by powerful muscles at the root of the wings, which can regulate angle of attack, stroke-frequency, amplitude, and the phase between forewings and hindwings [166]. The anatomy of a hindwing is shown in Figure F.2.

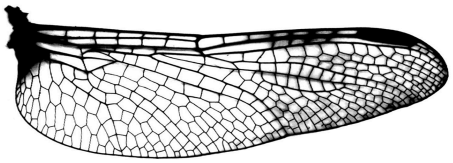

Figure F.2: Physical specimen of a dragonfly hindwing from Thomas et al [166].

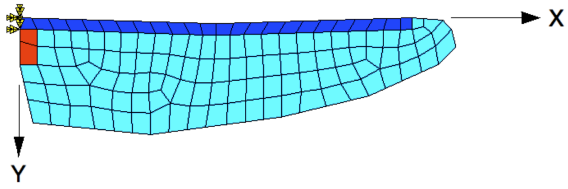

Figure F.3: Finite element mesh of a dragonfly wing from LaBryer and Attar [88]. The mesh is divided into three regions: (i) the leading edge (dark-blue), which contains the stiffest longitudinal veins, (ii) the root (red), which is thick and moderately stiff, and (iii) the wing membrane (light-blue), which is thin and relatively compliant.

The nonlinear structural dynamics of a dragonfly wing can be modeled with the FE method. For this problem, we suggest the geometrically nonlinear VC1 plate elements of Attar [167], which are based upon von Kármán plate theory [168] and contain four nodes, each capable of translations (u, v, w) in (x, y, z) and rotations (θ, ϕ) in (x, y). In addition to the displacement DOFs, the VC1 elements contain two internal shear DOFs for a total of twenty-two DOFs. The VC1 plate elements have proven to be accurate and efficient for small to moderate deflections in comparison to elements based upon higher-order plate theories [167]. For complicated geometries and large deflections (beyond what one would expect to find in a dragonfly wing), elements based upon higher-order plate theories may be appropriate.

LaBryer and Attar [88] recently used the geometrically nonlinear VC1 elements to simulate the nonlinear structural dynamics of a dragonfly with prescribed root rotations in a vacuum (no aerodynamic loads). Their finite element model, shown in Figure F.3, contains approximately 10^3 DOFs. The wing geometry and constitutive behavior are based on previous experimental work by Bao and his colleagues [169].

The finite element model in Figure F.3 has a length from root to tip of $L = 3$ cm and is divided into three regions: (i) the dark-blue leading edge area, which contains the strongest longitudinal veins, (ii) the red anal veins area, and (iii) the light-blue wing membrane area. Regions (i, ii, iii) have thicknesses of (0.135 mm, 0.135 mm, 0.025 mm) and elastic modulii of (60 GPa, 12 GPa, 3.7 GPa), respectively. The true viscoelastic behavior of the wing is approximated with a viscous damping coefficient of 0.05, a uniform density of 1200 kg/m^3, and a lumped mass matrix. The Poisson ratio is unknown, and is assumed to be 0.25 [169].

Previous works have modeled the flapping motion of insect wings with so-called "figure-of-eight" kinematics [170–172]. For the dragonfly wing, we adapt the following equations developed by Berman and his colleagues [171] to prescribe wing rotations at the root

$$\begin{aligned} \phi(t) &= \frac{\phi_m}{\sin^{-1} K} \sin^{-1}\left(K \sin\left(2\pi f t\right)\right) \\ \theta(t) &= \theta_m \cos\left(2\pi N f t + \Phi_\theta\right) + \theta_0 \\ \eta(t) &= \frac{\eta_m}{\tanh C} \tanh\left(C \sin\left(2\pi f t + \Phi_\eta\right)\right), \end{aligned} \tag{F.14}$$

where ϕ is the upstroke angle, θ is the forward stroke angle, and η is the pitch angle. Zero root displacements are assumed. All together, there are eleven parameters with which to prescribe the stroke. The system of equations in (F.14) become the Dirichlet-type boundary conditions for the root surface in (F.13). Specification of the stroke parameters can be considered part of the engineering design problem.

The final task is to simulate the fluid dynamics of the air flow. Due to the low Reynolds number of insect flight ($Re < 1000$), the air is assumed to be incompressible. Viscous effects, however, are known to be important [145], and the air should be treated as a Newtonian fluid according to Section F.2. On the outer surface, the Dirichlet and Neumann boundary conditions in (F.9) should be specified according

to the design objectives. To hover, for example, the free stream velocity should be set to zero. In order to discretize the incompressible Navier-Stokes equations in space, we suggest a high-order accurate FD scheme. In order to discretize the equations in time, we suggest the implicit Euler scheme in (2.30) modified for OPSTROM. Simulations can be carried out with the FDL3DI Navier-Stokes solver [173,174] with the addition of subgrid-scale models for OPSTROM.

Nomenclature

Roman

$\mathbf{A}$	Wavenumber matrix for the harmonic balance method
$\boldsymbol{\mathcal{A}}$	Constant coefficient for the multi-point stochastic estimate
$(\mathcal{A}_i)_j^n$	i^{th} state of $\boldsymbol{\mathcal{A}}$ at spatial node j and timestep n
$(\mathcal{A}_i)$	Homogeneous (in space and time) constant coefficient
A	Linear time-derivative operator
$\boldsymbol{\mathcal{B}}$	Linear coefficient for the multi-point stochastic estimate
$(\mathcal{B}_{i\alpha})_{j\xi}^{n\mu}$	i^{th} state of $\boldsymbol{\mathcal{B}}$ at spatial node j and timestep n
$(\mathcal{B}_{i\alpha})_{\xi}^{\mu}$	Homogeneous (in space and time) linear coefficient
$\mathbf{b}_{\text{F}}$	Fluid body forces
$\mathbf{b}_{\text{S}}$	Structural body forces
$\boldsymbol{\mathcal{C}}$	Quadratic coefficient for the multi-point stochastic estimate
$(\mathcal{C}_{i\alpha\beta})_{j\xi\eta}^{n\mu\nu}$	i^{th} state of $\boldsymbol{\mathcal{C}}$ at spatial node j and timestep n
$(\mathcal{C}_{i\alpha\beta})_{\xi\eta}^{\mu\nu}$	Homogeneous (in space and time) quadratic coefficient
$\mathbf{D}$	Time-derivative operator matrix for the HDHB method
$\mathbf{E}$	*A posteriori* errors with components E_i
$\bar{\mathbf{E}}$	*A posteriori* errors for the harmonic amplitudes in Fourier space
E_ω	*A posteriori* frequency error
$\mathbf{e}$	*A priori* errors with components e_i
$\boldsymbol{\mathcal{F}}$	Discrete Fourier transform operator matrix
$\boldsymbol{\mathcal{F}}^{-1}$	Inverse discrete Fourier transform operator matrix

$\mathcal{F}(x,t)$	Transverse loading function for the beam
F	External forcing amplitude for the Duffing oscillator and beam
ΔF	Forcing amplitude increment
$\boldsymbol{f}(\tilde{\mathbf{u}},\boldsymbol{\tau})$	Joint PDF of $\tilde{\mathbf{u}}$ and $\boldsymbol{\tau}$
$\boldsymbol{f}(\boldsymbol{\tau}\|\tilde{\mathbf{u}})$	Conditional PDF of $\boldsymbol{\tau}$ on $\tilde{\mathbf{u}}$
f	Temporal frequency
$G(\mathbf{x},t)$	Filtering kernel in physical space and time
$\mathcal{G}(l,k)$	Filtering kernel in Fourier space
$\mathbf{g}$	Gravitational acceleration
$\mathbf{I}$	Identity matrix
$\boldsymbol{\mathcal{K}}$	Non-Markovian component of $\boldsymbol{\mathcal{M}}$ (projection onto past data)
$\boldsymbol{\mathcal{M}}(\tilde{\mathbf{u}},\mathbf{x},t)$	Subgrid-scale model
$(\mathcal{M}_i)_j^n$	i^{th} state of $\boldsymbol{\mathcal{M}}$ at spatial node j and timestep n
$(\mathcal{M}_i)$	Homogeneous (in space and time) subgrid-scale model
M_N	Spatial stencil for the subgrid-scale model
M_S	Number of states for the subgrid-scale model
M_T	Temporal stencil for the subgrid-scale model
$\boldsymbol{\mathcal{N}}$	Noise component of $\boldsymbol{\mathcal{M}}$ (orthogonal to the chosen data)
N_D	Number of spatial dimensions in a system
N_H	Number of harmonics
N_N	Number of spatial nodes
N_P	Number of peaks in the response
N_S	Number of states in a system
N_T	Number of timesteps
$\mathbf{n}_{\text{F}}$	Outward unit normal vector to the fluid surface
$\tilde{\mathbf{n}}_{\text{F}}$	Filtered outward unit normal vector to the fluid surface

$\mathbf{n}_{\mathrm{S}}$	Outward unit normal vector to the structural surface
$\tilde{\mathbf{n}}_{\mathrm{S}}$	Filtered outward unit normal vector to the structural surface
$\mathcal{O}(h)$	Terms on the order of h and higher
$\boldsymbol{\mathcal{P}}$	Markovian component of $\boldsymbol{\mathcal{M}}$ (projection onto present data)
p	Fluid pressure
$\tilde{p}$	Filtered fluid pressure
Q_{ik}	Quantity by which moments amongst τ_i and $\tilde{u}_k$ are normalized
$\mathbf{R}(\mathbf{u}, \mathbf{x}, t)$	Nonlinear system function with components R_i
$(R_i)_j^n$	i^{th} state of $\mathbf{R}$ at spatial node j and timestep n
Re	Reynolds number
St	Strouhal number
T	Forcing period or response period
$\mathcal{T}$	Normalized simulation time with respect to the FRS time
$\mathbf{t}_{\mathrm{FSI}}$	Prescribed tractions on the fluid-structure interface
$\mathbf{t}_{\mathrm{F}}^{\mathrm{N}}$	Prescribed tractions on the Neumann fluid surface
$\mathbf{t}_{\mathrm{S}}^{\mathrm{N}}$	Prescribed tractions on the Neumann structural surface
t	Time
t^n	n^{th} timestep
Δt	Uniform timestep
$(\Delta t)_j^n$	Nonuniform timestep
Δt^{FRS}	Timestep for a fully resolved simulation
Δt^{ROM}	Timestep for a reduced order model
$\mathcal{U}$	Characteristic velocity for the Burgers flow
$\mathbf{u}(\mathbf{x}, t)$	State vector with components $u_i(x_k, t)$
$\tilde{\mathbf{u}}$	Filtered state vector
$\hat{\mathbf{u}}$	Residual state vector

$\bar{\mathbf{u}}$	Harmonic amplitudes of $\mathbf{u}$ in Fourier space
$\mathbf{u}_{\text{FSI}}$	Time-dependent displacements on the fluid-structure interface
$\tilde{\mathbf{u}}_{\text{S}}^{\text{D}}$	Prescribed displacements on the Dirichlet structural surface
$(u_i)_j^n$	i^{th} state of $\mathbf{u}$ at spatial node j and timestep n
u_4^*	Transverse velocity of the beam at the midpoint location
u_5^*	Transverse displacement of the beam at the midpoint location
$\mathbf{v}$	Fluid velocity
$\tilde{\mathbf{v}}$	Filtered fluid velocity
$\mathbf{v}_{\text{F}}^{\text{D}}$	Prescribed velocities on the Dirichlet fluid surface
$\mathbf{x}$	Spatial location with components x_k
$(x_k)_j$	Spatial grid coordinates
Δx_k	Uniform spatial grid parameter
$(\Delta x_k)_j^n$	Nonuniform spatial grid parameter
Δx_k^{FRS}	Spatial grid for a fully resolved simulation
Δx_k^{ROM}	Spatial grid for a reduced order model

Greek

$\boldsymbol{\alpha}(\mathbf{u}, \tilde{\mathbf{u}}, \mathbf{x}, t)$	Subgrid-scale acceleration
$\boldsymbol{\alpha}_{\text{F1,F2}}$	Subgrid-scale accelerations for the fluid
$\boldsymbol{\alpha}_{\text{S}}$	Subgrid-scale accelerations for the structure
$(\alpha_i)_j^n$	i^{th} state of $\boldsymbol{\alpha}$ at spatial node j and timestep n
α	Nonlinear damping coefficient for the van der Pol oscillator
$\boldsymbol{\beta}_{\text{F}}^{\text{D}}$	Subgrid-scale Dirichlet-type BCs for the fluid
$\boldsymbol{\beta}_{\text{F}}^{\text{N}}$	Subgrid-scale Neumann-type BCs for the fluid
$\boldsymbol{\beta}_{\text{F}}^{\text{FSI}}$	Subgrid-scale BCs for the fluid on the fluid-structure interface

$\boldsymbol{\beta}_{\mathrm{S}}^{\mathrm{D}}$	Subgrid-scale Dirichlet-type BCs for the structure
$\boldsymbol{\beta}_{\mathrm{S}}^{\mathrm{N}}$	Subgrid-scale Neumann-type BCs for the structure
$\boldsymbol{\beta}_{\mathrm{S}}^{\mathrm{FSI}}$	Subgrid-scale BCs for the structure on the fluid-structure interface
$\boldsymbol{\Gamma}_{\mathrm{FSI}}$	Fluid-structure interface (total wetted area)
$\boldsymbol{\Gamma}_{\mathrm{F}}^{\mathrm{D}}$	Fluid surface subject to Dirichlet-type BCs
$\boldsymbol{\Gamma}_{\mathrm{F}}^{\mathrm{N}}$	Fluid surface subject to Neumann-type BCs
$\boldsymbol{\Gamma}_{\mathrm{S}}^{\mathrm{D}}$	Structural surface subject to Dirichlet-type BCs
$\boldsymbol{\Gamma}_{\mathrm{S}}^{\mathrm{N}}$	Structural surface subject to Neumann-type BCs
$\boldsymbol{\gamma}(\mathbf{u}, \tilde{\mathbf{u}}, \mathbf{x}, t)$	Subgrid-scale force
$\boldsymbol{\gamma}_{\mathrm{F1,F2}}$	Subgrid-scale forces for the fluid
$\boldsymbol{\gamma}_{\mathrm{S}}$	Subgrid-scale forces for the structure
$(\gamma_i)_j^n$	i^{th} state of $\boldsymbol{\gamma}$ at spatial node j and timestep n
δ	Infinitesimal separation used to calculate λ
ϵ_t	Temporal discretization errors
ϵ_x	Spatial discretization errors
ζ	Damping ratio for the Duffing oscillator and beam
η	Pitch angle in the "figure-of-eight" flapping wing motion
θ	Forward stroke angle in the "figure-of-eight" flapping wing motion
$\boldsymbol{\kappa}$	Memory kernel for the generalized Langevin description of $\boldsymbol{\mathcal{M}}$
Λ	Slenderness ratio for the beam
λ	Lyapunov exponent
μ	Dynamic fluid viscosity
ν	Kinematic fluid viscosity
ρ_{F}	Fluid density
ρ_{S}	Structural density
$\boldsymbol{\sigma}_{\mathrm{F}}$	Fluid stress tensor

$\widetilde{\boldsymbol{\sigma}}_{\mathrm{F}}$	Filtered fluid stress tensor
$\boldsymbol{\sigma}_{\mathrm{S}}$	Structural stress tensor
$\widetilde{\boldsymbol{\sigma}}_{\mathrm{S}}$	Filtered structural stress tensor
$\boldsymbol{\tau}(\mathbf{u}, \tilde{\mathbf{u}}, \mathbf{x}, t)$	Subgrid-scale dynamics
$\boldsymbol{\tau}_{\mathrm{F1,F2}}$	Subgrid-scale dynamics for the fluid
$\boldsymbol{\tau}_{\mathrm{S}}$	Subgrid-scale dynamics for the structure
$(\tau_i)_j^n$	i^{th} state of $\boldsymbol{\tau}$ at spatial node j and timestep n
$\boldsymbol{\phi}$	Subset of $\tilde{\mathbf{u}}$ onto which $\boldsymbol{\tau}$ is projected for the model, $\boldsymbol{\mathcal{M}}$
ϕ	Upstroke angle in the "figure-of-eight" flapping wing motion
$\boldsymbol{\Omega}$	Spatial domain in which the system resides
$\boldsymbol{\Omega}_{\mathrm{F}}$	Spatial domain in which the fluid resides
$\boldsymbol{\Omega}_{\mathrm{S}}$	Spatial domain in which the structure resides
ω	External forcing frequency for the Duffing oscillator and beam
ω_p	Peak frequency of the backbone curve
$\Delta\omega$	Forcing frequency increment

Symbols

0^+	Upper limit of zero
∇	Gradient operator
$\nabla\cdot$	Divergence operator
$\nabla\times$	Curl operator
∇^2	Laplacian operator
$\times$	Vector cross product
$\rightarrow$	Approaches
:	Such that

$\forall$	For all
$\in$	An element of
$\cup$	The union of
$\cap$	Intersected with
$\langle \mathbf{u} \rangle$	Mean or expectation of $\mathbf{u}$
$\langle \mathbf{u} \vert \mathbf{v} \rangle$	Mean of $\mathbf{u}$ conditional on $\mathbf{v}$
$\langle \mathbf{u}, \mathbf{v} \rangle$	Inner product of $\mathbf{u}$ and $\mathbf{v}$
$\Vert \mathbf{u} \Vert$	L^2 norm of $\mathbf{u}$
$\mathbf{u}^{\mathrm{T}}$	Transpose of $\mathbf{u}$
$\sum_{i}^{N}$	Summation from i to N

Abbreviations

ALE	Arbitrary Lagrangian-Eulerian
BC	Boundary condition
BTCS	Backward in time, centered in space
CC	Clamped-clamped
CF	Clamped-free
CFD	Computational fluid dynamics
CPU	Central processing unit
CSD	Computational structural dynamics
DFT	Discrete Fourier transform
DNS	Direct numerical simulation
DOF(s)	Degree(s) of freedom
FD	Finite-difference
FE	Finite-element

FRS	Fully resolved simulation
FSI	Fluid-structure interaction
FSUT	Fully-resolved in space and under-resolved in time
FV	Finite-volume
HB	Harmonic balance
HDHB	High dimensional harmonic balance
HMM	Heterogeneous multiscale method
HPC	High performance computing
IC	Initial condition
IE	Implicit Euler
LCO	Limit cycle oscillation
LES	Large-eddy simulation
MAV	Micro aerial vehicle
MD	Molecular dynamic
NF	Not feasible
NMA	Normal modal analysis
NP	Not possible
NR	Newton-Raphson
ODE	Ordinary differential equation
OLES	Optimal large-eddy simulation
OPSTROM	Optimal spatiotemporal reduced order model(ing)
OPSROM	Optimal spatial reduced order model(ing)
OPTROM	Optimal temporal reduced order model(ing)
PDE	Partial differential equation
PDF	Probability density function
POD	Proper orthogonal decomposition

QFC	Quarter-forcing cycle
RAM	Random access memory
RK4	Fourth-order accurate Runge-Kutta
RKCS	Runge-Kutta in time, centered in space
RKPM	Reproducing kernel method
ROM	Reduced order model(ing)
SS	Simply supported
USFT	Under-resolved in space and fully-resolved in time
USUT	Under-resolved in space and under-resolved in time
VC1	Geometrically nonlinear Von Kármán plate elements
VMS	Variational multiscale